



UNIVERSITÀ DEGLI STUDI DI PERUGIA  
FACOLTÀ DI SCIENZE MATEMATICHE, FISICHE E NATURALI  
CORSO DI LAUREA SPECIALISTICA IN SCIENZE CHIMICHE

European Master in TCCM  
*Tesi di laurea specialistica*

## Atmospheric reentry calculations and extension of the formats of Quantum Chemistry data to Quantum Dynamics

*Towards Grid interoperability in quantum chemistry  
and quantum dynamics calculations*

*Calcoli per il rientro in atmosfera ed estensione dei formati dei dati di  
Chimica Quantistica alla Dinamica Quantistica.*

*Verso l'interoperabilità dei calcoli di chimica e dinamica quantistica su Grid*

RELATORE

Prof. Antonio Laganà

LAUREANDO

CO-RELATORE

Marco Verdicchio

Dr. Leonardo Pacifici

CONTRO-RELATORE

Prof. Stefano Evangelisti

ANNO ACCADEMICO 2008-2009

## Contents

<b>Introduction</b>	<b>1</b>
<b>1 Theory and computation for electronic structure calculations</b>	<b>5</b>
1.1 The Born-Oppenheimer separation . . . . .	6
1.2 Theory and computation . . . . .	8
1.2.1 Møller-Plesset perturbation theory . . . . .	10
1.2.2 Coupled Cluster method . . . . .	11
1.2.3 Basis Set Superposition Error . . . . .	13
1.3 Used Computational Procedures . . . . .	14
1.3.1 GAMESS-US . . . . .	15
1.3.2 GAMESS bench input . . . . .	17
1.3.3 GAMESS bench output . . . . .	19
<b>2 Theory and computation for nuclei dynamics: the atom diatom case</b>	<b>21</b>
2.1 Atom diatom equations for the nuclei . . . . .	22
2.1.1 The Jacobi vectors . . . . .	22
2.1.2 Space and Body Fixed reference coordinate frame . . . . .	24
2.1.3 The partial wave expansion . . . . .	26
2.2 Time-dependent (TD) quantum dynamics . . . . .	27
2.2.1 The time dependent equation . . . . .	27
2.2.2 Wavepacket representation . . . . .	28
2.2.3 The formulation of the initial wavepacket . . . . .	30
2.3 The propagation of the wavepacket . . . . .	31
2.3.1 Methods for the hamiltonian evaluation . . . . .	32
2.3.2 Evaluation of the effect of the hamiltonian on the wavepacket . . . . .	35
2.3.3 Wavepacket propagation and analysis . . . . .	37

2.4	The time independent (TI) method . . . . .	41
2.4.1	Hyperspherical coordinates . . . . .	41
2.4.2	Delves hyperspherical coordinates . . . . .	44
2.4.3	Hyperspherical adiabatic coordinates . . . . .	45
2.5	Hamiltonian formulation and boundary conditions . . . . .	48
2.5.1	Asymptotic boundary conditions . . . . .	49
2.5.2	The scattering, reactance and transition matrices . . . . .	51
2.5.3	BF Jacobi wavefunctions . . . . .	53
2.6	The integration of TI scattering equations . . . . .	56
2.6.1	The propagation in Delves coordinates . . . . .	57
2.6.2	Delves to Jacobi projection . . . . .	59
2.6.3	Coupled Channel equations . . . . .	60
2.7	From Theory to experimental observables . . . . .	63
2.7.1	Exact probabilities, cross sections and rate coefficients . . . . .	63
2.7.2	Approximate quantum methods . . . . .	64
2.8	<i>J</i> -shift approximation . . . . .	65
<b>3</b>	<b>Computing GRID</b> . . . . .	<b>67</b>
3.1	EGEE: the European Grid for e-science . . . . .	68
3.1.1	The key features of the Grid . . . . .	68
3.1.2	The Middleware . . . . .	69
3.1.3	Building on national projects . . . . .	71
3.2	The European project EGEE . . . . .	72
3.2.1	The grid for scientific communities . . . . .	72
3.2.2	COMPChem: the molecular science Virtual Organization . . . . .	73
3.2.3	COMPChem applications . . . . .	75
3.3	Aiming at interoperability . . . . .	78
3.3.1	Data Formats for Quantum Chemistry . . . . .	78
3.3.2	The QC-Markup Language . . . . .	79
3.3.3	The QC-ML structure . . . . .	80
3.4	The proposed format . . . . .	82
3.4.1	The Q5cost tool . . . . .	83
3.4.2	The Q5cost library . . . . .	86
3.4.3	The Wrappers . . . . .	87
3.5	Towards the European Grid Initiative . . . . .	88

3.5.1	The Chemistry and Material Sciences and Technologies SSC . . . . .	88
3.5.2	Web service approach . . . . .	90
3.5.3	The quality evaluation . . . . .	91
<b>4</b>	<b>The <math>N(^4S) + N_2(^1\Sigma_g^+)</math> and <math>N_2(^1\Sigma_g^+) + N_2(^1\Sigma_g^+)</math> reactions</b>	<b>93</b>
4.1	The electronic structure of $N + N_2$ and its Many Body representation . . . . .	94
4.1.1	The many body expansion . . . . .	95
4.1.2	The two body terms . . . . .	96
4.1.3	The three body term . . . . .	99
4.2	From Many Body to Many Process LAGROBO representations . . . . .	100
4.2.1	From LEPS to ROBO . . . . .	100
4.2.2	The LAGROBO functional and the Many Process Expansion . . . . .	103
4.2.3	The characteristics of the various $N + N_2$ LAGROBO PESs . . . . .	106
4.3	The reactive properties of $N + N_2$ . . . . .	115
4.3.1	From LEPS to LAGROBO PESs results . . . . .	115
4.3.2	L3 Vs LEPS . . . . .	117
4.3.3	The new LAGROBO PES L4 and related results . . . . .	126
4.4	The $N_2(^1\Sigma_g^+) + N_2(^1\Sigma_g^+)$ reaction . . . . .	141
4.4.1	Previous work on $N_2 + N_2$ . . . . .	142
4.4.2	Our MP and CCSD <i>ab initio</i> calculations . . . . .	143
4.4.3	Computational Details . . . . .	145
4.5	The Interaction Energy . . . . .	147
4.5.1	MP <i>ab initio</i> results . . . . .	147
4.5.2	CCSD(T) <i>ab initio</i> results . . . . .	156
4.5.3	MP2 versus CCSD(T) . . . . .	158
4.6	Building an overall potential energy surface . . . . .	162
4.6.1	Possible reactive processes . . . . .	166
4.6.2	Four atom systems fitting tools . . . . .	167
4.6.3	An estimate of the thermal rate coefficient . . . . .	169
<b>5</b>	<b>Conclusions</b>	<b>175</b>
	<b>The bibliography</b>	<b>177</b>

VIRT&L-COMM.9.2016.3

## Introduction

*L'approccio teorico a diverse applicazioni scientifiche di tipo ambientale e tecnologico si è notevolmente evoluto grazie al formidabile sviluppo degli strumenti delle Tecnologie per la Comunicazione e l'Informazione (TCI). Di fatto, gli scienziati hanno sempre meno a che fare con problemi puramente teorici. Al contrario, sempre maggiore è l'impegno che essi approfondono in problemi pratici la cui soluzione, però, necessita di ricerche scientifiche avanzate e notevoli investimenti in termini di risorse computazionali.*

*Fortunatamente, i recenti sviluppi delle TCI mettono a disposizione dei ricercatori piattaforme computazionali sempre più evolute il cui utilizzo consente la risoluzione di problemi di sempre maggior complessità. Attualmente la Grid computazionale sta diventando rapidamente la piattaforma di riferimento. Essa sfrutta la rete Internet per fare leva sulla potenza di diverse migliaia di computer geograficamente distribuiti, per farli operare insieme grazie a middleware appositamente sviluppati. La grid computazionale rende possibile l'esecuzione contemporaneamente un grosso numero di applicazioni (programmi) e quindi portare a termine sofisticate simulazioni in tempi relativamente brevi.*

*Nel mio lavoro di tesi, all'interno dei lavori svolti dal gruppo Computational Dynamics and Kinetics (CDK) del Dipartimento di Chimica dell'Università di Perugia, ho impiegato le potenzialità della grid per studiare alcuni problemi della modellistica per il rientro in atmosfera. In tale situazione la navetta spaziale non risente solamente delle condizioni estreme del regime fluidodinamico del gas circostante, ma anche di diversi processi critici che possono avvenire all'interno della fase gassosa e tra la fase gassosa e il rivestimento della navetta stessa. Nello specifico il mio lavoro è stato incentrato sullo studio delle reazioni in fase gassosa e più precisamente sullo studio teorico delle collisioni reattive dei processi  $N + N_2$  e  $N_2 + N_2$ . La comprensione di questi tipi di collisione è, infatti, necessaria per razionalizzare le proprietà (energetiche e di composizione) dell'aria che fluisce attorno ad una navicella al rientro e per comprendere la loro natura microscopica.*

*Uno dei problemi associati all'uso della Grid per questo tipo di studi, sta nella possibilità di comporre vari strumenti di chimica e dinamica quantistica per effettuare estesi calcoli computazionali, utilizzando un workflow comune e modelli e rappresentazioni comuni dei dati. Il lavoro associato a questo sforzo deve essere ancora dispiegato nella sua interezza e la mia tesi vuole essere un primo passo nella direzione di una generalizzazione a sistemi con un numero crescente di atomi. Per questi motivi la tesi è stata articolata nelle seguenti sezioni:*

- *Sezione 1 descrive i fondamenti teorici e le procedure computazionali sviluppate per il calcolo delle strutture elettroniche per i sistemi presi in esame;*
- *Sezione 2 descrive i fondamenti teorici e le procedure computazionali sviluppate per simulare la dinamica dei nuclei;*
- *Sezione 3 descrive le innovative tecnologie computazionali necessarie per l'uso della Grid come piattaforma computazionale per effettuare calcoli complessi e ottenere un'elevata interoperabilità;*
- *Sezione 4 descrive i progressi fatti nello studio della reazione atomo diatomo  $N + N_2$  e nell'impostare il lavoro per il diatomo-diatomo  $N_2 + N_2$ ;*
- *Sezione 5 vengono presentate le conclusioni e le linee guida per lavori futuri.*



Theoretical approaches to various environmental and technological scientific applications have significantly evolved thanks to the impressive evolution of Information and Communication Technology (ICT) means. As a matter of fact, scientists are seldom facing purely theoretical problems. On the contrary, they are more and more getting involved in practical problems whose solutions, however, require advanced scientific research and impressive investment in terms of computing.

Fortunately, recent evolution of ICT is increasingly offering to scientists computational platforms whose exploitation allows to solve computational problems of high complexity. At present the computing grid is rapidly becoming the platform of reference. The computing grid exploits internet connections to leverage on the power of several thousands of geographically dispersed computers concurrently operating thanks to *ad hoc* designed middlewares. The computing grid makes it feasible to run concurrently large batches of jobs and perform several complex simulations in

relatively short time.

In my thesis work I exploited, within the activities of the Computational Dynamics and Kinetics (CDK) group of the Department of Chemistry of the University of Perugia, the potentialities of grid computing when dealing with the problem of modeling atmospheric reentry. In this situation a spacecraft experiences not only extreme conditions for the fluid dynamics regime of surrounding gases, but also undergoes the effect of several gas-gas and gas surface critical chemical processes. In particular, my work has focused on the study of the two pure gas phase reactions  $N + N_2$  and  $N_2 + N_2$ . The understanding of these reactive collisions is, in fact, necessary to rationalize the energetic and composition properties of air flowing around a reentering spacecraft and to understand their microscopic nature.

A problem associated with the exploitation of the Grid for this type of calculations is the possibility of composing various quantum chemistry and quantum dynamics tools to perform extended computational campaigns, using a common workflow and common models and representation for data. The associated work is still largely to be deployed in its entirety and my thesis work represents a first step in the direction of a generalization to systems with an increasing number of atoms. Accordingly, the thesis is articulated into the following sections:

- Section 1 describes the theoretical foundations and the computational procedures concerning the calculation of the electronic structure of the chemical systems considered;
- Section 2 describes the theoretical foundations and the computational procedures developed to calculate the dynamics of the nuclei;
- Section 3 describes the innovative computational technologies needed to use the Grid as a computing platform and the first steps accomplished to obtain high interoperability;
- Section 4 describes the results obtained for the study of the atom-diatom  $N + N_2$  reaction, putting the foundations for the study of the diatom-diatom  $N_2 + N_2$  reaction;
- Section 5 draws some conclusions and illustrates some guidelines for future work.



## Chapter 1

# Theory and computation for electronic structure calculations

*In questo capitolo, come già specificato nell'introduzione, poniamo i fondamenti teorici e le procedure computazionali utilizzate per lo studio delle strutture elettroniche dei sistemi considerati. Nella sezione 1.1 analizziamo brevemente le basi dell'approssimazione Born-Oppenheimer che ci permette di diminuire la dimensionalità del problema separando il moto dei nuclei da quello degli elettroni.*

*Nella sezione 1.2 vengono invece analizzate in dettaglio le avanzate tecniche teoriche usate per il recupero dell'energia di correlazione, uno degli ostacoli più grandi per quanto riguarda lo studio delle strutture elettroniche, e il metodo adottato per la correzione del Basis Set Superposition Error. Nella sezione 1.3 viene esaminata la procedura computazionale utilizzata, e le specifiche del codice impiegato.*

• • •

The theoretical treatment of chemical reactions is, in principle, well established. It starts by considering the overall system as made of various fragments depending on the values of the inter-nuclear distances (which are arranged differently in the reactant and product arrangements). The system is then modeled as an ensemble of  $M$  nuclei (each nucleus is considered as a single entity) and  $N$  electrons. At this point, the equations deriving from the first principles are written by properly

formulating an Hamiltonian operator  $\hat{H}$  and a mathematical function  $\Psi$  (called system wavefunction) that has the property of describing the spatial and temporal distribution of the system.

## 1.1 The Born-Oppenheimer separation

The general expression of the (non relativistic) hamiltonian describing the evolution from reactants to products for a reactive system with  $M$  nuclei and  $N$  electrons is given by:

$$\begin{aligned} \hat{H} = & - \sum_{i=1}^N \frac{\hbar^2}{2m_e} \nabla_i^2 - \sum_{A=1}^M \frac{\hbar^2}{2M_A} \nabla_A^2 \\ & - \sum_{i=1}^N \sum_{A=1}^M \frac{Z_A e^2}{r_{iA}^*} + \sum_{i=1}^N \sum_{j>i}^N \frac{e^2}{r_{ij}^*} + \sum_{A=1}^M \sum_{B>A}^M \frac{Z_A Z_B e^2}{R_{AB}^*} \end{aligned} \quad (1.1)$$

where  $\hbar = h/2\pi$  (with  $h$  being the Planck's constant),  $m_e$  is the mass of the electron,  $M_A$  is the mass of the nucleus  $A$ ,  $e$  is the charge of the electron,  $Z_A e$  is the charge of the nucleus  $A$ ,  $r_{iA}^*$  is the distance between the electron  $i$  and the nucleus  $A$ ,  $r_{ij}^*$  is the distance between the electrons  $i$  and  $j$ , and  $R_{AB}^*$  is the distance between the nuclei  $A$  and  $B$ . In eq. 1.1 the first and the second terms represent the electronic and the nuclear (differential) kinetic operators, respectively, while the third, the fourth and the fifth terms represent attraction between electrons and nuclei, repulsion between electrons and the repulsion between nuclei coulombic potential (multiplicative) operators, respectively.

The general description of the position of the system at any instant, is given by the wavefunction  $\Psi(\mathbf{R}^*, \mathbf{r}^*, t)$  which is solution of the time-dependent Schrödinger equation:

$$\hat{H}\Psi(\mathbf{R}^*, \mathbf{r}^*, t) = i\hbar \frac{\partial}{\partial t} \Psi(\mathbf{R}^*, \mathbf{r}^*, t) \quad (1.2)$$

where  $\mathbf{R}^*$  and  $\mathbf{r}^*$  represent collectively the nuclear and the electronic position vectors, respectively, referred to an arbitrary system of reference.

The solution of equation 1.2 is extremely difficult and cannot in general be expressed in a closed form. To simplify the equation one may consider to adopt decoupling and/or simplification schemes. Usually, the first move is to separate the center of mass (c.m.) of the system. Then, one exploits the fact that the nuclei are much heavier than the electrons and introduces the approximation of separating the nuclear from the electronic motion (Born-Oppenheimer approximation). Finally one adopts an appropriate technique to integrate related equations.

The first step of decoupling the equations for the center of mass is based on the fact that its motion remains unaltered when no external forces act on the system. Accordingly, one can express the hamiltonian as a sum of terms referred to the c.m. and a sum of terms associated with the relative motion of the particles. To this end a new system of unstarred position vectors referred to the position vector of the c.m.  $\mathbf{S}$  can be defined [1]:

$$\mathbf{S} = \frac{1}{M_{\text{tot}}} \left( \sum_{A=1}^M M_A \mathbf{R}_A^* + \sum_{i=1}^N m_e \mathbf{r}_i^* \right) \approx \frac{1}{M_0} \sum_{A=1}^M M_A \mathbf{R}_A^*$$

$$\mathbf{r}_i = \mathbf{r}_i^* - \mathbf{S} \quad i = 1, \dots, N$$

$$\mathbf{R}_A = \mathbf{R}_A^* - \mathbf{S} \quad A = 1, \dots, M$$

where  $M_0$  represents the total mass of the nuclei,  $M_0 = \sum_{A=1}^M M_A$ , and  $M_{\text{tot}}$  is the total mass of the system,  $M_{\text{tot}} = M_0 + Nm_e$ . The  $\mathbf{r}_i$  vector indicates the position of the electron  $i$  with respect to the c. m. and the  $\mathbf{R}_A$  vector indicates the position of the nucleus  $A$  with respect to the c.m. Since the mass of the system is in practice almost entirely localized in the nuclei, the position vector of the center of mass,  $\mathbf{S}$ , can be approximated by the position vector of the center of mass of the nuclei only.

By placing the center of mass at the origin of the coordinate system one has that the coordinate of one of the atoms of the system (say C) is related to the position of all the other atoms ( $A \neq C$ ) as follows:

$$\mathbf{R}_C = -\frac{1}{M_C} \sum_{A=1, A \neq C}^M M_A \mathbf{R}_A$$

Using these new coordinates, the hamiltonian operator can be written as:

$$\begin{aligned} \hat{H} = & -\frac{\hbar^2}{2M_{\text{tot}}} \nabla_S^2 - \frac{\hbar^2}{2} \left( \frac{1}{m_e} + \frac{1}{M_0} \right) \sum_{i=1}^N \nabla_i^2 - \frac{\hbar^2}{2M_0} \sum_{i=1}^N \sum_{i>j}^N \nabla_i \nabla_j \\ & - \frac{\hbar^2}{2} \sum_{A=1, A \neq C}^M \left( \frac{1}{M_A} + \frac{1}{M_0} \right) \nabla_A^2 + \frac{\hbar^2}{2M_0} \sum_{A=1, A \neq C}^M \sum_{B>A, B \neq C}^M \nabla_A \nabla_B \\ & - \sum_{i=1}^N \sum_{A=1}^M \frac{Z_A e^2}{r_{iA}} + \sum_{i=1}^N \sum_{j>i}^N \frac{e^2}{r_{ij}} + \sum_{A=1}^M \sum_{B>A}^M \frac{Z_A Z_B e^2}{R_{AB}} \end{aligned} \quad (1.3)$$

It is important to emphasize here that since the electrostatic interaction between nuclei and electrons depends on their relative distance, the last three terms of this expression coincide with those of eq. 1.1. The only term dependent on the center of mass coordinates is the first one which represents the translational motion of the whole system and therefore it simply adds a constant to the total energy of the reactive system.

The second step of separating the the equations of the nuclei from those of the electrons (the already mentioned Born-Oppenheimer (or adiabatic) approximation, based on the fact that since the mass of the nuclei is much larger than that of the electrons allowing so far the electrons to move around quite a lot in the time it takes the nuclei to move a short distance) can be tackled by rewriting the hamiltonian of eq. 1.3 (after the separation of the center of mass motion) as follows:

$$\hat{H} = \hat{T}_N + \hat{T}_e + U_{eN} + U_{ee} + U_{NN} = \hat{T}_N + \hat{H}_e \quad (1.4)$$

where  $\hat{H}_e = \hat{T}_e + U_{eN} + U_{ee} + U_{NN}$  with

$$\begin{aligned} \hat{T}_N &= -\frac{\hbar^2}{2} \sum_{A=1}^M \left( \frac{1}{M_A} + \frac{1}{M_0} \right) \nabla_A^2 + \frac{\hbar^2}{2M_0} \sum_{A=1}^M \sum_{B>A}^M \nabla_A \nabla_B \\ \hat{T}_e &= -\frac{\hbar^2}{2} \left( \frac{1}{m_e} + \frac{1}{M_0} \right) \sum_{i=1}^N \nabla_i^2 - \frac{\hbar^2}{2M_0} \sum_{i=1}^N \sum_{j>i}^N \nabla_i \nabla_j \\ U_{eN} &= -\sum_{i=1}^N \sum_{A=1}^M \frac{Z_A e^2}{r_{iA}} \quad U_{ee} = \sum_{i=1}^N \sum_{j>i}^N \frac{e^2}{r_{ij}} \quad U_{NN} = \sum_{A=1}^M \sum_{B>A}^M \frac{Z_A Z_B e^2}{R_{AB}} \end{aligned}$$

In a solution scheme in which the Schrödinger equation 1.2 is integrated by expanding the total wavefunction as a linear combination of the electronic functions  $\Phi_n(\mathbf{r}; \mathbf{R})$  as follows:

$$\Psi(\mathbf{R}, \mathbf{r}, t) = \sum_n \chi_n(\mathbf{R}, t) \Phi_n(\mathbf{r}; \mathbf{R}) \quad (1.5)$$

where the coefficients of the expansion, the nuclear functions  $\chi_n(\mathbf{R}, t)$ , depend on time and on the nuclear coordinates only, while the electronic functions  $\Phi_n(\mathbf{r}; \mathbf{R})$  depend on both the electronic coordinates and (parametrically) on the nuclear coordinates, one has first to construct the set of  $\Phi_n$  electronic eigenfunctions (at all the needed fixed values of  $\mathbf{R}$  (adiabatic representation)) by solving the eigenvalue ( $E_n$ ) problem:

$$\hat{H}_e \Phi_n(\mathbf{r}; \mathbf{R}) = E_n \Phi_n(\mathbf{r}; \mathbf{R}) \quad (1.6)$$

## 1.2 Theory and computation

By replacing eq. 1.5 in the Schrödinger equation 1.2 one obtains:

$$\left( \hat{T}_N + \hat{H}_e \right) \sum_n \Phi_n(\mathbf{r}; \mathbf{R}) \chi_n(\mathbf{R}, t) = i\hbar \sum_n \Phi_n(\mathbf{r}; \mathbf{R}) \frac{\partial}{\partial t} \chi_n(\mathbf{R}, t) \quad (1.7)$$

Multiplying this expression by  $\Phi_{n'}^*$ , integrating over electronic coordinates and considering the orthonormality of the basis functions ( $\langle \Phi_n | \Phi_{n'} \rangle = \delta_{nn'}$ ), eq. 1.7 can be written for a given electronic

state  $n$  as:

$$\left[ E_{nn} + \hat{a}_{nn} + \hat{b}_{nn} + \hat{T}_N \right] \chi_n(\mathbf{R}, t) + \sum_{n' \neq n} \hat{c}_{nn'} \chi_{n'}(\mathbf{R}, t) = i\hbar \frac{\partial}{\partial t} \chi_n(\mathbf{R}, t) \quad (1.8)$$

being

$$\begin{aligned} \hat{c}_{nn'} &= E_{nn'} + \hat{a}_{nn'} + \hat{b}_{nn'} \\ E_{nn'} &= \langle \Phi_n(\mathbf{r}; \mathbf{R}) | \hat{H}_e | \Phi_{n'}(\mathbf{r}; \mathbf{R}) \rangle \\ \hat{a}_{nn'} &= -\frac{\hbar^2}{2} \sum_{A=1}^M \left( \frac{1}{M_A} + \frac{1}{M_0} \right) \langle \Phi_n | \nabla_A^2 | \Phi_{n'} \rangle + 2 \langle \Phi_n | \nabla_A | \Phi_{n'} \rangle \nabla_A \\ \hat{b}_{nn'} &= \frac{\hbar^2}{2M_0} \sum_{A=1}^M \sum_{B>A}^M \langle \Phi_n | \nabla_A \nabla_B | \Phi_{n'} \rangle + 2 \langle \Phi_n | \nabla_A | \Phi_{n'} \rangle \nabla_B \end{aligned}$$

Accordingly, Equation 1.8 contains non-diagonal terms. The non-diagonal terms  $\hat{c}_{nn'}$  represent the coupling between different adiabatic electronic states, the non-diagonal terms  $E_{nn'}$  represent the interactions between electronic states while  $\hat{a}_{nn'}$ ,  $\hat{b}_{nn'}$  are the electronic state coupling elements associated with nuclear motion. The diagonal terms  $E_{nn}(\mathbf{R})$  (or simply  $E_n(\mathbf{R})$ ) are the energies of the electronic states for different nuclear positions, that is, the adiabatic potential energy surface (PES) for the electronic state  $n$ .

Equation 1.8 formulates rigorously the coupled Schrödinger equation for the nuclear wavefunction in the adiabatic representation. The direct calculation of the nonadiabatic coupling, however, is a very difficult task in quantum chemistry and the strength of the adiabatic representation lies in neglecting the off-diagonal  $\hat{c}_{nn'} (n \neq 0)$  coupling terms. Moreover the diagonal terms  $\hat{a}_{nn}$  and  $\hat{b}_{nn}$  are usually small and most often negligible. As a result, one lands into the need for solving decoupled differential equation for each value of  $n$ :

$$\left[ \hat{T}_N(\mathbf{R}) + E_n(\mathbf{R}) \right] \chi_n(\mathbf{R}, t) = i\hbar \frac{\partial}{\partial t} \chi_n(\mathbf{R}, t) \quad n = 0, 1, 2, \dots \quad (1.9)$$

where  $n$  is the label of the given adiabatic single potential energy surface  $E_n(\mathbf{R})$ . In the remainder of the thesis we shall consider only reactionis taking place on the ground electronic state and this will allow us to drop the electronic state index.

The physical meaning of the assumption on which the adiabatic approximation is based is simple: the slow nuclear motion only leads to the deformation of the electronic states but not to transitions between them. The electronic wavefunction deforms instantaneously to adjust to the slow motion of nuclei. The general criterion for the validity of the adiabatic approximation is that the nuclear kinetic energy be small with respect to the energy gap between electronic states such

that the nuclear motion does not cause transitions between electronic states. This approximation is good enough when one is dealing with low translational energy collisions and in this case it is possible to study the dynamics of the collisions as occurring on a single adiabatic potential energy surface. However, sometimes, there are regions of the PES in which the nonadiabatic coupling is far from being negligible and it is necessary to consider the influence of other electronic states on the adiabatic one.

### 1.2.1 Møller-Plesset perturbation theory

The Møller-Plesset (MP) perturbation theory (PT) is known to be a good compromise between accuracy and computational cost. The major problem of the MP method is that convergence of the MP series is not guaranteed a priori [2–4].

The Møller-Plesset theory is a special application of the Rayleigh-Schrödinger (RS) perturbation theory. In the common perturbation theory one considers an unperturbed Hamiltonian  $\hat{H}_0$  to which a small perturbation  $\hat{V}$  is added. In MP theory the zero-order wave function is an exact eigenvalue of the Fock operator which is taken as the unperturbed operator and the perturbation is considered as the "correlation operator". In perturbation theory we could express the Schrödinger equation as

$$\left(\hat{H}_0 + \hat{V}\right) |\psi\rangle = E |\psi\rangle \quad (1.10)$$

and the wave function and the perturbed energy as power series:

$$|\psi\rangle = \sum_{i=0}^{\infty} |\psi^{(i)}\rangle \quad (1.11)$$

$$E = \sum_{i=0}^{\infty} E^{(i)} \quad (1.12)$$

As a result from the eq. 1.10 one can obtain a form for the energy corrections:

$$E^{(i+1)} = \langle \psi^{(0)} | \hat{V} | \psi^{(i)} \rangle \quad (1.13)$$

which are easy to calculate once the wave function's correction is determined. In the RS-PT each term of the eq. 1.11 is expressed as:

$$|\psi^{(i)}\rangle = \frac{1 - |\psi^{(0)}\rangle\langle\psi^{(0)}|}{E^{(0)} - \hat{H}_0} \left[ (\hat{V} - E^{(1)}) |\psi^{(i-1)}\rangle - \sum_{k=2}^{i-1} E^{(k)} |\psi^{(i-k)}\rangle \right] \quad (1.14)$$

If we consider the perturbation operator as the difference between the real Hamiltonian and the Fock operator:

$$\hat{V} = - \sum_i \left[ \hat{J}(i) - \hat{K}(i) \right] + \sum_{i>j} \frac{1}{r_{ij}} \quad (1.15)$$

we obtain the formalism of the Møller-Plesset Perturbation Theory where the zeroth-order energy is the sum of the orbital's Fock energy:

$$E_{MP0} = 2 \sum_{i=1}^{N/2} \epsilon_i \quad (1.16)$$

and the zeroth plus first order correction yields the Hartree Fock (HF) energy. In order to obtain the MP2 formula for a closed-shell molecule, the second order RS-PT formula is written on basis of doubly-excited Slater determinants. (Singly-excited Slater determinants do not contribute because of the Brillouin theorem):

$$E_{MP2} = \sum_{\substack{a>b \\ p>q}} \frac{|V_{ab[pq]}|^2}{\epsilon_p + \epsilon_q - \epsilon_a - \epsilon_b} \quad (1.17)$$

where  $\epsilon_p, \epsilon_q$  are the energies of the  $p$ -th and  $q$ -th occupied orbitals, while  $\epsilon_a, \epsilon_b$  are the energies of the  $a$ -th and  $b$ -th unoccupied orbitals. In this way the total total electronic energy is given by the Hartree-Fock energy plus the second-order MP correction:

$$E \approx E_{HF} + E_{MP2}. \quad (1.18)$$

## 1.2.2 Coupled Cluster method

The Coupled-Cluster (CC) method is one of the most popular post-Hartree-Fock *ab initio* quantum chemistry methods in the field of computational chemistry due to its accuracy in treating electron correlation.

The coupled cluster method defines the exact wave function, solution of the time-independent Schrödinger equation, as an exponential expression:

$$|\Psi\rangle = e^{\hat{T}} |\Phi_0\rangle \quad (1.19)$$

where  $|\Phi_0\rangle$  is a Slater determinant usually constructed from Hartree-Fock molecular orbitals, and  $\hat{T}$  is the *cluster operator*. This operator can be expanded as a sum of cluster operators for each excitation degree:

$$\hat{T} = \hat{T}_1 + \hat{T}_2 + \hat{T}_3 + \dots \quad (1.20)$$

more easily expressed in the second quantization formalism as:

$$\begin{aligned}\hat{T}_1 &= \sum_{a,r} t_a^r \hat{a}_r^\dagger \hat{a}_a \\ \hat{T}_2 &= \sum_{\substack{a<b \\ r<s}} t_{ab}^{rs} \hat{a}_r^\dagger \hat{a}_s^\dagger \hat{a}_b \hat{a}_a \\ \hat{T}_3 &= \sum_{\substack{a<b<c \\ r<s<t}} t_{abc}^{rst} \hat{a}_r^\dagger \hat{a}_s^\dagger \hat{a}_t^\dagger \hat{a}_b \hat{a}_a \hat{a}_c\end{aligned}\quad (1.21)$$

where  $t_a^r, t_{ab}^{rs}, t_{abc}^{rst}, \dots$  are the cluster amplitudes. Taking into consideration the structure of  $\hat{T}$ , the exponential operator in 1.19 may be expanded into Taylor series:

$$e^{\hat{T}} = 1 + \hat{T} + \frac{\hat{T}^2}{2!} + \dots = 1 + \hat{T}_1 + \hat{T}_2 + \frac{\hat{T}_1^2}{2} + \hat{T}_1 \hat{T}_2 + \frac{\hat{T}_2^2}{2} + \dots \quad (1.22)$$

due to the finite size of the set of occupied molecular orbitals, as is for the number of excitations, the series is finite in practice. In order to simplify the task of finding the coefficients  $t$ , the expansion of  $\hat{T}$  is truncated at second order slightly higher level of excitation (rarely exceeding four).

### CCSD approximation

The first level of approximation in CC methods consists of truncating the cluster expansion at the double excitation:  $\hat{T} = \hat{T}_1 + \hat{T}_2$ , leading to the CC single and double (CCSD) approximation.

The following expression of the wave function is obtained:

$$|\Psi^{CCSD}\rangle = e^{(\hat{T}_1 + \hat{T}_2)} |\Phi_0\rangle = \left( \hat{1} + \hat{T}_1 + \hat{T}_2 + \frac{1}{2}(\hat{T}_1 + \hat{T}_2)^2 + \frac{1}{3!}(\hat{T}_1 + \hat{T}_2)^3 + \dots \right) |\Phi_0\rangle \quad (1.23)$$

In order to evaluate the correlation energy and the cluster amplitude we have to project the equation:

$$\left( \hat{H} - E_0 \right) e^{(\hat{T}_1 + \hat{T}_2)} |\Phi_0\rangle = E_{corr} e^{(\hat{T}_1 + \hat{T}_2)} |\Phi_0\rangle \quad (1.24)$$

on each excitation  $|\Phi_{abc\dots}^{rst\dots}\rangle$  to be obtained for the correlation energy:

$$\langle \Phi_0 | \hat{H}_0 - E_0 | \left( \hat{1} + \hat{T}_1 + \hat{T}_2 + \frac{1}{2}\hat{T}_1^2 \right) \Phi_0 \rangle = E_{corr} \quad (1.25)$$

and for the amplitudes:

$$\langle \Phi_a^r | \hat{H}_0 - E_0 | \left( \hat{T}_1 + \hat{T}_2 + \hat{T}_1 \hat{T}_2 + \frac{1}{2}\hat{T}_1^2 + \frac{1}{3!}\hat{T}_1^3 \right) \Phi_0 \rangle = t_a^r E_{corr} \quad (1.26)$$

and so on.

One of the most important features of this method is its *size-consistency* and its separability independently from the truncation of the  $\hat{T}$  operator.

Nowadays, there are different methods to go beyond double excitations and include the effect of the triple excitation, in the exact, as CC single, double and triple (CCSDT) or approximate form, such as CC3 or CCSD(T) (this last treats singles and doubles excitation fully while triples are calculated using perturbation theory approach) that is the computational procedure used routinely in the present Thesis.

### 1.2.3 Basis Set Superposition Error

The interaction energies between two monomers **A** and **B**, are typically calculated as the energy difference between the product complex **AB** and its components **A** and **B**:

$$\Delta E(\hat{R}) = E(AB, \hat{R})^{\{ab\}} - E(A)^{\{a\}} - E(B)^{\{b\}}. \quad (1.27)$$

where  $\hat{R}$  is the intermolecular distance, and the symbols  $\{..\}$  represent the applied basis-set for the calculation. These types of calculations, using finite basis sets, are susceptible to Basis Set Superposition Error (BSSE).

As the two monomers approach each other, their basis functions overlap and this leads to a stabilization of the complex. This is due to the fact that the description of A in the complex is improved by the presence of the basis function of B which are different from zero in the space region around A and the same is for B. In the eq. 1.27 the short-range energies from the mixed basis sets must be compared with the long-range energies from the unmixed sets, and this mismatch introduces an error in the evaluation of the binding energy.

The BSSE is tightly connected to the dimension of the basis set. The use of a small basis set, in fact, excessively stabilizes the complex with respect to the isolated monomers and brings to a large BSSE.

Two methods exist to eliminate this problem: the chemical Hamiltonian approach (CHA) and the counterpoise procedure (CP) proposed by Boys and Bernardi [5]. The CHA replaces the conventional Hamiltonian with one that prevents basis set mixing *a priori*, by removing all the projector-containing terms which would allow basis set extension. The counterpoise approach, instead, estimates the magnitude of the BSSE by performing an additional calculation on each isolated fragment including the basis set of both the monomers. This energy is then subtracted to the energy of the isolated monomer to obtain:

$$BSSE = E(A)^{\{a\}} - E(A, \hat{R})^{\{ab\}} + E(B)^{\{b\}} - E(B, \hat{R})^{\{ab\}}. \quad (1.28)$$

This correction is at the end added to the interaction energy (see Eq. 1.27) to obtain the CP corrected energy:

$$\Delta E_{CP}(\hat{R}) = E(AB, \hat{R})^{\{ab\}} - E(A, \hat{R})^{\{ab\}} - E(B, \hat{R})^{\{ab\}}. \quad (1.29)$$

### 1.3 Used Computational Procedures

The key goal of quantum chemistry (QC) is to implement the developed theoretical methods as computational procedures aimed at predicting and interpreting the actual electronic structure and reactivity of real chemical systems. Current *ab initio* calculations originate from the Self-Consistent Field (SCF) method proposed by Hartree and Fock in 1930 to overcome the impossibility of working out exact solutions of the Schrödinger equation for many electron systems. However, the SCF calculations were not to become operative until the introduction of the Linear Combination of Atomic Orbital (LCAO) approximation. The introduction of basis sets transformed the numerical problem of solving integro-differential equations into that of solving linear algebra equations which is limited only by the availability of sufficient data storage and efficient computing algorithms. For this reason, the development of more accurate *ab initio* approaches is tightly bond to the evolution of computer technologies. In 1970, thanks also to significant ICT improvements due to the introduction of extended capacities in memory handling and CPU operating associated with the advent of mainframes, the Multi Configurational (MC) SCF methods were developed. MCSCF methods amend the inability of the classical SCF method to describe bond breaking and unpaired electrons. However, as shown by the Figure 1.1, SCF is only the first step towards an accurate description of most chemical systems. It suffers in fact for the drawback of describing the electronic motion in terms of the average field of the other electrons and is therefore unable to correlate the different motions (although this can still be included *ex post* even if one starts from an orbital set obtained from an SCF or an MCSCF treatment. Related methods are often referred to as *post* Hartree-Fock and belong to three main categories: Configuration Interaction (CI), CC and PT methods. The increase of computer power has allowed these method to become widespread and many algorithms to be developed to optimize geometries, to locate transition states and to calculate observable properties. Nowadays, this type of program packages are available for distribution and the development of infrastructures like Grid or the increased availability of cost effective Parallel Computing are continuously increasing their popularity.

Among these packages GAUSSIAN [6] is the most widely used because of its various options. It was developed by John Pople and his work group. First available through the Quantum Chem-

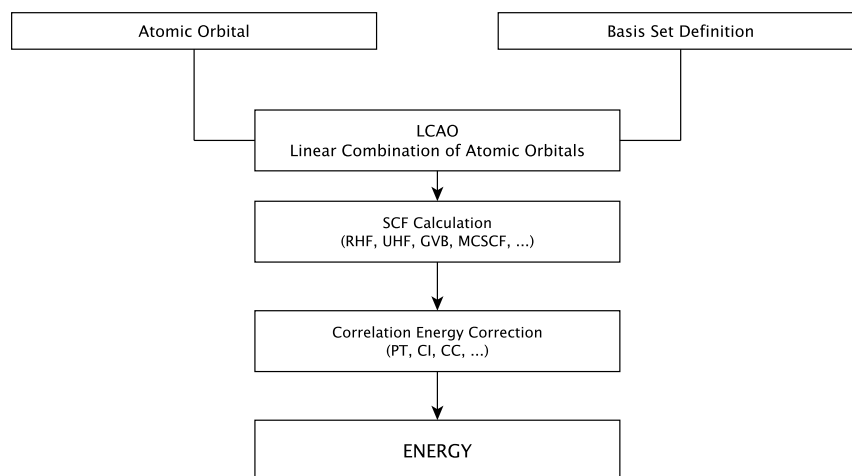


Figure 1.1: Flux diagram of an *ab initio* procedure for a wave function-based method.

istry Program Exchange, since 1987 it has been developed and licensed by Gaussian, Inc. and is presently implemented on the Grid platform of the Computational Chemistry Cluster of which details will be given in chapter 3. Among the other programs developed for the same purpose we mention here DALTON [7] and GAMESS-US (R3) [8] because of their availability on the above mentioned Grid platform. In particular DALTON allows an accurate evaluation of magnetic and (frequency-dependent) electric properties and is particularly suited to study potential energy surfaces, both for static and dynamical investigations. On its side GAMESS is particularly suited for simple systems and has been used in my thesis work for which reason is analyzed here in more details.

### 1.3.1 GAMESS-US

GAMESS is a program for *ab initio* molecular quantum chemistry whose name stands for "General Atomic and Molecular Electronic Structure System". The original version of the program led in 1981 to the two GAMESS-UK [9] and GAMESS-US packages [8]. The GAMESS-US package is at present maintained by the members of the Gordon research group at Iowa State University. This program can perform SCF calculations using RHF (restricted HF), UHF (unrestricted HF), ROHF (restricted open-shell HF), GVB (Generalized Valence Bond) and MCSCF methods. The correlation energy to the related SCF wavefunctions could be calculated using different methods, ranging from Möller-Plesset Perturbation Theory to Coupled-Cluster (including also the density functional theory (DFT) ones). GAMESS enables the calculation of the nuclear gradient for automatic geom-

etry optimization, transition state searches, or reaction path following. Using GAMESS it is also possible to calculate vibrational frequencies with a computation of the hessian, or simulate solvent action with different methodologies such as Polarizable Continuum Model. For very large systems the Fragment Molecular Orbital method, implemented in the latest version of the program, permits the use of many of the previous treatments by dividing the computation in small fragments. The computational tasks of the program are listed in Table 1.1. As shown by the table the outcomes of the various tasks of the package are mainly the electronic energy of the geometry considered and its gradient with respect of the nuclear coordinates (for the SCF also the Hessian is delivered). The listed properties are computable using the basic SCF (without inclusion of the correlation energy), MP2, CI, CC, DFT, time dependent (TD) DFT, equation of motion (EOM) coupled-cluster or semi-empirical (MOPAC) methods.

SCFTYP =	RHF	ROHF	UHF	GVB	MCSCF
SCF Energy	CDpF	CDp	CDp	CDp	CDpF
SCF analytic gradient	CDpF	CDp	CDp	CDp	CDpF
SCF numerical Hessian	CDpF	CDp	CDp	CDp	CDp
SCF analytic Hessian	CDp	CDp	-	CDp	Dp
MP2 energy	CDpF	CDp	CDp	-	CDp
MP2 gradient	CDpF	Dp	CDp	-	-
CI energy	CDp	CDp	-	CDp	CDp
CI gradient	CD	-	-	-	-
CC energy	CDpF	CD	-	-	-
EOM energy	CD	-	-	-	-
DFT energy	CDpF	CDp	CDp	-	-
DFT gradient	CDpF	CDp	CDp	-	-
TD-DFT energy	CDpF	-	CDp	-	-
TD-DFT gradient	CDp	-	-	-	-
MOPAC energy	yes	yes	yes	yes	-
MOPAC gradient	yes	yes	yes	-	-

Table 1.1: Table from GAMESS-US manual. C=conventional storage of integrals on disk; D= direct AO integral computation; P=parallel execution; F=Fragment MO compatibility.

The main reasons for choosing GAMESS to carry out the *ab initio* calculations of my thesis work are (behind its intrinsic qualities) its free availability and the existence of a validated distributed

version on the segment of the EGEE Grid infrastructure available to the virtual organizations (VO) COMPCHEM and VOCE (of which further details will be given in section 3). An important advantage of performing calculations on the Grid is the fact that we can construct the PES by calculating the energies associated to all relevant geometries "at the same time" with a considerable reduction of the wall clock computing time. GAMESS runs on any Linux-based system with the use of a script which passes the input (a formatted text file) to the program. The output produces two files: the ".log" file, which contains the result of each step of the calculation and the ".dat" file which contains all the vectors, the coordinates and the hessian matrix in a formatted structure. In the followings we analyze in detail a simple GAMESS input showing the most important options adopted for a single geometry energy calculation.

### 1.3.2 GAMESS bench input

The input needed for a typical run of the GAMESS program is a simple text file. It is modular and its variables are arranged in groups so as to permit to control the different options of the calculation.

In the following lines a typical input for a single energy calculation on a space fixed chemical system are shown

```

$CONTRL SCFTYP=RHF CCTYP=CCSD(T) RUNTYP=ENERGY COORD=UNIQUE UNITS=ANGS \\  

$END  

$SYSTEM MWORDS=500 $END  

$BASIS GBASIS=STO NGAUSS=3 $END  

$GUESS GUESS=HUCKEL $END  

$DATA  

CCSD(T) energy calculation / Basis-set: STO-3G  

Cnv 2  
  

N1, 7, 0, 0, 0.5471693  

N2, 7, 0, 0, -0.5471693  

N3, 7, 0, 0.5471693, 4.1  

$END

```

in which all commands have a \$ character in the second column and are closed by a \$END tag. In the list only a few of the many options present in the INPUT description chapter of the official manual available from the Gordon Research Group website [10] are given. In the followings a brief description of the most relevant options among those we used for the calculations is given:

\$SYSTEM is the group that allows the control of the information for the computer's operations like the job's time limit, the replicated memory availability and other platform dependent information.

\$CONTRL is the most important group containing the basic options of the job. With SCFTYP and RUNTYP one can decide the type of wavefunctions and the type of calculations to be performed (energy, optimization, hessian, etc.). In this group the units (UNITS), which type of coordinates to be used to define the system (COORD), the correlation energy correction method (CCTYP MPLEVL CITYP etc.) and other useful options can be chosen.

\$BASIS is the group allowing an easy use of the most common basis set families available for quantum chemistry calculations. If this group is missing, the basis set form of each atom must be given in the \$DATA group.

\$GUESS is the group that indicates the method used by the program for calculating the initial Molecular Orbitals which will be optimized throughout the calculation.

\$DATA is the group in which the system must be specified. This group describes the total molecular data such as point group symmetry, nuclear coordinates and possible basis set. In the first line of this group a title for the job must be given; in the second line the Schoenflies symbol indicating the symmetry group the system belongs to must be given. Subsequent lines contain the position coordinates of the nuclei given in the form specified by the COORD= option in the \$CONTRL group.

### 1.3.3 GAMESS bench output

As already mentioned, GAMESS produces two principal output files: the `.log` and the `.dat` files. The `.log` contain all the information that the job produces such as the energy, the final geometry of an optimization process, the corresponding molecular orbitals etc. while `.dat` contains formatted numerical data such as MO vectors (\$VEC), gradient (\$GRAD) or hessian (\$HESS) useful to restart incomplete runs or the subsequent step of a multi step process (like the saddle point search which might take, for example, several optimization and hessian computations).

All the relevant information resulting by a QC calculation is contained in the `log` file. In the following we are going to describe more in detail the most important section of this file for an input of the type described in the previous section.

GAMESS is believed to have the most verbose (though helpful) output files among all the electronic structure software packages. All the information are grouped in different section with a verbose description of what is happening.

The first part of the log file summarizes some basic information of the system under inspection. After an echo of the input file, the program shows:

- the point group symmetry of the system
- the geometry of the system in Cartesian and Z-matrix fashion and the relative internuclear

distances

- an explicit description of the basis set with a list of the alpha values and contraction coefficients
- the computational characteristics of the run

The sequence of computational steps undergone by the program are shown in the remaining part of the output file. That are:

- routine for the calculations of the one and two electrons integrals
- the result of each iteration of the SCF calculation specify the energy and the density convergence of every step
- molecular orbital information (such as coefficients of the LCAO, the energy and the symmetry)
- the properties of the self-consistent field wavefunction (Mulliken population analysis, electrostatic moments, etc.)
- the result of the method for determining the correlation energy (if required).

## Chapter 2

# Theory and computation for nuclei dynamics: the atom diatom case

*In questo capitolo sono raccolti i fondamenti teorici per lo studio della dinamica dei nuclei per sistemi atomo-diatomo. Nella prima sezione vengono esaminate le equazioni di base dello scattering quantistico e la formulazione dei sistemi di riferimento Space e Body fixed.*

*Nelle sezioni 2.2 e 2.3 vengono descritte nel dettaglio le equazioni fondamentali del metodo Time Dependent e le tecniche utilizzate per propagare ed analizzare il pacchetto d'onda. Nelle sezioni 2.4, 2.5 e 2.6 vengono descritte nel dettaglio le equazioni fondamentali del metodo Time Independent, la scelta e le proprietà delle coordinate ipersferiche nonché le tecniche utilizzate per propagare ed analizzare la soluzione. Nella sezione 2.7 vengono discussi i metodi utilizzati per ricavare le osservabili dai risultati di un calcolo di dinamica quantistica.*



To specialize the formalism of quantum reactive dynamics to deal with atom-diatom systems, in the followings details will be given about the coordinate system used for the hamiltonian representation, the reference system employed for the hamiltonian representation, the coupled differential equations integrated to calculate the scattering amplitudes, to conclude with the methods used to estimate observable properties out of scattering results.

## 2.1 Atom diatom equations for the nuclei

The atom-diatom systems are a particular case of the three atom ones in which two atoms (say B and C) are bond together while the third one (say A) is considered as free (it is obviously arbitrary the way of naming each atom). In a generic atom-diatom reaction  $A + BC$  there are three possible processes:  $A + BC \rightarrow A + BC$  (elastic and inelastic non reactive collisions),  $A + BC \rightarrow B + AC$  and  $A + BC \rightarrow C + AB$  (atom exchange reactive collisions). The three processes are known as rearrangement ones and do not include the  $A + BC \rightarrow A + B + C$  dissociation that needs a different treatment. Each of the three processes is usually named  $a$ ,  $b$  and  $c$ , respectively after the free atom notation.

### 2.1.1 The Jacobi vectors

In rearrangement processes, once the separation of the center of mass is performed, the relative motion of the three atoms can be defined using three different systems of Jacobi internal vectors. These three systems are displayed in Figure 2.1. As apparent from the Figure, the definition of the vectors is cyclical with respect to the assignment of the A, B and C labels to the atoms and most often (like hereafter) instead of  $a$ ,  $b$  and  $c$  labels the generic indices  $\lambda$ ,  $\nu$  and  $\kappa$  are used. The Jacobi vectors are defined as:

$$\mathbf{R}_\lambda = \mathbf{x}_\lambda - \frac{M_\nu \mathbf{x}_\nu + M_\kappa \mathbf{x}_\kappa}{M_\nu + M_\kappa} \quad \mathbf{r}_\lambda = \mathbf{x}_\kappa - \mathbf{x}_\nu \quad (2.1)$$

where  $M$  and  $\mathbf{x}$  are, respectively, the atomic masses and the atom position vectors referred to the center of mass of the system.

The  $\mathbf{R}_\lambda$  Jacobi vector represents the vector between the atom  $\lambda$  and the center of mass of the molecule  $\nu\kappa$  and the  $\mathbf{r}_\lambda$  vector corresponds to the internuclear vector between the atom  $\nu$  and the atom  $\kappa$ . The angle  $\Theta_\lambda$  formed by  $\mathbf{R}_\lambda$  and  $\mathbf{r}_\lambda$  is:

$$\Theta_\lambda = \arccos \frac{\mathbf{R}_\lambda \cdot \mathbf{r}_\lambda}{|\mathbf{R}_\lambda| |\mathbf{r}_\lambda|} \quad (2.2)$$

Obviously, the range of vector values included between the pair  $|\mathbf{R}_\lambda|=0, |\mathbf{r}_\lambda|=0$  and the pair  $|\mathbf{R}_\lambda| \rightarrow \infty, |\mathbf{r}_\lambda| = \text{finite}$ , defines the rearrangement channel  $\lambda$ . The relationship between the three sets of Jacobi vectors is defined by the transformation (called kinematic rotation) depending only on the atomic masses:

$$\begin{pmatrix} \mathbf{R}_\nu \\ \mathbf{r}_\nu \end{pmatrix} = \begin{pmatrix} \cos \beta_{\nu\lambda} & -\sin \beta_{\nu\lambda} \\ \sin \beta_{\nu\lambda} & \cos \beta_{\nu\lambda} \end{pmatrix} \begin{pmatrix} \mathbf{R}_\lambda \\ \mathbf{r}_\lambda \end{pmatrix} \quad (2.3)$$

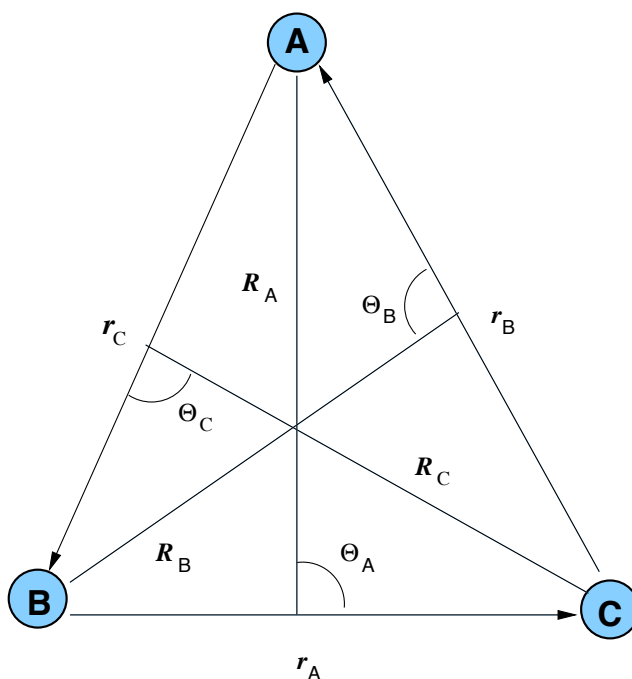


Figure 2.1: Definition of the Jacobi coordinates.

where

$$\cos \beta_{\nu\lambda} = \left[ \frac{M_\lambda M_\nu}{(M_\lambda + M_\kappa)(M_\nu + M_\kappa)} \right]^{1/2}$$

$$\sin \beta_{\nu\lambda} = \left[ \frac{M_\kappa (M_\lambda + M_\nu + M_\kappa)}{(M_\lambda + M_\kappa)(M_\nu + M_\kappa)} \right]^{1/2}$$

In chemical reaction dynamics the angle  $\beta_{\nu\lambda}$  is known as the skewing angle and represents the rotational angle between the Jacobi vectors of different rearrangement channels.

Using the Jacobi vectors the Schrödinger equation 1.9 of the nuclei can be formulated as:

$$\left[ -\frac{\hbar^2}{2\mu_{\lambda,\nu\kappa}} \nabla_{\mathbf{R}_\lambda}^2 - \frac{\hbar^2}{2\mu_{\nu\kappa}} \nabla_{\mathbf{r}_\lambda}^2 + V(\mathbf{R}_\lambda, \mathbf{r}_\lambda) \right] \Psi^\lambda(\mathbf{R}_\lambda, \mathbf{r}_\lambda, t) = i\hbar \frac{\partial}{\partial t} \Psi^\lambda(\mathbf{R}_\lambda, \mathbf{r}_\lambda, t) \quad (2.4)$$

where  $\mu_{\lambda,\nu\kappa}$  is the reduced mass for the triatom in the  $\lambda + \nu\kappa$  arrangement,  $\mu_{\nu\kappa}$  is the reduced mass for the diatom  $\nu\kappa$  and  $\lambda$  is the label indicating the rearrangement channel and the related wavefunction. Obviously, wavefunction representations associated with different rearrangement channels are equivalent. Nevertheless, the effectiveness of the various representations in describing the global wavefunction varies with the different arrangement channels. For that reason, in reaction dynamics the global wavefunction can be obtained by determining its form for the three rearrangement channels and then matching them properly.

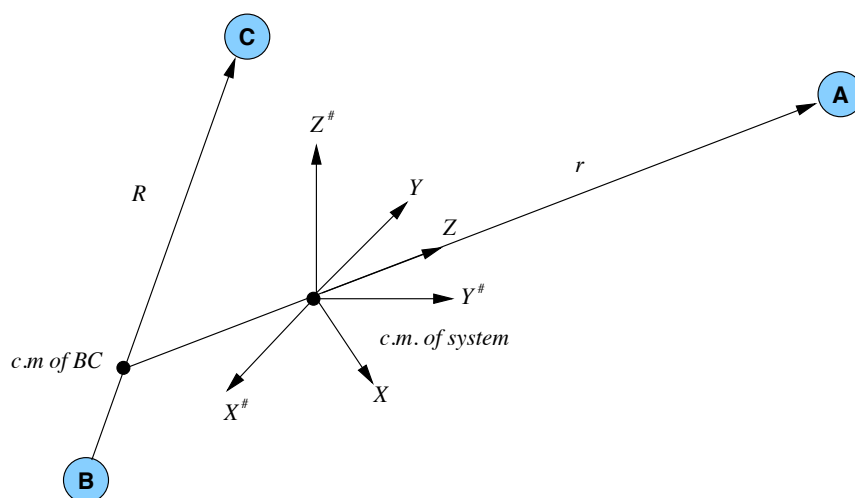


Figure 2.2: Space fixed (primed axes) and body fixed (unprimed axes) reference frames.

### 2.1.2 Space and Body Fixed reference coordinate frame

The choice of a reference coordinate system is another key element of a rigorous quantum treatment of reactive collisions. The choice of a suitable spatial orientation of the reference axis coordinate frame allows a proper exploitation of the properties of the algebra of angular momenta. In fact, in an atom-diatom system, the total angular momentum,  $\mathbf{J} = \mathbf{l}_\lambda + \mathbf{j}_\lambda$ , is conserved. However, both the orbital angular momentum,  $\mathbf{l}_\lambda$ , (corresponding to the motion of the atom around the diatom) and the rotational angular momentum,  $\mathbf{j}_\lambda$ , (corresponding to the rotation of the  $\nu\kappa$  diatom) vary significantly especially in the regions where the rearrangement of reactants to products occurs. Therefore, a formulation based on the total angular momentum can provide great advantages in the global treatment.

The two popular choices of the reference system in quantum dynamics are the space fixed (SF) and the body fixed (BF) ones [11–16]. Figure 2.2 sketches the two reference systems. The SF reference system is denoted as  $OX^\#Y^\#Z^\#$  while the BF one as  $OXYZ$ . Both reference frames are centered in the center of mass of the global system. In the SF frame the axes always lay in a fixed direction in space (with no change during the process). On the contrary, in the BF frame the direction of the axes varies continuously in order to follow the molecular motion in a way that, for example, its reference axis for quantization (say the axis  $Z$ ) always coincides with the Jacobi vector  $\mathbf{R}$ . Therefore, while in the SF frame the quantization axis remains fixed, in the BF frame it follows the motion of the  $\mathbf{R}$  vector.

In the SF representation the coordinates used to describe the Jacobi vectors  $\mathbf{R}_\lambda^\#$  and  $\mathbf{r}_\lambda^\#$  are  $R_\lambda^\#$ ,  $\theta_{R_\lambda}$ ,  $\varphi_{R_\lambda}$ ,  $r_\lambda^\#$ ,  $\theta_{r_\lambda}$  and  $\varphi_{r_\lambda}$ , where  $R_\lambda^\#$  and  $r_\lambda^\#$  are the vector moduli and  $\theta_{R_\lambda}$ ,  $\varphi_{R_\lambda}$ ,  $\theta_{r_\lambda}$  and  $\varphi_{r_\lambda}$  are the associated polar and azimuthal angles in a polar representation (and  $X_{R_\lambda}$ ,  $Y_{R_\lambda}$  and  $Z_{R_\lambda}$  and  $X_{r_\lambda}$ ,  $Y_{r_\lambda}$  and  $Z_{r_\lambda}$  in a cartesian representation).

In the BF representation the coordinates used to describe the Jacobi vectors are the vector moduli  $R_\lambda$  and  $r_\lambda$ , the angle  $\Theta_\lambda$  formed by the  $\mathbf{R}_\lambda$  and  $\mathbf{r}_\lambda$  vectors and three angles,  $\varphi_\lambda$ ,  $\theta_\lambda$  and  $\psi_\lambda$ , which describe the  $Z$  axis orientation and are called Euler angles. For simplicity, the three atoms are placed onto the  $X^\#Z^\#$  plane (i.e., the Euler angle  $\psi_\lambda$  is set to zero).

The choice of the reference frame allows us to write the Schrödinger equation 2.4 in a more explicit way. In the SF frame it results in atomic units ( $\hbar = 1$ ):

$$\left[ - \left( \frac{1}{2\mu_{R_\lambda}} \frac{\partial^2}{\partial R_\lambda^{\#2}} + \frac{1}{2\mu_{r_\lambda}} \frac{\partial^2}{\partial r_\lambda^{\#2}} \right) + \frac{\hat{l}_\lambda^2}{2\mu_{R_\lambda} R_\lambda^{\#2}} + \frac{\hat{j}_\lambda^2}{2\mu_{r_\lambda} r_\lambda^{\#2}} \right] \Psi^\lambda (\mathbf{R}_\lambda^\#, \mathbf{r}_\lambda^\#, t) = i\hbar \frac{\partial}{\partial t} \Psi^\lambda (\mathbf{R}_\lambda^\#, \mathbf{r}_\lambda^\#, t) + V (R_\lambda, r_\lambda, \Theta_\lambda) \Psi^\lambda (\mathbf{R}_\lambda^\#, \mathbf{r}_\lambda^\#, t) \quad (2.5)$$

and in the BF frame it results:

$$\left[ - \left( \frac{1}{2\mu_{R_\lambda}} \frac{\partial^2}{\partial R_\lambda^2} + \frac{1}{2\mu_{r_\lambda}} \frac{\partial^2}{\partial r_\lambda^2} \right) + \frac{(\hat{J} - \hat{j}_\lambda)^2}{2\mu_{R_\lambda} R_\lambda^2} + \frac{\hat{j}_\lambda^2}{2\mu_{r_\lambda} r_\lambda^2} \right] \Psi^\lambda (\mathbf{R}_\lambda, \mathbf{r}_\lambda, t) = i\hbar \frac{\partial}{\partial t} \Psi^\lambda (\mathbf{R}_\lambda, \mathbf{r}_\lambda, t) + V (R_\lambda, r_\lambda, \Theta_\lambda) \Psi^\lambda (\mathbf{R}_\lambda, \mathbf{r}_\lambda, t) \quad (2.6)$$

where the reduced mass for the triatomic  $\lambda + \nu\kappa$  system is represented by  $\mu_{R_\lambda}$  and the reduced mass for the diatomic  $\nu\kappa$  system by  $\mu_{r_\lambda}$ .

The main difference between the SF and BF formulation of the Schrödinger equations is that the orbital angular momentum,  $\mathbf{L}_\lambda$ , cannot be used in the BF representation because the  $\hat{l}^2$  operator does not commute with the hamiltonian operator. Therefore in the BF equation the orbital angular momentum  $\mathbf{L}_\lambda$  is rewritten as  $\mathbf{J} - \mathbf{j}_\lambda$ . In other words, in the SF formulation the wavefunctions are eigenfunctions of the  $\hat{J}^2$ ,  $\hat{J}_{Z^\#}$ ,  $\hat{j}^2$  and  $\hat{l}^2$  operators, being  $J_{Z^\#}$  the projection of the total angular momentum onto the  $Z^\#$  axis. In the BF representation the wavefunctions are eigenfunctions of  $\hat{J}^2$ ,  $\hat{J}_{Z^\#}$ ,  $\hat{j}^2$  and  $\hat{J}_Z$ , where with respect to the SF representation  $\hat{l}^2$  is replaced by the projection of  $\mathbf{J}$  onto the  $Z$  axis (usually called helicity) and its quantum numbers are denoted by  $\Omega_\lambda$ . Since  $\mathbf{L}_\lambda$  and  $\mathbf{R}_\lambda$  are orthogonal, the quantum number  $\Omega_\lambda$  also represents the quantum number for the projection of the rotational angular momentum  $\mathbf{j}_\lambda$  onto the BF  $Z$  axis.

In both SF and BF formulations the PES is represented as a function of  $R_\lambda$ ,  $r_\lambda$  and  $\Theta_\lambda$  because the interaction depends only on the relative positions of the atoms. Other sets of three coordinates, such

as the three internuclear distances, can also be used and are often preferred for particular purposes (like for graphical representations of the potential energy surface).

The quantum formulations of reactive collisions in either SF or BF frames are, obviously, formally equivalent and the relationships between the wavefunction in both approaches is a unitary transformation. Nevertheless, the practical suitability of each formulation depends on the nature of the considered process. Thus, while the BF frame is more adequate for close collisions and strong interaction processes, the SF one is more convenient for the description of weak interactions and processes taking place at long distance.

### 2.1.3 The partial wave expansion

To integrate the Schrödinger equations 2.5 or 2.6, the approach more generally used in quantum reaction dynamics is to expand the overall wavefunction in terms of partial waves. In the SF representation the total angular momentum operators,  $\hat{J}^2$ , and its  $Z^\#$  component,  $\hat{J}_{Z^\#}$ , commute between each other and with the hamiltonian. Therefore, they are a constant of the motion. Thus, the eigenfunctions of  $\hat{J}^2$  and  $\hat{J}_{Z^\#}$ , with eigenvalues  $J(J+1)$  and  $M$ , can be used to form the partial wave basis of  $\Psi_\lambda^{JM}$  to expand the wavefunction as follows:

$$\Psi_\lambda \left( \mathbf{R}_\lambda^\#, \mathbf{r}_\lambda^\#, t \right) = \sum_{J=0}^{\infty} \sum_{M=-J}^J C_\lambda^{JM} \Psi_\lambda^{JM} \left( \mathbf{R}_\lambda^\#, \mathbf{r}_\lambda^\#, t \right) \quad (2.7)$$

where the coefficients  $C_\lambda^{JM}$  are the Clebsch-Gordan coefficients.

Then the partial waves  $\Psi_\lambda^{JM}$  are further expanded in terms of the BF wavefunctions  $\psi_\lambda^{J\Omega_\lambda}$  as:

$$\Psi_\lambda^{JM} \left( \mathbf{R}_\lambda^\#, \mathbf{r}_\lambda^\#, t \right) = \sum_{\Omega_\lambda=-J}^J D_{M\Omega_\lambda}^J(\varphi_\lambda, \theta_\lambda, 0) \psi_\lambda^{J\Omega_\lambda} (R_\lambda, r_\lambda, \Theta_\lambda, t) \quad (2.8)$$

where the  $D_{M\Omega_\lambda}^J(\varphi_\lambda, \theta_\lambda, 0)$  coefficients are the Wigner rotation matrix elements performing the transformation from the SF reference system to the BF one (please notice that we deal with a BF representation in which  $\psi_\lambda = 0$ ).

At this point it is convenient to indicate that the wavefunctions  $\psi_\lambda^{J\Omega_\lambda}$  have a parity  $(-1)^p = (-1)^{(j_\lambda + J_\lambda - \Omega_\lambda)}$  with respect to inversion in space. Moreover, only the wavefunctions with the same parity couple between each other. For this reason, it is possible to separate the coupled equations in two groups, one for the even parity wavefunctions and the other for the odd parity wavefunctions. This feature contributes to further simplify the quantum treatment of the reactive collisions.

## 2.2 Time-dependent (TD) quantum dynamics

A method that has rapidly emerged (though only in recent times) to calculate the BF wavefunctions  $\psi^{J\Omega p}$  is the time-dependent (TD) or wavepacket (WP) one. The TD method allows to integrate in a single run the Schrödinger equation for a given initial state of the reactants (or a given mixture of them) and a range of energies by following the evolution in time of a WP initially shaped to describe the reactants' configuration. Wavepackets have been used for quantum scattering calculations since the late 1960's [17–19]. However, they did not become popular until the late 1980's due to computer limitations [20]. Recent reviews of the wavepacket approach has been given by Sathyamurthy *et al.* [21], Zhang [22] and Althorpe and Clary [23]. A wavepacket method propagating only the real part of the wavepacket and resulting in a significant memory saving has been developed by Gray and Balint-Kurti [24]. In most cases, the WP approach has only been used to calculate reaction probabilities and integral cross sections, i.e. quantities depending only on the modulus of the  $S$  matrix elements (see for example refs. [25–32]). However, Althorpe used a novel way to finesse the coordinate problem and thus used the time-dependent method to calculate  $S$  matrix elements themselves and differential cross sections for the  $H + H_2$  system [33]. Differential cross sections are also calculated by a new quantum wavepacket computer code (DIFFREALWAVE) recently developed by Balint-Kurti *et al.*

### 2.2.1 The time dependent equation

More in detail, in the TD quantum dynamics, the overall solution strategy involves the following three steps. First, an initial ( $t=0$ ) wavefunction  $\psi(\mathbf{R}, \mathbf{r}, t)$  that describes the range of energies and initial conditions that one wants to simulate is chosen. The wavefunction is usually called wavepacket and is most often formulated in Jacobi coordinates,  $\mathbf{R}$  and  $\mathbf{r}$  (either of the reactants or of the products or even initially of the reactants and then, after a certain time, of the products). Second, the TD Schrödinger equation

$$i\hbar \frac{\partial \psi(\mathbf{R}, \mathbf{r}, t)}{\partial t} = \hat{H} \psi(\mathbf{R}, \mathbf{r}, t) \quad (2.9)$$

is integrated in time for an interval long enough to describe the scattering process of interest. When  $\hat{H}$  is explicitly time-independent, as in laser free scattering cases, the formal solution of eq. 2.9 is obtained as the time evolution of the wavepacket described by the equation

$$\psi(\mathbf{R}, \mathbf{r}, t + \lambda) = e^{-i\hat{H}\lambda/\hbar} \psi(\mathbf{R}, \mathbf{r}, t) \quad (2.10)$$

Third, the desired scattering information, such as the outgoing flux of the wavepacket deformation is worked out. This calculation usually implies an expansion of the wavefunction in the product basis functions in the asymptotic product region and the recovery of the scattering information out of the related expansion coefficients.

One aspect of the method, which virtues have been realized only recently, is the fact that the hamiltonian  $\hat{H}$  in eq. 2.9 can be replaced by any (single valued) function of  $\hat{H}$  leading to the same solution [24,34]. If this function is chosen to be  $\arccos(\hat{H})$ , then the resulting solution making use of the Chebyshev integration method is exact and exceptionally simple.

The initial wavepacket is often chosen to be a Gaussian function of the translational coordinate, with mean velocity and width chosen to describe the range of interest. In making this choice, one needs to consider how the spatial part of the Schrödinger equation is to be handled, i.e., whether the dependence of the wavepacket on spatial coordinates has to be represented on a grid or in terms of basis functions.

For the calculations of my thesis the quantum wavepacket code RWAVEPR developed in the CDK laboratory [35–37] has been used. The code integrates the TD Schrödinger equation for the generic atom-diatom reaction:



where  $v$  and  $j$  are the vibrational and rotational quantum numbers of the reactants (the analogous quantities for products are primed) by propagating in time the complex wavepacket in time using product coordinates. Then, state-to-state probabilities are calculated.

### 2.2.2 Wavepacket representation

A key problem of any quantum dynamical treatment is the selection of a suitable set of coordinates to give an appropriate representation of the wavefunction. This selection is associated with several aspects of the calculations. Namely, the definition of a continuity variable to use for integrating the Schrödinger equation, the expansion of the wavefunction and the formulation of both initial and final conditions. In TD approaches the problem of defining a suitable continuity variable is easy to solve because the time itself is an ideal continuity variable. The crucial problem resides, therefore, in the definition of both the initial and the final conditions of the wavefunction which in reactive processes refer usually to different sets of coordinates since, as is the case of the Jacobi

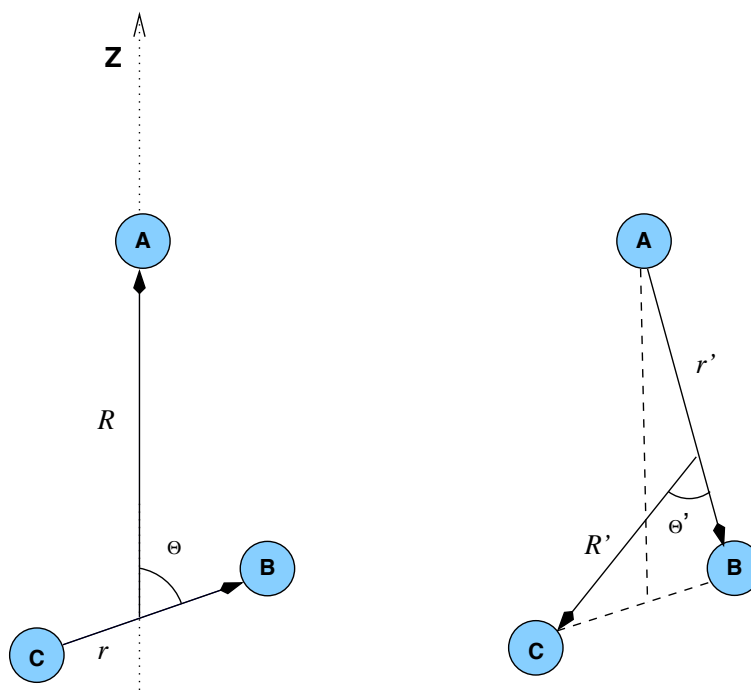


Figure 2.3: Reactant (unprimed) and product (primed) Jacobi coordinates for a triatomic system. Reactant Jacobi coordinates are shown on the product Jacobi coordinates as dashed lines.

ones, they are arrangement dependent. In Figure 2.3 the reactant and product Jacobi coordinates for a triatomic system used in this work are displayed. Obviously, initial conditions are properly specified in the reactant coordinates, while any final state analysis, needed for instance to determine the quantum state distribution of the products, must be performed in the appropriate set of product coordinates. The most straightforward choice is to carry out the calculations using reactant coordinates. This makes it immediate to define initial conditions. When one is interested in computing the properties of the products the wavefunction has to be mapped onto the final diatomic molecule wavefunctions and the related  $r'$  coordinate has to be used. Accordingly, the wavefunction, initially set up in reactant Jacobi coordinates  $R$ ,  $r$  and  $\Theta$  needs to be represented in the product ones  $R'$ ,  $r'$  and  $\Theta'$ . Note that for simplicity the  $\lambda$  label used in previous notation and in Figure 2.1 has been now replaced by unpriming (reactant) and priming (product) the Jacobi coordinates.

In principle, the analysis of the wavefunction in the product region requires at each step of the evolution a mapping of the wavefunction onto the product coordinates. As an alternative one can transform the entire wavepacket onto a product coordinate representation at a given appropriate time, for example when the wavepacket is concentrated in the strong interaction region. The propagation then proceeds in product coordinates which are suitable for the final state analysis. It may

be also desirable, to reduce the computational effort, to perform a short propagation in the entrance channel using reactant Jacobi coordinates and then transform the wavepacket to product Jacobi coordinates [38]. Recently some interesting and efficient methods have been developed to perform the transformation from reactant to product Jacobi coordinates [39].

### 2.2.3 The formulation of the initial wavepacket

As already mentioned, the wavepacket is usually expanded in terms of partial waves  $\psi^{J\Omega p}(R, r, \Theta, t)$  i.e. functions of the total angular momentum quantum number  $J$  and its projections  $\Omega$  on the BF quantization axis. Then, initially ( $t=0$ ) the atom-diatom  $A + BC$  partial wave is formulated as (for simplicity the parity index is dropped):

$$\psi^{J\Omega}(R, r, \Theta, t = 0) = \chi^J(R) \varphi_{vj}^{BC}(r, \Theta) \quad (2.12)$$

where the function  $\chi^J(R)$  represents the dependence on  $R$  of the initial wavepacket and the function  $\varphi_{vj}^{BC}(r, \Theta)$  is the the wavefunction of the initial rovibrational state of the molecule  $BC$ .

The function  $\chi^J(R)$  is expressed as a Gaussian function  $e^{-\alpha(R-R_0)^2}$ , where  $R_0$  is the center of the wavepacket, multiplied by a phase factor of the form  $e^{-ik_0(R-R_0)}$  which gives the initial wavepacket a relative kinetic energy,  $k_0$ , towards the interaction region. This factor is made up of appropriate incoming Ricatti-Hankel functions, thus avoiding the problem of having to start the wavepacket propagation sufficiently far away from the centrifugal barrier. Therefore, the function  $\chi^J(R)$  is formulated by:

$$\chi^J(R) = N e^{-\alpha(R-R_0)^2} e^{-ik_0(R-R_0)} h_l^1(k(R-R_0)) \quad (2.13)$$

where  $k_0$  is the wavenumber which determines the relative kinetic energy of the collision partners and  $h_l^1$  is the Hankel function of the first order.

The function  $\varphi_{vj}^{BC}(r, \Theta)$  is set up from a vibrational function  $\phi_v^{BC}(r)$  multiplied by an angular function:

$$\varphi_{vj}^{BC}(r, \Theta) = \phi_v^{BC}(r) P_j^\Omega(\Theta) \quad (2.14)$$

where  $P_j^\Omega(\Theta)$  are the normalized associated Legendre polynomials.

The function of eq. 2.13 describes a Gaussian wavepacket traveling inwards with an average momentum of  $k_0\hbar$ . The wavepacket is localized in space. Due to Heisenberg uncertainty Principle

this means that it has a spread in momentum (or kinetic energy). Since the total energy is a constant of motion, each portion of the wavepacket with a definite total energy may be considered to scatter independently of other parts of the same wavepacket which have different total energies.

In order to evaluate the reaction probability one needs to know which portion of the original wavepacket has a particular total energy. This means that, since the internal energy is fixed, one needs to know the amplitude of the initial wavepacket having a particular momentum (or kinetic energy). This is obtained by a Fourier transform of the initial wavepacket:

$$g(k) = \frac{1}{\sqrt{2\pi}} \int_{R=0}^{\infty} \exp(-ikR) \chi^J(R) dR \quad (2.15)$$

where  $\chi^J(R)$  is the gaussian wavepacket in space and  $g(k)$  is the component of wavepacket with momentum  $k\hbar$ .

### 2.3 The propagation of the wavepacket

To integrate eq. 2.9 one has to evaluate the action of the hamiltonian operator onto the partial wavepacket  $\psi^{J\Omega}(R, r, \Theta, t)$ . In an exact quantum time-dependent treatment the time differentiation of the system wavefunction is related to the application of the hamiltonian  $\hat{H}$  to the wavefunction itself. Accordingly, the partial wave equations to be integrated read:

$$\hat{H}\psi^{J\Omega} = \left[ \hat{T}_{R,r,\Theta,J,\Omega} + V(R, r, \Theta) \right] \psi^{J\Omega} + C_{\Omega,\Omega\pm 1}^J \psi^{J\Omega\pm 1} \quad (2.16)$$

being

$$\begin{aligned} \hat{T}_{R,r,\Theta,J,\Omega} &= \hat{T}_R + \hat{T}_r + \hat{T}_\Theta + \frac{J(J+1) - 2\Omega^2}{2\mu_R R^2} \\ \hat{T}_R &= -\frac{1}{2\mu_R} \frac{\partial^2}{\partial R^2} \\ \hat{T}_r &= -\frac{1}{2\mu_r} \frac{\partial^2}{\partial r^2} \\ \hat{T}_\Theta &= -\left( \frac{1}{2\mu_R R^2} + \frac{1}{2\mu_r r^2} \right) \left( \frac{1}{\sin \Theta} \frac{\partial}{\partial \Theta} \sin \Theta \frac{\partial}{\partial \Theta} - \frac{\Omega^2}{\sin^2 \Theta} \right) \\ C_{\Omega,\Omega\pm 1}^J &= \frac{[J(J+1) - \Omega(\Omega \pm 1)]^{1/2} [j(j+1) - \Omega(\Omega \pm 1)]^{1/2}}{R^2} \end{aligned}$$

where  $\hat{T}_R$  and  $\hat{T}_r$  are radial kinetic energy terms,  $\hat{T}_\Theta$  is the angular kinetic energy term,  $(J(J+1) - 2\Omega^2)/2\mu_R R^2$  is the centrifugal term,  $V(R, r, \Theta)$  is the potential energy term and the last two terms

correspond to the coupling between wavepackets having different values of  $\Omega$ , i.e., the non-diagonal terms of the Coriolis coupling.

In this work, two methods are used to evaluate the hamiltonian. They are the fast Fourier transform method, to evaluate the radial terms, and the discrete variable representation method to evaluate the angular ones.

### 2.3.1 Methods for the hamiltonian evaluation

In this work, two methods are used to evaluate the hamiltonian. They are the fast Fourier transform method to evaluate the radial terms and the discrete variable representation method to evaluate the angular ones. The introduction of the fast Fourier transform (FFT) method by Feit *et al.* [40,41] and Kosloff [42] for computing the action of the kinetic energy part of the hamiltonian on the wavepacket function was a significant development in TD quantum calculations. To compute the second derivative of the wavefunction the FFT method performs a Fourier transform from the coordinate space to the momentum space, multiplies it by  $-k^2$  (where  $k$  is the wavenumber), and transforms it back to the coordinate space by an inverse Fourier transform. These steps can be formulated as:

$$\begin{aligned}\psi(k) &= \frac{1}{\sqrt{2\pi}} \int_{-\infty}^{\infty} \psi(x) \exp(-ikx) dx = \text{FFT}[\psi(x)] \\ \psi(x) &= \frac{1}{\sqrt{2\pi}} \int_{-\infty}^{\infty} \psi(k) \exp(-ikx) dx = \text{FFT}^{-1}[\psi(k)] \\ \frac{d\psi(x)}{dx} &= \frac{1}{\sqrt{2\pi}} \int_{-\infty}^{\infty} \psi(k)(ik) \exp(-ikx) dk = \text{FFT}^{-1}[(ik)\psi(k)] \\ \frac{d^2\psi(x)}{dx^2} &= \frac{1}{\sqrt{2\pi}} \int_{-\infty}^{\infty} \psi(k)(ik)^2 \exp(-ikx) dk = \text{FFT}^{-1}[-k^2\psi(k)]\end{aligned}\tag{2.17}$$

where  $x \equiv R, r$ . Since the kinetic energy operator is local in the momentum space, its action on the wavefunction is evaluated very accurately, just as in the case of the potential energy operator in the coordinate space. The method requires that the wavefunction satisfies periodic boundary conditions and is exact for band-limited functions. If the wavefunction is not band-limited and/or boundary conditions are not satisfied, the wavefunction would wrap around the opposite side introducing errors in the calculation (aliasing effects).

It is worthwhile to add that, in a discrete representation, operators corresponding to physical observables in the original Hilbert space are mapped onto a discrete Hilbert space. Thus operators in

the discrete Hilbert space should obey all quantum mechanical commutation relations observed by corresponding physical observables in the original Hilbert space. In this case a one-to-one mapping of the operators to the discrete space is achieved. It has been shown that this is indeed the case with the Fourier discretization for a band limited function with a finite support that is, of finite extent in configuration as well as in momentum space [42]. This reconfirms the versatility of the Fourier transform method over that of other methods. In cases where the wavefunction is not periodic or band-limited, one has to employ a semilocal approximation for the kinetic energy operator (as is the case of the finite difference scheme or the discrete variable representation described later in this section).

It is worth comparing the kinetic energy discrete spectrum in the Fourier discretization and in the finite difference (FD) approximation. For the wavefunction given in eq. 2.17, the former gives the exact kinetic energy spectrum [42]:

$$T_{\text{FFT}}(k) = \frac{\hbar^2}{2m} k^2 \quad (2.18)$$

while the latter yields [43]:

$$T_{\text{FD}}(k) = \frac{\hbar^2}{2m} \left[ \frac{2 \sin(k\Delta x/2)}{\Delta x} \right]^2 \quad (2.19)$$

Upon inspection it becomes clear that, if the mesh size  $\Delta x$  is chosen to be very small, the kinetic energy discrete spectrum in the FD scheme approaches the exact one given by the FFT discretization. Thus a for comparable accuracy one should employ a finer mesh in the FD scheme than for the FFT discretization. An alternative way of constructing discrete representations is the discrete variable representation (DVR) method. The DVR method was originally introduced in Molecular Reaction Dynamics by Light and coworkers for solving the time-dependent Schrödinger equation [44–46]. This method is a very general and powerful method and has extensively been used in the evaluation of the hamiltonian operation on the wavefunction in time-dependent calculations [47–51]. It is applied to one-dimensional problems or direct product basis functions in multidimensional problems.

The DVR method is a localized (in coordinate space) discrete representation. For any given finite basis set  $\phi_n(x)$  ( $n = 1, 2, 3, \dots, N$ ), one can define a unique DVR by diagonalizing the matrix:

$$x_{mn} = \langle \phi_m | \hat{x} | \phi_n \rangle \quad (2.20)$$

which generates  $n$  eigenvalues  $x_n$  and eigenfunctions:

$$|X_n\rangle = \sum_m |\phi_m\rangle C_{mn} \quad (2.21)$$

such that:

$$\hat{x}|X_n\rangle = x_n|X_n\rangle \quad (2.22)$$

This equation implies that, in this  $N$ -dimensional vector space, the coordinate operator  $\hat{x}$  is approximated by:

$$\hat{x} = \sum_{m=1}^N \sum_{n=1}^N |\phi_m\rangle x_{mn} \langle \phi_n| = \sum_{n=1}^N |X_n\rangle x_n \langle X_n| \quad (2.23)$$

With this prescription for the operator  $\hat{x}$ ,  $|X_n\rangle$  is also an eigenstate of any operator function  $F(\hat{x})$ , i.e.:

$$F(\hat{x})|X_n\rangle = F(x_n)|X_n\rangle \quad (2.24)$$

Since the DVR basis set  $|X_n\rangle$  is related to the finite basis set  $\phi_n(x)$  through a unitary or orthogonal transformation of the eq. 2.21, it is an equivalent basis set to  $\phi_n(x)$  in this  $N$ -dimensional vector space. The DVR basis functions are highly localized in coordinate space, i.e.  $\langle x|X_n\rangle$  is highly peaked near  $x = x_n$ . Due to this particular local property of the DVR basis, the matrix element of any local operator in the DVR basis is approximately diagonal. For example, the matrix element of the potential energy operator in the DVR basis is approximated by:

$$\langle X_m|V(\hat{x})|X_n\rangle = \delta_{mn}V(x_n) \quad (2.25)$$

This result applies to any local operator which is a function of coordinates only, and should be understood in the sense that the coordinate operator is approximated by eq. 2.23 in the  $N$ -dimensional vector space. As the dimension of the vector space increases, the approximation in eq. 2.25 becomes increasingly better. Since the most potential energy operators are local in functions of coordinates, they are diagonal in the DVR representation, and the integration over the coordinates to construct the potential matrix can be eliminated.

If the basis functions used to define DVR are polynomials  $P_n(x)$  that are orthogonal with the weighting function  $W(x)$ :

$$\langle P_m|P_n\rangle = \int_a^b W(x)P_m(x)P_n(x)dx = \delta_{mn} \quad (2.26)$$

then one can use a Gaussian quadrature to evaluate the integral:

$$\langle P_m|P_n\rangle = \sum_{k=1}^N P_m(x_k)P_n(x_k)w_k = \delta_{mn} \quad (2.27)$$

where  $x_k$  and  $w_k$  are Gaussian nodes and weights, respectively. The property of Gaussian quadrature guarantees that eq. 2.27 is exact for  $m, n = 0, 1, 2, \dots, N-1$ . Thus for orthogonal polynomials,

the associated DVR points are just Gaussian nodes, and the orthogonal transformation between the DVR and the polynomial basis is simply given by the relation:

$$\langle P_n | X_k \rangle = \sqrt{w_k} P_n(x_k) \quad (2.28)$$

If one evaluates the matrix element of a local operator such a potential  $V(x)$  in the basis of orthonormal polynomials by Gaussian quadrature, one has:

$$\begin{aligned} \langle P_m | V | P_n \rangle &= \sum_{k=1}^N P_m(x_k) V(x_k) P_n(x_k) w_k \\ &= \sum_{k=1}^N \langle P_m | X_k \rangle V(x_k) \langle X_k | P_n \rangle \end{aligned} \quad (2.29)$$

which is equivalent to inserting a complete DVR set  $\sum_k |X_k\rangle\langle X_k|$  directly into the integral and using DVR result:

$$V | X_k \rangle = V(x_k) | X_k \rangle \quad (2.30)$$

This means that one can think of the Gaussian quadrature as a special case of DVR when the associated basis functions are orthogonal polynomials. Thus evaluating the potential matrix elements of a local operator, such as the potential operator, in an orthogonal polynomial basis by the DVR method is equivalent to using Gaussian quadrature to evaluate the matrix element. This directly relates the approximation used in the DVR evaluation of the potential matrix to that of numerical quadrature.

Computationally, the DVR method scales as  $N^2$  compared to the  $N \log N$  scaling of the FFT method. The advantage of the DVR approach is that, unlike the FFT one, the wavefunction needs not to be transformed to the momentum space forth and back every time step, avoiding, so far, a considerable overhead. Furthermore, it is possible to keep at a minimum the number of the basis functions required for the expansion if an appropriate basis is chosen according to the nature of the potential.

### 2.3.2 Evaluation of the effect of the hamiltonian on the wavepacket

As already apparent in eq. 2.16, the evaluation of  $\hat{H}\psi$  can be nicely separated in two parts: the evaluation of  $\hat{T}\psi^{J\Omega}$  and of  $V\psi^{J\Omega}$  where, as already mentioned,  $\hat{T}$  is the kinetic energy operator and  $V$  the potential energy one. The evaluation of the potential term is a relatively simple task. In fact, this is a local operation being the potential energy operator diagonal if one uses the representation of Jacobi coordinates. Therefore, the  $V\psi^{J\Omega}$  term is obtained by multiplying the wavepacket at each

grid point by  $V(R_i, r_j, \Theta_k)$ , where  $R_i, r_j$  and  $\Theta_k$  represent respectively the  $i$ th point of the  $R$  grid, the  $j$ th point in the  $r$  grid and the  $k$ th point in the  $\Theta$  grid. However, the evaluation of the action of the kinetic operator on the wavepacket is a more complicated issue, since  $\hat{T}\psi^{J\Omega}$  term is not local in the representation adopted.

The effect of applying the  $R$  term of the kinetic operator,  $\hat{T}_R$ , is expressed as:

$$\hat{T}_R\psi^{J\Omega}(R, r, \Theta, t) = -\frac{1}{2\mu_R} \frac{\partial^2}{\partial R^2} \psi^{J\Omega}(R, r, \Theta, t) \quad (2.31)$$

This operation can be performed in three steps. The first one is a first Fourier transform:

$$\begin{aligned} \psi^{J\Omega}(k_R, r, \Theta, t) &= \frac{1}{\sqrt{2\pi}} \int_{-\infty}^{\infty} \exp(-ikR) \psi^{J\Omega}(R, r, \Theta, t) dR \\ &= \text{FFT} [\psi^{J\Omega}(R, r, \Theta, t)] \end{aligned} \quad (2.32)$$

to obtain the momentum representation of the wavepacket. The second step is the multiplication of the previous result by  $k^2/2\mu_R$  (which is the representation of the kinetic operator in the momentum space) and is a local operation at each grid point of the momentum space. The third step consists in an inverse Fourier transform. Accordingly, the action of  $\hat{T}_R$  on the wavepacket is accomplished by:

$$\hat{T}_R\psi^{J\Omega}(R, r, \Theta, t) = \text{FFT}^{-1} \left[ \frac{k^2}{2\mu_R} \text{FFT} [\psi^{J\Omega}(R, r, \Theta, t)] \right] \quad (2.33)$$

A similar procedure can be adopted for the  $r$  term of the kinetic operator,  $\hat{T}_r$ .

As for the angular term of the kinetic operator,  $\hat{T}_\Theta$ , one can realize that:

$$\left\{ -\frac{1}{\sin \Theta} \frac{\partial}{\partial \Theta} \sin \Theta \frac{\partial}{\partial \Theta} \right\} P_j(\cos \Theta) = j(j+1)P_j(\cos \Theta) \quad (2.34)$$

and then its grid representation is:

$$T_{li} = \sum_{j=0}^{N_\theta} U_{lj} j(j+1) U_{ij}^T \quad (2.35)$$

where  $U$  is the matrix that transforms the Legendre polynomial basis set to the grid representation:

$$U_{ij} = P_j(\cos \Theta_i) \sqrt{w_i} \quad (2.36)$$

where  $w_i$  are the Gauss-Legendre weights  $w_i = \sin \Theta_i$ . Note that this equation is the application of the general DVR eq. 2.28 to the angular part of the kinetic operator.

Therefore, the action of the angular part of the kinetic energy operator at a given point  $l$  is formulated as:

$$\{\hat{T}_\Theta\psi\}_l = \left( \frac{1}{2\mu_R R^2} + \frac{1}{2\mu_r r^2} \right) \sum_i^{N_\theta} T_{li} \psi_i \quad (2.37)$$

### 2.3.3 Wavepacket propagation and analysis

The evolution in time of the wavepacket requires that the evolution operator  $\exp(-i\hat{H}\tau/\hbar)$  is applied onto the wavefunction (eq. 2.10). A Taylor expansion for the evolution operator reads:

$$\exp\left(\frac{-i\hat{H}\tau}{\hbar}\right)\psi(\mathbf{R}, \mathbf{r}, t) = \left\{ 1 - \left(\frac{i\hat{H}\tau}{\hbar}\right) - \frac{1}{2!}\left(\frac{\hat{H}\tau}{\hbar}\right)^2 + \frac{i}{3!}\left(\frac{\hat{H}\tau}{\hbar}\right)^3 + \dots \right\} \psi(\mathbf{R}, \mathbf{r}, t) \quad (2.38)$$

Therefore, the propagation method requires the knowledge of the result of applying the hamiltonian operator onto the wavefunction to solve the TD Schrödinger equation. The coordinates used will strongly affect the efficiency and precision of the propagation. Several methods can be employed for the propagation of them. The most popular are the split operator [40,52], the Lanczos recursive [53–55] and the Chebyshev [56,57]. In the work reported here, the Chebyshev iteration has been used. In the followings we describe it in some detail.

The Chebyshev expansion for the evolution operator reads:

$$\exp\left(\frac{-i\hat{H}\tau}{\hbar}\right)\psi(\mathbf{R}, \mathbf{r}, t) = \exp\left(\frac{-i\left(\frac{\Delta E}{2} + V_{\min}\right)\tau}{\hbar}\right) \sum_{n=0}^N (2 - \delta_{n0}) J_n\left(\frac{\Delta E \tau}{2\hbar}\right) P_n(-i\hat{H}_s) \quad (2.39)$$

where  $P_n$  are the Chebyshev polynomials of complex argument (the first three Chebyshev polynomials are:  $P_0(-ix) = 1$ ,  $P_1(-ix) = -2ix$  and  $P_2(-ix) = -4x^2 + 1$ ). They obey the recursion formula  $P_{n+1} = -2i\hat{H}_s P_n + P_{n-1}$ , where  $\hat{H}_s$  is a normalized hamiltonian whose eigenvalues are confined into the interval  $-1$  and  $+1$ . This normalization is performed by finding the range of the hamiltonian operator ( $\Delta E = E_{\max} - E_{\min}$ ):

$$\hat{H}_s = \frac{\hat{H} - \hat{I}\left(\frac{\Delta E}{2} + V_{\min}\right)}{\frac{\Delta E}{2}} \quad (2.40)$$

Since it is essential to limit the range of the hamiltonian a potential cut off is applied to make  $V = V_{\max}$  when  $V > V_{\max}$ .

In eq. 2.39,  $J_n$  are Bessel functions. They play a very important role in the convergence of the expansion. For  $n$  values greater than the argument  $\Delta E \tau / 2\hbar$ ,  $J_n$  decreases exponentially in value. One can therefore predict that the number of terms needed in the expansion is approximately

$N \approx \Delta E \tau / 2\hbar$ . This means that the number of terms required to expand the time evolution operator is proportional to the range of the hamiltonian operator. Or, equivalently,  $N$  is the number of operations that the hamiltonian operator must perform in order to propagate the wavepacket forward by  $\tau$ .

The wavepacket is subsequently propagated using the modified TD Schrödinger equation suggested by Balint-Kurti and Gray [24]. According to this scheme, the hamiltonian  $\hat{H}$  in the ordinary TD Schrödinger equation is substituted by an analytic function of itself, denoted here by  $f(\hat{H})$ . If this analytic function is chosen appropriately (for instance  $f(\hat{H}) = -\arccos \hat{H}_s$ ), the subsequent propagation of the wavepacket by the Chebyshev scheme is significantly simplified. Thus, the propagation equation used is :

$$f(\hat{H})\psi = i\hbar \frac{\partial \psi}{\partial t}$$

To carry out the propagation, the wavepacket is located on a regularly spaced grid on  $R$  and  $r$  and on a grid of Gauss-Legendre quadrature points in the Jacobi angle  $\Theta$ . The initial wavepacket is transformed into the Jacobi product coordinates  $R'$ ,  $r'$  and  $\Theta'$  of the channel of interest and the entire propagation is carried out in these coordinates. At the initial time ( $t=0$ ) the wavepacket is placed far in the reactant channel and it is mapped into a product coordinate grid. The product coordinate grid has to be large enough to contain the initial wavepacket and to properly describe the wave packet during its evolution in time including the region where the analysis line is drawn and the interaction region. At the same time, the grid has to be fine enough to accurately describe the structure of the wavefunction. Figure 2.4 shows a typical grid domain in the reactant  $R$  and  $r$  coordinates. As time progresses, the wavepacket moves into the interaction region. At the grid edges, an absorption region is introduced to prevent the wavepacket amplitude from reaching the edge of the grid and causing the already mentioned problem of aliasing in Fourier transform theory [58, 59]. In this absorption region the wavepacket is multiplied by a damping function of the form:

$$\phi(R) = \exp\left(-\frac{(R - R_a)^2}{2b^2}\right) \quad (2.41)$$

where  $b$  is a measure of the effective length of the potential and  $R_a$  is the value of  $R$  beyond which the value of the function differs from unity. The wavepacket is then propagated in time until it has mainly been absorbed near the edge of the grid. The wavepacket is analysed at every time step along an analysis line in the asymptotic region of the product channel [24, 60] so as to accumulate the data needed for the computation of the detailed state to state  $S$  matrix elements  $S_{vj\Omega, v'j'\Omega'}^{Jp}(E_{tr})$  at the various values of the collision energy,  $E_{tr}$ , contained within the wavepacket.

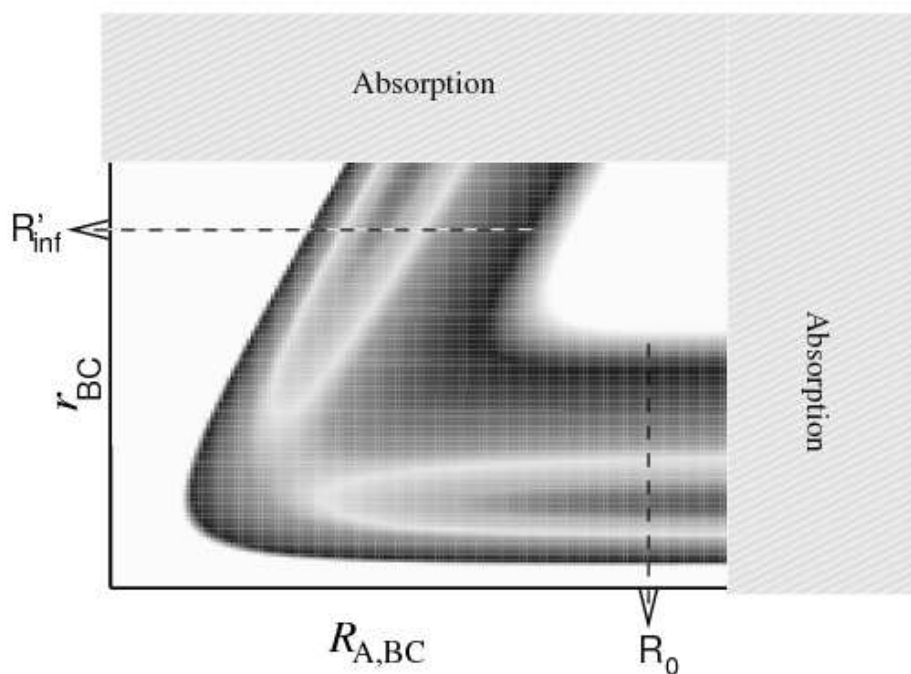


Figure 2.4: Schematic representation of the grid domain in the reactant  $R \equiv R_{A,BC}$  and  $r \equiv r_{BC}$  coordinates. The starting point  $R = R_0$  of the propagation is placed in reactant channel and the analysis line  $R' = R_{inf}$  is drawn in the product channel.

Before the propagation starts, suitable representations of the hamiltonian to be used are calculated and stored in memory. The values of the potential energy surface are calculated for all points of the grid used and are stored in the diagonal positions of an array. Also the diagonal elements of the hamiltonian which are local in the coordinate representation (and therefore can be regarded as parts of the potential energy) are calculated and stored in the diagonal positions of the same array. Then, once the propagation starts, the corresponding off-diagonal terms, both local and non-local in coordinate space are calculated and stored in the appropriate off-diagonal positions of the same array.

At each stage of the propagation, the overlap of the wavepacket with each of the open product channels is calculated and stored. Since the product wavefunction are effectively localized in the product region, this overlap is zero at early times and attains high values only for relative narrow time window for a direct reaction (as  $N + N_2$  is on the PES considered). At the end of the propagation, the  $S$  matrix elements for all open product channels and for all energies of interest are computed using the overlap values calculated throughout the propagation by a half-Fourier transform, taking into account the fact that  $f(\hat{H})$  rather than  $\hat{H}$  was used to propagate the wavepacket. There are mainly two well known methods to analyse the wavepacket: the asymptotic analysis [24, 26, 61] and the flux method [62]. In the asymptotic analysis method (the one used in this Thesis to study the  $N + N_2$  reaction) the wavepacket is analysed along an asymptotic cut (analysis line) of at the product channel at each time step. The analysis is performed by projecting the corresponding cut taken through the wavepacket at the analysis line onto the product eigenfunctions,  $\phi_{v'j'}^{AB}(r')$ . This yields a time dependent coefficient for each possible final quantum states of the system through the following integration:

$$C_{vj\Omega, v'j'\Omega'}^{Jp}(t) = \int_{r'} dr' \int_{\Theta} \sin \Theta' P_{j'}^{\Omega'}(\Theta') \phi_{v'j'}^{BC}(r') \psi^{J\Omega p}(R' = R'_{\infty}, r', \Theta') d\Theta' \quad (2.42)$$

The  $C$  coefficients are then Fourier transformed in order to obtain the elements of the energy-dependent collision matrix  $A$ :

$$A_{vj\Omega, v'j'\Omega'}^{Jp}(E) = \frac{1}{2\pi} \int_{t=0}^{\infty} \exp(iEt/\hbar) C_{vj\Omega, v'j'\Omega'}^{Jp}(t) dt \quad (2.43)$$

from which the  $S$  matrix elements are calculated using the expression:

$$S_{vj\Omega, v'j'\Omega'}^{Jp}(E) = \left( \frac{k_{vj} k_{v'j'}}{\mu \mu'} \right)^{1/2} \frac{\hbar A_{vj\Omega, v'j'\Omega'}^{Jp}(E)}{g(-k_{vj})} \exp(-ik_{v'j'} R'_{\infty}) \quad (2.44)$$

where  $k_{vj}$  and  $k_{v'j'}$  are the wavenumber of the reactant and product rovibrational states,  $\mu$  and  $\mu'$  is the reduced mass of the reactants and products, and  $g(-k_{vj})$  is the amplitude of the initial wavepacket with momentum  $-\hbar k_{vj}$ .

## 2.4 The time independent (TI) method

Time independent techniques are conceptually more complex than time dependent ones since they require two computational steps: the calculation of a lower dimensionality basis set and the propagation along a properly defined reaction coordinate of the scattering coupled differential equations. This is due to the fact that by eliminating time from the equations one needs to adopt a new continuity variable by working out an appropriate mathematical variable (reaction coordinate) smoothly connecting reactant and product asymptotic regions. In my thesis work I focused the attention on the popular choice of adopting a set of orthogonal coordinates undergoing a smooth transformation from a reactant to a product biased arrangement by performing a gradual kinematic rotation from the reactants to the products geometry, embodying the description of the proceeding of the reaction in a single variable (reaction coordinate). The remaining coordinates, orthogonal to this one, support the description of the bound motion of the system.

### 2.4.1 Hyperspherical coordinates

A conceptually simple example of this type of coordinates are the natural coordinates  $(\rho_\eta, \rho_\sigma)$  [63], shown in figure 2.5 for a collinear reaction ( $\Theta = 180^\circ$ ). The reaction coordinate  $\rho_\eta$  can be chosen to coincide either with the minimum energy path (Minimum Energy Path, MEP) connecting the two asymptotes or with the maximum gradient path (Steepest Descent or SD) connecting the saddlepoint to the asymptotes. These two curves, though having a complicated exact formulation, are very useful for qualitative discussions of the dynamics of chemical systems. To such popularity of the natural coordinates for qualitative discussions about dynamical effects, does not correspond, however, an adequate formal development because of the problems arising in the formulation of the scattering equations for reactions especially when, as is the case of the homonuclear reactions such as  $\text{H} + \text{H}_2$  and  $\text{N} + \text{N}_2$ , branching among different product channels may occur.

A coordinate which is able to describe with continuity the evolution of the geometry of the system between two different asymptotic arrangements (passing through a global aggregate) is the hyperradius  $\rho$  of the hyperspherical coordinates [64–71, 71–73]. It is defined as

$$\rho^2 = R_\lambda^2 + r_\lambda^2 = R_{\lambda+1}^2 + r_{\lambda+1}^2 = R_{\lambda+2}^2 + r_{\lambda+2}^2 \quad (2.45)$$

and so it is independent of the reference arrangement  $\lambda$ . The other two hyperspherical coordinates

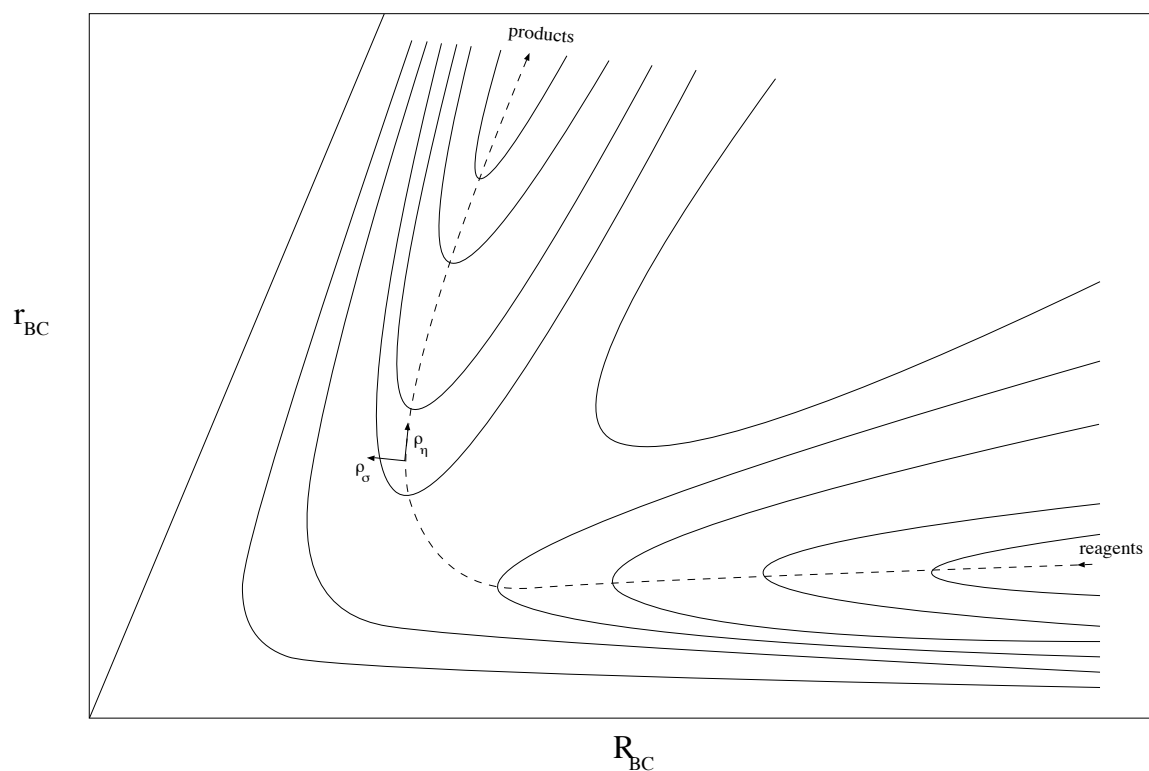


Figure 2.5: Sketch of the natural coordinates for the reaction  $H + H_2$ .

are angles which can be defined either in a symmetric or in an asymmetric way [66–71,71–74]. For the asymmetric set of hyperspherical coordinates one takes the plane defined by a fixed value of the collision angle  $\Theta_\lambda$ , and the angle  $\psi_\lambda$  defined as

$$\psi_\lambda = \arctan \frac{R_\lambda}{r_\lambda} \quad (2.46)$$

(called  $\chi_\lambda$  in the formalism of ref. [64]) and coincides with Smith's kinematic angle  $\Psi_\lambda$  [65] for less than a different choice of the origin. In order to clarify the relationships relating the hyperspherical coordinates to the Jacobi and physical coordinates, we can use the internal cartesian coordinates  $\xi_\lambda$ ,  $\eta$  and  $\zeta_\lambda$ . The relationships linking the cartesian internal coordinates to the Jacobi coordinates are:

$$\begin{aligned} \xi_\lambda &= \frac{2}{\rho} (\mathbf{r}_\lambda \cdot \mathbf{R}_\lambda) = \frac{2}{\rho} |\mathbf{r}_\lambda| |\mathbf{R}_\lambda| \cos \Theta_\lambda, \\ \eta &= \frac{2}{\rho} (\mathbf{r}_\lambda \times \mathbf{R}_\lambda) = \frac{2}{\rho} |\mathbf{r}_\lambda| |\mathbf{R}_\lambda| \sin \Theta_\lambda, \\ \zeta_\lambda &= \frac{1}{\rho} (|\mathbf{r}_\lambda|^2 - |\mathbf{R}_\lambda|^2), \end{aligned} \quad (2.47)$$

where  $\cdot$  and  $\times$  indicate respectively the scalar and vectorial products (the modulus of the vectorial product equals two times the area of the triangle defined by the three particles (area =  $\eta\rho/4$ )). If we

introduce the polar representation of the Jacobi vectors:

$$\begin{aligned} r_\lambda &= \rho \cos \psi_\lambda, \\ R_\lambda &= \rho \sin \psi_\lambda, \end{aligned} \quad (2.48)$$

it can be immediately seen that the expression of the internal coordinates  $\xi_\lambda$ ,  $\eta$  and  $\zeta_\lambda$  in the non symmetric hyperspherical parametrization,  $(\rho, \psi_\lambda$  and  $\Theta_\lambda)$ , exhibits a double interval for the angle  $\psi_\lambda$ . Moreover, the relationship linking the internal angles  $2\psi_\lambda$  and  $\Theta_\lambda$  of the non symmetric parametrization to the internal cartesian coordinates allows also to link the angles of the symmetric parametrization  $2\Theta$  and  $2\Psi_\lambda$  ( $\Phi_\lambda$  in [64]) as follows

$$\begin{aligned} \xi_\lambda &= \rho \sin 2\psi_\lambda \cos \Theta_\lambda = \rho \cos 2\Theta \sin 2\Psi_\lambda, \\ \eta &= \rho \sin 2\psi_\lambda \sin \Theta_\lambda = \rho \sin 2\Theta, \\ \zeta_\lambda &= \rho \cos 2\psi_\lambda = \rho \cos 2\Theta \cos 2\Psi_\lambda. \end{aligned} \quad (2.49)$$

These two different choices of the internal angles represent the two main alternative hyperspherical parametrizations. All other parametrizations can be obtained from these two by the introduction of appropriate scaling factors. The relationships linking the three internal cartesian coordinates to the set of coordinates of two internuclear distances and the angle that they form are:

$$\begin{aligned} \xi_\lambda &= \frac{2}{\rho} (r_{\lambda+2,\lambda+1} r_{\lambda,\lambda+1} \cos \Phi_\lambda - \frac{m_{\lambda+2}}{m_{\lambda+2} + m_{\lambda+1}} r_{\lambda+2,\lambda+1}^2), \\ \eta &= \frac{2}{\rho} (r_{\lambda+2,\lambda+1} r_{\lambda,\lambda+1} \cos \Phi_\lambda), \\ \zeta_\lambda &= \frac{d^2}{\rho} \left( [d^{-4} - (\frac{m_{\lambda+2}}{m_{\lambda+1} + m_{\lambda+2}})^2] r_{\lambda+2,\lambda+1}^2 - r_{\lambda,\lambda+1}^2 + 2 \frac{m_{\lambda+2}}{m_{\lambda+1} + m_{\lambda+2}} \right. \\ &\quad \left. \times r_{\lambda+2,\lambda+1} r_{\lambda,\lambda+1} \cos \Phi_\lambda \right) \end{aligned} \quad (2.50)$$

( $\Phi_\lambda$  is the  $\delta$  of ref. [64]). The bond angle is related to the distances by the relationship

$$\cos \Phi_\lambda = \frac{r_{\lambda+2,\lambda+1}^2 + r_{\lambda,\lambda+1}^2 - r_{\lambda,\lambda+2}^2}{2 r_{\lambda+2,\lambda+1} r_{\lambda,\lambda+1}}, \quad (2.51)$$

so that cartesian internal coordinates can be related to physical distances and angles. The expression that relates the hyperradius to the distances and to the internal cartesian coordinate is

$$\rho^2 = \mu \sum_{\lambda=1}^3 \frac{r_{\lambda+1,\lambda+2}^2}{M_\lambda} = (\xi_\lambda^2 + \eta^2 + \zeta_\lambda^2). \quad (2.52)$$

### 2.4.2 Delves hyperspherical coordinates

In reactive scattering the asymmetric hyperspherical coordinates were first introduced as Delves coordinates [70], which make use of the angle  $\theta_{D_\lambda}$  defined as

$$\theta_{D_\lambda} = \arctan(r_\lambda/R_\lambda), \quad (2.53)$$

and of the angle  $\Theta_\lambda$ . Delves hyperspherical coordinates, though referring to one definite atom-diatom geometry, are not particularly suited to describe the related asymptotic situation, as true for all the hyperspherical coordinate systems. Hyperspherical coordinates, in fact, due to the use of an angle for the final diatom description (rather than the related arc which would tend instead to the internuclear distance), do not have a decoupled formulation at large values of  $\rho$  (see also ref [75]). Therefore, at large values of  $\rho$ , it is preferable to perform a transformation into Jacobi coordinates. The volume element and coordinate ranges of Jacobi and Delves coordinates are, for an arbitrary function  $F$  [74]

$$\int F d\mathbf{R}_\lambda d\mathbf{r}_\lambda = \int_0^\infty R_\lambda^2 dR_\lambda \int_0^\infty r_\lambda^2 dr_\lambda \int d\hat{R}_\lambda \int F d\hat{r}_\lambda \quad (2.54)$$

and

$$\int F d\mathbf{R}_\lambda d\mathbf{r}_\lambda = \frac{1}{4} \int_0^\infty \rho^5 d\rho \int_0^{\pi/2} \sin^2(2\theta_{D_\lambda}) d\theta_{D_\lambda} \int d\hat{R}_\lambda \int F d\hat{r}_\lambda. \quad (2.55)$$

Then, in the reference SF system, the following relationship can be used:

$$d\hat{R}_\lambda d\hat{r}_\lambda = \sin \vartheta_{R_\lambda} d\vartheta_{R_\lambda} d\varphi_{R_\lambda} \sin \vartheta_{r_\lambda} d\vartheta_{r_\lambda} d\varphi_{r_\lambda},$$

and in the  $BF_\lambda$  system

$$d\hat{R}_\lambda d\hat{r}_\lambda = d\alpha_\lambda \sin \beta_\lambda d\beta_\lambda d\gamma_\lambda \sin \Theta_\lambda d\Theta_\lambda,$$

so that both angular integrations cover the usual  $(4\pi)^2$  sr. The surface of the hypersphere is the five-dimensional surface defined by the angles  $\theta_{D_\lambda}$ ,  $\Theta_\lambda$ ,  $\alpha$ ,  $\beta$  and  $\gamma$ , though sometimes, improperly, the hypersphere is meant to be only the two-dimensional surface of the internal coordinate half-sphere defined by  $\theta_{D_\lambda}$  and  $\chi_i$ .

While  $\rho$  gives an idea of the overall size of the ABC system (and thus of its moving towards fragments),  $\theta_{D_\lambda}$  and  $\Theta_\lambda$  describe the shape of the triangle formed by the three particles. For these reasons, it is often very helpful to view things on the surface of the internal sphere as functions of  $\theta_{D_\lambda}$  and  $\Theta_\lambda$  at  $\rho$  fixed. Since  $\theta_{D_\lambda}$  and  $\Theta_\lambda$  cover the upper half of the surface of a sphere, we can

make plots using the projection most commonly used in making maps of the Earth as viewed from the North pole, and that is the *stereographic projection*, in which the  $X$  and the  $Y$  on the plot are defined by

$$X = \tan\left(\frac{1}{2}\theta_{D\lambda}\right) \cos \Theta_\lambda, \quad Y = \tan\left(\frac{1}{2}\theta_{D\lambda}\right) \sin \Theta_\lambda. \quad (2.56)$$

To give an example of the use of these coordinates to draw isoenergetic contours of a potential energy surface, we plot in Fig 2.6 the contour maps of the LAGROBO4 PES for the system  $N + N_2$  (for a more detailed description see later) at the hyperradius of the transition state ( $\rho = 4.39$  bohr).

### 2.4.3 Hyperspherical adiabatic coordinates

To get a set of coordinates more adequate for the description of the geometries of the strong interaction region, before building the hyperspherical representation the Jacobi coordinates can be transformed into a set of coordinates which adiabatically transform from a geometry to another by continuously redirecting  $R_\lambda$  along the principal axis of inertia (AP, Adiabatically adjusting Principal axis of inertia [74]). In fact, if we consider the arbitrary angle  $\chi_\lambda$  of the kinematic rotation (called kinematic angle) that transforms  $R_\lambda$  and  $r_\lambda$  in the vectors  $\mathbf{Q}$  and  $\mathbf{q}$ :

$$\begin{pmatrix} \mathbf{Q} \\ \mathbf{q} \end{pmatrix} = \mathbf{T}(\chi_\lambda) \begin{pmatrix} \mathbf{R}_\lambda \\ \mathbf{r}_\lambda \end{pmatrix}, \quad (2.57)$$

we can choose the value of  $\chi_\lambda$  which maximizes  $\mathbf{Q}$  and minimizes  $\mathbf{q}$ . Such angle is defined by the relationships:

$$\sin(2\chi_\lambda) = \frac{2\mathbf{R}_\lambda \cdot \mathbf{r}_\lambda}{[(R_\lambda^2 - r_\lambda^2)^2 + (2\mathbf{R}_\lambda \cdot \mathbf{r}_\lambda)^2]^{1/2}}, \quad (2.58)$$

$$\cos(2\chi_\lambda) = \frac{(R_\lambda^2 - r_\lambda^2)}{[(R_\lambda^2 - r_\lambda^2)^2 + (2\mathbf{R}_\lambda \cdot \mathbf{r}_\lambda)^2]^{1/2}} \quad (2.59)$$

The formulation of  $\mathbf{Q}$  and  $\mathbf{q}$  in terms of the Jacobian coordinates is therefore:

$$Q = \left( \frac{R_\lambda^2 + r_\lambda^2}{2} + \frac{[(R_\lambda^2 - r_\lambda^2)^2 + (2\mathbf{R}_\lambda \cdot \mathbf{r}_\lambda)^2]^{1/2}}{2} \right)^{1/2}, \quad (2.60)$$

$$q = \left( \frac{R_\lambda^2 + r_\lambda^2}{2} - \frac{[(R_\lambda^2 - r_\lambda^2)^2 + (2\mathbf{R}_\lambda \cdot \mathbf{r}_\lambda)^2]^{1/2}}{2} \right)^{1/2}. \quad (2.61)$$

Even if equations 2.60 and 2.61 are labeled by  $\lambda$ ,  $Q$  and  $q$  do not depend on a specific arrangement. In fact, the angles  $\chi_\lambda$  for different arrangements differ only for a determined phase.

LAGROBO4 PES (eV),  $\rho=4.39$  bohr

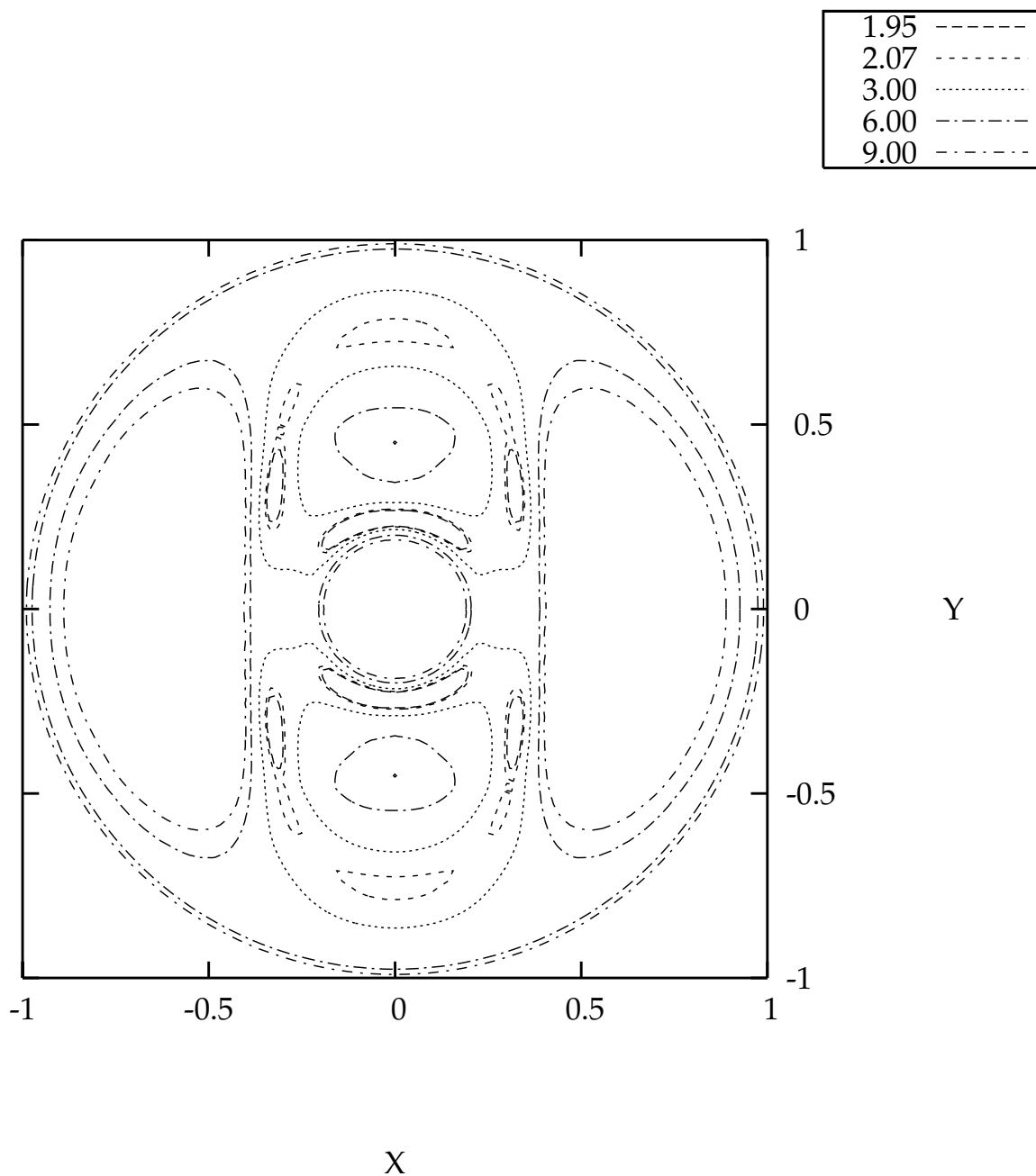


Figure 2.6: Stereographic projection of isoenergetic contours of the LAGROBO4 (for a definition of the LAGROBO potential see later) PES for the system  $N + N_2$  as a function of  $\theta_{D\lambda}$  and  $\Theta_\lambda$  on the surface of the sphere with the transition state hyperradius  $\rho = 4.39$  bohr. The distance from the center of the plot (North pole) is a measure of  $\theta_{D\lambda}$ , and the azimuthal angle  $\Theta_\lambda$  is measured from the positive  $X$  axis.

The choice of this particular angle lets the vector  $\mathbf{Q}$  tend to the Jacobian vector  $\mathbf{R}_\lambda$  when the latter gets large (that is when the atom  $\lambda$  lies far away from the diatom). This behaviour is important, given the specificity of the Jacobian coordinates to identify a given arrangement. Unfortunately, however,  $q$  does not tend to  $r_\lambda$  at the same time. As a consequence, the coordinate system  $(\mathbf{Q}, \mathbf{q})$  is not suitable to describe the asymptotic zone. As already mentioned, the study of the collisions requires sometimes a rotation of the cartesian axes in order to preserve certain properties (for instance, to have an axis that heads to the center of mass of the diatom). Such rotations are physical rotations. Let  $\mathfrak{R}(2 \leftarrow 1)$  be the rotation that carries some axes set 1 into axes set 2. Then the representation of  $\mathfrak{R}(2 \leftarrow 1)$  which acts on our column vectors is the  $6 \times 6$  matrix

$$\mathcal{R}(2 \leftarrow 1) = \begin{pmatrix} \mathbf{R} & \mathbf{0} \\ \mathbf{0} & \mathbf{R} \end{pmatrix}, \quad (2.62)$$

where  $\mathbf{0}$  is the  $3 \times 3$  null matrix and  $\mathbf{R}$  is the matrix of Euler angles. Then, the column vectors of coordinates relative to the two sets of axes are related by

$$\begin{pmatrix} \mathbf{R}_\lambda^2 \\ \mathbf{r}_\lambda^2 \end{pmatrix} = \mathcal{R}(2 \leftarrow 1) \begin{pmatrix} \mathbf{R}_\lambda^1 \\ \mathbf{r}_\lambda^1 \end{pmatrix}. \quad (2.63)$$

Equation 2.63 is used to define the rotation that carries a system 1 fixed in space (SF) into system 2 integral with the body (BF). In this case, if we choose the Euler angle  $\gamma_\lambda$  so that the coordinate  $r_\lambda$  has a zero  $\varphi$  angle in the  $\text{BF}_\lambda$  system - that is  $r_\lambda$  lies in the  $\text{BF}_\lambda XZ$  plane with a non negative  $X$  component - by choosing the  $\text{BF}_\lambda$  system so that  $R_\lambda$  lies along the axis  $Z$ , each BF reference system for  $\lambda = A, B$  and  $C$  has a common  $Y$  axis. Because of this, the transformation between the two systems is obtained by simply rotating about the common  $Y$  axis.

The procedure followed to maximize  $\mathbf{Q}$  - and minimize  $\mathbf{q}$  - is equivalent to make the reference BF system an instantaneous principal axes system and to make these two coordinates coincide with the principal axes of the tensor of inertia itself.

There is a line for which  $R_\lambda = r_\lambda$  and  $\mathbf{R}_\lambda \cdot \mathbf{r}_\lambda = 0$  (and thereby  $Q=q$ ). This makes that the denominator and the numerator of the equations 2.58 and 2.59 become null, making  $\chi_\lambda$  undefined. Out of the AP coordinates one can define the APH coordinates (Adiabatically adjusting Principal axis of inertia Hyperspherical coordinates [74]). APH coordinates are the symmetric version of the hyperspherical coordinates often easier to use in the treatment of the strong interaction region. The expressions that links the APH coordinates to the AP ones are:

$$\begin{aligned} \rho^2 &= Q^2 + q^2, \\ \theta &= \frac{\pi}{2} - 2 \arctan q/Q, \end{aligned} \quad (2.64)$$

where  $\rho \in [0, \infty)$  is the hyperradius and  $\theta \in [0, \pi/2]$  is one of the two hyperangles. The remaining hyperangle,  $\chi_\lambda \in (-\pi/2, \pi/2]$ , is such that maximizes  $\mathbf{Q}$ . The coordinate ranges cover the upper half of a sphere and can be visualized as polar spherical coordinates of the internal space. The line undefined in  $\chi_\lambda$  is now the line  $\theta = 0$  which, like in polar spherical coordinates, does not cause any problem. The three APH coordinates can be directly expressed as functions of the Jacobian coordinates:

$$\begin{aligned}\sin(2\chi_\lambda) &= \frac{2\mathbf{R}_\lambda \cdot \mathbf{r}_\lambda}{[(R_\lambda^2 - r_\lambda^2)^2 + (2\mathbf{R}_\lambda \cdot \mathbf{r}_\lambda)^2]^{1/2}}, \\ \cos(2\chi_\lambda) &= \frac{(R_\lambda^2 - r_\lambda^2)}{[(R_\lambda^2 - r_\lambda^2)^2 + (2\mathbf{R}_\lambda \cdot \mathbf{r}_\lambda)^2]^{1/2}}, \\ \tan \theta &= \frac{[(R_\lambda^2 - r_\lambda^2)^2 + (2\mathbf{R}_\lambda \cdot \mathbf{r}_\lambda)^2]^{1/2}}{2R_\lambda r_\lambda \sin \Theta_\lambda},\end{aligned}\quad (2.65)$$

and

$$\rho^2 = (R_\lambda^2 + r_\lambda^2)^{1/2}, \quad (2.66)$$

where we note how these two polar coordinates are  $\lambda$ -independent, that is do not depend on a particular arrangement. The inverse formulae are:

$$R_\lambda = \frac{\rho}{\sqrt{2}} \{1 + \sin \theta \cos[2(\chi_i - \chi_{\lambda i})]\}^{1/2}, \quad (2.67)$$

$$r_\lambda = \frac{\rho}{\sqrt{2}} \{1 - \sin \theta \cos[2(\chi_i - \chi_{\lambda i})]\}^{1/2}, \quad (2.68)$$

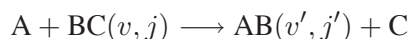
and

$$\cos \Theta_\lambda = \frac{\sin \theta \sin[2(\chi_i - \chi_{\lambda i})]}{\{1 - \sin^2 \theta \cos^2[2(\chi_i - \chi_{\lambda i})]\}^{1/2}}. \quad (2.69)$$

These equations are useful because we can generate using them (eq. 2.68 in particular) the internuclear distances relative to a triple of  $\rho$ ,  $\theta$  and  $\chi_i$ . The BF axes are fixed on the instantaneous principal axes of inertia, and they adiabatically adjust to follow any atom which leaves the other two. The internal coordinates treat all arrangements equivalently, and also switch smoothly between reactant and product arrangement during the course of the reaction.

## 2.5 Hamiltonian formulation and boundary conditions

For the generic atom-diatom reaction:



the stationary scattering Schrödinger equation has the general form [74,76,77]:

$$[H_N - E] \Xi_{\lambda_i v_i j_i m_i}^{(+)}(\mathbf{R}_\lambda, \mathbf{r}_\lambda) = 0, \quad (2.70)$$

where  $i$  implies “initial” or “incident” and the quantum numbers  $\lambda, v, j$ , and  $m$  label, respectively, the arrangement channel, vibration, angular momentum, and SF  $Z$  component of the angular momentum of the initial diatomic molecule (sometimes  $i$  will be used as a composite quantum number that includes all of them). The (+) label implies the usual (see eq. 2.74) incident plane wave - outgoing scattered waves boundary condition.

The nuclear hamiltonian  $H_N$  has the form given in eq. 2.4 that can be further compacted using a mass scaled version of the Jacobi vectors  $\mathbf{R}_\lambda$  and  $\mathbf{r}_\lambda$ :

$$-\frac{\hbar^2}{2\mu}(\nabla_{\mathbf{R}_\lambda}^2 + \nabla_{\mathbf{r}_\lambda}^2) + V(R_\lambda, r_\lambda, \Theta_\lambda) \quad (2.71)$$

and hence it is hexadimensional. Recently, its solution directly in the six cartesian projections has been attempted. Most often, as done in eqs. 3.5 and 3.6 it is found convenient to exploit the algebra of angular momenta by expressing the hamiltonian in terms of the rotational  $\mathbf{j}_\lambda$  and orbital  $\mathbf{l}_\lambda$  angular momentum operators (or of the total angular momentum  $\mathbf{J}$  [76] and  $\mathbf{j}_\lambda$ ) and reformulate the hamiltonian either as

$$H_N = -\frac{\hbar^2}{2\mu} \left( \frac{1}{\mathbf{R}_\tau} \frac{\partial^2}{\partial \mathbf{R}_\tau^2} \mathbf{R}_\tau + \frac{1}{\mathbf{r}_\tau} \frac{\partial^2}{\partial \mathbf{r}_\tau^2} \mathbf{r}_\tau - \frac{\mathbf{l}_\lambda^2}{\mathbf{R}_\tau^2} - \frac{\mathbf{j}_\lambda^2}{\mathbf{r}_\tau^2} \right) + V(\mathbf{R}_\tau, \mathbf{r}_\tau, \Theta_\lambda). \quad (2.72)$$

or as

$$H_N = -\frac{\hbar^2}{2\mu} \left( \frac{1}{\mathbf{R}_\tau} \frac{\partial^2}{\partial \mathbf{R}_\tau^2} \mathbf{R}_\tau + \frac{1}{\mathbf{r}_\tau} \frac{\partial^2}{\partial \mathbf{r}_\tau^2} \mathbf{r}_\tau \right) + \frac{1}{2\mu} \left( \frac{1}{\mathbf{R}_\tau^2} + \frac{1}{\mathbf{r}_\tau^2} \right) \mathbf{j}_\lambda^2 \quad (2.73)$$

$$+ \frac{1}{2\mu \mathbf{R}_\tau^2} (\mathbf{J}^2 - \mathbf{J}_- \cdot \mathbf{j}_+ - \mathbf{J}_+ \cdot \mathbf{j}_- + -2J_z j_z) + V(\mathbf{R}_\tau, \mathbf{r}_\tau, \Theta_\lambda).$$

In equation 2.73,  $j_z$  is the  $Z$  axis component of  $\mathbf{j}$ , while  $\mathbf{J}_\pm$  and  $\mathbf{j}_\pm$  represent the displacement operators related to  $\mathbf{J}$  and  $\mathbf{j}$ .

## 2.5.1 Asymptotic boundary conditions

The scattering asymptotic boundary condition at  $R \rightarrow \infty$  is:

$$\begin{aligned} \Xi_i^{(+)}(\mathbf{R}_\lambda, \mathbf{r}_\lambda) &\xrightarrow{R \rightarrow \infty} \frac{1}{r_{\lambda_i}} \exp(i\mathbf{k}_i \cdot \mathbf{R}_{\lambda_i}) \mathcal{X}_{v_i j_i}(r_{\lambda_i}) Y_{j_i m_i}(\hat{r}_{\lambda_i}) \\ &+ \sum_{\lambda_f v_f j_f m_f} \frac{1}{R_{\lambda_f} r_{\lambda_f}} f(\lambda_f v_f j_f m_f \leftarrow \lambda_i v_i j_i m_i | \mathbf{k}_i, k_f, \hat{R}_{\lambda_f}) \\ &\times \mathcal{X}_{v_f j_f}(r_{\lambda_f}) Y_{j_f m_f}(\hat{r}_{\lambda_f}) \exp(ik_f S_{\lambda_f}). \end{aligned} \quad (2.74)$$

The  $\mathcal{X}$ 's and  $Y$ 's are the vibrational and rotational wavefunctions, respectively, of the three possible diatomic molecules. Subscript  $f$  (which will sometimes be used as a composite index) runs over all possible final states including  $f = i$  (elastic scattering). With the symbol “ $\hat{\cdot}$ ” we label a versor (unitary vector having verse and direction of the original vector). The function  $f(\lambda_f v_f j_f m_f \leftarrow \lambda_i v_i j_i m_i | \mathbf{k}_i, k_f, \hat{R}_{\lambda_f})$  is defined as scattering amplitude. The terms in the sum with  $\lambda_f \neq \lambda_i$  represent reactive scattering, and those with  $\lambda_f = \lambda_i$  include elastic and inelastic scattering. The wavenumbers  $k_f$  are given by

$$k_f = \left[ \frac{2\mu}{\hbar^2} (E - \epsilon_f) \right]^{1/2}, \quad (2.75)$$

where  $\epsilon_f = \epsilon_{v_f j_f}$  are diatomic vibration-rotation energies<sup>1</sup>.

It should be noted that the incident direction  $\mathbf{k}_i$  in eq. 2.74 has been kept arbitrary for convenience in calculating kinetic theory cross sections, and all coordinates are relative to SF directional axes. Furthermore, the partial wave expression of  $\Xi$  in the total angular momentum representation is:

$$\begin{aligned} \Xi_i^{(+)}(\mathbf{R}_\lambda, \mathbf{r}_\lambda) &= \frac{2\pi}{k_i^{1/2}} \sum_{J M l_i} i^{l_i+1} C(j_i l_i J; m_i, M - m_i, M) \\ &\times Y_{l_i, M - m_i}^*(\hat{k}_i) \Psi^{J M \lambda_i v_i j_i l_i}, \end{aligned} \quad (2.76)$$

where  $C$  is a Clebsch-Gordan coefficient and  $\Psi$  is an eigenfunction of the total angular momentum with eigenvalue  $J$  and projection  $M$ . We note that we are here using spaceframe (SF) Jacobi coordinates because they are convenient at large distances, but equation 2.76 is valid at all distances. In these SF Jacobi coordinates,  $\Psi$  can be written as

$$\begin{aligned} \Psi^{J M \lambda_i v_i j_i l_i} &= \sum_{\lambda_f v_f j_f l_f} \frac{1}{R_{\lambda_f} r_{\lambda_f}} G_{\lambda_f v_f j_f l_f}^{J \lambda_i v_i j_i l_i}(R_{\lambda_f}) \mathcal{X}_{v_f j_f}(r_{\lambda_f}) \\ &\times \mathcal{Y}_{j_f l_f}^{J M}(\hat{r}_{\lambda_f}, \hat{R}_{\lambda_f}), \end{aligned} \quad (2.77)$$

where, as usual,

$$\begin{aligned} \mathcal{Y}_{j_f l_f}^{J M}(\hat{r}_{\lambda_f}, \hat{R}_{\lambda_f}) &= \sum_{m_f} C(j_f l_f J; m_f, M - m_f, M) Y_{j_f, m_f}(\hat{r}_{\lambda_f}) \\ &\times Y_{l_f, M - m_f}(\hat{R}_{\lambda_f}), \end{aligned} \quad (2.78)$$

and the  $Y$ 's are spherical harmonics [77]. The radial function  $G$  must be regular everywhere, and,

<sup>1</sup>We confine our treatment to systems at energies well below the collision-induced dissociation (CID) threshold: to include CID would require addition of an outgoing term to eq. 2.74 written in hyperspherical coordinates.

at asymptotic distances, satisfy the usual boundary conditions:

$$G_{\lambda_f v_f j_f l_f}^{J \lambda_i v_i j_i l_i}(R_{\lambda_f}) \xrightarrow{R_{\lambda_f} \rightarrow \infty} \frac{1}{k_f^{1/2}} \{ \delta_{\lambda_f \lambda_i} \delta_{v_f v_i} \delta_{j_f j_i} \delta_{l_f l_i} \exp[-i(k_f R_{\lambda_f} - \frac{\pi}{2} l_f)] - S^J(\lambda_f v_f j_f l_f | \lambda_i v_i j_i l_i) \exp[-i(k_f R_{\lambda_f} - \frac{\pi}{2} l_f)] \}. \quad (2.79)$$

## 2.5.2 The scattering, reactance and transition matrices

In equation 2.79, use is made of  $S^J(\lambda_f v_f j_f l_f | \lambda_i v_i j_i l_i)$ , the elements of the scattering matrix  $\mathbf{S}^J$ . Another matrix relevant to the scattering calculations is the transition  $\mathbf{T}^J$  matrix. The  $\mathbf{T}^J$  matrix is related to  $\mathbf{S}^J$  by simple relationships and turns out to be useful for a compact formulation of the differential cross section:

$$\begin{aligned} \sigma_R^{\lambda_i v_i j_i m_i, \lambda_f v_f j_f m_f}(k_i, k_f, \hat{k}_i, \hat{R}_f) &= (k_f/k_i) | f(f \leftarrow i) |^2 = \\ &= \left| \frac{2\pi}{k_i} \sum_{J M l_i l_f} i^{l_i - l_f + 1} A_i A_f T^J(\lambda_f v_f j_f l_f | \lambda_i v_i j_i l_i) \right|^2, \end{aligned} \quad (2.80)$$

where

$$\begin{aligned} A_i &= C(j_i l_i J; m_i, M - m_i, M) Y_{l_i, M - m_i}^*(\hat{k}_i), \\ A_f &= C(j_f l_f J; m_f, M - m_f, M) Y_{l_f, M - m_f}(\hat{R}_{\lambda_f}), \end{aligned}$$

whose elements are related to those of the  $\mathbf{S}^J$  matrix by the relationships

$$T^J(\lambda_f v_f j_f l_f | \lambda_i v_i j_i l_i) = \delta_{\lambda_f \lambda_i} \delta_{v_f v_i} \delta_{j_f j_i} \delta_{l_f l_i} - S^J(\lambda_f v_f j_f l_f | \lambda_i v_i j_i l_i). \quad (2.81)$$

In theory, boundary conditions can be applied at the asymptote only. In practice, it is desirable to apply boundary conditions at distances no larger than necessary. At distances ( $R_{\lambda_f}$ ) large enough that the atom-diatom potential of channel  $\lambda_f$  is negligible but centrifugal potentials are not negligible, using matrix notation  $\mathbf{G}^J = \{G_{fi}^J\}$  and composite indices for simplicity, one can write equation 2.79 as

$$\mathbf{G}^J = \mathcal{F} - \mathcal{O}\mathbf{S}^J, \quad (2.82)$$

where

$$\mathcal{F}_{fi} = \delta_{fi} k_f^{1/2} R_f h_{l_f}^{(2)}(k_f R_f)$$

and

$$\mathcal{O}_{fi} = i \delta_{fi} k_f^{1/2} R_f h_{l_f}^{(1)}(k_f R_f), \quad (2.83)$$

where the  $h_l^{(i)}$  are the incoming and outgoing spherical Bessel functions. In addition, it is convenient to deal with real functions for most of the calculations, i.e., to construct real functions  $\mathbf{F} = \mathbf{F}^J$  satisfying the same differential equation as the  $\mathbf{G}^J$ , but satisfying the boundary condition:

$$\mathbf{F}^J = \mathbf{a} - \mathbf{b}\mathbf{K}^J, \quad (2.84)$$

where  $\mathbf{K}^J$  is called the “reactance” matrix although it has no special relation to reactive scattering. For the open (asymptotically allowed) channels, the elements of  $\mathbf{a}$  and  $\mathbf{b}$  are simply proportional to the spherical Riccati-Bessel functions,

$$a_{fi} = \delta_{fi} k_f^{1/2} R_f j_{l_f}(k_f R_f)$$

and

$$b_{fi} = \delta_{fi} k_f^{1/2} R_f y_{l_f}(k_f R_f). \quad (2.85)$$

For asymptotically closed channels, we let

$$k_f = i\kappa_f, \quad (2.86)$$

where  $\kappa_f = |k_f|$  and choose

$$a_{fi} = \delta_{fi} \kappa_f^{1/2} R_f i^{-l_f} j_{l_f}(i\kappa_f R_f)$$

and

$$b_{fi} = \delta_{fi} \kappa_f^{1/2} R_f i^{l_f+2} h_{l_f}^{(1)}(i\kappa_f R_f). \quad (2.87)$$

The  $a_{fi}$  are real and closely related to the modified spherical Bessel functions  $I_{l_f+1/2}$  which are regular at the origin, and the  $b_{fi}$  are also real and closely related to the modified spherical Bessel functions  $K_{l_f+1/2}$  which die exponentially at large distances. The boundary conditions 2.79 can be applied before the dying closed channel functions  $b_{fi}$  are negligible and the complete  $\mathbf{K}^J$  matrix containing both open and closed channels can thus be generated. However, the calculation of cross sections only requires the scattering matrix between open channels, and it can be easily shown that the desired  $\mathbf{S}^J$  matrix is obtained from the reactance matrix through

$$\mathbf{S}^J = (\mathbf{1} + i\mathbf{K}^J)(\mathbf{1} - i\mathbf{K}^J)^{-1}, \quad (2.88)$$

where  $\mathbf{1}$  is the unit matrix, and only the open channel - open channel block of  $\mathbf{K}^J$  is to be included in the equation.

In actual practice, the present calculations generate the Wigner  $\mathbf{R}^J$  matrix,

$$\mathbf{R}^J = \mathbf{F}(\mathbf{F}')^{-1}, \quad (2.89)$$

where the prime implies the derivative with respect to the appropriate  $R_{\lambda_f}$ :

$$F'_{fi} = \frac{\partial F_{fi}}{\partial R_{\lambda_f}}. \quad (2.90)$$

On substitution of eq. 2.84 into eq. 2.89, one readily finds that

$$\mathbf{K}^J = [\mathbf{R}^J \mathbf{b}' - \mathbf{b}]^{-1} [\mathbf{R}^J \mathbf{a}' - \mathbf{a}] \quad (2.91)$$

gives the  $\mathbf{K}^J$  matrix from the  $\mathbf{R}^J$  matrix.

$\mathbf{F}$  and  $\mathbf{G}^J$  have the same  $\mathbf{R}^J$  matrix. They satisfy the same coupled equations and differ only in their initial wave boundary conditions, so that it can be shown that  $\mathbf{G}^J = \mathbf{F}\mathbf{A}$  or

$$G^J_{fi} = \sum_n F_{fn} A_{ni}, \quad (2.92)$$

where the linear combination only mixes *initial* components. Thus, the  $\mathbf{R}^J$  matrix is

$$\mathbf{R}^J_G = \mathbf{G}^J (\mathbf{G}^{J'})^{-1} = \mathbf{F}\mathbf{A}(\mathbf{F}'\mathbf{A})^{-1} = \mathbf{F}\mathbf{A}\mathbf{A}^{-1}(\mathbf{F}')^{-1} = \mathbf{F}(\mathbf{F}')^{-1} = \mathbf{R}^J_F. \quad (2.93)$$

We note that the coefficient matrix  $\mathbf{A}$  is unimportant here. What is important is that the same  $\mathbf{R}^J$  matrix is obtained from any radial wavefunctions differing only by a rearrangement of their initial indices. Hence, the useful property of the  $\mathbf{R}^J$  matrix will hold for *all regular* solutions of a given set of coupled equations.

We also note that the functions of eq. 2.77 have a well defined parity  $p$  under inversion of the SF axes. The parity is carried by the  $\mathcal{Y}$  functions of eq. 2.78 and is well known to be

$$(-1)^p = (-1)^{j_i+l_i} = (-1)^{j_f+l_f}. \quad (2.94)$$

Functions of different parities are not coupled together.

### 2.5.3 BF Jacobi wavefunctions

The just discussed SF Jacobi formulation is conveniently used at large distances where no exchange is occurring and atom-diatom interactions in the arrangement channels are weak. Yet, at smaller distances, but still outside the exchange region, it is sometimes convenient to use the body-frame formalism. As is well known, the problem can be entirely formulated in the BF, but to avoid

all concerns about phases we simply transform wavefunctions. The spherical harmonics in the  $\mathcal{Y}$  of eq. 2.78 can be written as

$$Y_{l_f, M-m_f}(\hat{R}_f) = \left( \frac{2l_f + 1}{4\pi} \right)^{1/2} D_{0, M-m_f}^{l_f}(\alpha_f, \beta_f, \gamma_f) \quad (2.95)$$

and

$$Y_{j_f m_f}(\hat{r}_f) = \sum_{\Omega_f} Y_{j_f \Omega_f}(\Theta_f, 0) D_{\Omega_f m_f}^{j_f}(\alpha_f, \beta_f, \gamma_f), \quad (2.96)$$

where  $R_f$  means  $R_{\lambda_f}$ ,  $\alpha_f$  means  $\alpha_{\lambda_f}$ , etc. Here  $f$  can be any possible final state (including  $f = i$ ), and  $\lambda_f$  is the arrangement channel of state  $f$  and  $\Omega$ , as already mentioned in section 2.1.2, is the component of the total angular momentum  $\mathbf{J}$  along BF  $Z$  axis<sup>2</sup>. The Euler angles are those of the BF Jacobi coordinates. The spherical harmonics on the left-hand side of eqs. 2.95 and 2.96 have angles relative to the SF. The spherical harmonic on the right-hand side of the equations depends on a BF angle  $\Theta_{\lambda_f}$  (the angle between  $\mathbf{R}_{\lambda_f}$  and  $\mathbf{r}_{\lambda_f}$ ). The Wigner  $D$  functions here are those consistent with the  $3 \times 3$  rotation matrix of eq. 2.62.

Substituting eqs. 2.95 and 2.96 into eq. 2.78, and using the coupling rule for the  $D$  functions and the orthogonality of the Clebsch-Gordan coefficient, we obtain:

$$\begin{aligned} \mathcal{Y}_{j_f l_f}^{JM}(\hat{r}_f, \hat{R}_f) &= \left( \frac{2l_f + 1}{4\pi} \right)^{1/2} \sum_{\Omega_f} C(j_f l_f J; \Omega_f 0 \Omega_f) \\ &\times Y_{j_f \Omega_f}(\Theta_f, 0) D_{\Omega_f M}^J(\alpha_f, \beta_f, \gamma_f). \end{aligned} \quad (2.97)$$

At this point we note that this equation could also be written as

$$\begin{aligned} \mathcal{Y}_{j_f l_f}^{JM}(\hat{r}_f, \hat{R}_f) &= \left( \frac{2l_f + 1}{4\pi} \right)^{1/2} \sum_{\Omega_f} C(j_f l_f J; \Omega_f 0 \Omega_f) \\ &\times Y_{j_f \Omega_f}(\Theta_f, \gamma_f) D_{\Omega_f M}^J(\alpha_f, \beta_f, 0). \end{aligned} \quad (2.98)$$

We note that eqs. 2.97 and 2.98 are exactly the same function  $\mathcal{Y}_{j_f l_f}^{JM}$  and involve the same coordinates. They simply correspond to different points of view. Equation 2.98 takes two nonzero Euler angles; then in the BF the variable  $\hat{r}_f$  has two nonzero angles and its basis functions are ordinary spherical harmonics. In this view, the  $\gamma_f$  dependence is part of the internal or BF wavefunction. On the other hand, eq. 2.97 takes three nonzero Euler angles and leaves the BF  $\hat{r}_f$  with only one angle, so that  $\gamma_f$  is then not part of the internal or BF wavefunction. The two approaches give exactly the same set of coupled equations to solve, and choice between them is simply a matter of convenience.

---

<sup>2</sup>This component is sometimes labelled using  $\Omega$  [74].

For the present problem, eq. 2.97 simplifies the relationship between the three different  $BF_{\lambda_f}$  coordinate system, and we use it. In writing eq. 2.97 it is often convenient to use normalized basis functions,

$$\hat{P}_{j\Omega}(\Theta) = (2\pi)^{1/2} Y_{j\Omega}(\Theta, 0) \quad (2.99)$$

and

$$\hat{D}_{\Omega M}^J(\alpha, \beta, \gamma) = \left[ \frac{(2J+1)}{8\pi^2} \right]^{1/2} D_{\Omega M}^J(\alpha, \beta, \gamma), \quad (2.100)$$

for which

$$\int_0^\pi \hat{P}_{j'\Omega}^*(\Theta) \hat{P}_{j\Omega}(\Theta) d(\cos \Theta) = \delta_{j'j} \quad (2.101)$$

and

$$\int_0^{2\pi} \int_0^\pi \int_0^{2\pi} \hat{D}_{\Omega' M'}^{J'*}(\alpha, \beta, \gamma) \hat{D}_{\Omega M}^J(\alpha, \beta, \gamma) d\alpha d(\cos \beta) d\gamma = \delta_{J'J} \delta_{M'M} \delta_{\Omega'\Omega}. \quad (2.102)$$

$\hat{P}_{j\Omega}$  is actually real and, to within a phase due to the sign of  $\Omega$ , is just a normalized associated Legendre polynomial. With these functions, eq. 2.97 becomes:

$$\begin{aligned} \mathcal{Y}_{j_f l_f}^{JM}(\hat{r}_f, \hat{R}_f) &= \left( \frac{2l_f + 1}{2J + 1} \right)^{1/2} \sum_{\Omega_f} C(j_f l_f J; \Omega_f 0 \Omega_f) \hat{P}_{j_f \Omega_f}(\Theta_f) \\ &\quad \times \hat{D}_{\Omega_f M}^J(\alpha_f, \beta_f, \gamma_f), \end{aligned} \quad (2.103)$$

and eq. 2.77 becomes:

$$\begin{aligned} \Psi^{JM \lambda_i v_i j_i l_i} &= \sum_{\lambda_f v_f j_f \Omega_f} \frac{1}{R_f r_f} G_{\lambda_f v_f j_f \Omega_f}^{J \lambda_i v_i j_i l_i}(R_f) \mathcal{X}_{v_f j_f}(r_f) \\ &\quad \times \hat{P}_{j_f \Omega_f}(\Theta_f) \hat{D}_{\Omega_f M}^J(\alpha_f, \beta_f, \gamma_f), \end{aligned} \quad (2.104)$$

where

$$G_{\lambda_f v_f j_f \Omega_f}^{J \lambda_i v_i j_i l_i}(R_f) = \sum_{l_f} \left( \frac{2l_f + 1}{2J + 1} \right)^{1/2} C(j_f l_f J; \Omega_f 0 \Omega_f) G_{\lambda_f v_f j_f l_f}^{J \lambda_i v_i j_i l_i}(R_f). \quad (2.105)$$

The properties of the Clebsch-Gordan coefficients allow this transformation to be easily inverted to give

$$G_{\lambda_f v_f j_f l_f}^{J \lambda_i v_i j_i l_i}(R_f) = \sum_{\Omega_f} \left( \frac{2l_f + 1}{2J + 1} \right)^{1/2} C(j_f l_f J; \Omega_f 0 \Omega_f) G_{\lambda_f v_f j_f \Omega_f}^{J \lambda_i v_i j_i l_i}(R_f). \quad (2.106)$$

Transformations between SF and BF radial wavefunctions are well known; however, eqs. 2.105 and 2.106 are unusual in that they are half-transforms; both radial functions are labeled by the same incident SF partial wave  $l_i$ , so that the  $G_{l_f}^{l_i}$  are true SF functions but the  $G_{\Omega_f}^{l_i}$  are mixed functions with SF initial labels and BF final labels. They are useful here because, to avoid confusion about

different final BF axes, we intend to apply SF boundary conditions and generate the standard SF scattering matrix. To do so, we define the orthogonal matrix  $\mathbf{C}$  by

$$C_{fn} = \delta_{\lambda_f \lambda_n} \delta_{v_f v_n} \delta_{j_f j_n} \left( \frac{2l_f + 1}{2J + 1} \right)^{1/2} C(j_f l_f J; \Omega_n 0 \Omega_n). \quad (2.107)$$

Then eqs. 2.105 and 2.106 read, respectively,

$$\mathbf{G}_{BF}^J = \tilde{\mathbf{C}} \mathbf{G}_{SF}^J \quad (2.108)$$

and

$$\mathbf{G}_{SF}^J = \mathbf{C} \mathbf{G}_{BF}^J. \quad (2.109)$$

Then, one has

$$\begin{aligned} \mathbf{R}_{SF}^J &= \mathbf{G}_{SF}^J [(\mathbf{G}_{SF}^J)']^{-1} = \mathbf{C} \mathbf{G}_{BF}^J [\mathbf{C} (\mathbf{G}_{BF}^J)']^{-1} \\ &= \mathbf{C} \mathbf{G}_{BF}^J [(\mathbf{G}_{BF}^J)']^{-1} \mathbf{C}^{-1} = \mathbf{C} \mathbf{R}_{BF}^J \tilde{\mathbf{C}}, \end{aligned} \quad (2.110)$$

so that the SF  $\mathbf{R}^J$  matrix is a simple similarity transformation of the BF  $\mathbf{R}^J$  matrix, with a known transformation matrix.

From eq. 2.104 it is clear that  $G_{\lambda_f v_f j_f \Omega_f}^{J \lambda_i v_i j_i l_i}$  satisfies the usual BF coupled equations, and from the initial index it is clear that they have parity  $(-1)^p = (-1)^{j_i + l_i}$  under space inversion. This can be shown to imply that  $G_{\Omega_f}^J$  and  $G_{-\Omega_f}^J$  are simply proportional to one another and to split the coupled equations into sets of definite parity.

## 2.6 The integration of TI scattering equations

The actual integration of scattering equations in my thesis work has been carried out using the ABC program [78]. The Hamiltonian operator in Delves coordinates has the form

$$H_N = -\frac{\hbar^2}{2\mu\rho^5} \frac{\partial}{\partial\rho} \rho^5 \frac{\partial}{\partial\rho} + \frac{\Delta^2}{2\mu\rho^2} + V(\rho, \theta_{D\lambda}, \Theta_\lambda), \quad (2.111)$$

where  $\Delta^2$ , given here by

$$\Delta^2 = -\frac{\hbar^2}{\sin^2 2\theta_{D\lambda}} \frac{\partial}{\partial\theta_{D\lambda}} \sin^2 2\theta_{D\lambda} \frac{\partial}{\partial\theta_{D\lambda}} + \frac{\mathbf{l}_\lambda^2}{\cos^2 \theta_{D\lambda}} + \frac{\mathbf{j}_\lambda^2}{\sin^2 \theta_{D\lambda}}, \quad (2.112)$$

is the square of Smith's grand angular momentum operator [73]. The wavefunction of eq. 2.91 is expanded as

$$\Psi^{JM \lambda_i v_i j_i l_i} = 2 \sum_{\lambda_f v_f j_f l_f} \frac{\Gamma_{\lambda_f v_f j_f l_f}^{J \lambda_i v_i j_i l_i}(\rho)}{\rho^{5/2}} \frac{\Upsilon_{v_f j_f}(\theta_{D\lambda_f}; \rho)}{\sin(2\theta_{D\lambda_f})} \mathcal{Y}_{j_f l_f}^{JM}(\hat{r}_{\lambda_f}, \hat{R}_{\lambda_f}). \quad (2.113)$$

Here the three possible arrangement channels  $\lambda_f$  are distinctively included and the angular functions  $\mathcal{Y}$  are exactly the same as those used in the Jacobi wavefunctions of eqs. 2.77 and 2.78. The  $\Upsilon(\theta_{D_{\lambda_f}}; \rho)$  are vibrational wavefunctions which depend parametrically upon  $\rho$ ; the  $\Gamma$  are radial wavefunctions, and the same hyperradius  $\rho$  occurs in all arrangement channels. The 2 out front in eq. 2.113 is for convenience in working with the volume element of eq. 2.55 when the  $\Upsilon$  satisfy

$$\int_0^{\pi/2} \Upsilon_{v'_f j'_f}^*(\theta_{D_{\lambda_f}}; \rho) \Upsilon_{v_f j_f}(\theta_{D_{\lambda_f}}; \rho) d\theta_{D_{\lambda_f}} = \delta_{v'_f v_f}. \quad (2.114)$$

In problems where all potentials go to zero at large  $\rho$  or only depend on  $\rho$  the  $\Upsilon \mathcal{Y}$  become the analytically known hyperspherical harmonics. However, in all molecular reactive scattering problems of which we are aware, the potential between the atoms of the diatomic molecule of each  $\lambda_f$  arrangement confines the  $\Upsilon$  to a very localized region of  $\theta_{D_{\lambda_f}}$  space, and the hyperspherical harmonics would be a very poor basis set to use.

Because the same angular functions are used for the  $\lambda_f$  channel Delves and Jacobi wavefunctions, the BF Delves axes are the same as the BF Jacobi axes sets, and one can transform to BF angular functions via eq. 2.103 and get  $\Gamma_{l_f}^{l_i}$  that are related to the  $\Gamma_{l_f}^{l_i}$  via the same equations 2.108 and 2.109 that relate  $G_{\Omega_f}^{l_i}$  and  $G_{l_f}^{l_i}$ .

### 2.6.1 The propagation in Delves coordinates

For systems with long-range potentials, it is computationally faster to project the Delves solutions onto Jacobi solutions - as discussed in detail later - and propagate those solutions on out to where the boundary conditions can be applied via eqs. 2.91 and 2.88. However, it is conceptually simpler and often practical to propagate the Delves solutions out to the asymptotic region and apply the boundary conditions directly in Delves coordinates. To allow that, we now transform the boundary conditions into Delves coordinates. We note that the  $\Upsilon$  are obtained at a finite set of  $\rho$  values, at the centers of the propagation sectors. Thus, anywhere on sector  $\xi$ , with center at  $\rho_\xi$ , the  $\Upsilon(\theta; \rho_\xi)$  are independent of  $\rho$ , and eq. 2.113 can be written (using composite indices for brevity) as

$$\Psi^{JM_i} = 2 \sum_n \frac{\Gamma_{ni}^J(\rho)}{\rho^{5/2}} \frac{\Upsilon_n(\theta_{D_n}; \rho_\xi)}{\sin(2\theta_{D_n})} \mathcal{Y}_n^{JM}(\hat{r}_n, \hat{R}_n), \quad (2.115)$$

where  $\Gamma_n^{J_i} = \Gamma_{ni}^J$ . By projection, using eqs. 2.114 and 2.55 one has

$$\Gamma_{f_i}^J(\rho) = \frac{1}{4} \int_0^{\pi/2} \sin^2(2\theta_{D_f}) d\theta_{D_f} \int \left[ \frac{2\Upsilon_f \mathcal{Y}_f^{JM}}{\sin(2\theta_{D_f})} \right]^* (\rho^{5/2} \Psi^{JM_i}) d\hat{r}_f d\hat{R}_f, \quad (2.116)$$

$$\frac{\partial \Gamma_{fi}^J(\rho)}{\partial \rho} = \frac{1}{4} \int_0^{\pi/2} \sin^2(2\theta_{D_f}) d\theta_{D_f} \int \left[ \frac{2\Upsilon_f \mathcal{Y}_f^{JM}}{\sin(2\theta_{D_f})} \right]^* \frac{\partial(\rho^{5/2} \Psi^{JM_i})}{\partial \rho} d\hat{r}_f d\hat{R}_f. \quad (2.117)$$

The  $\Gamma$  functions which we propagate are real regular solutions, so that from eq. 2.77 for  $\Psi^{JM_i}$  with  $\mathbf{G}$  replaced by  $\mathbf{F}$  and using eqs. 2.45 and 2.53 we have

$$\rho^{5/2} \Psi^{JM_i} = \sum_n \frac{2\rho^{1/2}}{\sin(2\theta_{D_n})} F_{ni}^J(R_n) \mathcal{X}_n(r_n) \mathcal{Y}_n^{JM}(\hat{r}_n, \hat{R}_n). \quad (2.118)$$

With  $\rho$  outside the exchange region there is no overlap of functions with different  $\lambda_n$ , and the Delves and Jacobi  $\mathcal{Y}$ 's are the same functions, so that eqs. 2.116 and 2.117 become

$$\Gamma_{fi}^J(\rho) = \sum_n \delta_{\lambda_f \lambda_n} \delta_{j_f j_n} \delta_{l_f l_n} \rho^{1/2} \int_0^{\pi/2} \Upsilon_f^*(\theta_{D_f}; \rho_\xi) F_{ni}^J(R_f) \mathcal{X}_n(r_f) d\theta_{D_f}, \quad (2.119)$$

$$\frac{\partial \Gamma_{fi}^J(\rho)}{\partial \rho} = \frac{1}{2\rho} \Gamma_{fi}^J(\rho) + \sum_n \delta_{\lambda_f \lambda_n} \delta_{j_f j_n} \delta_{l_f l_n} \rho^{1/2} \int_0^{\pi/2} \Upsilon_f^* \frac{\partial [F_{ni}^J(R_f) \mathcal{X}_n(r_f)]}{\partial \rho} d\theta_{D_f}. \quad (2.120)$$

Now, by the chain rule,

$$\frac{\partial F \mathcal{X}}{\partial \rho} = \left( \cos \theta_{D_f} \frac{\partial}{\partial R_f} + \sin \theta_{D_f} \frac{\partial}{\partial r_f} \right) F \mathcal{X} = \cos \theta_{D_f} \mathcal{X} \frac{\partial F}{\partial R_f} + \sin \theta_{D_f} F \frac{\partial \mathcal{X}}{\partial r_f}. \quad (2.121)$$

Using this and eq. 2.84, we can write

$$\Gamma^J = \mathcal{A} - \mathcal{B} \mathbf{K}^J \quad (2.122)$$

and

$$\frac{\partial \Gamma^J}{\partial \rho} = \mathcal{E} - \mathcal{F} \mathbf{K}^J, \quad (2.123)$$

where

$$\mathcal{A}_{fi} = \delta_{\lambda_f \lambda_i} \delta_{j_f j_i} \delta_{l_f l_i} \rho^{1/2} \int_0^{\pi/2} \Upsilon_f^*(\theta_{D_f}; \rho_\xi) a_{ii}(R_f) \mathcal{X}_i(r_f) d\theta_{D_f}, \quad (2.124)$$

$$\mathcal{B}_{fi} = \delta_{\lambda_f \lambda_i} \delta_{j_f j_i} \delta_{l_f l_i} \rho^{1/2} \int_0^{\pi/2} \Upsilon_f^*(\theta_{D_f}; \rho_\xi) b_{ii}(R_f) \mathcal{X}_i(r_f) d\theta_{D_f}, \quad (2.125)$$

$$\mathcal{E} = \frac{1}{2\rho} \mathcal{A} + \mathcal{C}, \quad (2.126)$$

$$\mathcal{F} = \frac{1}{2\rho} \mathcal{B} + \mathcal{D}, \quad (2.127)$$

$$\mathcal{C}_{fi} = \delta_{\lambda_f \lambda_i} \delta_{j_f j_i} \delta_{l_f l_i} \rho^{1/2} \int_0^{\pi/2} \Upsilon_f^* \left[ \cos \theta_{D_f} \mathcal{X}_i \frac{\partial a_{ii}}{\partial R_f} + \sin \theta_{D_f} a_{ii} \frac{\partial \mathcal{X}_i}{\partial r_f} \right] d\theta_{D_f}, \quad (2.128)$$

$$\mathcal{D}_{fi} = \delta_{\lambda_f \lambda_i} \delta_{j_f j_i} \delta_{l_f l_i} \rho^{1/2} \int_0^{\pi/2} \Upsilon_f^* \left[ \cos \theta_{D_f} \mathcal{X}_i \frac{\partial b_{ii}}{\partial R_f} + \sin \theta_{D_f} b_{ii} \frac{\partial \mathcal{X}_i}{\partial r_f} \right] d\theta_{D_f}. \quad (2.129)$$

Once we complete the definition of the  $\Upsilon$ 's, these integrals all consist of known functions and can be performed by quadrature. It is also convenient in these formulae to now set  $\rho$  equal to  $\rho_\xi$ . Then, from eq. 2.123 the reactance matrix is

$$\mathbf{K}^J = (\mathbf{R}_\Gamma \mathcal{F} - \mathcal{B})^{-1} (\mathbf{R}_\Gamma \mathcal{E} - \mathcal{A}), \quad (2.130)$$

where  $\mathbf{R}_\Gamma = \Gamma^J (\partial \Gamma^J / \partial \rho)^{-1}$  is the Wigner  $\mathbf{R}$  matrix in the Delves coordinates. Thus, the  $\mathbf{K}^J$  - and hence  $\mathbf{S}^J$  - matrices can be obtained directly from the Delves wavefunctions. We note that, because of eq. 2.93,  $\Gamma$  need not satisfy any particular incoming conditions but can be any set of regular solutions of the Delves equations.

## 2.6.2 Delves to Jacobi projection

For systems with long-range potentials, it is often desirable to project from channel Delves functions onto Jacobi solutions and propagate them until the potentials are negligible. To do this projection, we note that eq. 2.77, with  $\mathbf{G}^J$  replaced by the real functions,  $\mathbf{F}$ , implies that

$$F_{fi} = \int dr_f \int \mathcal{X}_f(r_f) \mathcal{Y}_f^{JM*}(\hat{r}_f, \hat{R}_f) r_f R_f \Psi^{JM i} d\hat{r}_f \hat{R}_f \quad (2.131)$$

and

$$\frac{\partial F_{fi}}{\partial R_f} = \int dr_f \int \mathcal{X}_f(r_f) \mathcal{Y}_f^{JM*}(\hat{r}_f, \hat{R}_f) \frac{\partial (r_f R_f \Psi^{JM i})}{\partial R_f} d\hat{r}_f \hat{R}_f. \quad (2.132)$$

Substituting eq. 2.113 into these equations, using sector adiabatic  $\Upsilon$  functions, using

$$r_f R_f = \frac{\rho^2 \sin 2\theta_{D_f}}{2} \quad (2.133)$$

and evaluating the angular integrals, we obtain

$$F_{fi}(R_f) = \sum_n \int_0^\infty \rho^{-1/2} \mathcal{X}_f(r_f) \Gamma_{ni}(\rho) \Upsilon_n(\theta_{D_f}; \rho_\xi) \delta_{\lambda_f \lambda_n} \delta_{j_f j_n} \delta_{l_f l_n} dr_f \quad (2.134)$$

and

$$\frac{\partial F_{fi}}{\partial R_f} = \sum_n \int_0^\infty \mathcal{X}_f(r_f) \frac{\partial}{\partial R_f} [\rho^{-1/2} \Gamma_{ni}(\rho) \Upsilon_n(\theta_{D_f}; \rho_\xi)] \delta_{\lambda_f \lambda_n} \delta_{j_f j_n} \delta_{l_f l_n} dr_f. \quad (2.135)$$

Thus, all terms in the sums collapse except those over vibrational quantum numbers. Via the chain rule

$$\frac{\partial}{\partial R_f} = \frac{R_f}{\rho} \frac{\partial}{\partial \rho} - \frac{r_f}{\rho^2} \frac{\partial}{\partial \theta_{D_f}}, \quad (2.136)$$

one has

$$\frac{\partial F_{fi}}{\partial R_f} = \sum_n \delta_{\lambda_f \lambda_n} \delta_{j_f j_n} \delta_{l_f l_n} \left[ R_f \int_0^\infty \mathcal{X}_f \Upsilon_n(\theta_{D_f}; \rho_\xi) \left( \frac{1}{\rho^{3/2}} \frac{\partial \Gamma_{ni}(\rho)}{\partial \rho} - \frac{1}{2\rho^{5/2}} \Gamma_{ni} \right) dr_f - \int_0^\infty r_f \mathcal{X}_f(r_f) \Gamma_{ni} \frac{1}{\rho^{5/2}} \frac{\partial \Upsilon_n(\theta_{D_f}; \rho_\xi)}{\partial \theta_{D_f}} dr_f \right]. \quad (2.137)$$

Equations 2.134 and 2.137 are just one-dimensional quadratures over  $r_f$  with  $R_f$  held fixed. However, because of eqs. 2.45 and 2.53, both  $\rho$  and  $\theta_{D_f}$  vary with  $r_f$ , i.e., the lines of constant  $R_f$  are not lines of constant  $\rho$ . If the sectors of  $\rho$  about  $\rho_\xi$  were large enough that these quadratures could be carried out on a single  $\rho$  sector, they would be simple. In actual practice, several sectors are usually covered, and the integral must be carried out in a piecewise fashion with proper transformation to the functions  $\Upsilon$  and  $\Gamma$  used on each sector. If the quantity constructed is the Jacobi  $\mathbf{R}$  matrix, the normalization of the  $\Gamma$ 's obtained from the Delves  $\mathbf{R}$  matrix is arbitrary provided it is consistent from sector to sector.

### 2.6.3 Coupled Channel equations

Once the representation of the wavefunction and of the Hamiltonian has been chosen (as already said, such representation may be different according to the strength of interaction), in order to integrate numerically equation 2.70, it is necessary to determine the basis functions and the coupled equations that we get by expanding the function  $\Xi$  in eq. 2.70. In Jacobi coordinates it is convenient to use asymptotic vibrational wavefunctions. They satisfy

$$\left[ -\frac{\hbar^2}{2\mu} \frac{\partial^2}{\partial r_f^2} + \frac{\hbar^2 j_f(j_f + 1)}{2\mu r_f^2} + v_f(r_f) - \epsilon_{v_f j_f} \right] \mathcal{X}_{v_f j_f}(r_f) = 0, \quad (2.138)$$

where  $r_f = r_{\lambda_f}$  and  $v_f$  is the asymptotic diatomic potential of the diatomic molecule of the  $\lambda_f$  arrangement channel. The  $\mathcal{X}$  have the usual normalization,

$$\int_0^\infty \mathcal{X}_{v_f j_f}(r_f) \mathcal{X}_{v_f j_f}(r_f) dr_f = \delta_{v_f j_f}, \quad (2.139)$$

consistent with the factor of  $r_f^{-1}$  occurring in eq. 2.77. Expanding the wavefunction, multiplying by  $\mathcal{X}$  and integrating over  $r_f$  we get the usual SF coupled channel (CC, not to be confused with the Coupled Cluster acronym used in the *ab initio* formalism) equations,

$$\left[ \frac{d^2}{dR_f^2} + k_{v_f j_f}^2 - \frac{l_f(l_f + 1)}{R_f^2} \right] G_{\lambda_f v_f j_f l_f}^{J \lambda_i v_i j_i l_i}(R_f) = \frac{2\mu}{\hbar^2} \sum_{v_n j_n l_n} \langle \lambda_f v_f j_f l_f | V_f | \lambda_f v_n j_n l_n \rangle \times G_{\lambda_f v_n j_n l_n}^{J \lambda_i v_i j_i l_i}(R_f), \quad (2.140)$$

where  $V_f = V - v_f$  with  $V$  the total potential, so that  $V_f$  is the atom-diatom potential in arrangement  $f$ , and integrals involve the  $\mathcal{X}_{v_n j_n}$  and  $\mathcal{Y}_{j_n l_n}^{JM}$  basis functions. We note that this set of coupled equations is satisfied by the real functions  $F$  of eq. 2.84 as well as these  $G$ . The BF Jacobi wavefunctions use the same  $\mathcal{X}$ 's. The BF radial wavefunctions  $G_{\Omega_f}^{l_i}$  (and their real counterparts  $F_{\Omega_f}^{l_i}$ ) thus satisfy the usual BF CC equations,

$$\begin{aligned} & h_{\Omega_f, \Omega_f-1}^{j_f} G_{\lambda_f v_f j_f \Omega_f-1}^{J \lambda_i v_i j_i l_i} + h_{\Omega_f, \Omega_f}^{j_f} G_{\lambda_f v_f j_f \Omega_f}^{J \lambda_i v_i j_i l_i} + h_{\Omega_f, \Omega_f+1}^{j_f} G_{\lambda_f v_f j_f \Omega_f+1}^{J \lambda_i v_i j_i l_i} \\ &= \frac{2\mu}{\hbar^2} \sum_{v_n j_n} \langle v_f j_f \Omega_f | V_f | v_n j_n \Omega_f \rangle G_{\lambda_f v_n j_n \Omega_f}^{J \lambda_i v_i j_i l_i}(R_f), \end{aligned} \quad (2.141)$$

where

$$h_{\Omega_f, \Omega_f}^{j_f} = \frac{d^2}{dR_f^2} + k_{v_f j_f}^2 - \frac{[J(J+1) - 2\Omega_f^2 + j_f(j_f+1)]}{R_f^2}, \quad (2.142)$$

$$h_{\Omega_f, \Omega_f \pm 1}^{j_f} = \frac{\lambda_{\pm}(J, \Omega_f) \lambda_{\mp}(j_f, \Omega_f \pm 1)}{R_f^2}, \quad (2.143)$$

$$\lambda_{\pm}(J, \Omega) = [(J \pm \Omega + 1)(J \mp \Omega)]^{1/2}, \quad (2.144)$$

and

$$\begin{aligned} \langle v_f j_f \Omega_f | V_f | v_n j_n \Omega_f \rangle &= \int_0^\infty dr_f \int_{-1}^1 \mathcal{X}_{v_f j_f}(r_f) \hat{P}_{j_f \Omega_f}(\Theta_f) V_f(r_f, R_f, \Theta_f) \\ &\quad \times \mathcal{X}_{v_n j_n}(r_f) \hat{P}_{j_n \Omega_f}(\Theta_f) d(\cos \Theta_f). \end{aligned} \quad (2.145)$$

Usually, these BF and SF CC equations are to be used only to propagate an  $\mathbf{R}$  matrix on out to the asymptotic region that has already been propagated through the strong interaction exchange region in more appropriate coordinates and constructed by projection (one projection is discussed in section 2.6.2), so that the boundary conditions can be applied as discussed in sections 2.5.1, 2.5.2 and 2.5.3. In this process, the CC equations of the different arrangements channels can be propagated separately at these large distances, but, after each propagation step in arrangement channel  $\lambda_f$ , it is necessary to update all the blocks (including the reactive blocks) of the  $\mathbf{R}$  matrix that involve  $\lambda_f$ .

We note that the propagation of the CC equations in Jacobi coordinates in this region is faster than the propagation in hyperspherical coordinates not only because the different arrangements can be propagated separately with fewer coupled equations but also because the basis functions  $\mathcal{X}$  are independent of the propagation variable and need not to be redetermined at each step. In the  $\rho$  interval in which equations have to be carried out using hyperspherical coordinates (strong interaction region), the ‘‘sector-adiabatic’’ basis functions which are assumed to change from sector to sector (but not within a sector) for each  $\xi$ -*th* sector satisfy the eigenvalue equation

$$\left\{ \frac{\hbar^2}{2\mu\rho_\xi^2} \left[ -\frac{\partial^2}{\partial\theta_{D_f}^2} + \frac{j_f(j_f+1)}{\sin^2\theta_{D_f}} \right] + v_f - \mathcal{E}_{v_f j_f}(\rho_\xi) \right\} \Upsilon_{v_f j_f}(\theta_{D_f}; \rho_\xi) = 0, \quad (2.146)$$

where  $v_f(r_f) = v_f(\rho_\xi \sin \theta_{D_f})$  is the asymptotic diatomic potential of the  $\lambda_f$  arrangement as before. In so doing, we omit  $\theta_{D_f}$ -dependent terms of the form  $l_f(l_f + 1)/\cos^2 \theta_{D_f}$  which occur in eq. 2.112. If one were to use Delves coordinates at small  $\rho$ , one would need to include these terms in eq. 2.146, and the additional label on the  $\Upsilon$  would require solving for many more  $\Upsilon$  functions. When these  $\Upsilon$ 's are used in eq. 2.113 together with eqs. 2.111 and 2.112, the resulting SF CC equations are

$$\left\{ \frac{\partial}{\partial \rho^2} + \frac{2\mu}{\hbar^2} \left[ E - \frac{\rho_\xi^2}{\rho^2} \mathcal{E}_{v_f j_f}(\rho_\xi) \right] + \frac{1}{4\rho^2} \right\} \Gamma_{\lambda_f v_f j_f l_f}^{J \lambda_i v_i j_i l_i}(\rho) = \frac{2\mu}{\hbar^2} \times$$

$$\sum_{v_n j_n l_n} \langle \Upsilon_{v_f j_f} \mathcal{Y}_{j_f l_f}^{JM} | V - \frac{\rho_\xi^2}{\rho^2} v_f(\rho_\xi \sin \theta_{D_f}) + \frac{\hbar^2 l_n(l_n + 1)}{2\mu \rho^2 \cos^2 \theta_{D_f}} | \Upsilon_{v_n j_n} \mathcal{Y}_{j_n l_n}^{JM} \rangle \Gamma_{\lambda_f v_n j_n l_n}^{J \lambda_i v_i j_i l_i}(\rho). \quad (2.147)$$

All the terms on the right-hand side except  $V$  are diagonal in  $j$  and  $l$ . Across the sector centered at  $\rho_\xi$ ,  $\rho_\xi^2/\rho^2$  is nearly unity at large  $\rho$ , so that the  $v_f$  term in  $V$  is largely canceled in these integrals and the local wavenumber on the left-hand side is roughly that of eq. 2.75. This means that, when we keep all terms and evaluate all integrals by accurate numerical quadrature, these CC equations behave very similarly to the usual CC equations 2.140 and can be propagated by the same methods. The BF Delves CC equations are easily derived and have the same relation to eq. 2.141 as eq. 2.147 has to eq. 2.140.

The sector centered at  $\rho_\xi$  can be divided into as many intervals and steps as one wishes and the CC equations propagated across it using the  $\Upsilon(\theta_{D_f}; \rho_\xi)$  and the standard methods. At the boundary between the  $\xi$ -th and the  $(\xi + 1)$ st sectors one must transform to the new basis. By equating wavefunctions and their derivatives, one finds that the Delves  $\mathbf{R}$  matrix at the left edge of the  $(\xi + 1)$ st sector is related to that at the right edge of the  $\xi$ th sector by

$$\mathbf{R}_\Gamma^J(\xi + 1) = \mathbf{O} \mathbf{R}_\Gamma^J(\xi) \tilde{\mathbf{O}}, \quad (2.148)$$

where  $\mathbf{O}$  is the orthogonal overlap matrix,

$$\mathbf{O}_{fn} = \delta_{\lambda_f \lambda_n} \delta_{j_f j_n} \delta_{l_f l_n} \int_0^{\pi/2} \Upsilon_{v_f j_f}(\theta_{D_f}; \rho_{\xi+1}) \Upsilon_{v_n j_f}(\theta_{D_f}; \rho_\xi) d\theta_{D_f}. \quad (2.149)$$

These integrals are efficiently evaluated using Gauss-Hermite quadrature, and one can use either the  $\xi$ th or  $(\xi + 1)$ st quadrature provided one remembers that the equilibrium  $\theta_{D_f}$  and force constant change with  $\rho$  and is thus careful in the evaluation of Jacobians, weights, and functions.

## 2.7 From Theory to experimental observables

By summing the square modulus of the detailed  $S$  matrix elements obtained from the integration of the scattering equations over  $\Omega, \Omega'$  and  $p$  and one can evaluate state-to-state reaction probabilities:

$$P_{vj, v'j'}^J(E_{\text{tr}}) = \frac{1}{(2j+1)} \sum_{\Omega=-\Omega_{\text{max}}}^{\Omega_{\text{max}}} \sum_{\Omega'=-\Omega'_{\text{max}}}^{\Omega'_{\text{max}}} \sum_{p=0}^1 \left| S_{vj\Omega, v'j'\Omega'}^{Jp}(E_{\text{tr}}) \right|^2 \quad (2.150)$$

where  $E_{\text{tr}}$  is the relative collision energy (the total energy  $E$  minus the rovibrational energy of the initial state  $v_j$ ) and  $\Omega_{\text{max}} = \min(j, J)$ . In this equation, the  $S$  matrix elements are set equal to twice the value calculated for a single product arrangement channel because of the symmetry of the N + N<sub>2</sub> system.

### 2.7.1 Exact probabilities, cross sections and rate coefficients

The experimental observable more directly linked to the calculated  $S$  matrix elements is the product vibrational distribution (PVD). PVDs are obtained out the state to state probabilities calculated at a given initial vibrotational state of the reactants, by dividing them by the total probability associated with it. Another quantity relevant for comparison with measurements are the state specific probabilities, which are easily related to measurements performed for state selected reactants constrained to bear only a limited interval of values of  $J$ . The state specific reactive probabilities,  $P_{vj}^J(E_{\text{tr}})$ , are expressed as:

$$P_{vj}^J(E_{\text{tr}}) = \sum_{v'} \sum_{j'} P_{vj, v'j'}^J(E_{\text{tr}}) \quad (2.151)$$

after summation over  $v'$  and  $j'$ , in this summation probabilities for even  $j'$  states contributes twice because the nuclear spin of the N atom is one [79].

The most popular measurables obtainable from the experiment are the cross sections and the rate coefficients. The integral reactive state-specific cross section can be worked out using the formula:

$$\sigma_{vj}(E_{\text{tr}}) = \sum_{J=0}^{\infty} \sigma_{vj}^J(E_{\text{tr}}) = \sum_{J=0}^{\infty} \frac{\pi}{k_{vj}^2} (2J+1) P_{vj}^J(E_{\text{tr}}) \quad (2.152)$$

where  $k_{vj} = \sqrt{2\mu E_{\text{tr}}}/\hbar$  is the wavenumber of the system in the  $v_j$  state. Out of the cross section the state-specific rate coefficients can be calculated averaging over the translational energy by:

$$k_{vj}(T) = \left( \frac{8k_{\text{B}}T}{\pi\mu} \right)^{1/2} \frac{1}{(k_{\text{B}}T)^2} \int_0^{\infty} \sigma_{vj} \exp(-E_{\text{tr}}/k_{\text{B}}T) E_{\text{tr}} dE_{\text{tr}} \quad (2.153)$$

where  $T$  is the temperature (in this case, the translational temperature),  $\mu$  is the reduced mass of the reactive system and  $k_B$  the Boltzmann constant. By averaging over the  $v_j$  initial states (weighed for the proper thermal distribution function) one can calculate the thermal rate coefficient  $k(T)$ .

### 2.7.2 Approximate quantum methods

The calculation of the thermal rate coefficients implies the integration of the Schrödinger equation at all the populated  $v_j$  initial states, all the total angular momentum quantum number values  $J$  contributing to reaction and all the allowed projections  $\Omega$  of  $J$ . This makes the size of the single  $v_j$  calculations proportional to  $J^2$  frustrating, in practice, all the attempts to carry out a full  $J$  exact calculation. Even more, for high  $J$  values, calculations become increasingly difficult. In fact, the hamiltonian of eq. 2.16 for  $J=0$  becomes significantly simplified because the terms  $(J(J+1) - 2\Omega^2)/2\mu_R R^2$  and  $C_{\Omega, \Omega \pm 1}^J$  are zero. On the contrary, for non zero values of the total angular momentum the non-diagonal terms of the Coriolis coupling must be considered and one may need to propagate as many as  $2J + 1$  wavepackets. Thus, it is often necessary to find alternative simplified procedures.

To reduce the dimensionality of the problem, different approaches have been developed. Two of them are the sudden [80, 81] and the adiabatic [82–86] approximations. These theories make diametrically opposite assumptions about the internal angular motion. The sudden theory assumes that motion is frozen throughout the collision, whereas the adiabatic theory assumes it changes but with preservation of the bending quantum numbers. The sudden approximation is valid when the interaction time is short compared with the perturbed angular motion of the diatomic molecule. The adiabatic approximation applies in the opposite situation, i.e., when the interaction time is comparable or longer than that of the perturbed angular motion. In general, the angular motion of most molecules is slow compared with the interaction times for hyperthermal or even thermal collisions. However, if there is a large amount of induced angular hindering of the diatom by the atom, then simple sudden dynamics does not apply, except for high collision energies. For those reactions (which are angularly strongly constrained), the adiabatic approximation is the choice of election, even (as we shall discuss later) at hyperthermal collision energies. In the case of the  $N + N_2$  reaction, that is a direct one, a sudden approximation is more appropriate. In particular, we shall discuss here in detail the use of the centrifugal sudden (CS) approximation [87, 88].

In practice the CS approximation implies the cancellation of the centrifugal term. Accord-

ingly, the angular velocity of the system is slower than the collision velocity and, therefore, the collision can be considered instantaneous with respect to the orbiting and the projection of the total angular momentum along the BF  $Z$  axis be conserved during the collision. For this reason, the approximation is also called " $J_z$  conserving" or "helicity conserving" approximation. The CS approximation can be also seen as deriving from the assumption that  $\Omega$  is a good quantum number. Rigorously, only the total angular momentum  $J$  is a good quantum number whereas  $\Omega$  is not since the dynamics of the system mixes up different  $\Omega$  values. The different  $\Omega$  values are coupled by the "centrifugal coupling" terms in the hamiltonian operator of eq. 2.16. This indicates that one has a separate wavepacket,  $\psi^{J\Omega}(R, r, \Theta, t)$  for each value of  $\Omega$  and that these wavepackets are coupled together (one wavepacket couples with  $J + 1$  wavepackets when the total parity is even and with  $J$  wavepackets when the total parity is odd). The centrifugal coupling  $C_{\Omega, \Omega \pm 1}^J$  makes the hamiltonian representation tridiagonal (while the interaction potential is diagonal). Therefore, the CS approximation consists in simply neglecting the  $\Omega$  coupling in eq. 2.16. In other words, the CS approximation considers  $\Omega$  as a good quantum number and  $\Omega$  is conserved during the collision. Using the CS approximation, the hamiltonian representation becomes diagonal and the effort for its diagonalization does not exceed that of  $J = 0$ . This makes the CS based programs suitable for running on distributed computational platforms and extended CS calculations for all  $J\Omega$  pairs are ongoing.

## 2.8 $J$ -shift approximation

Yet, usually CS calculations are still so demanding that, even for moderately heavy systems (like the  $N + N_2$  considered here), they are often further simplified by adopting the so called  $J$ -shift model [85, 86]. In  $J$ -shift approximation, the calculation of the  $S$  matrix is performed for a low value of  $J$  (or a certain number of  $J$  values) and this value (or this set of values) is used to estimate the probabilities for the values of  $J$  for which calculations are not performed. In the most simplified version, exact probabilities are calculated only for  $J = 0$ .

In the  $J$ -shift approximation, the state-specific probabilities for  $J > 0$ ,  $P_{vj}^J(E_{tr})$ , are worked out by shifting in energy the probabilities obtained for  $J = 0$ ,  $P_{vj}^{J=0}(E_{tr})$ , as follows:

$$P_{vj}^J(E_{tr}) = P_{vj}^{J=0}(E_{tr} - \Delta E^J) \quad (2.154)$$

with  $\Delta E^J$  being defined as:

$$\Delta E^J = BJ(J + 1) \quad (2.155)$$

and corresponding to the rotational energy of the rigid collinear triatom geometry associated with the saddle to reaction.

When the saddle of the surface is bent, one can still fit the  $\Omega = 0$  probabilities calculated at different  $J$  values using eq. 2.155 as an empirical expression. A more theoretically sound approach is the one making the probability shift depend also on  $\Omega$  as follows:

$$P_{vj}^J(E_{\text{tr}}) = \frac{1}{2\Omega_{\text{max}} + 1} \sum_{\Omega=-\Omega_{\text{max}}}^{\Omega_{\text{max}}} P_{vj}^{J=0}(E_{\text{tr}} - \Delta E^{J\Omega}) \quad (2.156)$$

with  $\Delta E^{J\Omega}$  being defined as:

$$\Delta E^{J\Omega} = \bar{B}J(J+1) + (A - \bar{B})\Omega^2 \quad (2.157)$$

that is the homologous of eq. 2.155 for bent transition state systems when the calculations are performed only for  $\Omega=0$ . This approach is built on top of the approximation that the geometry of the system at the bent saddle is a prolate symmetric top one, where  $\bar{B} = (B + C)/2$  with  $A$ ,  $B$  and  $C$  being the three rotational constants of the triatom at the saddle.

## Chapter 3

### Computing GRID

*In questo terzo capitolo vengono presentate le caratteristiche delle principali tecnologie computazionali coinvolte nell' utilizzo della grid come piattaforma di calcolo.*

*Nella prima parte, sezioni 3.1 e 3.2, vengono esaminate le principali caratteristiche della Grid e dei codici scientifici attualmente utilizzabili su tale piattaforma. Nella seconda parte, sezioni 3.3 e 3.4, invece l'attenzione è focalizzata sullo sviluppo di data format specifici per la chimica quantistica e nella loro implementazione per una migliore interoperabilità degli attuali codici computazionali. Nell'ultima sezione del capitolo vengono brevemente analizzati i possibili futuri sviluppi del Grid computing.*



Essential to the feasibility of the present thesis has been the use of advanced computing technologies of the European computing grid that has allowed us to carry out the related extended computational campaigns. In the last decades the European Union has been promoting the development of large scale facilities equipped with concurrent computing platforms to support the solution of the so called Grand Challenges in computational sciences. As a matter of fact, the evolution of computer technologies has gone beyond the policy of individual large computer centers machines. It has, in fact, led to the gathering of an heterogeneous ensemble of computers (mainly made of cluster assembled using out of the shelves PCs) and to the creation of a Europe Wide Grid platform called EGEE [89]. The large amount of resources made available in this way has fostered the development and the implementation on the Grid of a large number of ICT applications in all fields of human

activities including Molecular and material sciences and technology (MMST). Such a distributed usage of the MMST knowledge on the Grid requires the support of new services (mainly based on intelligent tools for information representation and handling) and is one of the most complex tasks that can be performed on the Grid. In this contest, Computational Dynamics and Kinetics plays a key role because of its ability of designing and implementing realistic *a priori* simulations of the multiscale type starting from the microscopic level of molecular interactions.

### 3.1 EGEE: the European Grid for e-science

The mentioned EGEE project was born with the specific purpose of providing Europe with a Grid infrastructure that could carry out in acceptable times the massive calculations needed by scientific advances in experiments and related simulations. In particular, the first burst of funding was mainly associated with the need of gathering the computing power necessary to carry out the scientific project of CERN LHC (Large Hadron Collider). Only in the second and third biennium EGEE become more aware of the computing needs of other disciplines.

#### 3.1.1 The key features of the Grid

Grid computing is based on a joint extended effort of compute resources offering, innovative applications building and high throughput computing machineries assembling. In this respect, the Grid cannot be identified with parallel computing since its main interest is not high-performance and peak speeds achieved through fast connections of homogenous processors. Grid computing rather focuses on high-throughput computing of heterogenous nodes connected on the public network for complex computational applications which need the gathering of a large ensemble of computer resources and expertises.

Accordingly, the first feature of a Grid is given by the coordinated sharing of the hardware, software and knowledge that means an heterogeneous nature of the hardware platform and a composite nature of the applications considered. This means also that the establishing of a production Grid requires the implementation of several components including the composition of different skills related not only to the involved hardware, but also to the specific knowledge of the components of the problems tackled. The management of these competence based selection of instrumentation and tools requires great care.

The second feature of the Grid is given by the heterogeneous architecture of its nodes. The user can make direct use of just one type of computer, typically a desktop workstation, not only to write, debug and compile the codes but also to launch the simulation on the grid. A bunch of them can be used to run highly distributed parts of the application while a high performance supercomputer can take care of running the tightly coupled (better if parallelized) part of it. Other computers may be used to take care of rendering the results in a graphical form or to power a virtual reality display device.

The third feature of the Grid is given by the complexity of the communication software required to make the whole collection of codes user-friendly. Communication software has to bridge all of the heterogeneities between different computers, between computers and people and even between different people as well. This turns the physical connections between computers from a collection of individual machines into an interconnected computing system.

The fourth feature of the Grid is given by the variety of characteristics of the physical network that links the various machines, (modem, ISDN, standard Ethernet, FDDI, ATM, or other). Networks with high bandwidth and low latency are the most favored for providing rapid and reliable connections among the machines although, the grid is based on all sorts of network connections. To actually communicate over these physical connections it is also necessary to have some smart communication software running.

### **3.1.2 The Middleware**

Given an interconnected communicating network of computers, an operating system that can be used to configure, manage, and maintain the Grid computing environment, is still needed. This virtual environment needs to span the extent of the computational Grid and make it usable by both administrators and individual users. Such an environment will enable the machines and/or the instruments (which may be located in the same building, or separated by thousands of miles) to appear as a single system. This virtual environment, therefore, must provide the administrators with all the functions needed to tune the system to deal with a changing heterogeneous platform. This software needs also to speak the language of the user and has, therefore, to fall into the category of problem solving environments (PSE). More in detail such an environment has to allow the user to get the best from the platform both when preparing input data and when running the application with no need to involve him/her in managing related technicalities. The most popular name for this type

of software is “middleware” and existing middlewares are still in their infancy. Present, choice for the EGEE Grid is gLite [90]. Glite, derives from the Globus middleware [91] developed at the Argonne National Laboratory. It has grown through collaborative efforts of more than 80 people of 12 different academic and industrial research centers as part also of the EGEE Project.

Globus provides a toolkit based on a set of existing components with which a concurrent computing environment can be built. The implemented environment is a distributed one allowing to execute a set of applications using different computational models. Each user can select the application best suited for his/her system or adapt it for personal use. Graphic interfaces, called translucent, have been introduced to manage tools and applications and recognize and control mechanisms at low level. This gives the chance of optimizing performances and adapt all the configurations of the system to the user needs. An information system is part of the toolkit. Thanks to the grid configuration, it is possible to use different networks and computers with respect to problems related to hardware and software facilities. The programmer needs not to define an *a priori* static configuration of the application environment yet the grid offers tools which dynamically find out resources and configurations of the system for an efficient execution, and allocates them in a transparent way. From its very beginning Globus was organized around four main activities:

1. **Research:** the study of basic problems in areas such as resource management, information services, security and data management have been addressed. It focuses not only on the issues associated with the building of computational grid infrastructures, but also on problems arising from the design and the development of parallel applications which use grid services. Uniform and scalable mechanisms for naming, locating, and allocating computational and communication resources in distributed systems have been developed so far. Basic Grid services have been integrated into existing application development frameworks, environments and languages (e.g. CORBA, Java, Perl, Python). Collaborative efforts have been devoted to the design and the production of an infrastructure-level architecture for data management, called the data grid. Finally, requirements, designs and prototypes of a Grid information service as well as an enabler for dynamic application configuration and adaptation, have been worked out.
2. **Test beds:** Supports and assistance to initiatives for planning and building large-scale prototyped packages acting as test-bed ( both for internal research and for production use by other scientists and engineers) have been provided.
3. **Software tools:** Pieces of software running on a variety of platforms acting as general instru-

ments available on the grid have been developed and are continuously being updated.

4. **Applications:** Several large-scale packages have been designed and implemented in a cooperative fashion by scientists and engineers on the grid to serve as commonly used applicative software. To this end basic technologies enabling entirely new classes of applications have been developed. The net result is a set of programs allowing to advance in the understanding of how to build programs for the grid, how to focus the research efforts of the project and how to evaluate the utility of the tools developed.

Based on Globus toolkits many software components implementing the above described services have been developed. Out of it three different middlewares have been proposed: ARC, Unicore and gLite for the European grid. As already mentioned the one adopted by EGEE is gLite.

### 3.1.3 Building on national projects

In order to experiment the assemblage of a suitable Grid infrastructure in Italy, a national FIRB project [92] called “Piattaforme abilitanti per griglie computazionali ad alte prestazioni orientate a organizzazioni virtuali scalabili (shortly called GRID.IT)” was launched in the year 2002 [93]. GRID.IT was aimed at gathering together at national level the efforts of designing advanced networking hardware, defining appropriate middleware and implementing grid enabled applications. Within GRID.it a workpackage (WP13) was established to the end of designing grid enabled calculations codes for molecular simulation. As a matter of fact WP13 has assembled an *ab initio* Simulator called SIMBEX (SIMulator of Molecular Beam EXperiments). For this purpose a prototype Grid infrastructure called CHEMGRID was also built around a cluster of computers owned by the Chemistry Departments of the Universities of Bari, Bologna, Naples and Perugia and the Milan, Padua and Perugia local sections of the ISTM CNR Institutes plus the Computational Chemistry laboratory of ENEA at the Casaccia location. CHEMGRID, managed by the homonymous cluster of computers of the University of Perugia, was also linked to the computing resources of the Department of Physical Chemistry of the University of the Basque Country in Vitoria Gasteiz (Spain) and to the computing resources of the Department of Physical Chemistry of the University of Barcelona in Barcelona (Spain). Other projects were launched in Italy on a regional scale (POR), similar projects were launched in several other European countries with the support of National or regional governments.

## 3.2 The European project EGEE

Also at European level there have been several projects aimed at promoting the assemblage of grid platforms. As to the Chemistry area an important Europe wide project aimed at establishing a distributed computing platform has been the COST Chemistry action D23 [94] “METACHEM: Metalaboratories for complex computational Chemistry Applications” launched by our CDK laboratory in 1999. D23 was followed by the D37 Action “Gridchem Grid Computing in Chemistry” coordinated by the ETH of Zurich in which our laboratory was coordinating the working group QDYN (dealing with quantum reactive dynamics) and the HPC laboratory of the Department of Mathematics and Informatics the ELAMS one (dealing with e-science approaches to Molecular properties).

A more systematic approach to grid computing in chemistry became possible when the European Union funded within the Framework Programs 6 and 7 (FP6 and FP7) the design and the construction of a Europe wide production Computing Grid. The project, called as already mentioned, EGEE (European Grid for E-science) [89] has been first approved for two years and then renewed twice for additional two years each time (EGEE II and EGEE III respectively). EGEE has established a Consortium consisting of more than 90 partners from 32 countries, grouped into 13 federations and representing almost all major and national Grid efforts in Europe, as well as projects from the US and Asia (see Fig. 3.1). In addition, a number of related projects will extend the infrastructure further, to the Mediterranean area, Baltic States, India, Latin America and China. Combined with other related projects spurred out from or affiliated with EGEE, EGEE-II, and the present EGEE III, this project has played around the world.

### 3.2.1 The grid for scientific communities

With the existing Europe wide EGEE production grid platform consisting of about 100.000 processors researcher from academia and industry already benefit from an e-Infrastructure support to many applications from various scientific areas to which a shared pool of resources, independent of geographic location, with round-the-clock access to major storage, compute and networking facilities is guaranteed. The EGEE project aims also at significantly extending and consolidating this infrastructure that links national, regional and thematic Grid resources and interoperates as well as with other Grids around the globe. The resulting high capacity, world-wide infrastructure greatly surpasses the capabilities of local clusters and individual centres, providing a unique tool for collab-

orative computing in science (“e-Science”). So far, several large- and small-scale communities use the EGEE infrastructure as an every-day tool for their work. Applications deployed go from High Energy Physics to Life Sciences, Earth Sciences (including the industrial application EGEODE), Astrophysics. Thus include, as well, Computational Chemistry.

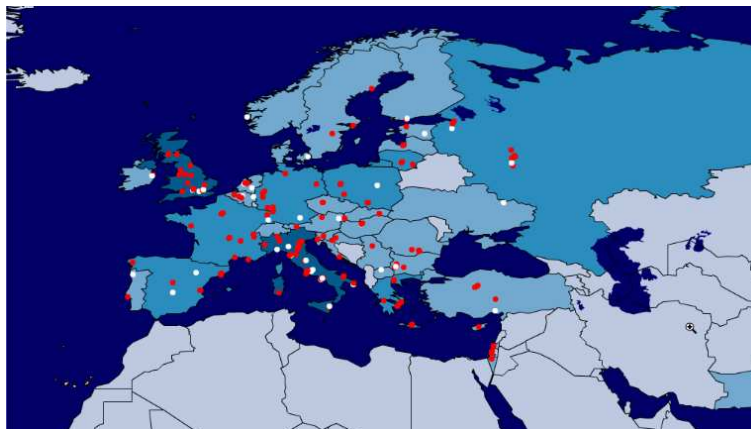


Figure 3.1: Partner countries of the EGEE project.

EGEE has also fostered the constitution of organized Virtual communities (called Virtual Organizations or VO) specifically devoted to the clustering on the grid of members of a given scientific community. Thanks to all this EGEE has been able to further develop its infrastructure into a truly pervasive global platform for e-Science.

### 3.2.2 COMPChem: the molecular science Virtual Organization

The VO for the Chemistry community is called COMPChem and has been recently launched by the CDK laboratory. COMPChem [95] has been assembled by a group of molecular and material sciences laboratories committed to implement their computer codes on the section of the production EGEE Grid infrastructure available to the VO. It has been admitted to EGEE II as an unfunded partner and then it has been funded by EGEE III with 9 FTEs (Full Time Expert) quotas.

COMPChem Virtual Organization offers to its members clear advantages for carrying out their computational campaigns (especially when they are so complex to not be feasible using other computing platforms). Only in this way the laboratories will take the burden of carrying out the extra duties necessary to work within a collaborative environment. Therefore the entry level of the VO offers to the user the possibility of implementing a code at wish for personal use. This entry

level membership situation has a limited validity and is targeted to check the laboratories on their real willingness to operate on a Grid platform. Already at this level, in fact, several competences necessary to restructure the code to run in a distributed way by exploiting the advantages of using a Grid platform need to be acquired. In return one gets the advantage of distributing the code on a much larger platform and an easier interaction with the codes of other users of the VO.

As sketched in Table 3.1 one becomes actual member of COMPCHEM only after committing him/ herself to open the code implemented on the Grid to a shared use by the other members of the VO. This implies the validation of a stable version of the code and the assemblage of all the necessary GUIs for use by other researchers. It also implies software maintenance services and user support. It may also imply the commitment to confer to the Grid additional hardware (especially for these suites of codes needing special devices) after a negotiation with the Management Committee (MC) of the VO about the relevance of such a commitment to the strategic choices of the virtual organization. Obviously, the conferring of both software and hardware to COMPCHEM will take place gradually due to the time needed to validate the software and to gridify the machines. A member will likely devote to VO related activities other unshared resources (e.g. for development work). To become member of the VO and acquire the status of “COMPCHEM stakeholder” a user should place a specific application to the MC. While the user status has a limited time validity (after which a user may become either a paying customer and/or a paid supplier of services) the status of member has no time limit (though its terms could be periodically revised). The status of COMPCHEM member may imply further levels of involvement. The stakeholder, in fact, should take care of maintaining the software and the local segment of Grid hardware (a particular attention is needed for the conferring of software, either commercial or not, with special constraints like the payment of fees since in this case commercial, legal and financial aspects are better dealt centrally).

The members of the VO are requested to be proactive in providing either their own work or attract financial resources specifically for the development of the VO. As to contributing by providing their own work this may be under the form of participation to the management of the Grid, to the development of WMs, etc.. As to attracting financial resources VO members should elaborate joint applications for funding, research projects and even develop within the VO commercial services. However, the most important contribution to the sustainability of COMPCHEM that is requested to the stakeholders is a high dynamism in research and in the transfer of its outcomes into innovation and developments (R&D). This means that, ideally, all members of the VO should excel in basic and applied research and that a proper reward for that has to be given in the VO. Work is ongoing in our laboratory to develop tools for that purpose.

Membership level	Description
User	<i>Passive:</i> Run a program implemented by other members of the VO <i>Active:</i> Implement at least one program for personal use
SW provider	<i>Passive:</i> Implement at least one program for use by other members <i>Active:</i> Interactive management of the implemented program for cooperative usage
Grid deployer	<i>Passive:</i> Confer to the Grid infrastructure at least a small cluster of nodes <i>Active:</i> Operates above the minimal level as support for the Grid deployment and management
Stakeholder	Take part to the development and the management of the VO

Table 3.1: Levels of membership in COMPCHEM.

### 3.2.3 COMPCHEM applications

As already mentioned the COMPCHEM main asset are the computational chemistry gridified applications for shared usage. Among them the most prominent one is GEMS the Grid Empowered Molecular Simulator. For this purpose several of its component programs have been ported to the Grid and have been run in production. Efforts are also underway to port additional applications to the EGEE infrastructure and to promote wider collaboration between the computational chemistry research groups.

Specific efforts have been addressed at implementing grid empowered versions of quantum reactive scattering codes dealing with atom-diatom systems which is also the task of the QDYN working group of the COST Action D37. A brief description of these programs follows:

- **ABCtraj** [96] calculates the observables of atom-diatom reactions in gas phase by integrating related Hamilton equations in Jacobi coordinates starting from selected or randomly initial

conditions. The program is linked to a molecular virtual reality environment that produces animated pictures of the trajectories and virtual monitors to read observable properties.

- **VENUS** [97] calculates the cross-sections and rate coefficients for elementary chemical reactions by integrating classical equations of motions whose initial conditions are either directly determined or sampled using a Monte Carlo scheme. This application is a modified version of the VENUS96 program by W.L.Hase (QCPE-671). It integrates the Hamilton equation in cartesian coordinates. Before the collision the molecules are selected at discrete internal energy states and after the collision a quantization of the internal energy is also enforced on the product molecule. A parallelized version based on MPI has been also implemented.
- **DL\_POLY** [98] is a package of subroutines, programs and data files, designed to facilitate molecular dynamics simulations of macromolecules, polymers, ionic systems, solutions and other molecular systems on a distributed memory parallel computer. The package was written to support the UK project CCP5 by Bill Smith and Tim Forester on grants from the Engineering and Physical Sciences Research Council. It is property of the Science and Technology Facilities Council (STFC). Two versions of DL\_POLY have been implemented. DL\_POLY\_2 is the earlier version and is based on a replicated data parallelism. It is suitable for simulations of up to 30.000 atoms on up to 100 processors. DL\_POLY\_3 is a domain decomposition version, written by I.T. Todorov and W. Smith, and is designed for systems beyond the range of DL\_POLY\_2 - up to 10.000.000 atoms (and beyond) and 1000 processors. More recently a new release and several bug fixing have been issued.
- **RWAVEPR** [35] integrates rigorously the three-dimensional time-dependent Schrödinger equation for a generic atom-diatom reaction by propagating wave packets. It calculates the elements of the **S** scattering matrix for given values of the vibrational quantum number, the rotational quantum number, the total angular momentum quantum number, the quantum number for the projection of the total angular momentum on the atom-diatom vector, for a given the parity and for a given range of total energies. Out of the value of the **S** matrix elements the state-to-state reaction probabilities are calculated. The centrifugal sudden approximation (i.e. to neglect the Coriolis coupling) can be also invoked.
- **COLUMBUS** [99] is a collection of programs for high-level *ab initio* molecular electronic structure calculations. The programs are designed primarily for extended multi-reference calculations on electronic ground and excited states of atoms and molecules.
- **GAMESS** [8] is a program for *ab initio* molecular quantum chemistry. Briefly, GAMESS can

compute SCF wavefunctions ranging from RHF, ROHF, UHF, GVB, and MCSCF. Correlation corrections to these SCF wavefunctions include Configuration Interaction, second order perturbation Theory, and Coupled-Cluster approaches, as well as the Density Functional Theory approximation. Geometry optimization, transition state searches, or reaction path following, vibrational frequencies with IR or Raman intensities and a variety of molecular properties, ranging from simple dipole moments to frequency dependent hyperpolarizabilities can be computed. Most computations can be performed using direct techniques, or in parallel on appropriate hardware. A detailed description of the program is available in the paper: “General Atomic and Molecular Electronic Structure System” M.W. Schmidt, K.K. Baldrige, J.A. Boatz, S.T. Elbert, M.S. Gordon, J.H. Jensen, S. Koseki, N. Matsunaga, K.A. Nguyen, S.Su, T.L. Windus, M. Dupuis, J.A. Montgomery *J. Comput. Chem.*, 14, 1347-1363(1993).

- **ABC** [100] is a program that uses a coupled-channel hyperspherical coordinate method to solve the Schrödinger equation for the motion of the three nuclei (A, B, and C) on a single Born-Oppenheimer potential energy surface. The coupled-channel method used involves a simultaneous expansion of the wavefunction in the Delves hyperspherical coordinates of all three chemical arrangements (A+BC, B+CA, C+AB). The quantum reactive scattering boundary conditions are applied exactly at the asymptotes potential, and the coupling between orbital and rotational angular momenta is also implemented correctly (though some approximations can also be introduced) for each value of the total angular momentum quantum number.
- **MCTDH** [101] is a program implementing the MultiConfigurational Time-Dependent Hartree (MCTDH) method that is nowadays considered as one of the most powerful tools for calculating rate coefficients and dealing with multidimensional systems using quantum techniques. Unlike conventional wave packets methods, in the MCTDH approach the wave function is expressed on a basis of time-dependent one dimensional functions, which evolve along with time. The use of this time-dependent basis set turns up into a much smaller basis dimension and thus a greater computational efficiency with respect to standard wave packet approaches.
- **FLUSS** [102] is a program performing a modified Lanczos iterative diagonalisation of the thermal flux operator. The output of the code is a set of eigenvalues and eigenstates which can afterwards be used to calculate the thermal rate coefficient of the reactive process. A Krylov space is generated by recursive application of the thermal flux operator onto an initial wave function, typically a Gaussian-type wave packet located in the vicinity of the transition state. The matrix representation of the operator in the Krylov-type basis is diagonalized to

obtain eigenstates and eigenvalues.

- **SC-IVR** [103] is a program using the Semiclassical (SC) initial value representation (IVR) methods are used to calculate the thermal rate coefficients for the atom-diatom reaction (like  $H + H_2$ ,  $N + N_2$ ,  $O + O_3$ ). This program uses Cartesian coordinates in the full space to carry out the calculations. As is customary in quantum mechanical treatments SC-IVR does not invoke the conservation of total angular momentum  $J$  to reduce the problem to fewer degrees of freedom and solve the problem separately for each value of  $J$ . The various ingredients of the SC-IVR program are: first the semiclassical coherent-state propagator of Herman Kluk (HK) is applied. Second, the Boltzmannized flux operator is tuned continuously between the traditional half-split and the Kubo forms. Third, the normalization integral is expressed in terms of simple constrained partition functions.

### 3.3 Aiming at interoperability

A fascinating problem prompted from the cooperative nature of the grid is interoperability. This means the possibility for programs to run on the different machines of an heterogeneous (distributed) platform. The other aspect of interoperability is the possibility of utilizing data coming from different program in a cooperative fashion in which data produced from a program need to be used (if it is the case also together with data from another program) by another program.

#### 3.3.1 Data Formats for Quantum Chemistry

Significant efforts along this direction have been already spent to develop common models and shared formats for Quantum Chemistry. Quantum Chemistry codes are nowadays very popular and their use is not confined to the community of theoreticians but it is open to the chemistry community at large. For this reason these programs include various tools for the calculation of different properties of atoms and molecules. These additional utilities are extended continuously by various group of developers. The new tools often refer to programs modified for internal use. For this reason tools developed by different groups are not, in general, interoperable. As a matter of fact, they

- i) use different input and output formats

- ii) do not bear common communication channels
- iii) cannot import features from another code (in the case of commercial codes it is often also illegal)

All these difficulties make the collaboration between research groups awkward and often lead to a duplication of work. A common platform for program development and for allowing the use of different tools and different computer programs, was proposed by Angeli et al. [104] within the activities of the Working Group “A meta-laboratory for code integration in *ab initio* methods” [105, 106] of the COST in Chemistry D23 project “MetaChem”. In order to integrate different QC codes in a common workflow a first problem is the coordination of the different formats adopted by the various codes. Of course, in order not to invent “yet another format” the driving idea was to design a format as general as possible in coordination with other similar initiatives in Europe and elsewhere. This type of problems have been already discussed in the literature and the scheme adopted in my thesis relies on the related literature. In particular, for general data storage the XML [107] format and the HDF5 (Hierarchical Data Format) technology [108] have been proposed. Several well know chemistry programs adopt an XML based format for their internal storage. Along this line a project based on the use of CML (Chemistry Markup Language) [109] as a new approach for managing molecular information has been started in UK in the year 2000. More recently its computational variant, CMLComp, has begun to be developed to the end of including entities relevant for the computational domain. In QC calculations two different kinds of information have been identified: small data, mainly ASCII coded, and large data, normally binary coded. While ASCII coded data are described in the proposed format with a specifically designed Mark-up language (QC-ML), large binary data files are organised in a HDF5 based format called Q5cost. In the following section this two kinds of data storing schemes are described more accurately.

### 3.3.2 The QC-Markup Language

The general description of the chemical system of interest can be given at quantum chemistry level by a collection of data of different kinds (the already mentioned “small data”). This type of data can be classified as:

- **Base facts:** initial data describing the physics of the system like stoichiometry, geometry, symmetry and basis set information.

- **Derived facts:** quantities computed from the previous ones using QC algorithms like energies, properties, integrals, coefficients, input data specifying the type of computation, the level of theory and so on.

In the first category we can devise three different classes of data, describing respectively:

**Symmetry:** the symmetry of the system in terms of group name and other symmetry data;

**Geometry:** the atomic composition of the system and its cartesian coordinates;

**Basis:** the basis set information, either given by name or in detail.

For this set of “small” data a mark-up language is adopted (this enhances the readability and the standardization) that is called QC-ML (Quantum Chemistry Markup Language). The QC-ML is defined by a XML-Schema that can be found on the internet (<http://abigrid.cineca.it/>), together with the proper html documentation.

### 3.3.3 The QC-ML structure

The structure of a QC-ML file is divided into two sections. The first part contains the description of the already mentioned Base Facts, grouped in the tag `<molecule>` containing as attributes the number of electron, the electric charge and the spin multiplicity. In those groups we can find other groups specifying the spatial symmetry (`<symmetry>`) of the molecule, the atomic composition and geometry (`<geometry>`) and the atomic basis set (`<basis>`). Such structure can be so represented as:

```
<molecule nElectrons charge spinMultiplicity>  
  <symmetry ..... />  
  <geometry ..... />  
  <basis ..... />  
</molecule>
```

The system **symmetry** is described using the group name that references a repository containing all possible Abelian Symmetry Groups described with their generator.

The system **geometry** is described by a list of atoms and their cartesian coordinates; the user can choose to list all atoms or only the ones which are unique for symmetry. In this case the coordinates of the missing atoms are generated using the group generator contained in the symmetry tag.

The system **basis** is described by means of Gaussian type basis functions for each atom, with their exponent and contraction coefficients. The user can specify all these quantities with the use of different tags like `<angularMom>`, `<exponents>`, `<contraction>` etc. As an alternative it is possible to define a basis for each atom by means of standard names for the basis set family (cc-DVZ, Sadlej, etc.); in this case the contraction coefficients and the exponent are retrieved from the EMSL database.

The second section of a QC-ML file is intended to contain the Derived Facts, e.g. data that can be produced as an effect of running a QC program. Now it is clear that while the first section is kept untouched during the calculation, the second one is constantly modified or upgraded during the QC runs. The fundamental tag defining this section is `<computedData>` which may contain three fundamental subtags: energy, properties and file.

```
<computedData>
  <energy unit levelOfTheory quality value>
    <state spaceSymmetry spinMultiplicity excitationLevel />
  </energy>
  <property unit levelOfTheory quality value>
    <state ''bra'' spaceSymmetry spinMultiplicity excitationLevel />
    <state ''ket'' spaceSymmetry spinMultiplicity excitationLevel />
    <operator order name/>
  </property>
  <file address URL/>
</computedData>
```

The tag `<energy>` contain the computed value of the molecular energy. It requires the presence of the attributes to define the unit system and the level of theory of the calculation, and of the subtags `<state>` to specify the electronic state to which it refers.

The tag `<property>` is used for the storage of theoretical properties of any order, in the usual perturbation theory sense. It requires the same attribute of `<energy>` but more child tags: the left hand (“bra”) state and the right hand (“ket”) state, as well as the operators involved.

The tag `<file>` contains the linking information to a separate binary file that stores all the computed “large” binary data, like one and two electron integrals and MO coefficients. This file is generally identified by its Uniform Resource Location (URL) that is a standard and unique way to identify a file over the network. The file data format is Q5cost based on HDF5 and is described in the next section. Since FORTRAN is the most common programming language used by QC programmers a specific FORTRAN 90-XML library was written to manage the XML format to be used to produce wrappers. The library is based on publicly available C binding (gdome2 [110]), it implements a DOM model and it allow users to write or read any specific XML element using a FORTRAN Application Programming Interface.

### 3.4 The proposed format

For the large set of binary data (typical of quantum chemistry) a technology combining portability, efficiency, FORTRAN linkability, data compression and easy access to information is needed. The HDF5 [108] library has been suggested for that purpose and for the definition of the related abstract model. HDF5 abstract model for managing and storing data as well as the related library implementing the model is developed and maintained by NCSA/UIUC (<http://hdf.ncsa.uiuc.edu>). The main reason for choosing HDF5 is that it can support unlimited size file, is extensible and portable. It also addresses the issues of efficient data access and storage, of describe an unlimited variety of data types and of containing efficient tools for data compression and file inspection.

### 3.4.1 The Q5cost tool

HDF5 has a hierarchical structure and appears to the user as a direct graph (conceptually similar to the UNIX type file system). The components of this tree-like structure are:

- Groups (corresponding to “directories”)
- Dataset (corresponding to “files”)
- Attributes (or metadata: low dimensional data describing the other data)

All these components can be easily managed by the HDF API. Moreover HDF5 is unique in its ability to distinguish data from metadata even if they are stored together.

Accordingly, the common interchange format for large binary data coming from quantum chemistry calculations Q5cost and the related library have been defined.

This abstract data model of Q5cost is based on the following criteria:

1. Importance of the metadata concept;
2. Matrices are common data structure in QC;
3. Chemical data are related within a hierarchical structure.

**Metadata.** When a large quantity of different types of simple data must be handled (nuclear energy, molecular orbitals labels, molecular symmetry and so on.) they are called metadata to distinguish them from the real large information on the chemical system such as the integral values. Metadata represent well known chemical entities and belong to three generic classes: scalar, vector and n-index arrays. For example, among QC data the nuclear energy is a floating point scalar, molecular orbitals are an (N,M) floating point 2-indices array, the associated orbital energies are floating point vector, the molecular orbital labels are a vector of strings and so on. The library should provide an interface for accessing these data both as generic or specialized entities.

**Matrices data structure.** Large matrices with an arbitrary number of indices are common data structure in quantum chemistry. This is the case for entities like two-electron integrals (rank-4 arrays) or for other more application-specific information, like the four particle density matrices (rank-8 array). These large data arrays share the following common features:

- they are usually integrals, whose evaluation involves one or more operators and a given number of functions. These functions are referred by the indices of the matrix.
- the rank of the matrix depends on the operator involved, an n-particle operator giving rise to a rank-2 array. Atomic basis set overlap is described by two indices, and can be stored as a rank-2 array. Two-electron integrals have four indices imposing a rank-4 array and the four particle density matrix has eight indices, requiring a rank-8 array.
- additional information is needed to identify the operator involved. The latter is in general a tensor in the physical space, so we also need to specify the component (cartesian/spherical) for each matrix. Moreover for each operator component one has to specify the spatial symmetry and real/imaginary nature of the stored values (e.g. magnetic dipole). Symmetry may also reduce the number of matrices to be stored.

All these data objects could be described as one “generic property”. Since some of these “properties” are well known chemical entities and chemists are used to refer to them by name a specific library access to most of them was proposed in addition to a general interface to handle the “generic properties” to ensure both ease of use and flexibility of the library.

**Hierarchical structure.** All these chemical objects are related within a hierarchical structure and logical containment relation can be defined for them. A root container, named System, represents the molecular system and its structural information. We can associate to this container all the metadata that are invariant at the level, mainly information about the spatial reference frame. A system may contain several “Domains”. The role of Domains is to group together properties related to the same kind of functions. Three domains have been formulated as fundamental: AO for atomic orbital, MO for molecular orbital and WF for wave-functions. Each domain can contain other containers. Moreover a set of invariant metadata, different for each type of domain, is associated to it and stored as Scalar, Vector and Matrix entities.

The **AO Domain** holds properties referring to the atomic basis set functions: overlap, one-electron and two-electron integrals on the atomic basis set, in addition to the generic property. The invariant metadata consist in information on the atomic orbitals, like their number, the labels and symmetry. The **MO Domain** holds properties referring to molecular orbitals: one-electron and two-electron integrals on the MO basis set, in addition to generic properties. The descriptive metadata for the domain refer to the MO basis description. Their number, labels and symmetry, the AO basis they were derived from, the matrix collecting the coefficients of the MO expansion on the AO basis,

orbital energies, classification and occupation numbers.

The **WF Domain** holds properties referring to the electronic states. The complete definition of this container is not available yet. It is still subject of research and development, given its non-critical nature for the first deployment and test of the library. For each domain, different occurrences can be defined by means of an identifier (tag) chosen by the user, with a default value if no tag is provided. The aim is to provide storage of multiple entries for each Domain, like in the case of multiple molecular orbitals in the MO Domain, or multiple basis sets in the AO Domain.

The bottom level of the hierarchical scheme is made of the properties. Even if from the user point of view many different “properties” are available, all of them are different instances of the same “generic property” object. This object holds the true data, i.e. the integral values and the corresponding index values. Also here, in order to fully define the nature of the actual property, some metadata are needed: name, rank, symmetry and type (i.e., real, imaginary or complex). In *ab initio* codes, the two-electron integrals, either on the atomic or the molecular basis set, are among the largest data set. For this reason, an efficient management of these integrals is crucial for obtaining a good performance. The whole set of N integrals, with the corresponding indices, can be stored within a linear structure like one reported below:

```
(val1; i1, j1, k1, l1)  
...  
(valN; iN, jN, kN, lN)
```

where `val` is the floating value of the integral with integer indices `i,j,k,l`. The simplest solution is to store both the integrals and the four indices, so the order of the records does not matter. Moreover, null or small integrals can be simply omitted from the list, a fact particularly important when working with local orbitals. For this reason, at the moment, this is the only strategy that was adopted in the Q5cost data format. The price one has to pay is the additional storage of the four integer orbital labels, leading to a memory/disk occupation that could be three times larger than the one if only integrals were stored. In the case of very large integral files, this overhead can be extremely heavy. For this reason, in many QC programs the integrals are stored in a well defined order, the “standard order”, so that the orbital labels can be omitted without loss of information. (In the presence of spatial symmetry, a large number of zero integrals are present, and the standard order can be modified in order to take into account this fact). At present only the simplest solution has been implemented in Q5cost.

### 3.4.2 The Q5cost library

The Q5Cost library provides read and write access to files defined in accordance with the data model described before (Q5cost data model). It provides a specifically designed high-level access for quantum chemistry developers. The rationale is to provide a FORTRAN interface based on well known chemical entities, rather than groups or datasets like in the original HDF5 interface. HDF5 takes care of the low level management of the file, and Q5Cost provides the high-level Application Programmer Interface for storage and retrieval of chemical entities.

#### Library structure

The Q5cost library is written in FORTRAN 95 and consists of several modules of which the most important are: Q5cost, Q5core and Q5error.

**Q5cost** is the main reference for the final user. It provides subroutines to read and write HDF5 files in the Q5cost format with a high level of abstraction. Using this library the users can deal with high level concepts without worrying about low level implementation details. If a finer access is required for the underlying HDF5 file, the Q5Core module provides this type of access in a simpler way with respect to the raw HDF5 routines. One important aspect of this format is that the user is not forced to enter all the quantities; he can store the quantities which are actually available, or in which he is interested, and add other data later when available.

**Q5core** is a low level module designed to provide wrapping facilities between HDF5 and Q5Cost. At the moment it is focused on providing additional debug information, reference counting for HDF5 objects, additional low-level API for simplifying common tasks and so on. This module provides path-based management of Scalar, Vector and Matrix entities (in contrast with the context-based approach of the Q5Cost module, which focuses on chemical concepts rather than HDF5 path). It also provides routines for the easy handling of the Property data (indices and values), relative to a CompactMatrix class (CM). End users in general should not access Q5Core module routines. The Q5Core module guarantees the transparency of the Q5cost data model with respect to the underlying technology. In case we decide to use another storage format in place of HDF5, only this module should be modified.

**Q5error** module provides subroutines for debugging and monitoring the behaviour of the library and the application code.

### 3.4.3 The Wrappers

Based on the Q5-ml/Q5cost common data format and using the specific libraries for the I/O operations, some interface programs (wrappers), for converting data from *ab initio* program system to the common format, are written. In general, wrappers accomplish a quite simple goal: read quantities stored in a given data format and write them in a different data format using the specific I/O library for the two formats.

For a given QC code, the **input wrapper** reads data from the common format file and converts them into the QC code specific input while the **output wrapper** reads data from the QC code specific output and adds them to the common format file. A future development of this technology is related to the definition and the set-up of a “machinery” for running user-defined workflows based on heterogeneous codes, located on different platforms and communicating through the common format. This grid based infrastructure should work, from a logical point of view, as reported in fig. 3.2. The idea is to have a sort of central repository, based on the common format, containing all

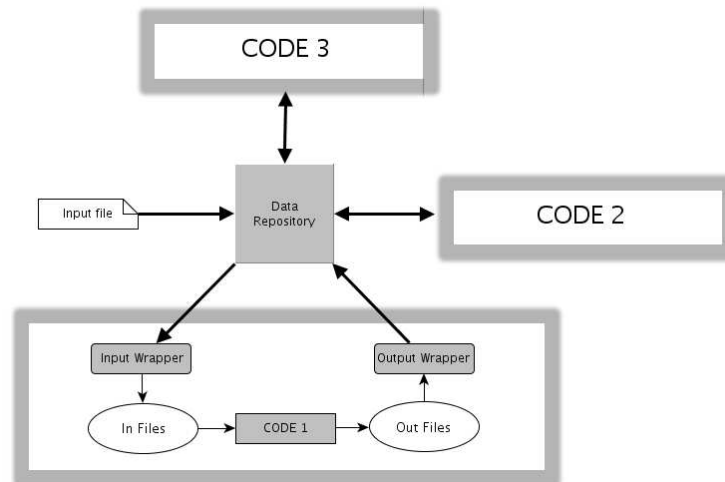


Figure 3.2: A logical scheme of the workflow machinery.

information about the chemical system under investigation. When a specific program has to be run, a code specific input-wrapper will translate the data from the repository into the code specific input files. Then the program can be executed. The output data produced, through the output-wrapper, will be used to update the central repository. The infrastructure must satisfy both grid requirements (fault tolerance, reliability) and human interface requirements (web-based interfaces, user-friendly environments).

### **3.5 Towards the European Grid Initiative**

The EGEE III project is going to expire the end of April 2010 and the EU has already launched its successor EGI (European Grid Initiative). The most important novelty of EGI is that while its stakeholders will be the National Grid Initiatives (NGI)s of the countries which are ready to contribute in terms of funds and efforts, the scientific lead will largely be taken by the thematic Specialized Support Centres (SSC). The SSCs will gather together the communities associated with the VOs belonging to a common research European area.

#### **3.5.1 The Chemistry and Material Sciences and Technologies SSC**

An SSC called CMST (Chemistry and Material Sciences and Technologies) will be proposed by the related communities. The proposed CMST SSC will take care of the user VOs of COMPCHEM, GAUSSIAN (from the homonymous QC package), VOCE (a material science communities). Other communities like the ones associated to the material science community of Northern Europe (Finland, Sweden, Norway, Denmark), ENEA, etc. as well as other Chemistry communities will be assisted to develop grid skills and to implement their codes on the European Grid. The above mentioned pool of laboratories have already established themselves as the third ranking community operating on the EGEE production grid. Moreover, they have developed the necessary skills to manage an SSC.

This will primarily mean to support the related infrastructure and help the members of the related community in implementing and using an environment of shared hardware and Software resources on the grid. The net result of that effort will be an encouragement to implement on the grid of the large variety of computer codes and algorithms designed by or for the members of the molecular

and material science community.

The SSC will be, in fact, operating in the direction of lowering the technological barriers to the use of the grid created by the rapid evolution of computer technologies (which remain hard to master for CMST researchers who are experts in other domains of scientific knowledge). This will be achieved by offering the necessary assistance and guidance to the CMST researchers wishing to implement their programs on the grid. In this respect the SSC will inherit also the Hands on school for molecular and material sciences applications already established by COMPCHEM (held in Trieste on September 2008 and already planned for reiteration by the end of this year) and plans to extend it to offer a broader training on the implementation of molecular and material sciences softwares on the grid. The SSC will also make available to the members of the community some stable versions of codes of interest for the community as a grid version of some program exchange libraries. These codes could be either implemented on the grid by its members, or gathered from existing scientific libraries or available as open source or for free circulation. Special agreements could be also arranged for some commercial codes. To help the users and members with a user friendly utilization of the codes the CMST SSC will be engaged also in developing (for some of them) specific interfaces and will encourage its members to develop even more complex (and at the same time more realistic) grid enabled collaborative simulations. This will further motivate the development of specific portals, graphical interfaces, workflows etc. suited to user friendly handle the various simulation packages, render output and intermediate data, select the optimum segment of the grid, import and link the necessary tools etc. for which the support of an appropriate organization based on specific skills and procedures is necessary. This will also prompt the implementation on the grid of libraries and packages of support to scientific computing and the acquisition to the grid platform of high performance computing nodes with higher sizes of memory and various levels of parallelism as well as the adoption of appropriate parallelization tools.

The other important result will be the increase of efforts in the work aimed at developing models and standards concerning molecular and material sciences and technologies knowledge (data and programs). This will definitely boost the development of connections among the various codes of the community and the reuse of the available software products. In particular, for example, this will further enhance the development of models and standards for Quantum Chemistry (QC) data and its reuse by other computational applications. Typically this is the case of the already mentioned ab initio electronic structure outputs of several QC packages (each of which has its own format) which need to be assembled together or to be provided as an input for other programs in a row or in parallel in complex CMST simulations. The proposed standard for ab initio QC data, QC5cost, tailored on the DALTON package and meant to be ported on the grid has been already worked out as a result of

the EU collaborative initiative COST. Related procedures were specifically designed for porting on grid environments with the motivation that they will make the assemblage of repositories, tools and workflows easier and will advance, as well, efforts in prediction, design and analysis using multiple codes, across multiple disciplines, and for an open user base. An increasing availability of QC digital data (interfaced with users and codes) will have a profound impact in both the quality and rate of discovery of the CMST community. Future implementations can also be foreseen for an extension of the models and standards to Quantum Dynamics.

### 3.5.2 Web service approach

Most of the effort paid by the CMST SSC in providing software in a user friendly way will concentrate in developing a usage of the codes as grid services. This will be addressed both to simple users (who wish to get their goals accomplished without needing to know the details of the methods employed) as well as to the advanced users (who want to compose complex applications out of solid building blocks) while devoting their efforts to developing enhancements in the procedures by introducing significant (either in terms of conceptual innovation or in terms of gathering together non negligible amounts of different pieces of software) advances in the methodology. As a matter of fact, in the CMST community there is already a large fraction of people making massive use of well established (commercial and non commercial) packages. Traditionally, these researchers would try to get a copy of the package from an official library and implement it locally by surmounting the difficulties of a new installation.

In the case of the SSC, instead, a validated version of the codes of interest will be provided already implemented on the grid either for a black box usage or for a coordinated usage within a workflow. Typical examples of this type of packages for the CMST field are GAUSSIAN (or equivalent packages of ab initio calculations like GAMESS, MOLPRO, CASSCF, etc.) and/or quantum and classical dynamics codes as ABC or RWAVEPR for the first type of codes or ABCtraj, VENUS or even DL\_POLY (or equivalent packages for Molecular dynamics calculations for the second type of codes). This effort is considered to be a big step forward along the line of making the SSC sustainable. This is to be understood in two different ways. The first one is the possibility of collecting revenues for the services provided. Although this aspect needs still to be fully investigated there are already commercial companies operating in this way and developing tools for that. The second way is to use web services as a means for contributing to the activities of the SSC itself. In this respect, in fact, the organization of internal activities allows to quantify the contributions provided by the

members to the community as well as the services used in view of constructing a grid economy for the community

### 3.5.3 The quality evaluation

An important element of the web service approach just described is that in order to build a community it has to be accompanied by the development of Quality evaluation tools. This is indeed a difficult task and will have to be addressed in different ways for different objectives. The first and obvious objective is the service. The establishment of rules and tools to work out Quality of Service (QoS) parameters will have to count on various aspects. The simplest ones are availability (or time to response), accessibility, integrity, performance, reliability, regulatory and security. The most difficult ones are innovation and research. In this case concepts like simplification of the procedure, efficiency, simplicity, savings in terms of times, costs, material, energy etc. need to be exploited. Another type of quality to be quantified is that of members. Evaluation of members will have to be implemented by measuring the quality of service (QoS) they are able to provide not only to the other members but also to the users and third parties by using objective and subjective parameters. This means that also evaluation of users will have to be implemented by measuring their quality (QoU) in using grid resources and in providing feedbacks and indications on how to extend and improve the use of the grid. Once a reliable set of quality evaluation tools have been established a means for rewarding members more committed to service the SSC will have to be implemented. This can be achieved by constructing a grid economy through the award of credits and the offer of appropriate conditions to redeem them. This will be particularly difficult especially for those immaterial services (like research) which are difficult to inscribe inside a metric. However, the SSC will have to reward also those research efforts and investment in research which often do not provide short term return. This may be used also to promote the achievements of social interest and at large of more general interest. Credits will be redeemed through a better access to services, research funding and other returns that the SSC will establish as congruent with its activities.



## Chapter 4

### The $\text{N}(^4\text{S}) + \text{N}_2(^1\Sigma_g^+)$ and $\text{N}_2(^1\Sigma_g^+) + \text{N}_2(^1\Sigma_g^+)$ reactions

*Questo capitolo è interamente dedicato ai risultati degli studi teorici effettuati sui due sistemi presi in considerazione.*

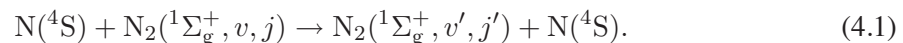
*Nella sezione 4.1 vengono esaminate le informazioni teoriche sulla struttura elettronica del sistema  $\text{N} + \text{N}_2$  e presentati i funzionali adoperati per lo studio teorico di questa reazione.*

*Nella sezione 4.2 sono mostrate le proprietà reattive del sistema atomo diatomo e analizzati i diversi risultati ottenuti quindi le principali PES utilizzate vengono analizzate e comparate.*

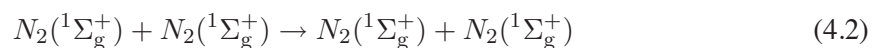
*Le sezioni 4.3 e 4.4 espongono, invece, le caratteristiche principali della reazione  $\text{N}_2 + \text{N}_2$  e gli studi teorici preliminari condotti su questo sistema.*

• • •

As already mentioned, the reactions considered in my thesis work as a case study are



and



The investigation of these reactions is useful from a theoretical point of view to assess the role played by internal and traslational motions in promoting vibrational deexcitation when the reactive

systems are not as light as  $H + H_2$  [111] or  $H_2 + H_2$  [112]. The modeling of reactions 4.1 and 4.2 has been usually based upon the assumption that they have a purely classical behaviour and that the conversion between translational and vibrational energy is the least effective step of the complex mechanism leading to vibrational excitation of nitrogen molecules and, as a consequence, to its ionization and dissociation [113].

However, the accurate evaluation of state-to-state cross sections and rate coefficients of these reactions represents a highly demanding computational task even in classical approaches. They require, in fact, the integration of extended sets of trajectory calculations for several initial states of the reactants and a converged sum with  $J$  of the related partial probabilities. As a matter of fact, massive quasiclassical trajectory (QCT) calculations of the rate coefficients of the  $N + N_2$  reaction were carried out in the past using parallel and distributed computing and related outcomes were compared with those of a reduced dimensionality quantum infinite order sudden (RIOS) computational campaign [114]. In that case the calculations were performed on an empirical PESs [115–117] and the objective was to model nitrogen plasmas [118] and processes occurring around reentering spacecrafts [119]. QCT calculations for the  $N + N_2$  reaction were extended using the same PES to vibrational relaxation and dissociation rates for the whole ladder of reactant vibrational states [120,121]. Calculations based on semiclassical initial value representation techniques were also performed to evaluate thermal rate coefficients [122]. Improved PES of  $N + N_2$  were worked out using functional forms based on a rotating model potential. QCT and quantum RIOS calculations performed on these PESs singled out the different dynamical behaviour of the system on the various surfaces [123]. A time dependent quantal study of this reaction using a PES derived from high level *ab initio* potential energy values is reported in ref. [124]. As to the  $N_2 + N_2$  system only some preliminary studies of the intermolecular potential have been reported, as will be discussed later on in the second part of this chapter.

#### 4.1 The electronic structure of $N + N_2$ and its Many Body representation

As already mentioned, the first electronic structure information on the  $^4A''$  (ground) global PES for the  $N+N_2$  reaction was formulated empirically by the CDK group out of gas kinetics data. To this end, a London-Eyring-Polanyi-Sato (LEPS) functional expression was used. The proposed LEPS has a linear transition state of 1.55 eV [114].

However, subsequent *ab initio* investigations performed by Petrongolo pointed out that the PES provided a new description of the main features of the interaction of the  $N + N_2$  system, especially at the saddle to reaction [125,126]. In particular, these *ab initio* calculations showed that the geometry of the system at the saddle to reaction is bent and that the  $\widehat{NNN}$  angle has a value around  $120^\circ$  in contrast with the collinear geometry associated with the saddle of the LEPS surface. This finding motivated the assemblage of some new PESs (LAG0, LAG1, LAG2 and LAG3, sometimes called also L0, L1, L2 and L3) [123] based on the so called largest angle generalization of the rotating bond order (LAGROBO) functional [127–129].

Particular care has been put into the assemblage of the LAG3 PES to make it have a barrier slightly lower than that of the LEPS and a bent geometry at the saddle (as indicated by Petrongolo). This surface has been used for extended dynamical investigations. More recently, a new global PES (WSHDSP) was fitted to 3326 *ab initio* values obtained from open shell CCSD(T)/aug-cc-pVTZ calculations [130]. The WSHDSP PES exhibits a double barrier (i.e. two saddle points connected by a shallow well), besides a transition state 0.49 eV higher than that of the LEPS. Unfortunately, neither the WSHDSP PES nor the *ab initio* values to which it has been fitted are available for distribution. For this reason, we repeated the *ab initio* calculations to which we assembled a new LAGROBO potential energy surface called LAG4 (also called L4).

#### 4.1.1 The many body expansion

For three atom and four atom systems the calculation of the potential energy values on a large grid of nuclear positions (say at least 10 points per dimension) and their subsequent fit using a suitable functional form is the most popular way of creating a PES. In fact, for reactive systems, extended regions of the molecular geometries become accessible during the collision and the accurate determination of the related structures (these include intermediate wells, barriers, ridges as well as long range and asymptotic reactant and product regions) is of vital importance for the evaluation of scattering and kinetic properties. For this reason, sometimes, additional sets of points need to be computed, in order to better define the most critical of them, like minimum energy paths and saddles to reaction. As a result, this part of the procedure usually handles a fairly large amount of *ab initio* values and is quite laborious since it includes also the incorporation of corrections into *ab initio* points when they are found to be inadequate. Only after this phase, usually the (adjusted) *ab initio* values are fitted using an appropriate functional form. The most popular of these functional forms adopts the many-body expansion method (also known as Sorbie-Murrell method) that is a

global method able, in principle, to fit potential energy surfaces for reactions involving any number of atoms [131]. The expression of the many-body expansion for a three-atom system is given as a sum of one-body, two-body and three-body terms:

$$\begin{aligned}
 V(r_{AB}, r_{BC}, r_{AC}) = & V_A^{(1)} + V_B^{(1)} + V_C^{(1)} + \\
 & V_{AB}^{(2)}(r_{AB}) + V_{BC}^{(2)}(r_{BC}) + V_{AC}^{(2)}(r_{AC}) + \\
 & V_{ABC}^{(3)}(r_{AB}, r_{BC}, r_{AC})
 \end{aligned}
 \tag{4.3}$$

The one-body terms,  $V_A^{(1)}$ ,  $V_B^{(1)}$  and  $V_C^{(1)}$ , are the electronic energies of the atoms in the dissociation configurations. Since we normally deal only with electronic ground state potential energy surfaces these terms are set equal to zero:

$$V_A^{(1)} = 0; \quad V_B^{(1)} = 0; \quad V_C^{(1)} = 0
 \tag{4.4}$$

In the original approach followed by Sorbie and Murrell the interaction was expressed using internuclear distances. In our approach we make use of Bond Order (BO) variables  $n$ . The BO variable for the  $ij$  atom is related to the internuclear distance  $r_{ij}$  as follows:

$$n_{ij} = \exp[-\beta_{ij}(r_{ij} - r_{eq,ij})]
 \tag{4.5}$$

In Eq. 4.5  $\beta_{ij}$  is an empirical parameter and  $r_{eq,ij}$  is the equilibrium distance for the  $ij$  diatom.

### 4.1.2 The two body terms

If the potential energy curve of a diatomic molecule is plotted against the related BO coordinate, it has a parabolic shape (see Fig. 4.1, where the plot of a diatomic potential as a function of the internuclear distance (left hand side panel) and as a function of the related BO coordinate (right hand side panel) is given).

The figure singles out some peculiar properties of the BO formulation of the diatomic interaction:

- the minimum of a diatomic curve plotted against the BO is always at  $n = 1$  ( $r_{ij} = r_{eq,ij}$ ), as shown also in Fig. 4.2 for the reactant and product fragments of  $H + ICl$  system;
- in physical coordinate plots the dissociation limit ( $A + B$ ) ( $r_{ij} \rightarrow \infty$ ) lies outside the graph and the repulsive region is located at short distance. On the contrary, in BO coordinates the dissociation limit is located at the coordinate origin and the repulsive potential is at large (though finite) values of  $n_{ij}$ .

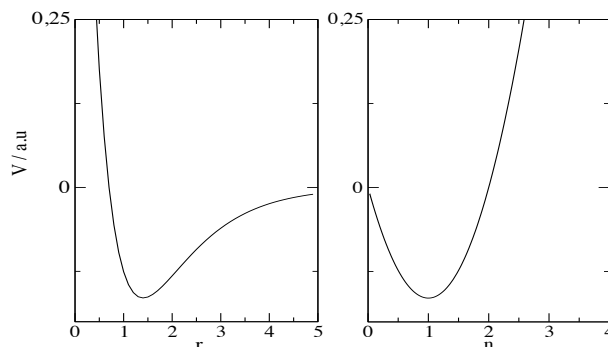


Figure 4.1: Comparison of diatomic potential represented as a function of the internuclear distance  $r$  (left hand side panel) and as a function of the corresponding BO coordinate  $n$  (right hand side panel)

These considerations evidence the advantages of using BO coordinates for modeling potential energy functions: the zero asymptotic limit is naturally built into the BO representation of the potential, the finiteness of the space makes it easier to build grids, minimum energy paths (MEPs) are more easy to locate.

When using BO coordinates, the two-body terms can be therefore expressed as follows [132]:

$$V_{ij}^{(2)}(n_{ij}) = D_{ij} \sum_{k=0}^N a_{ij}^{(k)} n_{ij}^k \quad ij = AB, BC, AC \quad (4.6)$$

where  $D_{ij}$  is the dissociation energy of the  $ij$  diatom, while the  $a_{ij}^{(k)}$  are the expansion coefficients, with no need for using damping factors to kill the increasing trend at long range. These coefficients, jointly with the  $\beta_{ij}$  parameter of Eq. 4.5, are chosen so as to minimize the rms deviation of the fitted values from the input points (i.e. the *ab initio* values). It is obvious that, when the expansion of Eq. 4.6 is truncated to  $k = 2$ , the BO potential has the form of the usual Morse potential. In this case  $b$  can be identified as the Morse  $\beta$  parameter and  $a_1$  and  $a_2$  respectively with 2 and  $-1$ . Accordingly, when  $\beta_{ij}$  can be related to the force constant of the diatom by the relationship:

$$\beta_{ij} = \omega_{e,ij} \sqrt{\frac{\pi \mu_{ij}}{D_{ij}}} \quad (4.7)$$

where  $\omega_{e,ij}$  is the harmonic vibrational constant of and  $\mu_{ij}$  the reduced mass of the considered diatom. When higher terms are included the parameters of the BO functional loose their  $k=2$  physical meaning of the corresponding Morse potential. If expansion 4.6 is truncated to the fourth power,

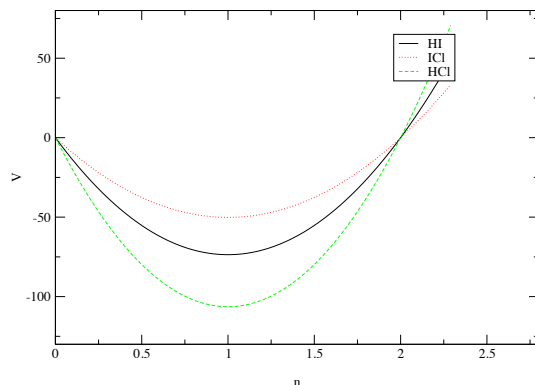


Figure 4.2: Diatomic (asymptotic) curves plotted against the related BO variables for the HICl system.

a relationship between the BO coefficients and the force constants can still be established. The method (often called FCBO) equates the derivatives of the potential at the minimum to the related force constants deduced from spectroscopic data. This leads to the following system of equations (for simplicity we dropped the indices  $ij$ ):

$$\begin{aligned}
 c_1 &= \frac{1}{6}(G_3/\beta^3) + \frac{3}{2}(G_2/\beta^2) + 4 & (4.8) \\
 c_2 &= -\frac{1}{2}(G_3/\beta^3) - 4(G_2/\beta^2) - 6 \\
 c_3 &= \frac{1}{2}(G_3/\beta^3) + \frac{7}{2}(G_2/\beta^2) + 4 \\
 c_4 &= -\frac{1}{6}(G_3/\beta^3) - (G_2/\beta^2) - 1 \\
 0 &= G_4 + 10G_3\beta + 32G_2\beta^2 + 24\beta^4
 \end{aligned}$$

where  $G_k = -F_k/D_e$  with  $F_k$  being the  $k$ -th force constant of the diatom  $ij$ . The fifth equation is numerically solved in order to work out the  $\beta$  parameter. In general, such an equation, has only one positive solution. In the few cases when more than one positive solution are available the largest one, in better agreement with extrapolation from solutions obtained by second and third power truncation of the expansion, is adopted. A similar (though slightly more complex) set of equations can be obtained when  $k=6$  or larger. Eventually, additional constraints like the reproduction of some components (or the overall) of the long range interaction is enforced. Therefore, in the case in which the expansion procedure does not lead to satisfactory results and a sufficient number of asymptotic

potential energy values are available (possibly adjusted to reproduce the dissociation energy and the equilibrium position) this alternative procedure is to be preferred.

### 4.1.3 The three body term

After working out the diatomic terms the values of the three body energies are obtained by subtracting the two body components from the whole set of *ab initio* values (after having adjusted the *ab initio* values to reproduce the main features of the reaction channel, including spectroscopic and reactivity properties).

Then the three body values are fitted using a polynomial of order  $M$  in the relevant three BO variables:

$$V_{ABC}^{(3)}(n_{AB}, n_{BC}, n_{AC}) = \sum_{l=0}^M \sum_{m=0}^M \sum_{n=0}^M c_{lmn} n_{AB}^l n_{BC}^m n_{AC}^n \quad (4.9)$$

$$l + m + n \leq M,$$

$$l + m + n \neq k \neq m \neq n$$

in which all single variable terms are excluded. It is worth noting that the values of the  $\beta$  parameters are still the ones estimated for the diatomic potentials. This fact implies that the surface has the correct asymptotes and that the spurious features that can arise in the long range region when different functional forms are used for diatomic and three body interaction terms do not occur. Moreover, in this formulation the damping function, normally used in the many-body expansion to make sure that the three body term becomes zero at asymptotic configurations (i.e. when any of the internuclear distances becomes large), is not needed because the three-body term is zero when either  $n_{AB}$  or  $n_{BC}$  or  $n_{AC}$  is zero (i. e. at atom+diatom and at full dissociation configurations). The optimization of the  $c_{lmn}$  coefficients is performed using a linear regression.

An example of an atom diatom potential energy surface represented using the BO coordinates, the isoenergetic contours of the collinear  $H + H_2$  reaction are shown in Fig. 4.3.

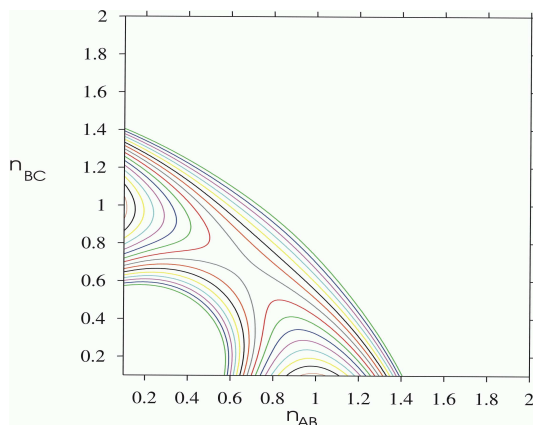


Figure 4.3: Sketch of the BO isoenergetic contours for the H + H<sub>2</sub> system.

## 4.2 From Many Body to Many Process LAGROBO representations

When dealing with three or more atoms the polynomial representation of all the components of the interaction may find valid alternatives. In fact, though in a polynomial representation the determination of the coefficients is straightforward the result may be affected by the fact that no *a priori* chemical knowledge has been built-in into the functional representation.

### 4.2.1 From LEPS to ROBO

A typical example of a more “chemically oriented” formulation of the atom diatom PES is indeed the LEPS potential. The LEPS potential has been derived from an extremely simplified *ab initio* approach. As shown in the followings the LEPS functional ( $V^{\text{LEPS}}$ ) can also be formulated using a many-body expansion scheme [134] and be written as:

$$V^{\text{LEPS}}(r_{ij}, r_{jk}, r_{ik}) = V^{(2\text{B-LEPS})} + V^{(3\text{B-LEPS})} \quad (4.10)$$

where  $i, j$  and  $k$  label the atoms of the system. The two body terms of the functional read:

$$V^{(2\text{B-LEPS})} = \sum_l {}^1E_l(r_l) \quad (4.11)$$

with  $l$  being the sequential label for the  $ij, jk$  and  $ik$  diatomic pairs and  ${}^1E_l(r_l)$  being the Morse diatomic potential defined as

$${}^1E_l(r_l) = D_l \left( e^{-2\beta_l(r_l - r_{el})} - 2e^{-\beta_l(r_l - r_{el})} \right) \quad (4.12)$$

The three body term reads:

$$V^{(3B-LEPS)} = - \sum_l J_l - \sqrt{\frac{1}{2} \sum_l \sum_{m>l} (J_l - J_m)^2} \quad (4.13)$$

with

$$2J_l = {}^1E_l(r_l) - \frac{1 - \Delta_l}{1 + \Delta_l} {}^3E_l(r_l) \quad (4.14)$$

and

$${}^3E_l(r_l) = \frac{D_l}{2} \left( e^{-2\beta_l(r_l - r_{el})} + 2e^{-\beta_l(r_l - r_{el})} \right) \quad (4.15)$$

in which  ${}^3E_l(r_l)$  is the anti-Morse diatomic potential,  $\Delta_l$  is the  $l_{th}$  empirical (Sato) parameter and  $D_l$ ,  $\beta_l$  and  $r_{el}$  are, respectively, the dissociation energy, the force constant and the equilibrium distance of the diatom  $l$ . The Morse (eq. 4.12) and anti-Morse (eq. 4.15) parameters come from the spectroscopic data of the ( $X^1\Sigma_g^+$ ) electronic ground state of the  $N_2$  molecule [135]. They are: internuclear equilibrium distance  $r_e = 1.0977 \text{ \AA}$ ; dissociation energy  $D_e = 9.905 \text{ eV}$ ; harmonic and anarmonic vibrational constants  $\omega_e = 2358.57 \text{ cm}^{-1}$  (0.292 eV) and  $\omega_e x_e = 14.324 \text{ cm}^{-1}$  (0.00178 eV). Using these data, one can easily calculate the value of  $\beta$  [79], that for  $N_2$  turns out to be  $\beta = 2.689 \text{ \AA}^{-1}$ . Since  $N+N_2$  reaction is homonuclear, all the Sato parameters will have the same value. To determine this value, it was assumed on the ground of measured rate coefficients that the barrier to reaction was 1.55 eV. This led to a value of  $-0.023$  [114]. The features of the plots of figures 4.1,4.2and 4.3 drawn in the BO space naturally have suggests the use of the polar or hyperspherical BO coordinates (HYBO). The BO coordinates can be transformed into the HYBO ones as follows:

$$\rho_j = (n_{ij}^2 + n_{jk}^2)^{1/2} \quad (4.16)$$

$$\alpha_j = \arctan \left( \frac{n_{ij}}{n_{jk}} \right) \quad (4.17)$$

for collinear systems.

The  $\rho_j$  and  $\alpha_j$  coordinates are perpendicular in the BO space [136,137]. The intervals of definition of these coordinates are:

$$0 \leq \rho_j \leq [\exp(2\beta_{ij}r_{eqij}) + \exp(2\beta_{jk}r_{eqjk})]^{1/2}$$

$$0 \leq \alpha_j \leq \pi/2$$

A plot of the isoenergetic contours of the HICl potential and a sketch of the HYBO coordinates are given in Fig. 4.4. These plots of  $H + H_2$  (see Fig. 4.3) and that of  $H + HICl$  (see Fig. 4.4) show

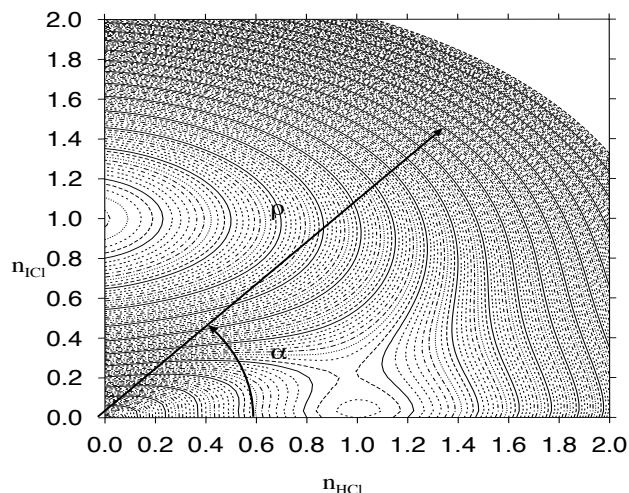


Figure 4.4: Plot of the isoenergetic contours for the  $HICl$  PES represented as a function of the  $n_{ICl}$  and  $n_{HCl}$ . Also the polar coordinates  $\rho$  and  $\alpha$  are indicated.

that the reaction channel can be described by a BO diatomic like functional rotating (from this the acronym ROBO) of  $\pi/2$ . As shown from Fig. 4.4, the  $\rho_j$  coordinate corresponds to the vibrational coordinate of the system (changing from the reactant diatom to the product one) and the  $\alpha_j$  coordinate corresponds to the reaction coordinate. This means that using the HYBO coordinates it is possible to describe the potential energy surface for a single process, say  $A + BC \rightarrow AB + C$ , by using a pseudo diatomic function like:

$$V_B^{\text{ROBO}}(\rho_B, \alpha_B; \phi_B) = \mathcal{D}_B(\alpha_B; \phi_B) \mathcal{F}_B(\rho_B; \alpha_B, \phi_B) \quad (4.18)$$

where  $\phi_B$  is the angle  $\widehat{ABC}$ . The function  $\mathcal{D}_B(\alpha_B; \phi_B)$  gives the fixed  $\phi_B$  evolution of the minimum energy path along  $\alpha_B$  when the system evolves from the reactant to the product configuration. The polynomial  $\mathcal{F}_B(\rho_B; \alpha_B, \phi_B)$  represents the cut (normalized to  $-1$  at the minimum) of the fixed  $\phi_B$  potential energy surface along  $\rho_B$  at a given value of  $\alpha_B$ .

Therefore, when  $\alpha$  is zero and  $\pi/2$ , for example, the ROBO potential coincides with the asymptotic diatomic potential of the reactants and products, respectively, as shown in Fig. 4.3. However, even for other values of  $\alpha$  (including that of the saddle) the cuts of the potential along  $\rho$  are properly described by a parabola (a Morse-like shape in physical coordinates).

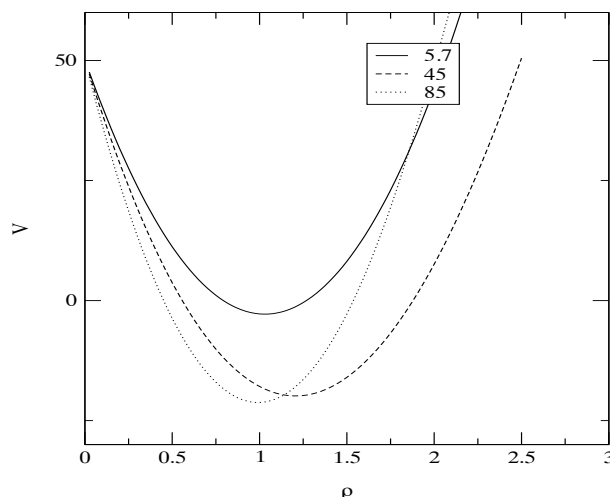


Figure 4.5: Cuts of the potential for the HICl system at three values of  $\alpha$  ( $5.7^\circ$ ,  $45^\circ$  and  $85^\circ$ ).

## 4.2.2 The LAGROBO functional and the Many Process Expansion

When dealing with a non fully symmetric reaction each channel will represent a different process. Accordingly, more than a single  $V_L^{\text{ROBO}}$  function (where  $L$  can be  $A$ ,  $B$  or  $C$  according to the chosen exchanged atom) have to be used to describe the whole process and a proper combination of ROBO functionals has to be taken.

This means that instead of an MBE (Many Body Expansion) we are using here an MPE (Many Process Expansion) model. In this model, the global potential energy surface function for a  $N$ -atoms system is expressed as a sum of the potential functions describing all the relevant atomic rearrangement processes <sup>1</sup> of the system. The general expression of this potential is:

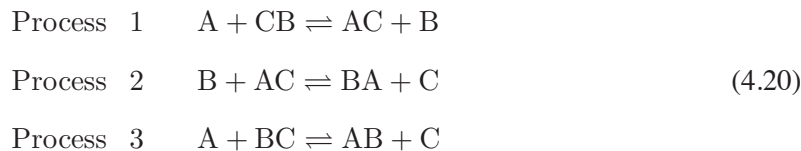
$$V_{ABC\dots N} = \sum_{\xi} w_{\xi}(\{s_{\xi}\} \cdot s_1 \cdot s_2 \dots) P_{\xi}(\{t_{\xi}\} \cdot t_1 \cdot t_2 \dots) \quad (4.19)$$

where  $\{s_{\xi}\}$  and  $\{t_{\xi}\}$  are the reaction coordinate and the pseudo diatomic coordinates related to the process transforming the reactant configuration into the product one, while  $s_1, s_2 \dots s_l$  and  $t_1, t_2 \dots t_l$  are the remaining  $N - 1$  coordinates.  $P_{\xi}(\{t_{\xi}\})$  represents the potential function of the process  $\xi$  and  $w_{\xi}(\{s_{\xi}\})$  is the related weight factor evaluating the relative importance of process  $\xi$ .

---

<sup>1</sup>We define atomic rearrangement process any reactive process taking place with the breaking of a bond in the molecule and the formation of a new one.

For a three atom reaction, one has the following rearrangement channels:



Then, one considers for each process the two BO coordinates involved in the atom exchange and the angle formed by the related internuclear distances (i.e. for process 3, these are  $n_{AB}$ ,  $n_{BC}$  and  $\phi_B$  coordinates) and works out the corresponding polar representation by generating the angular coordinates  $\alpha_B$ ,  $\alpha_C$ ,  $\alpha_A$  and the hyperradii  $\rho_B$ ,  $\rho_C$  and  $\rho_A$ , together with the related  $V_\xi^{\text{ROBO}}$  potential. Once the three ROBO potentials of the MPE have been built, the overall potential energy surface is obtained by the following linear combination:

$$\begin{aligned}
 V(r_{AB}, r_{BC}, r_{CA}) &= w_A(\phi_A) V_A^{\text{ROBO}}(\rho_A, \alpha_A; \phi_A) \\
 &+ w_B(\phi_B) V_B^{\text{ROBO}}(\rho_B, \alpha_B; \phi_B) \\
 &+ w_C(\phi_C) V_C^{\text{ROBO}}(\rho_C, \alpha_C; \phi_C)
 \end{aligned} \tag{4.21}$$

The weighing functions,  $w_A$ ,  $w_B$ ,  $w_C$  give the importance to the contribution of a given ROBO term to the overall potential.

A suitable formulation of the weight coefficients is the one that privileges the ROBO potential associated with the process taking place with the largest  $\phi$  value. This is in fact, the MPE term better describing the current geometrical configuration since, being the internuclear distance  $r_{AC}$  of the two opposite atoms large and the associated interaction small, the related fixed angle BO representation is the less perturbed one and therefore the one closer to circular contour representations. Therefore, simple functions of the angles  $\phi_A$ ,  $\phi_B$  and  $\phi_C$ , privileging the contribution of the most collinear geometry, can be used to build an overall switching function indicating the relative importance of the different contributions to the system interaction. When one  $\phi$  decreases then another angle may become prevalent (obviously, this coincides with a change in the reference geometry of the system). Accordingly, the expansion coefficients should vary so as to weigh more the potential associated with the new largest angle. Therefore, a suitable generalized MPE functional reads

$$V(r_{AB}, r_{BC}, r_{AC}) = \frac{\sum_{L=A,B,C} \omega_L(\phi_L) V_L^{\text{ROBO}}(\rho_L, \alpha_L; \phi_L)}{\sum_{L=A,B,C} \omega_L(\phi_L)} \tag{4.22}$$

where the individual weighing functions  $\omega_L$  are given by:

$$\omega_L(\phi_L) = \frac{u_L(\phi_L)}{\sum_{S=A,B,C} u_S(\phi_S)}. \tag{4.23}$$

In Eq. 4.23  $u_L(\phi_L)$  is a damping function defined as follows:

$$u_L(\phi_L) = \begin{cases} 0 & \text{if } \phi_L < \phi_L^0 - \Delta\phi_L \\ \frac{1}{2} \left( 1 + \sin \left( \frac{\pi(\phi_L - \phi_L^0)}{2\Delta\phi_L} \right) \right) & \text{if } \phi_L^0 - \Delta\phi_L \leq \phi_L \leq \phi_L^0 + \Delta\phi_L \\ 1 & \text{if } \phi_L^0 + \Delta\phi_L < \phi_L \end{cases}$$

if a sinusoidal switching function is chosen (in some cases a hyperbolic tangent function was chosen). This choice of  $u_L$  guarantees that for  $\phi_L$  values greater than  $\phi_L^0 + \Delta\phi_L$  the weighing function it exactly one, for  $\phi_L$  values smaller than  $\phi_L^0 - \Delta\phi_L$  it is exactly zero and for values ranging in the interval of width  $2\Delta\phi_L$  around  $\phi_L$  it smoothly varies from zero to one. For this reason this approach was called *Largest Angle Generalization of ROBO* (LAGROBO). Following eq. 4.18, for the generic process  $L$ ,  $V_L^{ROBO}$  is expressed by the product of  $\mathcal{D}_L$  and  $\mathcal{F}_L$  functions. Usually, for  $\mathcal{F}_L$  a second degree polynomial in  $\rho_L$ , i.e. a Morse-like formulation, is adopted. Accordingly, for arrangement  $B$  one has:

$$\mathcal{F}_B(\rho_B; \alpha_B, \phi_B) = \frac{\rho_B^2}{\rho_{0B}^2(\alpha_B, \phi_B)} - 2 \frac{\rho_B}{\rho_{0B}(\alpha_B, \phi_B)} \quad (4.24)$$

with  $\rho_{0B}(\alpha_B, \phi_B)$  being the value of  $\rho_B$  at the minimum that depends on  $\alpha_B$  and (parametrically) on  $\phi_B$ .

One advantage of the LAGROBO method is that the determination of best fit parameters can be carried out in a fast and straightforward manner using least square fits. This approach has been successfully used to work out some potential energy surfaces for three atom reactions (such as  $H + H_2$  [137],  $O + HCl$  [138]). The values  $D_L$  and  $\rho_{0L}$  at the asymptotes ( $\alpha_L = 0^\circ$  and  $90^\circ$  respectively) were chosen to reproduce the dissociation energy, the equilibrium internuclear distance and the exponential factor of the  $N_2$  Morse diatomic potential. In order to keep the formulation of the potential as simple as possible and to enforce the proper symmetry,  $D_L$  and  $\rho_{0L}$  were given a linear dependence on the  $\sin(\alpha_L)$ :

$$D_L(\alpha_L, \phi_L) = -D_e + b_{L1}(\phi_L) \sin(2\alpha_L) \quad (4.25)$$

$$\rho_{0L}(\alpha_L, \phi_L) = 1 + b_{L2}(\phi_L) \sin(2\alpha_L) \quad (4.26)$$

The variation of the  $b_{L1}(\phi_L)$  and the  $b_{L2}(\phi_L)$  coefficients with  $\phi_L$  was formulated as:

$$b_{Lj} = \sum_{k=1}^{k_{\max}} c_{Ljk} (\phi_{Lj}^{\text{TS}} - \phi_L)^\zeta \quad (4.27)$$

where  $\phi_{Lj}^{\text{TS}}$  is an angle of reference, usually the angle at the saddle geometry.

An advantage of the LAGROBO method is that the determination of best fit parameters can be carried out in a fast and straightforward manner using least square fits. This approach has been

successfully used to work out some potential energy surfaces for three atom reactions (such as  $\text{H} + \text{H}_2$  [137],  $\text{O} + \text{HCl}$  [138]).

### 4.2.3 The characteristics of the various $\text{N} + \text{N}_2$ LAGROBO PESs

The flexibility of the LAGROBO functional form allowed us to generate several LAGROBO PESs, called, as already mentioned, L0, L1, L2 and L3. The L0 LAGROBO PES was obtained by fitting the existing LEPS. In this case, see eq. 4.27, both  $\phi_{L1}^{\text{TS}}$  and  $\phi_{L2}^{\text{TS}}$  are  $180^\circ$ ,  $\zeta$  is  $2(k - 1)$  and  $k_{\text{max}}$  is 4. To modify the height and the location of the transition state of the LAGROBO PESs, one can play with the analytic formulation of the  $b_{Lj}$  coefficients of eq. 4.27 and with the value of the related  $c_{Ljk}$  and  $\phi_{Lj}^{\text{TS}}$  parameters. In fact, for the L1, L2 and L3 LAGROBO potentials the exponent  $\zeta$  was set equal to  $k - 1$  for  $b_{L1}$  and equal to  $2(k - 1)$  for  $b_{L2}$  (except for that of L2 for which the value  $k - 1$  was taken). At the same time,  $\phi_{Lj}^{\text{TS}}$  was set equal to  $120^\circ$  for L1 and L2 and equal to  $125^\circ$  for L3. The value of  $\phi_{L2}^{\text{TS}}$  was always set equal to  $180^\circ$ . In all cases,  $k_{\text{max}}$  was set at 4. The  $c_{L11}$  coefficient, which indicates the height of the saddle, was set to have the same height of the transition state as the LEPS in the L1 and L2 surfaces whereas in the L3 one was chosen so as to make the height of the transition state better agree with the indications of *ab initio* calculations of refs. [125, 126]. The value of the parameters for all the LAGROBO PESs are given in ref. [123]. The heights and bond lengths of the barriers to reaction for several internuclear angles  $\phi$  are given in Table 4.1. As clearly indicated by the Table, both the height and the geometry of L0 well reproduce those of the LEPS. The most significant difference, not apparent from the Table, is the slope of the MEP of L0, which is larger than that of the MEP of the LEPS (the MEP of L0 lies always slightly above that of the LEPS). The L1 and L3 PESs have a bent transition state. The location of the transition state is the key difference between the LEPS (L0) and the L1 surface. In fact, while the height of the transition state is the same (1.55 eV) for both surfaces, the location of the LEPS and L0 transition state is collinear while that of L1 is bent ( $\phi = 120^\circ$ ). At the same time, the transition state of L3 differs from that of L1 for the fact that it is high 1.40 eV and located at  $\phi = 125^\circ$ . The dependence of the barrier height on the internuclear angle  $\phi$  is shown for the LEPS, L1 and L3 surfaces in Figure 4.6 (the corresponding dependence for the L0 PES is not shown because it coincides with that of the LEPS PES). On the other hand, all PESs have almost the same dependence on the angle  $\phi$  of the N-N internuclear distance at the barriers. However, beside this agreement, the N-N distance at the transition state differs.

In order to analyse the global characteristics of the PES and find, if it exists, any spurious

Table 4.1: Barrier characteristics of the N+N<sub>2</sub> PESs

$\phi$	Height (in eV)				N-N distance (in Å)			
	LEPS	L0	L1	L3	LEPS	L0	L1	L3
180°	1.55	1.55	3.49	3.49	1.240	1.240	1.240	1.240
150°	1.61	1.62	1.93	1.79	1.243	1.244	1.244	1.244
125°	1.83	1.84	1.56	1.40	1.251	1.252	1.252	1.252
120°	1.92	1.91	1.55	1.42	1.254	1.254	1.254	1.254
90°	3.06	3.05	2.45	2.65	1.294	1.293	1.293	1.293
60°	7.69	7.69	7.69	7.69	1.530	1.522	1.522	1.522

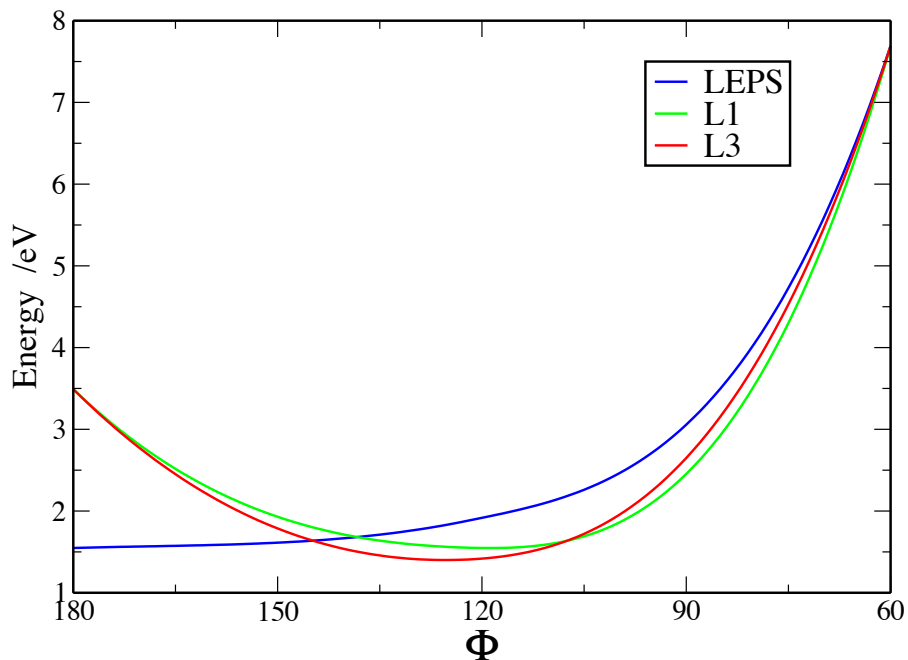


Figure 4.6: Barrier heights as a function of the angle  $\phi$  for the LEPS, L1 and L3 PESs.

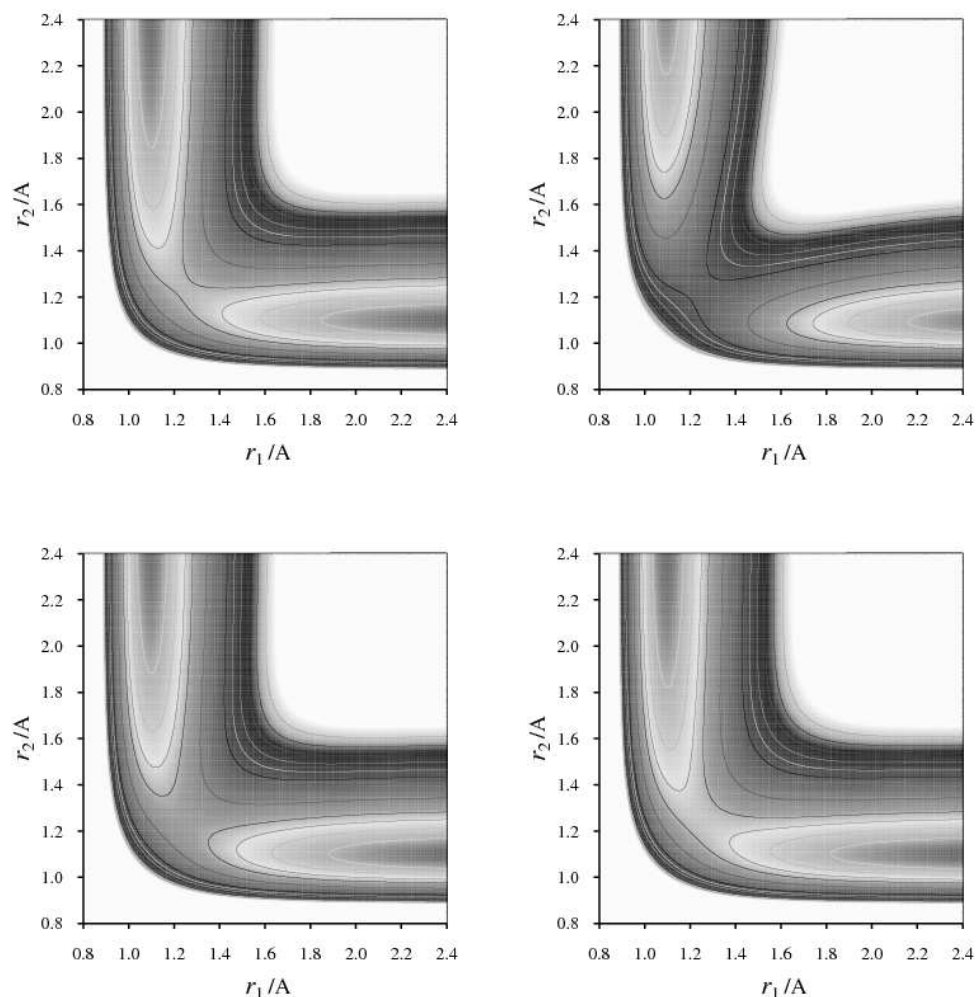


Figure 4.7: Isoenergetic contour maps for LEPS (left panels) and L3 (right panels) PESs for  $\phi = 180^\circ$  (upper panels) and  $\phi = 125^\circ$  (lower panels). The energy interval between two consecutive contours is 0.4 eV and the energy is referred to the entrance channel.

structure, it is necessary to plot the potential energy function. Obviously, a full four-dimensional plot of the PES is not possible. To reduce the dimensionality, the projection of the potential function onto a bidimensional space is needed. Generally this difficult is overtaken by resorting to the isoenergetic contour maps of the potential function [141]. In each plot, usually the internuclear angle  $\phi$  is fixed and the isoenergetic contours are obtained as a function of the  $r_1$  and  $r_2$  internuclear distances. Figure 4.7 shows these plots for the LEPS and the L3 PESs. The L0 and L1 contour plots have been omitted because they are almost equal to those of the LEPS and L3 ones, respectively. In the plots, the entrance channel is localized in the lower-right part of each panel and is extended up to ( $r_1 \rightarrow \infty$ ) asymptotic limit where one atom is far away from the diatomic molecule and therefore

the potential energy corresponds to the  $N_2$  diatomic potential. Reaction starts channel moving to the left direction to reach the saddle point. After the saddle, the reactive process progresses towards the products to reach the product asymptotic region ( $r_2 \rightarrow \infty$ ) located in the upper-left side of each panel. Obviously, the isoenergetic maps at a given  $\phi$  angle are symmetric, since the  $N + N_2 \rightarrow N_2 + N$  process is symmetric. The properties of the reaction channel of L4 is compared with those of LEPS and L3 PESs table 4.2. In particular, the geometry and the energy of the system at the barriers and at the bottom of the LAG4 well are reported. Note that the geometry of the system at the L4 barrier is asymmetric. The geometry at the bottom of the well is symmetric with  $r_1 = r_2 = 2.40$  bohr and  $E = 1.93$  eV. Accordingly, the depth of the well is 0.13 eV. The minimum energy paths are shown in figs. 4.8 and 4.9. For illustrative purposes we show the potential energy surface at fixed angles (t.s. angles for LEPS and L3, bottom-of-the-well angle for L4, see table 4.2) for the three PESs as a function of two internuclear distances in figs. 4.10, 4.11, 4.12.

LEPS t.s.	L3 PES t.s.	L4 PES t.s.	L4 PES well
$r_1 = 2.34$ bohr	$r_1 = 2.37$ bohr	$r_1 = 2.24$ bohr	$r_1 = 2.40$ bohr
$r_2 = 2.34$ bohr	$r_2 = 2.37$ bohr	$r_2 = 2.76$ bohr	$r_2 = 2.40$ bohr
$\phi = 180.0$ degrees	$\phi = 125.0$ degrees	$\phi = 116.8$ degrees	$\phi = 118.6$ degrees
$E_{ts} = 1.55$ eV	$E_{ts} = 1.40$ eV	$E_{ts} = 2.06$ eV	$E_{well} = 1.93$ eV

Table 4.2: Features of the reaction channel of the LEPS, L3, L4 PESs.

## Minimum Energy Path (variable angle)

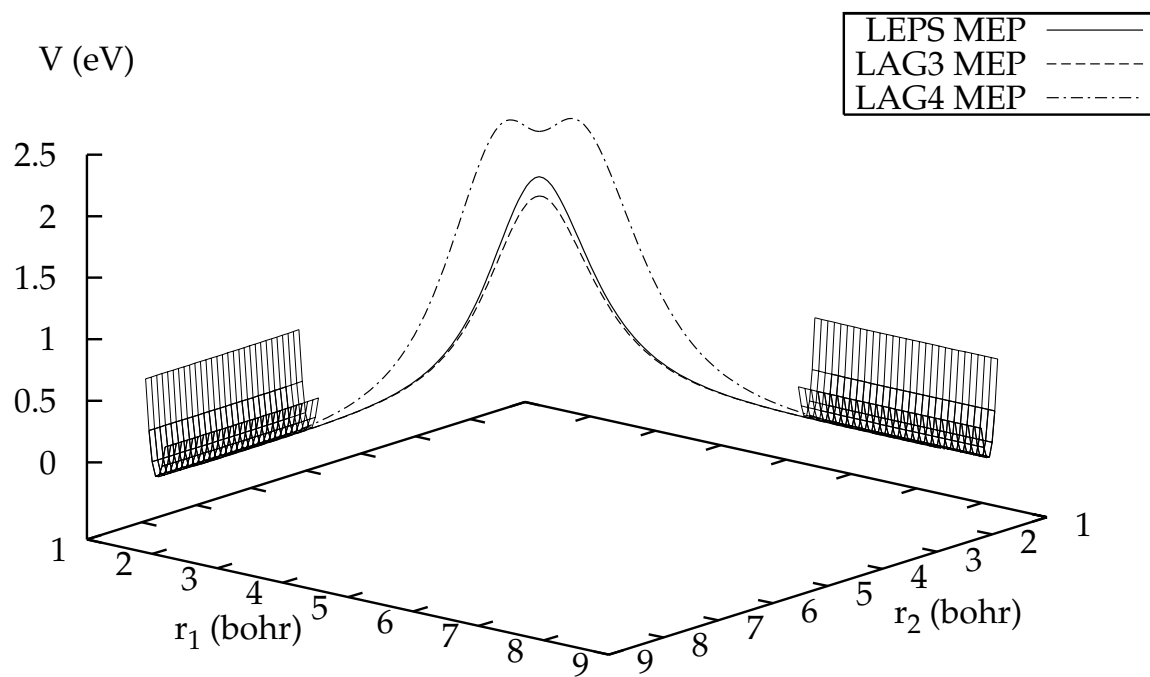


Figure 4.8: Minimum energy reaction path for the LEPS, LAG3, LAG4 PESs as a function of two internuclear distances with variable angle (see fig. 4.9). Asymptotic regions of the various channels are also shown.

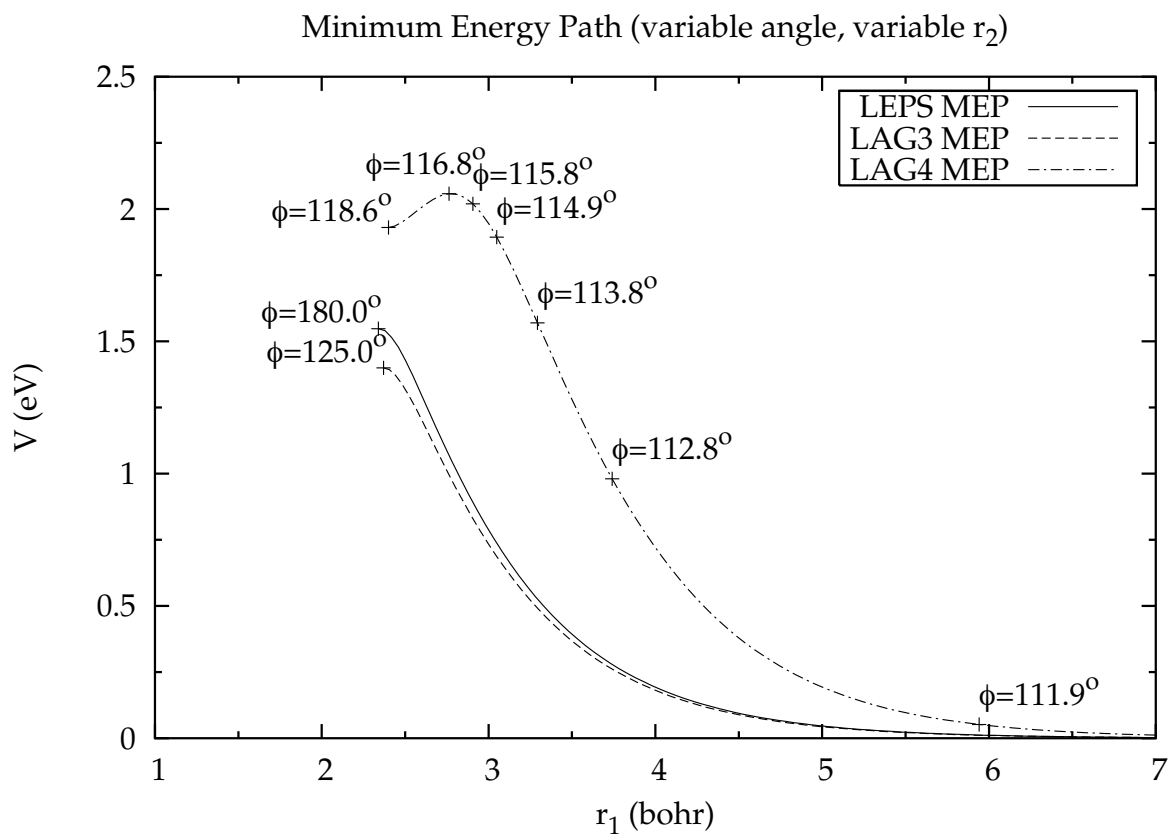


Figure 4.9: Minimum energy path connecting the exchange point to the asymptotic channel for the LEPS, LAG3, LAG4 PESs plotted as a function of one internuclear distance. The remaining two coordinates are variable.

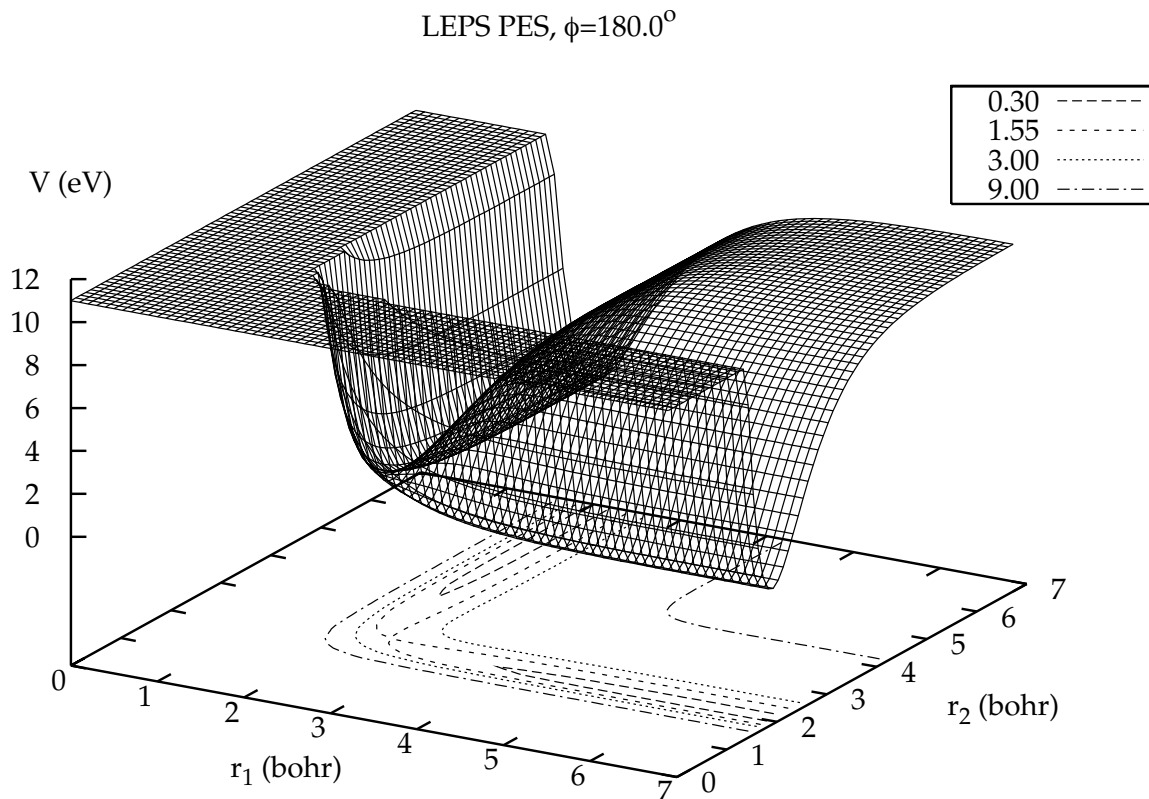


Figure 4.10: LEPS potential energy surface plotted as a function of two internuclear distances at a fixed angle of 180.0 degrees.

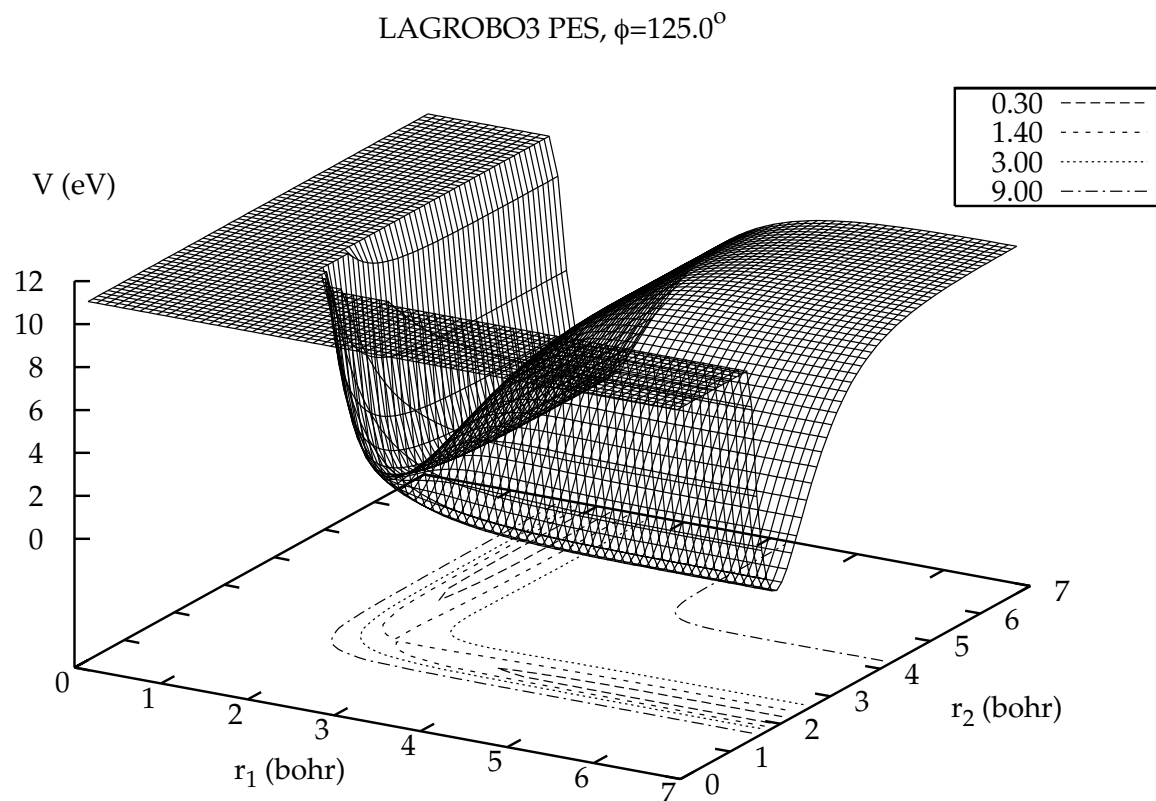


Figure 4.11: LAG3 potential energy surface plotted as a function of two internuclear distances at a fixed angle of 125.0 degrees.

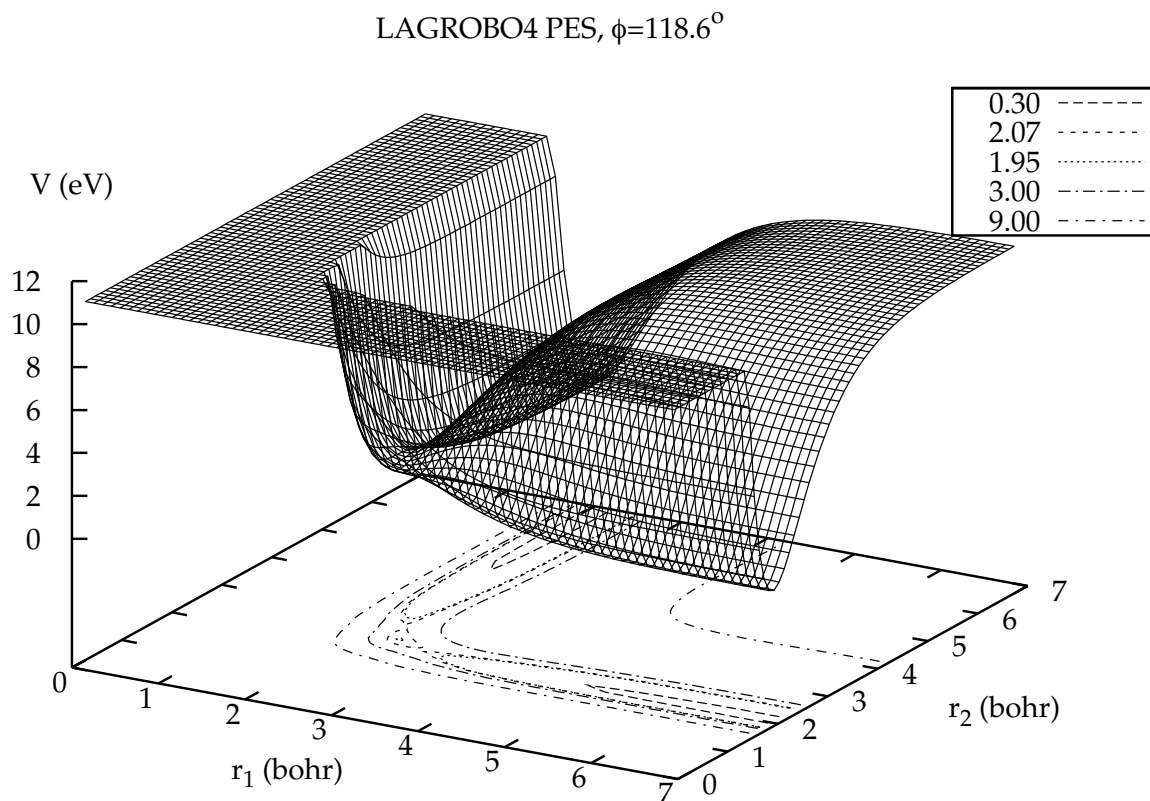


Figure 4.12: LAG4 potential energy surface plotted as a function of two internuclear distances at a fixed angle of 118.6 degrees.

### 4.3 The reactive properties of $N + N_2$

To compare the reactive efficiency of the system on the considered PESs, exact  $J=0$  state-to-state quantum reactive probabilities (excitation functions) were calculated for the ground rotational level of the first 6 vibrational states of the reactant  $N_2$  molecule and  $E_{tr}$  ranging from threshold up to 2 eV in steps of 0.001 eV by Garcia et al. [142].

#### 4.3.1 From LEPS to LAGROBO PESs results

A first batch of calculations were performed on the LEPS and on the L0 PESs. Plots of the reactive probability values calculated at  $J=j=0$  and  $v$  varying from 0 to 5 are given in Figure 4.13 as blue and magenta lines, respectively. The 3D quantum probabilities, although differing in absolute value from QCT and RIOS ones, confirm that, as expected, results obtained on LEPS and L0 are almost coincident. When calculations were performed also on L1 (to the end of investigating the effect of moving the barrier to reaction out of collinear geometries while preserving its height), the net result (see green lines of Figure 4.13) was at  $v=0$  a clear increase of the threshold energy and an associated strong decrease of the reactive probability about the threshold region (in the temperature range of interest, this means also a substantial decrease of the thermal rate coefficient). When the calculations were extended to L3 (to the end of investigating the effect of lowering the saddle to reaction in an attempt to contrast the decrease of the reactivity due to the adoption of a bent geometry at the saddle) the net result (see red lines of Figure 4.13) was a lowering of the threshold energy back almost entirely to the LEPS and L0 values and a sharp increase of the reactive probability in the energy region immediately following the threshold. This puts on an exact quantum ground the traditional QCT finding that on collinearly dominant PESs relative collision energy is exploited better than any other mode to the end of enhancing reactivity. Such an effect is particularly strong, however, only at  $v=0$  and for the just-past-the-threshold energy values. At larger  $v$  values, in fact, the picture is partially modified. The higher reactive efficiency of the collinearly dominated PESs (LEPS and L0) becomes weaker and the interplay between larger amounts of vibration and collision energy becomes so strong to efficiently enhance the reactivity also on PESs having a bent geometry at the saddle to reaction provided that the height of the barrier has been lowered as in L3. As shown by the green lines of Figure 4.13, in fact, L1 results (for which the barrier has not been lowered) remain lower than the reactive probabilities calculated on the other surfaces for a larger interval of relative collision energy even at  $v=5$ . A first consideration to make at this point is that

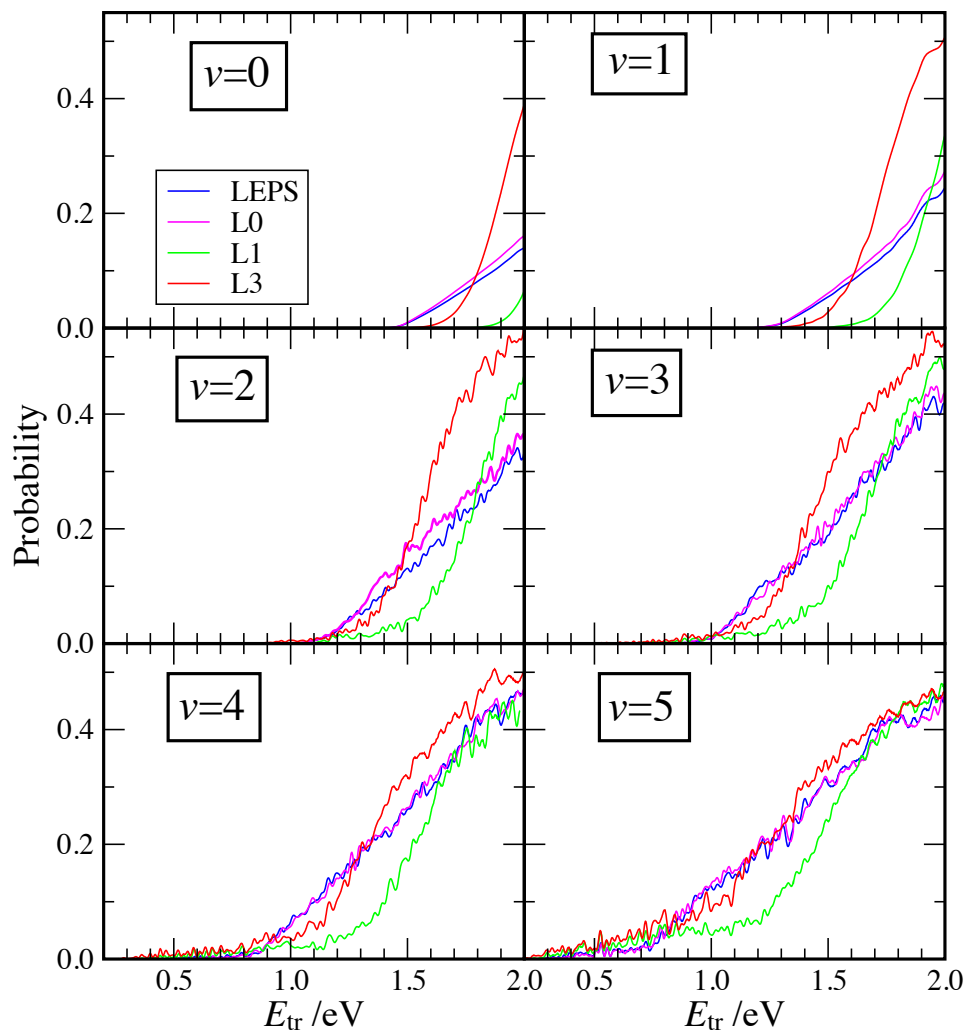


Figure 4.13: State-specific reactive probabilities,  $P_{v_j}^J(E_{tr})$ , calculated on the LEPS (blue line), L0 (magenta line), L1 (green line) and L3 (red line) PESs for  $v=0,1,2,3,4,5$  at  $j=J=0$  plotted as a function of the collision energy  $E_{tr}$ .

the LAGROBO PESs which have a bent transition state geometry (such as L1 and L3) are able to emulate the reactive efficiency of the collinearly dominant PESs (such as the LEPS and L0) only when the barrier to reaction is properly lowered (in our case, as already mentioned, this amount corresponds to the zero point difference between the transition state and the asymptote).

### 4.3.2 L3 Vs LEPS

To consider other properties of the  $N + N_2$  reactive system, we shall focus hereafter on the comparison between LEPS and L3 results. As discussed in the previous section, the key differences between the LEPS and L3 PESs are the height of the saddle to reaction and the geometry of the system associated with it. In particular, while the lowest saddle to reaction of the LEPS has an energy of 1.55 eV (36 Kcal/mol) and a value of the angle  $\phi_{N_2}$  (the angle formed by the bonds of the external nitrogen atoms  $N_1$  and  $N_3$  with the central one) of  $180.0^\circ$  (collinear geometry), the L3 has an energy of 1.40 eV and a value of the angle  $\phi_{N_2}$  of  $125.0^\circ$ . At the same time, however, they have a single barrier along the minimum energy path, and the length of the  $N_1N_2$  and  $N_2N_3$  bonds at the barrier is the same. To emphasize this difference we show different calculation from [143] performed at total angular momentum  $J=0$  for a range of 153 total energies (from 1.2 eV, some tenths of eV below the barrier, up to 3.1 eV, about two times the barrier, with an energy step of 0.0125 eV). The maximum internal energy in any channel has been set to 3.5 eV.

Exact  $J = 0$  state specific quantum reactive probabilities were extracted from the scattering matrix for the first 7 ground-vibrational states of the reactant  $N_2$  molecule. Related plots as a function of the total energy are shown in figs. 4.14-4.20 (to derive similar information for  $E_{tr}$  one can use the information of table 4.3). At higher vibrational states ( $v = 1, 2, 3, 4, 5$  and 6) this picture is

$v$	$E_{int}^{LEPS}$ (eV)	$E_{int}^{L3}$ (eV)
0	0.14566	0.14565
1	0.43375	0.43371
2	0.71752	0.71746
3	0.99697	0.99689
4	1.27210	1.27200
5	1.54293	1.54280
6	1.80943	1.80928

Table 4.3: Energies of the first 7 ground-vibrational states of  $N_2$  for the LEPS PES (lhs column) and the L3 PES (rhs column).

confirmed (figs. 4.15-4.20). The calculations show, in fact, that the reactive efficiency of the LEPS is, in general, larger than that of the L3 PES only for a short just-past-the threshold interval of energy. On the contrary, after that interval the combination of a larger amount of both vibration and collision energy is effective in enhancing the L3 reactivity to the point of making it larger than the one calculated on the LEPS. This puts again on an accurate quantum ground the other traditional QCT finding that to the end of enhancing reactivity PESs having a bent transition state better exploit vibrational energy than those having a collinear transition state.

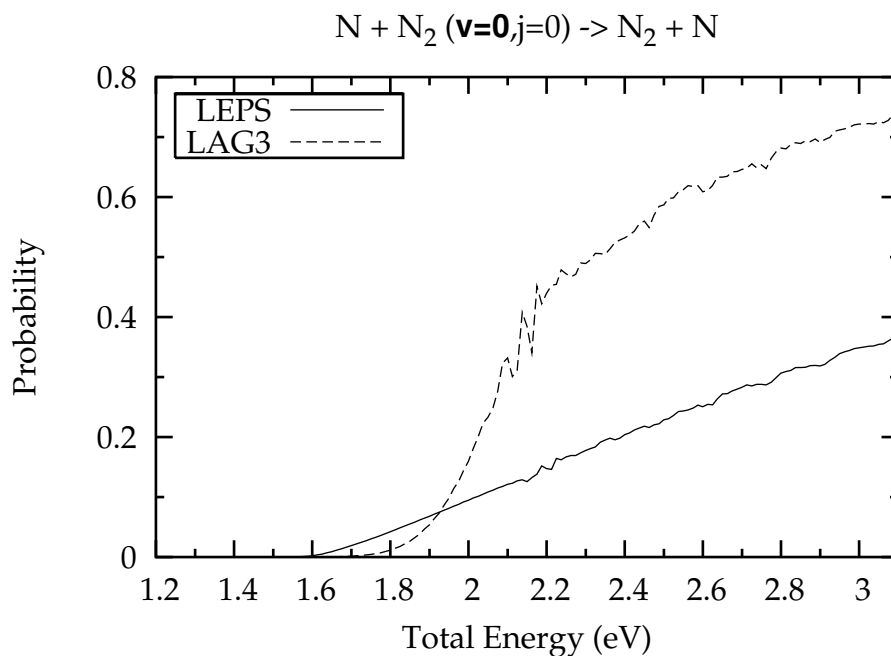


Figure 4.14: State specific reactive probabilities for  $v = 0$  at  $j = J = 0$  calculated on the LEPS (solid line) and the LAG3 (dashed line) PESs and plotted as a function of the total energy.

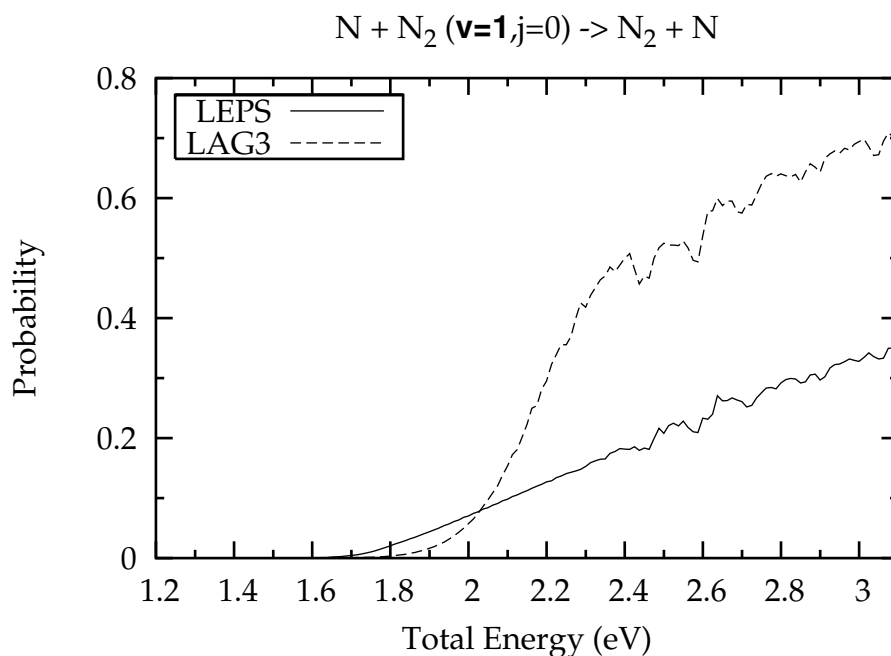


Figure 4.15: State specific reactive probabilities for  $v = 1$  at  $j = J = 0$  calculated on the LEPS (solid line) and the LAG3 (dashed line) PESs and plotted as a function of the total energy.

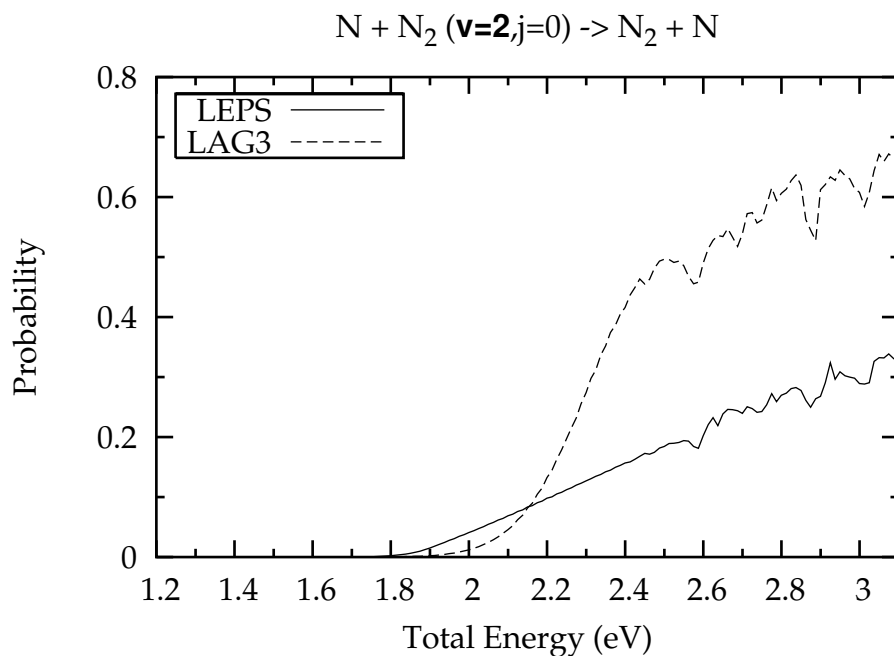


Figure 4.16: State specific reactive probabilities for  $v = 2$  at  $j = J = 0$  calculated on the LEPS (solid line) and the LAG3 (dashed line) PESs and plotted as a function of the total energy.

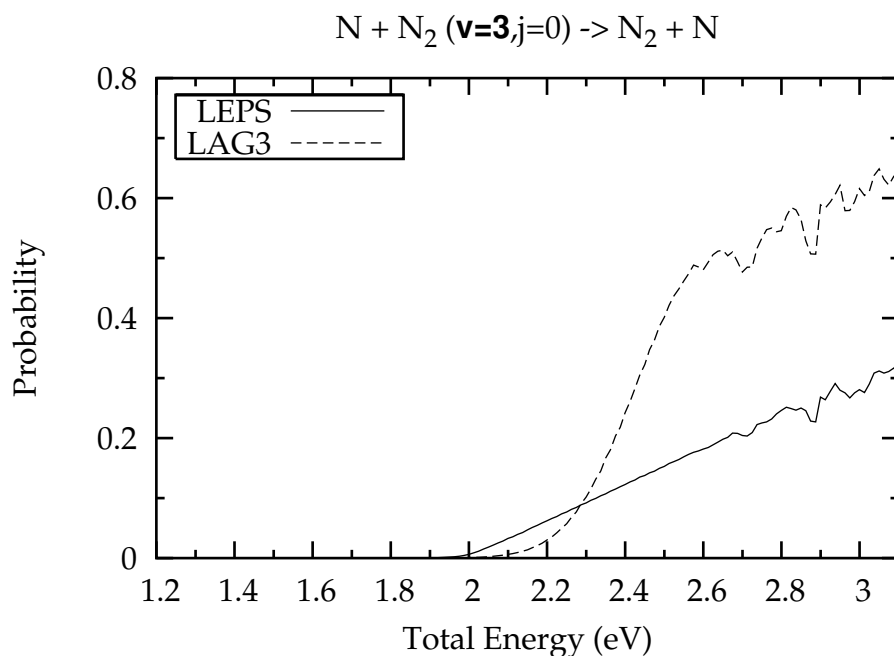


Figure 4.17: State specific reactive probabilities for  $v = 3$  at  $j = J = 0$  calculated on the LEPS (solid line) and the LAG3 (dashed line) PESs and plotted as a function of the total energy.

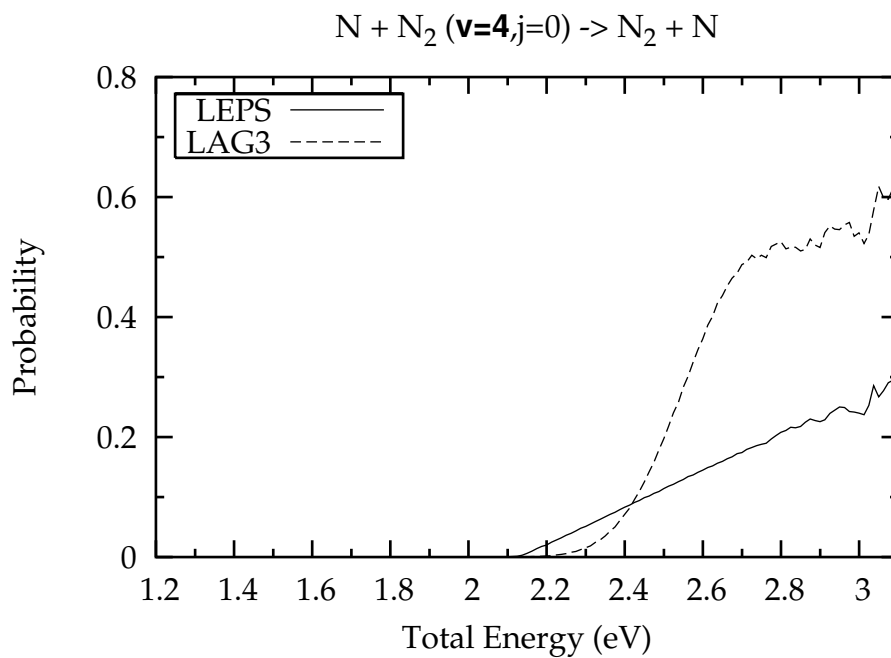


Figure 4.18: State specific reactive probabilities for  $v = 4$  at  $j = J = 0$  calculated on the LEPS (solid line) and the LAG3 (dashed line) PESs and plotted as a function of the total energy.

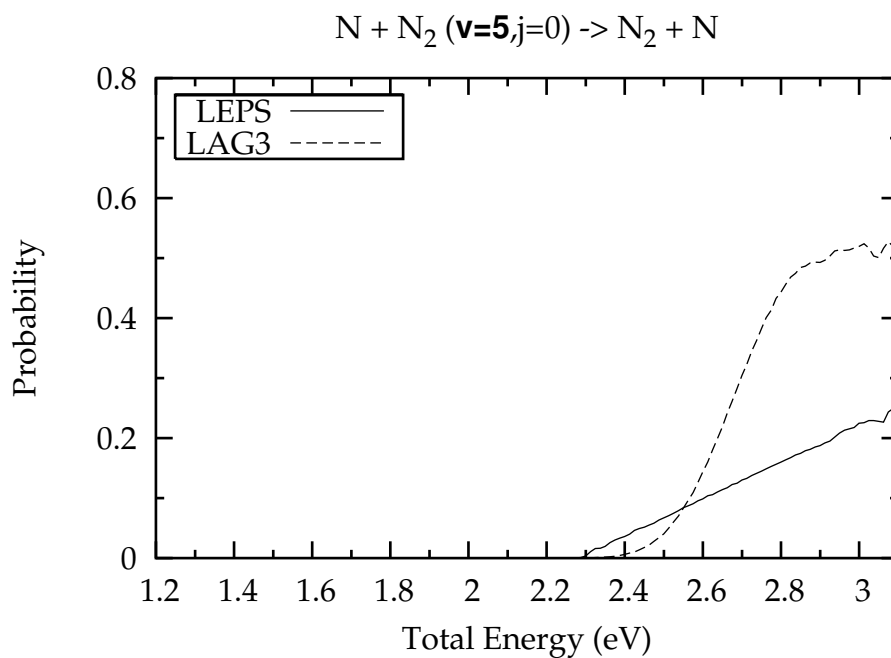


Figure 4.19: State specific reactive probabilities for  $v = 5$  at  $j = J = 0$  calculated on the LEPS (solid line) and the LAG3 (dashed line) PESs and plotted as a function of the total energy.

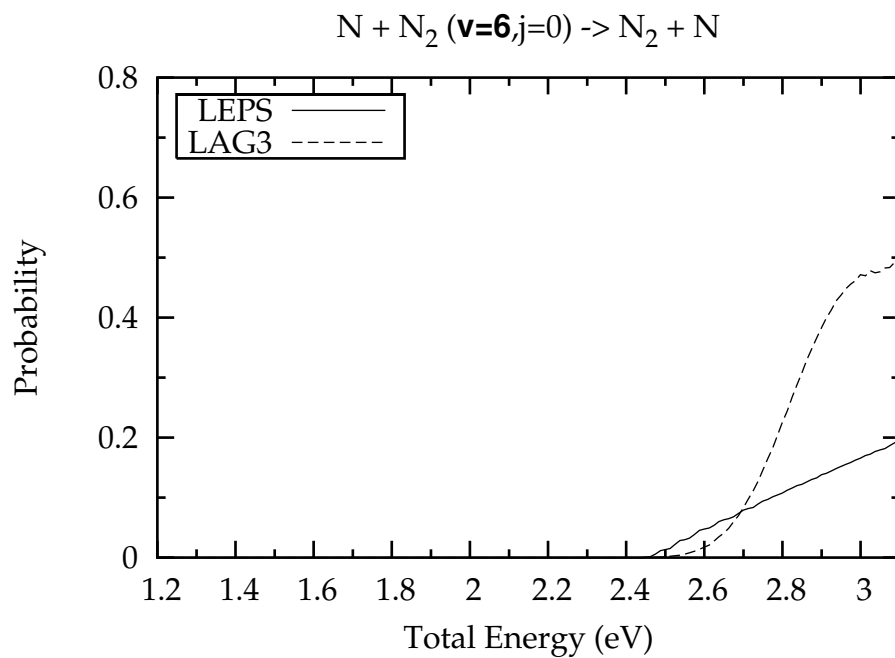


Figure 4.20: State specific reactive probabilities for  $v = 6$  at  $j = J = 0$  calculated on the LEPS (solid line) and the LAG3 (dashed line) PESs and plotted as a function of the total energy.

Interesting information about the dynamical behavior of the  $N + N_2$  system on the two potential energy surfaces considered here is also obtained by varying the rotational excitation of the reactant molecule. State specific reactive probabilities calculated for several rotational states at  $v = J = 0$  on the LEPS PES are shown in figures 4.21 and 4.22, on the L3 PES in figures 4.23 and 4.24 as a function of translational energy. As is apparent from the figure the threshold moves to lower relative collision energies as  $j$  increases with this effect being definitely more pronounced for the values calculated on the L3 PES. This shows that the already commented poor exploitation of the relative collision energy near the threshold to enhance reactivity on L3 at  $v = 0$  is largely compensated by an efficient exploitation of the rotational energy of the target in contrast with what happens on the LEPS PES. The lowering of the threshold with  $j$  is also accompanied by a simultaneous increase of the reactive probability on L3. Such an increase is dramatic at low  $j$  values on L3 while no such effect is found on the LEPS PES. This is, indeed, a distinctive feature of the L3 PES. The L3 PES, in fact, effectively leverages on the extra rotational energy of the low excited rotational states of the reactants to fill the reactivity gap associated with an inefficient use of  $E_{tr}$  at  $j = 0$  and overtake the saddle.

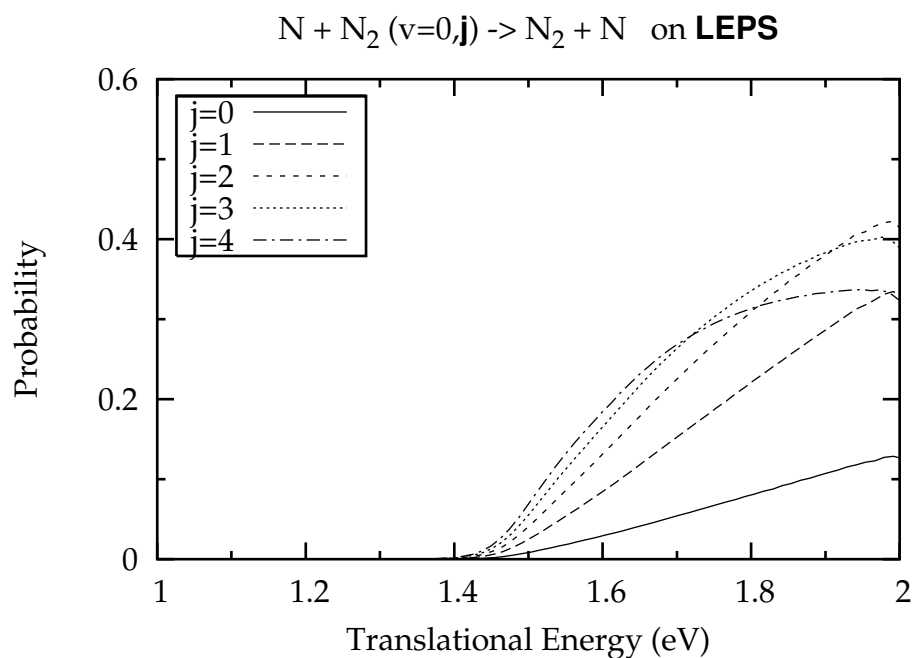


Figure 4.21: State specific reactive probabilities for  $j = 0, 1, 2, 3, 4$  at  $v = J = 0$  calculated on the LEPS PES and plotted as a function of the translational energy.

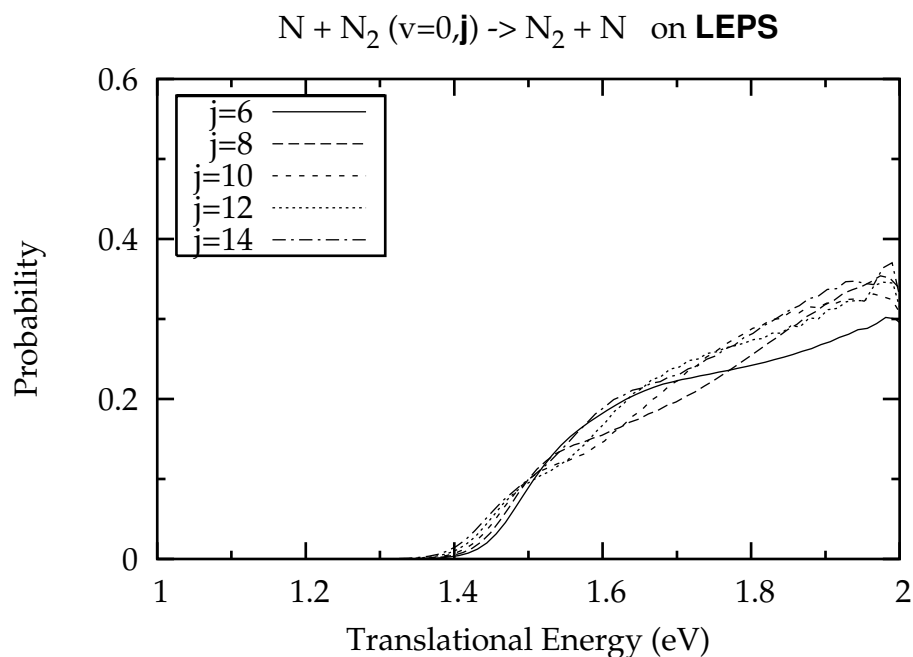


Figure 4.22: State specific reactive probabilities for  $j = 6, 8, 10, 12, 14$  at  $v = J = 0$  calculated on the LEPS PES and plotted as a function of the translational energy.

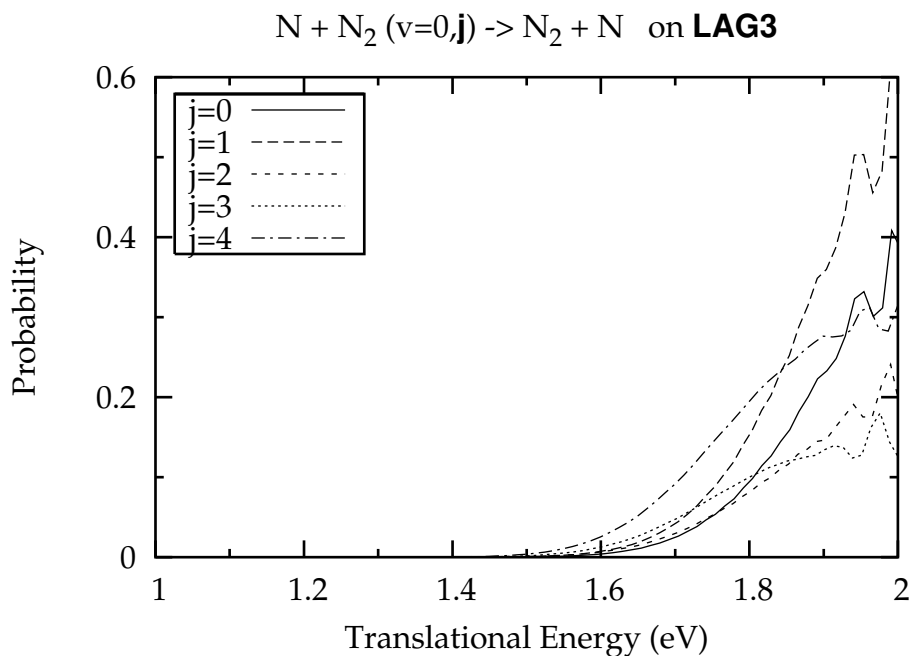


Figure 4.23: State specific reactive probabilities for  $j = 0, 1, 2, 3, 4$  at  $v = J = 0$  calculated on the LAG3 PES and plotted as a function of the translational energy.

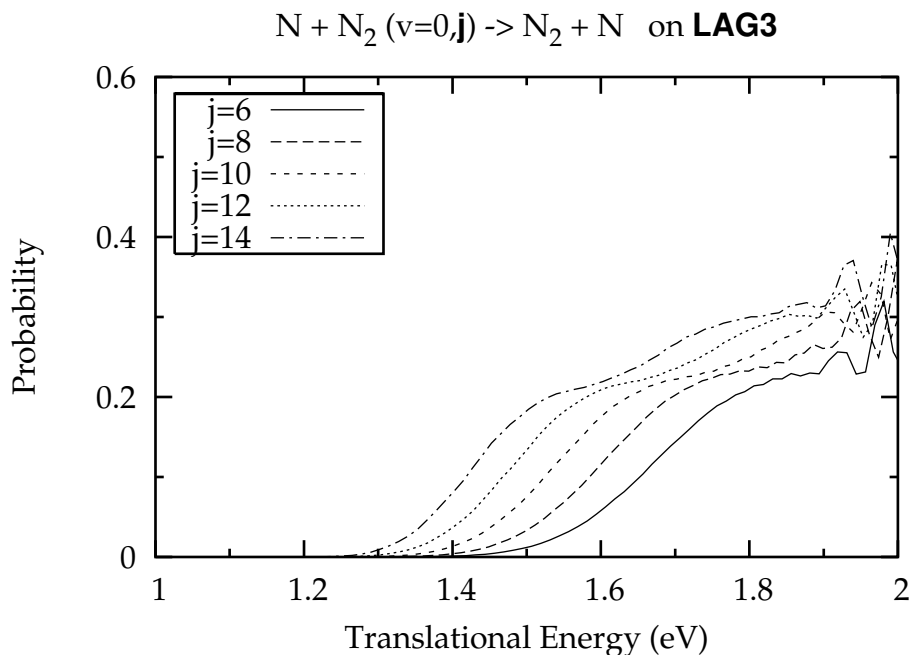


Figure 4.24: State specific reactive probabilities for  $j = 6, 8, 10, 12, 14$  at  $v = J = 0$  calculated on the LAG3 PES and plotted as a function of the translational energy.

### 4.3.3 The new LAGROBO PES L4 and related results

The L4 PES for the N + N<sub>2</sub> exchange reaction is based on the fitting of *ab initio* calculations carried out using an open shell CCSD(T)/aug-cc-pVTZ method, as implemented in the MOLPRO code [144]. Three sets of calculations have been performed.

The first set of calculations has been carried out to obtain a good description of the transition state. Unconstrained geometry optimization and harmonic frequency analysis have been performed to confirm the existence of a double barrier connected by a shallow well. Geometries (two bond distances,  $r_1$  and  $r_2$ , and the bond angle between them,  $\phi$ ) and energies obtained for both the transition states and the shallow well are shown in Table 4.4. The obtained values agree with the ones obtained in ref. [130]. Aim of the second type of *ab initio* calculations has been the description of the dependence on the bond angle  $\Phi$  of both the geometry and the energy of the well placed between the double barrier structure. In the calculations the bond angle  $\Phi$  has been fixed and then a geometry optimization (with  $r_1=r_2$ ) has been carried out. The explored range of angles varied from 180° to 85° ( $\phi_{N_2} = 116.8^\circ$ ). Figures 4.25 and 4.26 show the dependence on  $\Phi$  of the energy and of the location on  $\rho$  ( $\rho$  is the BO coordinate defined in eq. 4.16 as  $\rho = \sqrt{n_1^2 + n_2^2}$  where  $n_i = \exp[-\beta(r_i - r_{ei})]$  while the other polar BO coordinate is defined as  $\alpha = \arctan(n_2/n_1)$ ) of the well obtained in the *ab initio* calculations. The minimum of the energy is located at  $\Phi=118.6^\circ$ . The harmonic frequency analysis confirms that the optimized geometry is a well (a minimum) for  $\Phi$  ranging from 150° to 90°. Outside this range the optimized configuration corresponds to a saddle and, therefore, there is a single barrier between reactants and products.

Aim of the third set of *ab initio* calculations is the characterization of the MEPs at several bond angles  $\Phi$ . In the calculations, the angle  $\Phi$  and one of the internuclear distances have been fixed and then an optimization of the other internuclear distance has been carried out in order to minimize the energy. Figure 4.27 shows the energy profile of the fixed  $\Phi$  MEPs as a function of the BO polar angular coordinate  $\alpha$  (defined in eq. 4.17) from the reactants ( $\alpha=0^\circ$ ) to products ( $\alpha=90^\circ$ ). Note that the values at  $\alpha=45^\circ$ , where the two BO coordinates are equal,  $n_1=n_2$  (or equivalently to  $r_1=r_2$ ), are

Table 4.4: Geometry and energy (relative to reactants) for the well and the two transition states.

	$r_1 / \text{\AA}$	$r_2 / \text{\AA}$	$\Phi$	$\Delta E / \text{eV}$
Well	1.268	1.268	118.6°	1.93
Transition state A	1.174	1.505	116.5°	2.04
Transition state B	1.505	1.174	116.5°	2.04

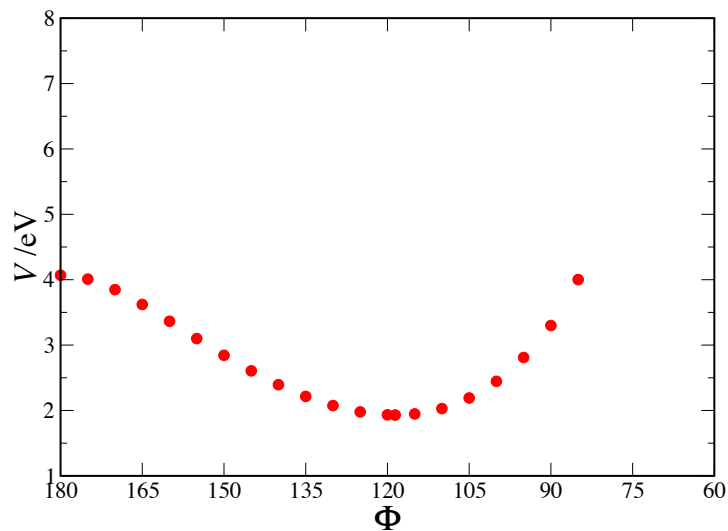


Figure 4.25: Ab initio optimized energy (relative to reactants) at the system geometry  $r_1=r_2$  plotted as a function of the bond angle  $\Phi$ .

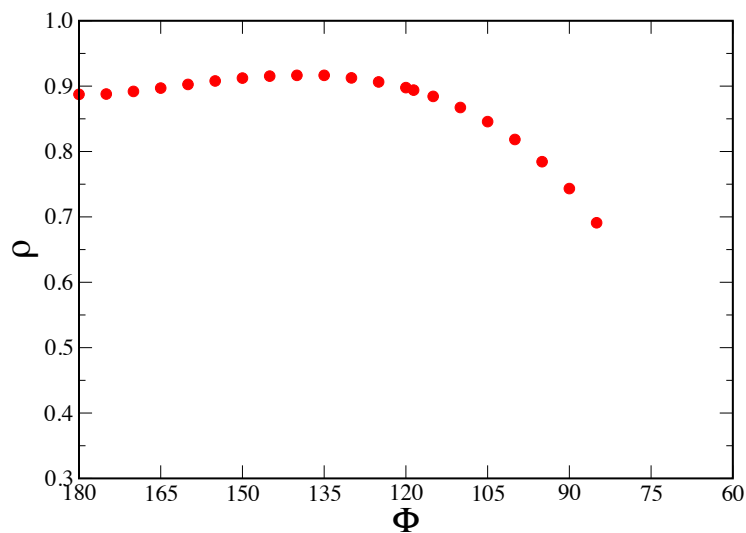


Figure 4.26: Value of  $\rho$  at the *ab initio* optimized system geometry  $r_1=r_2$  plotted as a function of the bond angle  $\Phi$ .

those plotted in Figure 4.25. As shown by the Figure, the double barrier structure (and the associated well) disappear at  $\Phi=180^\circ$ . On the other hand, Figure 4.28 shows the location on  $\rho$  of the fixed  $\Phi$  MEPs as a function of  $\alpha$ . In this case, a double peak also appears for several angles  $\Phi$ .

This study brings to a functional form with a bent transition state and an energy of about 2 eV sandwiched by two barriers (associated with an asymmetric  $N_1N_2N_3$  geometry, that is  $r_{N_1N_2} \neq r_{N_2N_3}$ ) symmetrically displaced in the entrance and exit channels.

Exact  $J = j = 0$  state specific quantum reactive probabilities were built out of the scattering matrix for the first 10 vibrational states of the reactant  $N_2$  molecule. The curves of the first 6 vibrational levels are plotted as a function of the reduced<sup>2</sup> total energy in figs. 4.29-4.34 (the internal energies of the considered levels are the same as those in the column L3 of table 4.3 at p. 117). Except for the position in the energy scale (for this reason the reduced total energy was adopted for the abscissa), the curves show clear similarities with those calculated on the L3 PES.

As to the differences (apart from the obvious larger threshold energy) L4 shows a clear regular oscillatory structure in the  $v = 0, j = 0$  plot of fig 4.29. These oscillations (as shown from fig. 4.37, as we shall discuss later) are mainly associated with the transitions from the ground reactant state to the lowest product vibrational states. In fact, not only the  $(v = 0, j = 0) \rightarrow (v' = 0, \text{all } j)$  transition probability shows the regular structure but also those to larger  $v'$  values despite their lower intensity. The distance between two neighbour peaks (about 0.075 eV) is a clear fingerprint of its origin. In fact, such a spacing corresponds to the spacing of the quasibound states supported by the well. A detailed study carried out by the authors of refs. [145, 146] on their WSHDSP surface has shown that the  $(v = 0, j = 0)$  state specific probabilities curve present resonances at total energies that correspond with the energy of quasibound bending modes supported by the potential well in the “Eyring Lake” region. The spacing between such bending modes in the WSHDSP PES (which is very similar to L4) is about 0.075 eV. Some shoulders are also observed at energies that correspond to combined bending and stretching modes. Such shoulders are clearly visible in fig. 4.37 of our calculation too. The dominance of bending resonances, however, is not surprising. The bond angles of the well minimum and of the barrier are very close, despite the bond distances are different. Stretching motions take the wavefunctions out of the exchange region into final products, whereas bending motions are more likely to keep the wavefunctions in the Eyring Lake region, resulting in a longer lifetime.

---

<sup>2</sup>The reduced total energy is obtained by dividing total energy by the energy of the barrier to reaction.

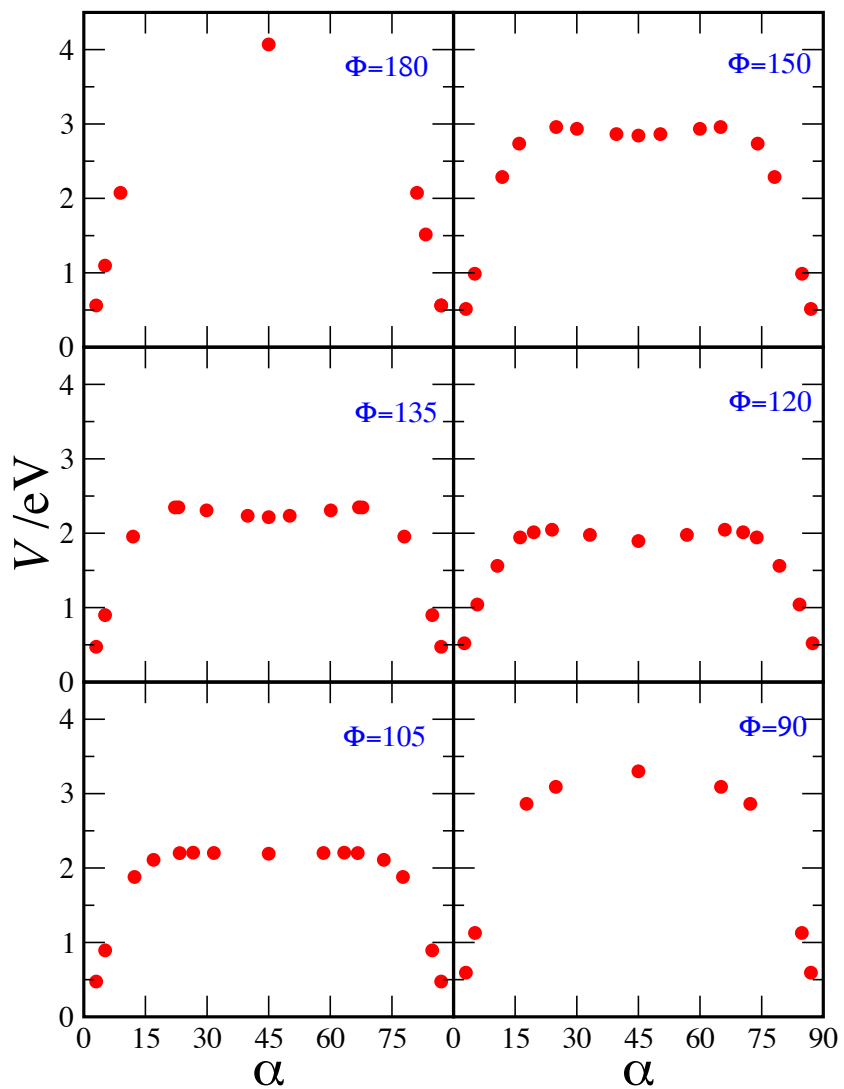


Figure 4.27: Ab initio energy (relative to reactants) of the fixed  $\Phi$  MEPs plotted as a function of the BO polar coordinate  $\alpha$ .

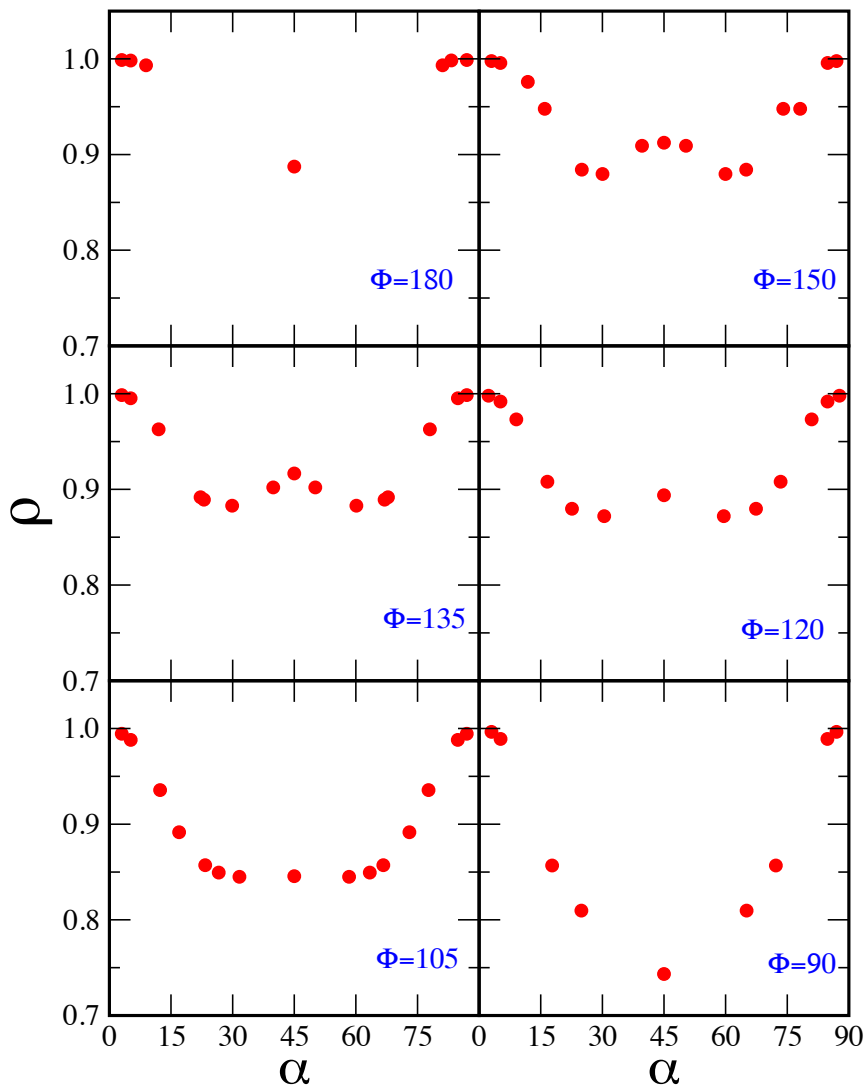


Figure 4.28: Ab initio location on  $\rho$  of the fixed  $\Phi$  MEPs plotted as a function of the BO polar coordinate  $\alpha$ .

It is important, however, to point out that a similar (though less clear) effect was found in state specific probabilities calculated on L3. In L3 probabilities (see fig. 4.29), in fact, there are three peaks which correspond to a great extent to three maxima of the L4 curve. Such an effect can only be due to dynamical trapping that is the trapping in the saddle well. The most important consequence of the trapping is a strong deexcitation effect. The deexcitation effect associated with potential wells (both in the entrance and in the exit channel) is extensively discussed in the literature. Scarce literature is instead available for cases, like the present one, in which the well sits on top of the saddle to reaction.

The analysis of the adiabaticity (solid line), deexcitation (dashed line) and excitation (dashed-dotted line) fractions can be performed with the help of the lower panel of figs. 4.37-4.41. The plots point out, in fact, strong deexcitation effects. As a matter of fact, figures 4.38-4.41 show that already at  $v = 1$  deexcitation is the dominant process. Starting from this state on, there is a region of about 1 eV past the threshold in which deexcitation is more than 50 %, that makes L4 results definitely differ from L3 ones.

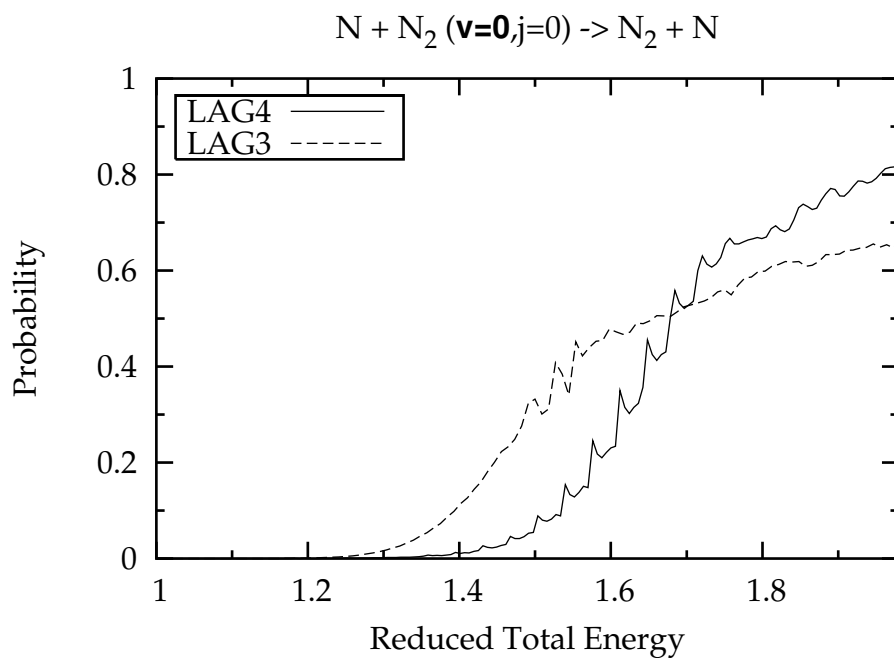


Figure 4.29: State specific reactive probabilities for  $v = 0$  at  $j = J = 0$  calculated on the LAG4 and the LAG3 PESs and plotted as a function of  $E_{\text{tot}}/E_{\text{bar}}$ .

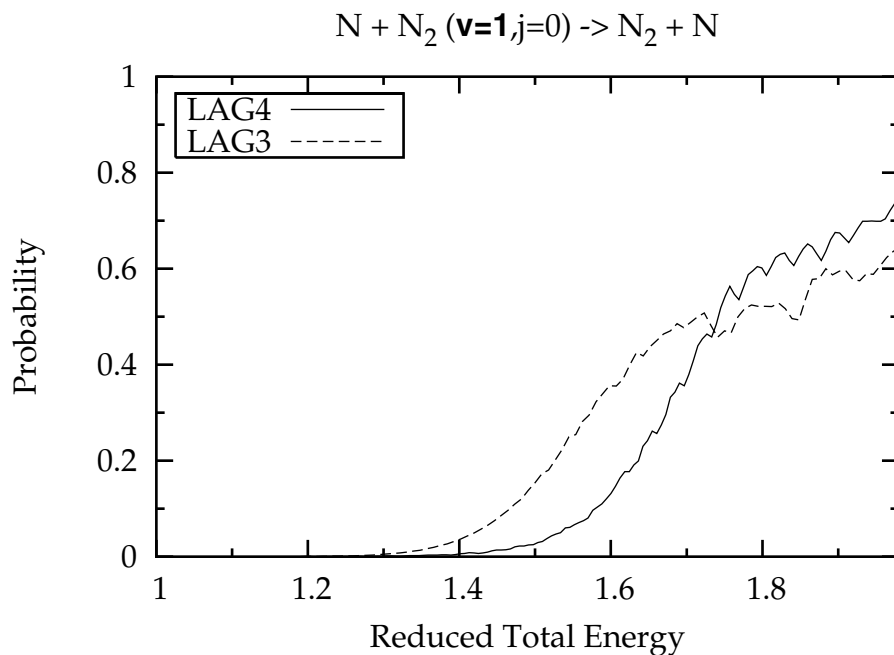


Figure 4.30: State specific reactive probabilities for  $v = 1$  at  $j = J = 0$  calculated on the LAG4 and the LAG3 PESs and plotted as a function of  $E_{\text{tot}}/E_{\text{bar}}$ .

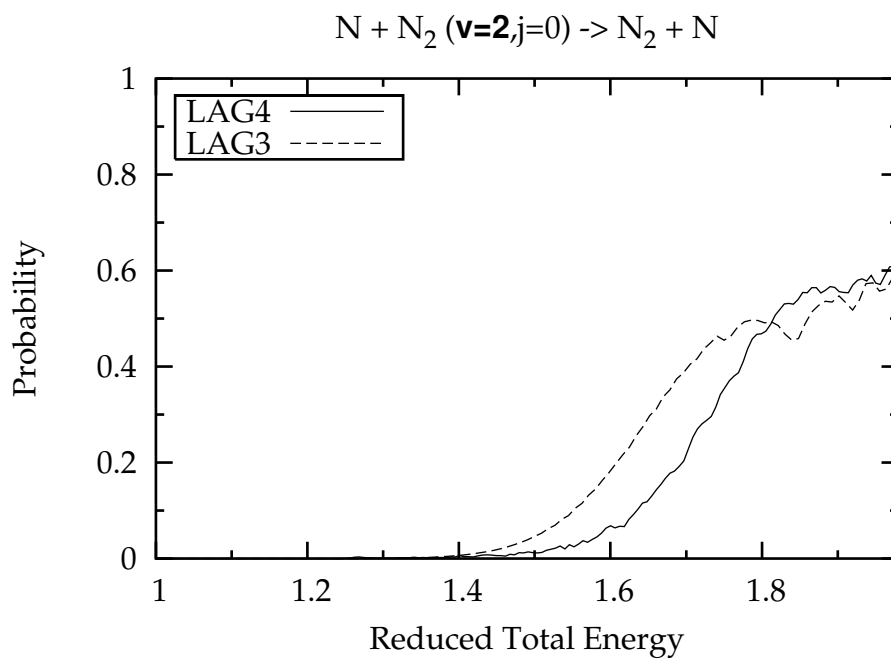


Figure 4.31: State specific reactive probabilities for  $v = 2$  at  $j = J = 0$  calculated on the LAG4 and the LAG3 PESs and plotted as a function of  $E_{tot}/E_{bar}$ .

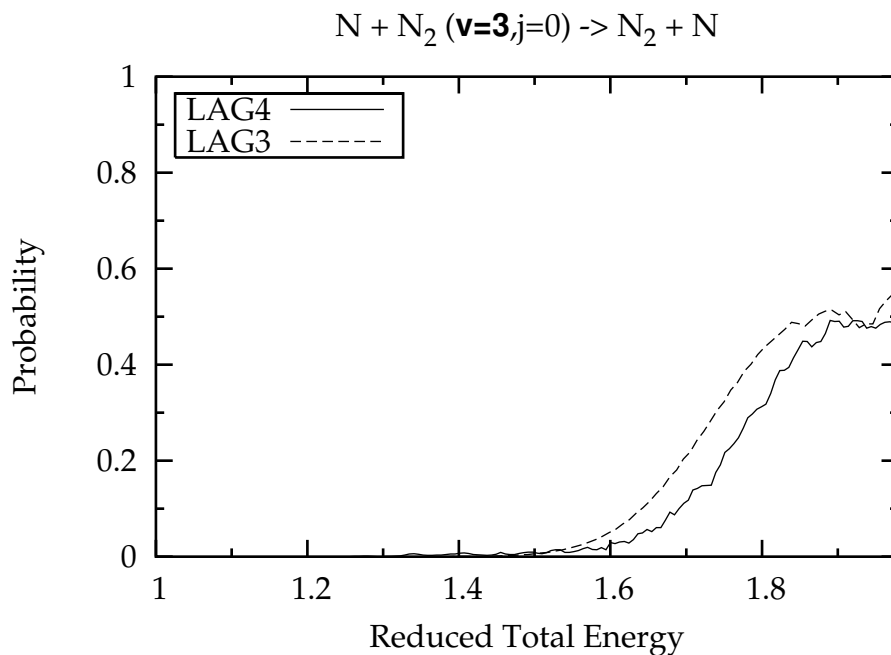


Figure 4.32: State specific reactive probabilities for  $v = 3$  at  $j = J = 0$  calculated on the LAG4 and the LAG3 PESs and plotted as a function of  $E_{tot}/E_{bar}$ .

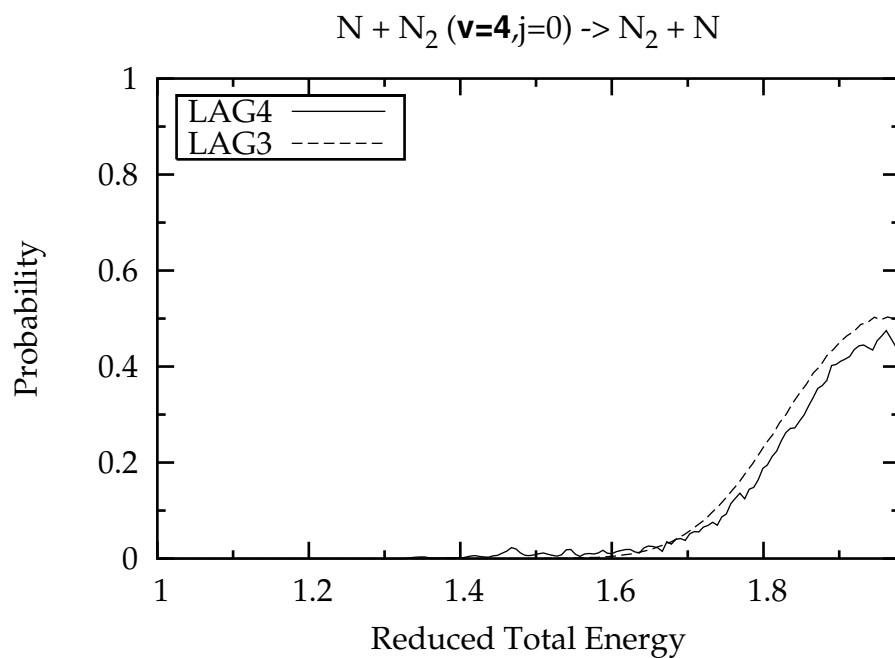


Figure 4.33: State specific reactive probabilities for  $v = 4$  at  $j = J = 0$  calculated on the LAG4 and the LAG3 PESs and plotted as a function of  $E_{\text{tot}}/E_{\text{bar}}$ .

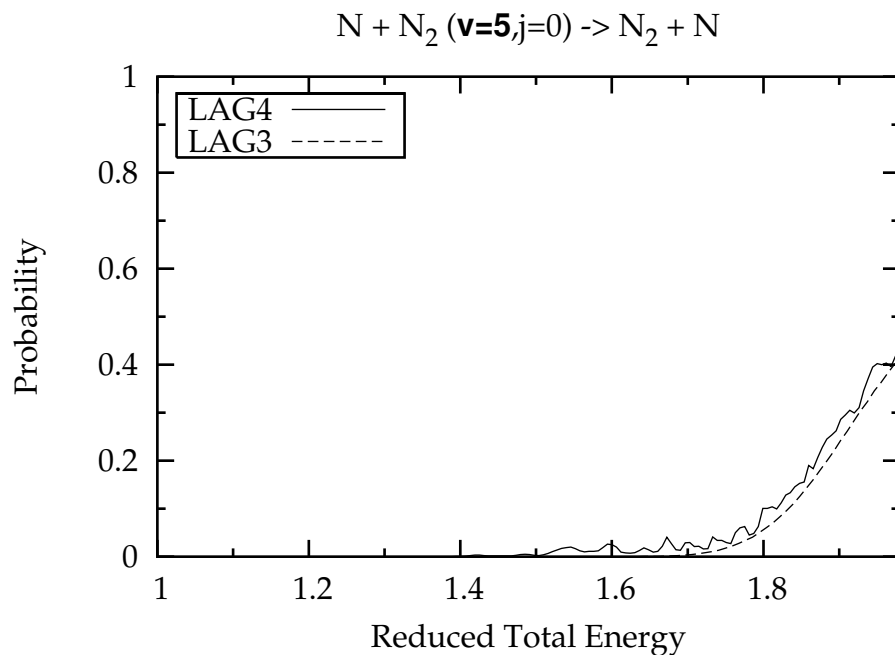


Figure 4.34: State specific reactive probabilities for  $v = 5$  at  $j = J = 0$  calculated on the LAG4 and the LAG3 PESs and plotted as a function of  $E_{\text{tot}}/E_{\text{bar}}$ .

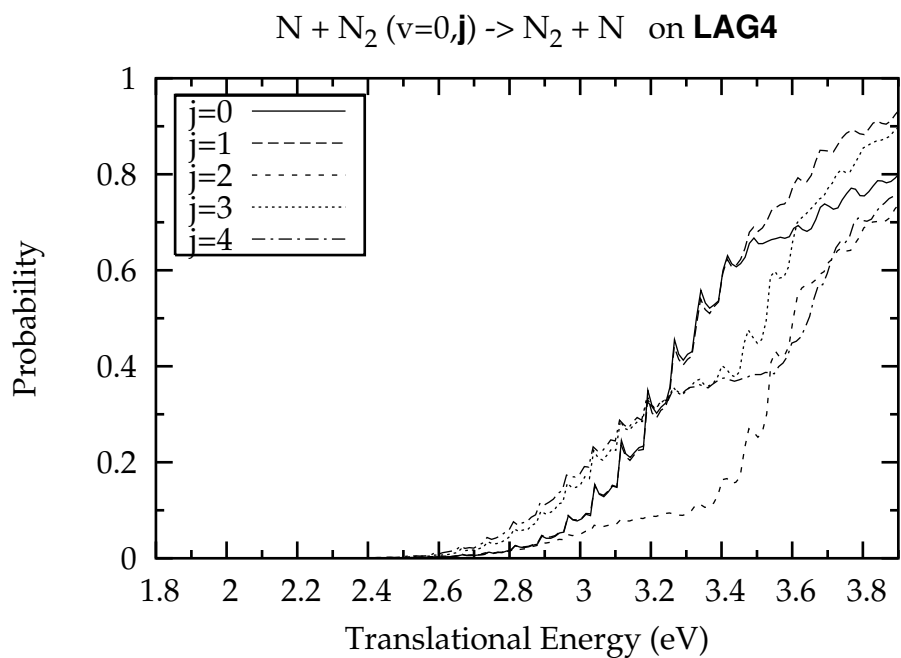


Figure 4.35: State specific reactive probabilities for  $j = 0, 1, 2, 3, 4$  at  $v = J = 0$  calculated on the LAG4 PES and plotted as a function of the translational energy. Please compare with figures 4.21 and 4.23.

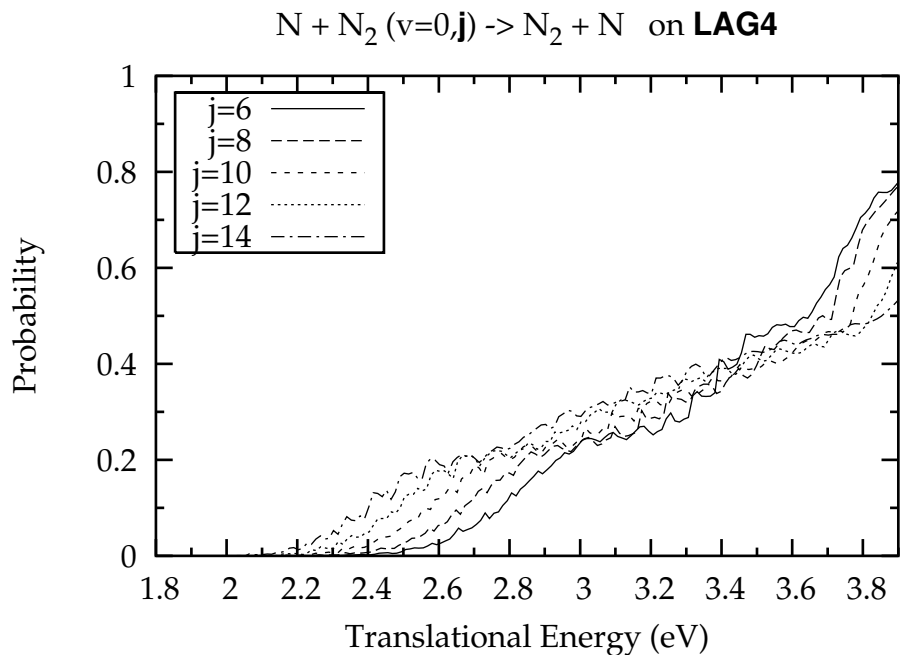


Figure 4.36: State specific reactive probabilities for  $j = 6, 8, 10, 12, 14$  at  $v = J = 0$  calculated on the LAG4 PES and plotted as a function of the translational energy. Please compare with figures 4.22 and 4.24.

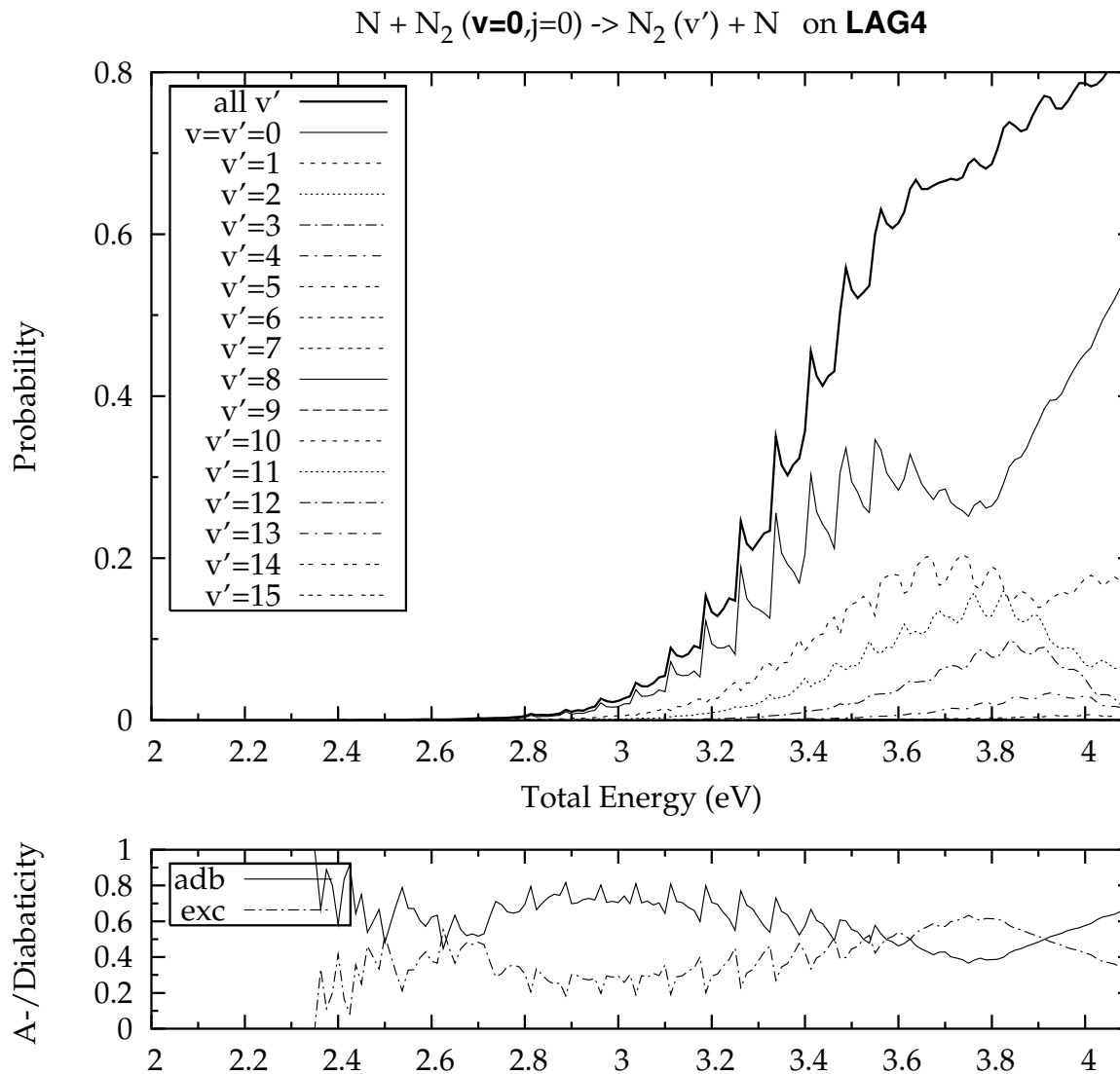


Figure 4.37: State to state and state specific (bold line) reactive probabilities for  $v = 0$  at  $j = J = 0$  calculated on the LAG4 PES and plotted as a function of the total energy in the upper panel. Related adiabaticity and excitation probabilities are plotted as a function of total energy in the lower panel.

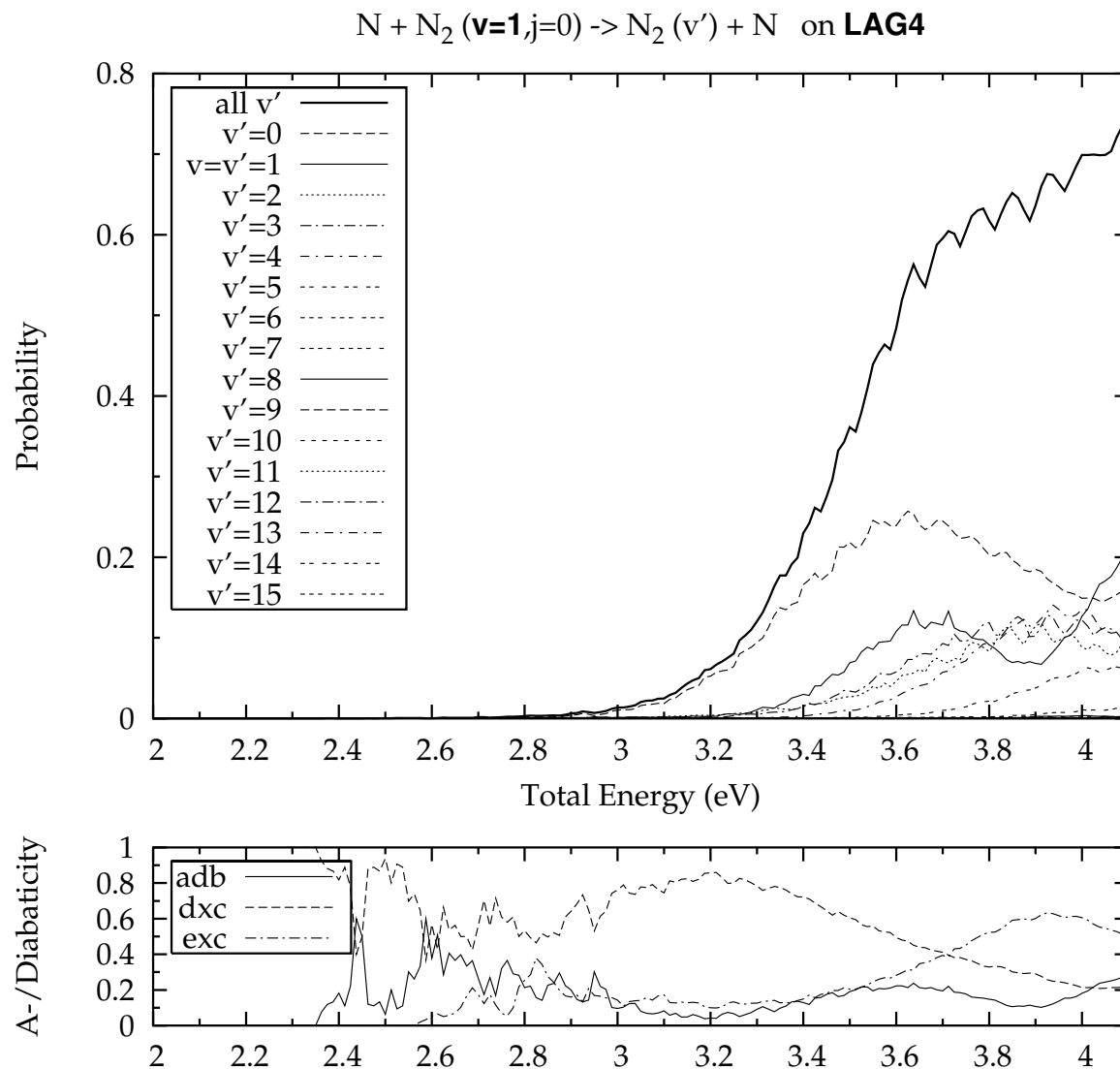


Figure 4.38: State to state and state specific (bold line) reactive probabilities for  $v = 1$  at  $j = J = 0$  calculated on the LAG4 PES and plotted as a function of the total energy in the upper panel. Related adiabaticity, deexcitation and excitation probabilities are plotted as a function of total energy in the lower panel.

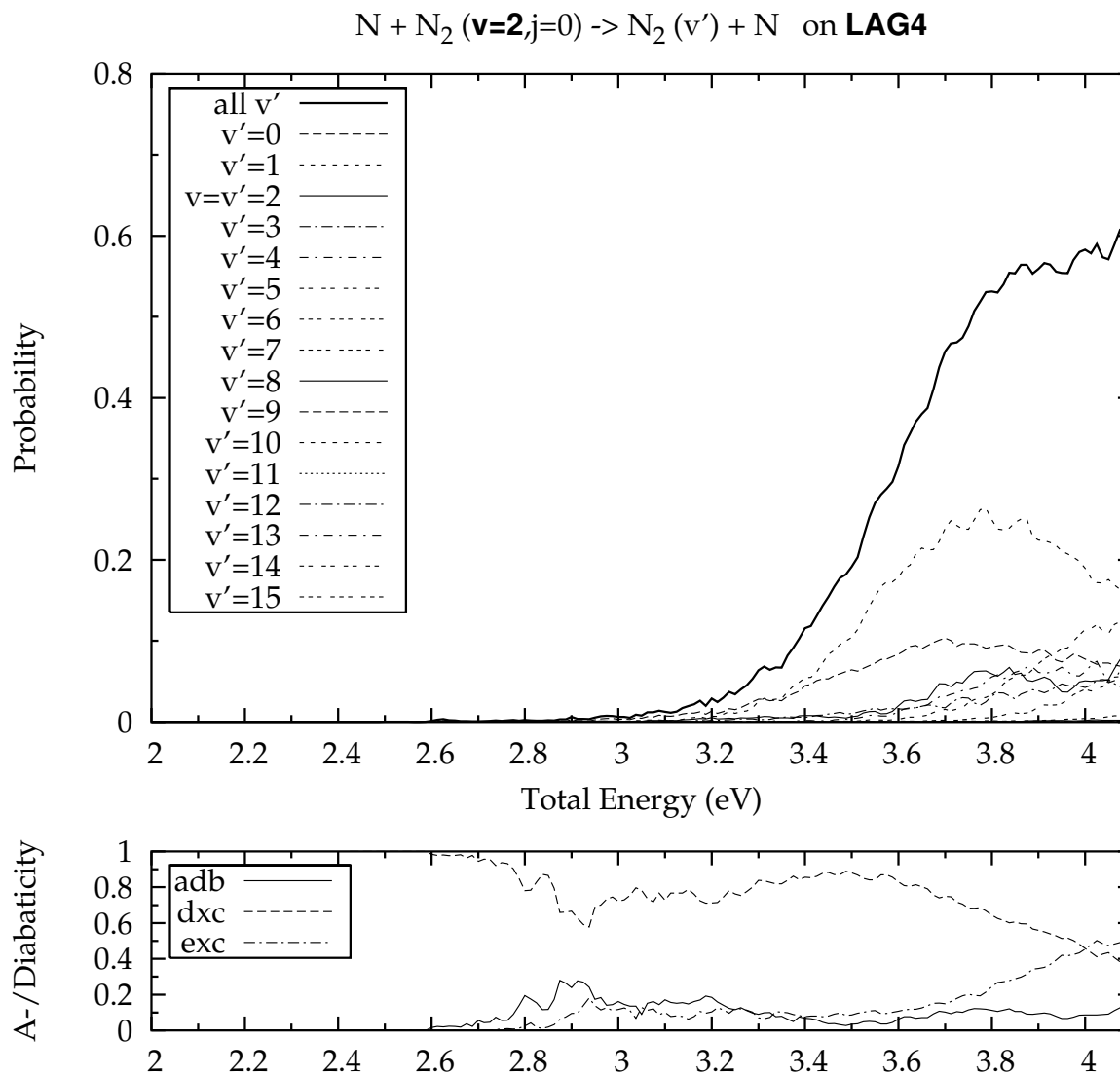


Figure 4.39: State to state and state specific (bold line) reactive probabilities for  $v = 2$  at  $j = J = 0$  calculated on the LAG4 PES and plotted as a function of the total energy in the upper panel. Related adiabaticity, deexcitation and excitation probabilities are plotted as a function of total energy in the lower panel.

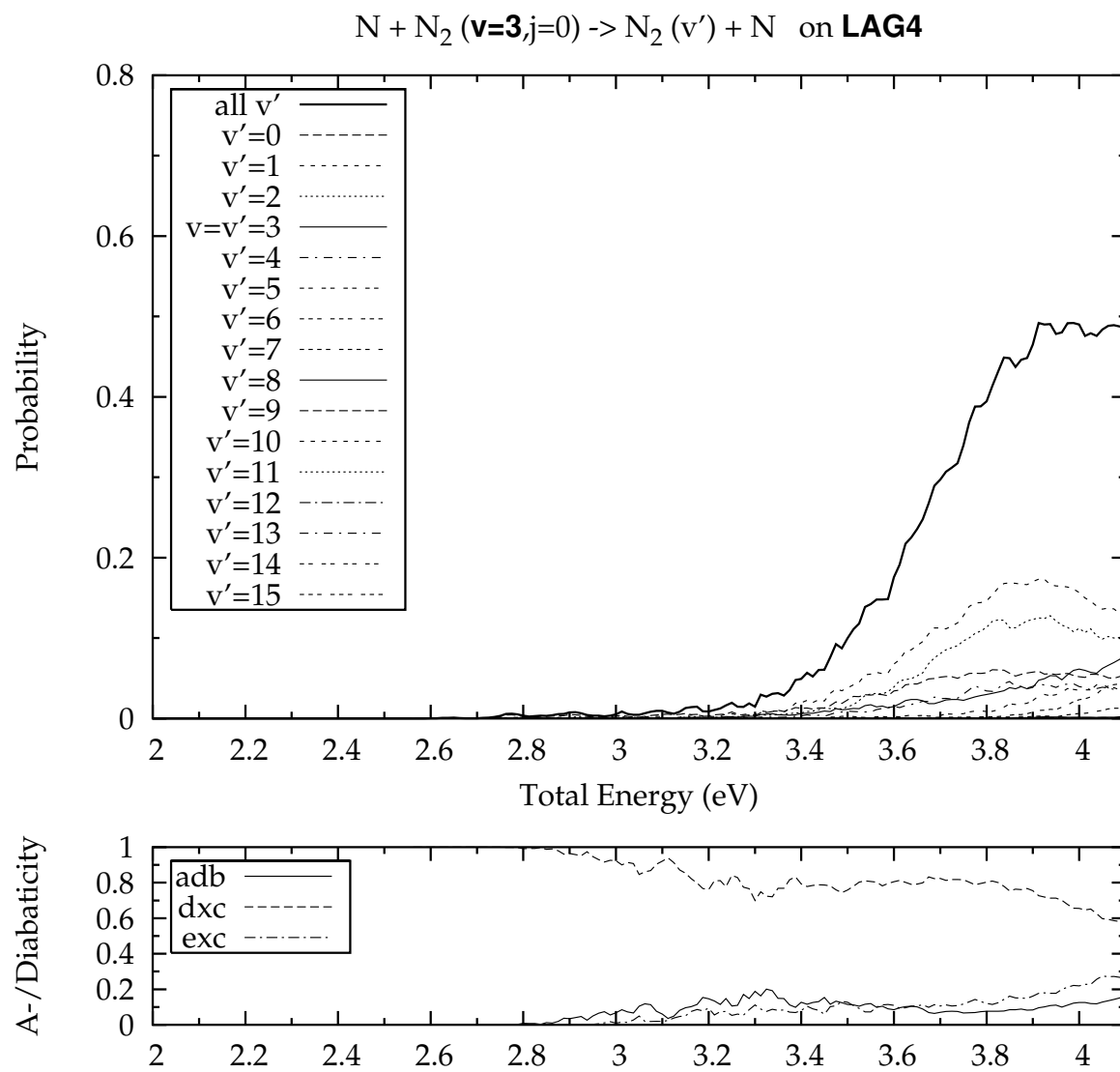


Figure 4.40: State to state and state specific (bold line) reactive probabilities for  $v = 3$  at  $j = J = 0$  calculated on the LAG4 PES and plotted as a function of the total energy in the upper panel. Related adiabaticity, deexcitation and excitation probabilities are plotted as a function of total energy in the lower panel.

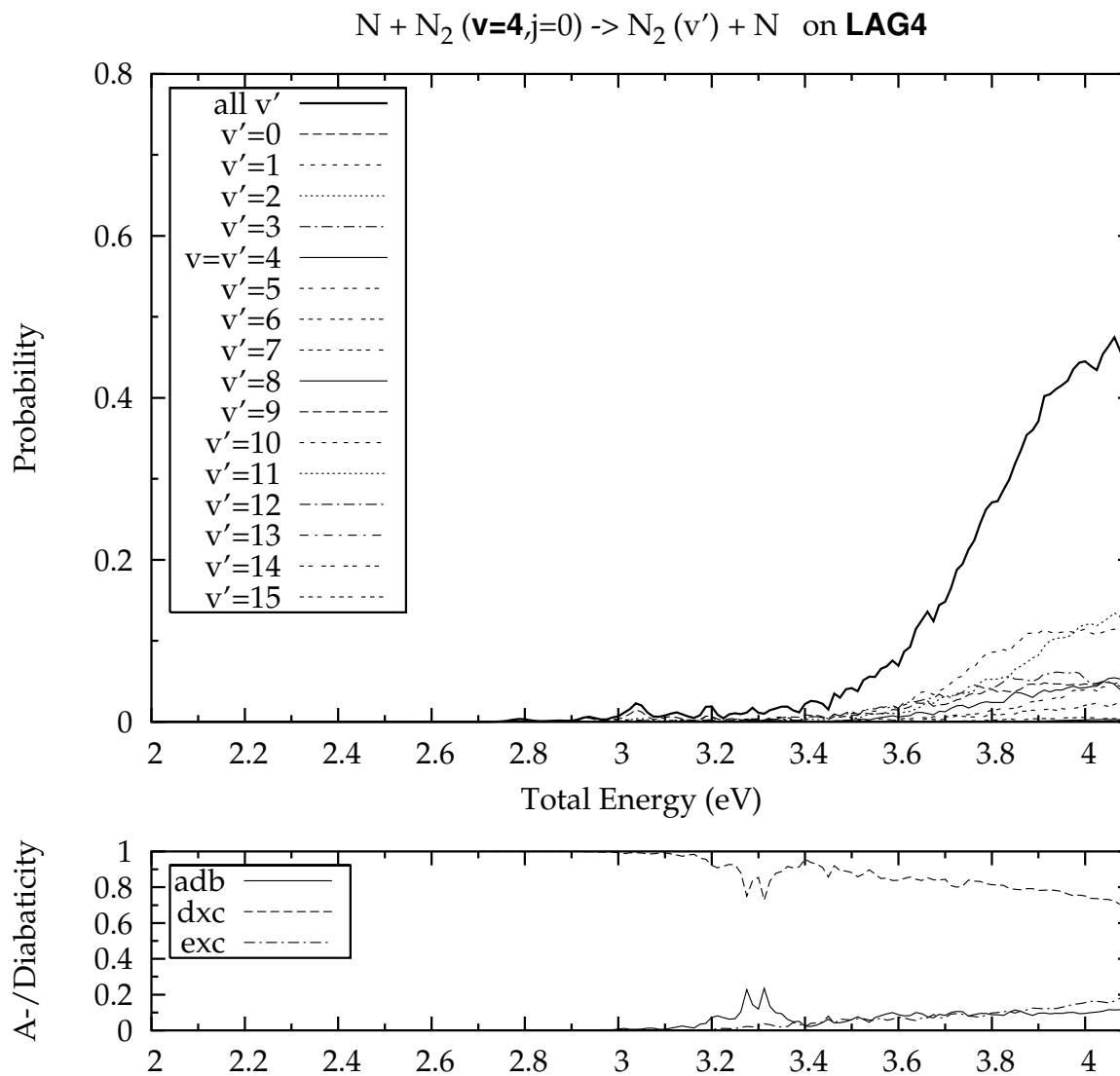


Figure 4.41: State to state and state specific (bold line) reactive probabilities for  $v = 4$  at  $j = J = 0$  calculated on the LAG4 PES and plotted as a function of the total energy (upper panel). Related adiabaticity, deexcitation and excitation probabilities are plotted as a function of total energy in the lower panel.

#### 4.4 The $N_2(^1\Sigma_g^+) + N_2(^1\Sigma_g^+)$ reaction

Chemical reactions of nitrogen molecules are the natural complement to the corresponding atom molecule ones in a variety of high temperature environments, such as shock tube experiments, meteor entry and spacecraft reentering into atmosphere.

In shock tube experiments, at first, the activation of nitrogen molecules was difficult to rationalize. At first, the idea that the reactivity shown by a gaseous mixture containing molecular nitrogen under electrical discharge could be attributed to  $N_2$  was difficult to accept because of its high inactivity. From this and similar experiments performed using various mixtures of hydrocarbons (which, in presence of nitrogen, form cyanidric acid) the assumption was made that some type of *active nitrogen* [147] would intervene.

Nitrogen molecules encounters play also a key role in modelling air composition both under equilibrium [148] and non-equilibrium [149] conditions, like the ones occurring around reentering spacecrafts due to the fact that, as it was already mentioned, nitrogen is the major constituent of some planetary atmospheres. A list of intervening molecule + molecule collision processes are given in

Reaction	Process
$N + N_2(v) \rightarrow N + N_2(v')$	Inelastic
$N + N_2(v) \rightarrow N + N_2(v')$	Reactive
$N + N_2(v) \rightarrow N + N + N$	Dissociation
$N + N \rightarrow N_2$	Recombination
$N_2(w) + N_2(v) \rightarrow N_2(w) + N_2(v')$	Inelastic
$N_2(w) + N_2(v) \rightarrow N_2(w') + N_2(v')$	Inelastic
$N_2(w) + N_2(v) \rightarrow N_2(w') + N_2(v')$	Reactive
$N_2(w) + N_2(v) \rightarrow N + N + N_2(v')$	Dissociation
$N_2(w) + N + N \rightarrow N_2(w') + N_2(v')$	Recombination

Table 4.5: Main high temperature processes involving nitrogen.

table 4.5 together with the corresponding atom diatom ones. In my thesis work the attention was focused on preliminary calculations of the *ab initio* (adiabatic) ground electronic potential energy values of the  $N_2 + N_2$  system. The aim was the tuning of the generation of *ab initio* values for the applications of the Q5cost model to four atom system.

#### 4.4.1 Previous work on $N_2 + N_2$

The first theoretical potential energy surface for the ground state of the system  $N_2-N_2$  (BvdA) was published in 1980 by Berns and A. van der Avoird [150]. In the following years van der Avoird et al. [151] produced a new PES (AWJ) using new *ab initio* calculations for the multipole and short range interaction combined with the theoretical long range electrostatic and dispersion interaction. This potential has been scaled using two adjustable parameters to represent the second virial coefficient within the experimental uncertainties. Despite the fact that AWJ potential can describe most of the macroscopic properties successfully [152,153], it is limited by the fact of using different approximations to treat the various regions of the PES. Moreover, it cannot reproduce consistently all the structural features of the  $N_2 + N_2$  interaction [154].

Other theoretical full *ab initio*  $N_2-N_2$  potentials were developed in the last ten years [155–160]. The improvement of these potentials over the BvdA and the AWJ ones is the uniform description of the interaction in all regions of the arrangement space providing reliable structural information and reasonable results on different physical contributions to the interaction energy. The first complete full *ab initio* PES was developed by Stallcop and Partridge [155]. It was based on CCSD(T) calculations combined with the values of the second virial coefficient to determine the interaction in the van der Waals region. On the same way, Wada et al. [156] investigated the structural features and the PES of  $N_2$  dimer by focusing their attention on the possibility of the in-plan gear-like motion of  $N_2$  dimers and the relative stability of some conformations. However, due to an incomplete correction of the BSSE, they did not obtain an analytical representation of *ab initio* results.

In 2002 Leonhard and Deiters [158] reported a full *ab initio* pair potential for nitrogen calculated at the CCSD(T) level of theory with two different basis sets. Extrapolated results to complete basis set limit (CBS) have been used to fit a five site model potential that was later used in Monte-Carlo simulations of thermodynamical properties of nitrogen. A new four-dimensional *ab initio* potential energy surface was proposed by Karimi et al. in 2005 [159]. They performed massive *ab initio* calculations for several geometries of the  $N_2$  dimer with a fixed internuclear bond length using the supermolecular Møller-Plesset perturbation theory up to second order (MP2) [161].

In the last year Gomez et al. built a new global fit of the ground state potential energy values for the van der Waals dimer using perturbative and supermolecular methods [160]. To characterize the potential of such system, they have used the well suited symmetry adapted perturbation theory (SAPT) method to generate the *ab initio* energies on the whole grid. The analytical expression used

in the fitting procedure implies the calculation of monomer multipole moments, as well as that of the long-range dispersion and induction coefficients. This last work can be considered as the best study available up to date for a fully *ab initio* PES for the ground state of the  $N_2$ - $N_2$  system.

On the experimental the available information on  $N_2$ - $N_2$  system is concerned with the estimate of the second virial coefficients and solid state data, derived for the first time in the late 70s. Out of those data the parameters of a simple Lennard-Jones model potential have been obtained through a fit [162–166].

In 1998, a group of the Perugia University [167] proposed a potential energy surface obtained by combining *ab initio* and experimental information through an expansion in bipolar spherical harmonics involving more than 20 terms. Subsequently [168], a more compact representation for the PES was introduced by Aquilanti et al. including an harmonic expansion functional form to describe the salient geometries of the dimer and account for the relative contributions to the intermolecular interaction from components of different nature. In particular, the parameters of the radial coefficients were derived from the analysis of the integral collision cross-section and the second virial coefficient (particularly sensitive to the strength of interaction and its anisotropy).

#### 4.4.2 Our MP and CCSD *ab initio* calculations

For the  $N_2$ - $N_2$  system we have carried out some sets of preliminary *ab initio* calculations by keeping the  $N_2$  internuclear distance and orientation in space fixed and varying  $R$  (see fig. 4.42) the distance between the centers of mass of the two molecules, using two different basis sets from the correlation consistent series developed by Dunning [169]. Three sets of calculations were performed. The choice of appropriate coordinate system for an electronic structure calculation is essential. In the case of two linear diatomic molecules (say a and b) it is often convenient to use a space fixed (or global) axis system in which the z-axis is taken as passing through the center of mass of the two molecules (see Fig. 4.42). In this scheme the position of each of the four atoms  $\kappa$ ,  $\lambda$ ,  $\mu$  and  $\nu$  is defined by two polar angles  $\theta$  and  $\varphi$ , of which the first is the angle formed by the internuclear axis and the space fixed  $z$  axis, the second is the difference between azimuthal angles  $\varphi = \varphi_a - \varphi_b$ . The dimer of two linear molecules can then be described by four internal coordinates  $(R, \theta_a, \theta_b, \varphi)$  where  $\theta$  defines the orientations of each monomer relative to  $R$  while  $\varphi$  defines the dihedral angle formed by the two planes (defined by the  $z$  axis and the axis of an  $N_2$  bond). The diatomic molecular bond lengths are set fixed at its experimentally determined equilibrium value of

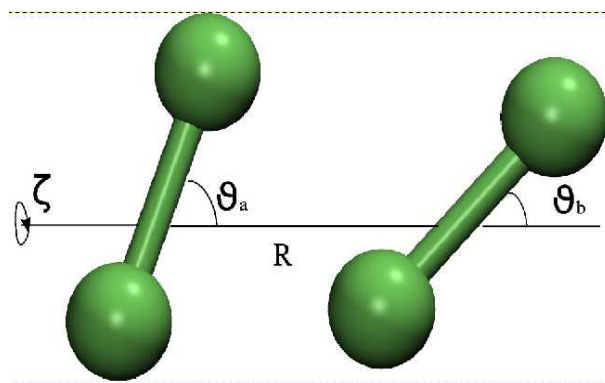


Figure 4.42: Diagrammatic representation of the  $(\text{N}_2)_2$  dimer and related coordinate system

1.094 Å [170]. With this choice of coordinate system the four conformations treated in this work and illustrated in Fig. 4.43, have been obtained by varying the set of four parameters: the L-shaped (linear,  $D_{\infty h}$ ), H-shaped (parallel,  $D_{2h}$ ), T-shaped (perpendicular,  $C_{2v}$ ) and X-shaped (crossing,  $D_{2d}$ ), corresponding respectively to the sets  $(0^\circ, 0^\circ, 0^\circ, R)$ ,  $(90^\circ, 90^\circ, 0^\circ, R)$ ,  $(0^\circ, 90^\circ, 0^\circ, R)$  and  $(90^\circ, 90^\circ, 90^\circ, R)$ . The first set of calculations were performed to obtain a general overview of the

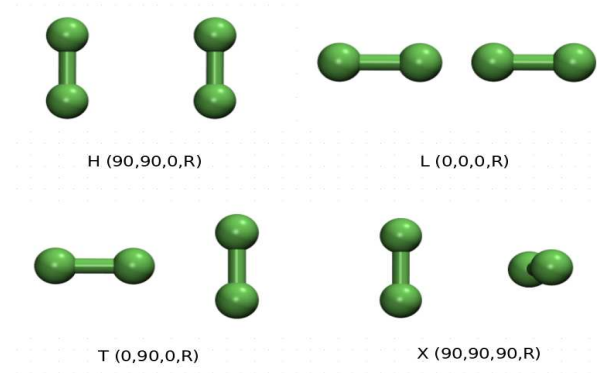


Figure 4.43: The four different configurations of the  $(\text{N}_2)_2$  dimer considered for the calculations.

interaction energy using the supermolecular Møller-Plesset perturbation theory up to second order for four types of  $(\text{N}_2)_2$  arrangements channels. To increase the accuracy and to include more correlation energy the calculations were repeated using the CCSD(T) (coupled cluster using single and double substitutions including triple excitation perturbatively) for all the four conformations with a distance of the centers of mass of the two molecules varying from 0.1 to 10 Å and correcting the result for the BSSE (basis set superposition error), by making use of the FCP procedure previously described. In the last set of calculations the attention was focused on reactive processes. To this end

we performed an automatic geometry optimization starting from two particular H conformation, in which one  $N_2$  bond is at its equilibrium length, while the other is stretched either of 0.8 Å ( $H_{0.8}$ ) or 1.4 Å ( $H_{1.4}$ ). All the calculations were carried out using the version of the GAMMES-US [8] *ab initio* package available on the COMPCHEM segment of the EGEE European GRID.

### 4.4.3 Computational Details

*Ab initio* calculations for the  $N_2$ - $N_2$  system have been carried out using two different methods with two basis sets from the correlation consistent series developed by Dunning [169], the cc-pVXZ with X=D,T. These families of basis sets are widely used since they are designed to converge systematically to the complete basis set (CBS) limit using extrapolation techniques. The 'cc-p', stands for 'correlation consistent polarized' and the 'V' indicates they are valence only basis sets. Correlation consistent basis sets are built up by adding shells of functions to a core sets of atomic Hartree-Fock functions. Each function in a shell contributes similar amounts of correlation energy in an atomic calculation. For the 1st and 2nd row atoms the cc-pVDZ (correlation consistent-polarized valence double zeta) basis set adds 1s, 1p, and 1d atomic orbital functions, while the cc-pVTZ set adds another s, p, d and f atomic orbital functions, etc. These basis sets can be augmented with core functions for geometric and nuclear property calculations, and with diffuse functions for electronic excited-state calculations, electric field properties calculations, and long-range interactions such as van der Waals forces.

The *ab initio* calculations were carried out using the GAMESS-US [8] package. As already mentioned, the interaction energy between two monomers is defined as:

$$\Delta E(\hat{R}) = E(AB, \hat{R})^{\{ab\}} - E(A)^{\{a\}} - E(B)^{\{b\}}. \quad (4.28)$$

To obtain the energy  $E(AB, \hat{R})^{\{ab\}}$  of the dimer at different  $\hat{R}$  we perform different energy calculations on the system increasing the distance of the center of mass of the two monomers. Two sets of calculations were performed for each of the above mentioned basis set. Namely:

- the first set of calculations have been carried out to obtain a general overview of the interaction energy using the supermolecular Møller-Plesset perturbation theory up to second order for each of the four configuration described in the previous section: L-shaped, H-shaped, T-shaped and X-shaped. The MP2 method is a good compromise between accuracy and computational cost and

therefore is well suited for obtaining a first idea of the PES. In fact, MP2 calculations do not require a large size memories and the time for a single calculation, on a fairly simple system like  $N_2-N_2$ , is short.

A major problem of the MP method is that the convergence of the MP series is not guaranteed *a priori*. In the present case, as shown by Karimi et al [159], numerical tests on the convergence of the calculated interaction energy have shown initial oscillations in the MP series up to fourth order with the MP2 results being more stable (negative) than those of the MP4.

-the calculations have been repeated using the CCSD(T) [171] method (coupled cluster using single and double substitutions including triple excitation perturbatively) for all of the four conformations with a distance of the center of mass of the two dimer varying from 0.1 to 8 Å in order to obtain values of increased accuracy including more correlation energy. To correct the BSSE using the FCP procedure [5] an additional batch of calculations were performed. This method let us to calculate the BSSE by re-performing all the calculations using the mixed basis sets, through the introduction of "ghost orbitals", and then subtracting this error *a posteriori* from the uncorrected energy.

The CCSD(T) technique is more accurate than the MP2 though the price to pay is the request of a large amount of memory. Moreover, coupled cluster calculations, making use of large basis sets, take long CPU time even if the system is made by few atoms. This difference in resource demand is shown clearly in table 4.6, where the CPU time and the memory request for the calculations on the parallel conformation, at a distance of the center of mass of 4 Å, of the  $N_2-N_2$  system is shown. As

	MP2		CCSD(T)	
	cc-pVDZ	cc-pVTZ	cc-pVDZ	cc-pVTZ
<b>CPU Time</b>	1.0	14.5	42.1	1717.4
<b>Memory allocated</b>	1.142	13.926	6.225	48.039

Table 4.6: CPU Total time [sec.] and Dynamic Memory allocated [Mwords] for a single geometry calculation for the  $N_2-N_2$  system with the CCSD(T) and MP2 method with cc-pVDZ and cc-pVTZ basis set.

we can see, the time for a single calculation increases remarkably in passing from MP2 to CCSD(T)

whereas the memory request depends on the dimension of the basis set (the two-electron integrals stored are proportional to the number of basis functions). As apparent from the table, CCSD(T) calculations with a large basis set for all the points of the grid at which the PES has to be calculated require long time and a big memory availability, not easily satisfied by single machines. This copes perfectly well with the nature of the Grid infrastructure [see Chap. 3] by distributing the calculations for different geometries on different Computing Elements and elaborate the results on the stored values. In this way the CPU time decrease proportionally with the number of the machines available having the needed memory size. However the CCSD(T) method becomes unusable on the Grid when the basis set become too large. For a single CCSD(T) calculation on that system with a cc-pVQZ basis set, in fact, the memory required for the CC integral sorting is 207062056 words, that is hard to satisfy by most of the Grid CEs. This prompts the need for HPC machines to be made available on the grid together with parallel computing tools. situation suggest us to perform these very accurate calculation on a parallel system instead of Grid infrastructure and this will be the aim of future studies.

## 4.5 The Interaction Energy

As already mentioned, the calculations were carried out at different levels of theory. In doing this, initially we focused on an overall (low level) *ab initio* analysis of the general features of the PES. In fact, due to the novelty represented by this type of calculations, we preferred to proceed step by step while trying to work out the potential energy surface for  $N_2 + N_2$ . Accordingly, the first calculations were carried out at MP2 RHF level of theory for the different configurations shown in Fig. 4.43. For each geometry described above, we calculated single point energy values by varying the intermolecular distance  $R$ , from 1.0 to 10.0 Å in step of 0.1 Å, while keeping fixed the  $N_2$  internuclear distance at its experimental equilibrium value (1.094 Å). As already mentioned, the BSSE correction was also evaluated.

### 4.5.1 MP *ab initio* results

Figures 4.44-4.47 show the behaviour of the calculated long range intermolecular pair potential energies of the dimer at different values of  $R$ , for all the investigated geometries of the dimer, using the cc-pVDZ basis set. For each investigated geometry the results of the *ab initio* MP calculations

(solid line), the related BSSE energy values (dotted line) and the sum between MP and BSSE results (calculated following the FCP procedure-dashed line) are plotted. From the figures it is apparent that, at this level of theory, the T-shaped geometry is the most stable of our atom complexes. As a matter of fact, the well stabilizing it is about  $-1.0 \times 10^{-3}$  Hartree deep while that of the other geometries are about one order of magnitude less deep. However, as can be also seen from the figures for all geometries the calculated BSSE correction is of the same order of magnitude, especially about the minimum. This is due to the fact that the used basis set is not sufficiently large. For this reason, we carried out similar calculations using the cc-pVTZ basis set. Related results are plotted in Figures 4.48- 4.51, using the same layout as the previous plots. The plots show that the new MP energy values decrease of about  $0.5 \times 10^{-4}$  Hartree around the minimum for the H and X-shaped geometries, while for the L and T-shaped geometries the *ab initio* energy values are smaller. The advantage of using a larger basis set can be appreciated by inspecting the BSSE correction plots. In fact, for the whole set of geometries, the related BSSE values decrease with respect to those calculated with the smaller basis set using the same level of theory. As a result, the position of the minimum, for all the geometries, does not vary so much when the BSSE correction is applied. It is important to notice also that when using the larger basis set the T-shaped geometry does not result anymore to be the most stable structure: its interaction energy value at the minimum becomes in fact comparable with that of the X-shaped one.

In order to better rationalize the results of the MP2 *ab initio* calculations, in Figures 4.52- 4.55 are compared, for each geometry, the potential energy curves calculated with the two basis set, and in Table 4.7 are listed, the location of the minimum, the interaction energy and the BSSE. It can be

	cc-pVDZ			cc-pVTZ		
	$R_{eq}$ (Å)	$E_{int}$ ( $\mu$ H)	BSSE ( $\mu$ H)	$R_{eq}$ (Å)	$E_{int}$ ( $\mu$ H)	BSSE ( $\mu$ H)
<b>H</b>	3.4	-630	867	3.6	-650	386
<b>L</b>	4.6	-409	603	5.0	-189	137
<b>T</b>	3.9	-1000	906	4.1	-719	307
<b>X</b>	3.4	-632	835	3.5	-717	461

Table 4.7: Intermolecular equilibrium distance, interaction energy ( $E_{int}$ ), BSSE correction, calculated at MP2 level with two different basis set.

pointed out that the value of  $R$  at the minimum does not depend strongly on the used basis set, in fact, for the H, T, X-shaped geometries, its value varies only of 0.2 Å when using the cc-pVTZ

basis set; the results found for the L-shaped geometry is quite anomalous, but we encountered some problems in the calculations for this geometry, in fact we have not been able to work out the interaction energy for some values of  $R$ , due to an error in the execution of the GAMESS-US code.

On the other hand, the BSSE correction is almost as large as the interaction energy when using the smaller basis set: this implies that the cc-pVDZ is very poor in describing the interaction of two nitrogen molecules in the vdW region. With the cc-pVTZ basis set the BSSE correction is reduced almost at the half with respect to the value calculated with the cc-pVDZ basis set. This means that a large basis set is essential in calculating the potential energy values of the nitrogen dimer. Finally, as already mentioned, the most stable structure is the T-shaped one with the cc-pVDZ but, when the cc-pVTZ basis set is used the relative stability of the T-shaped geometry becomes comparable to that of the X-shaped geometry.

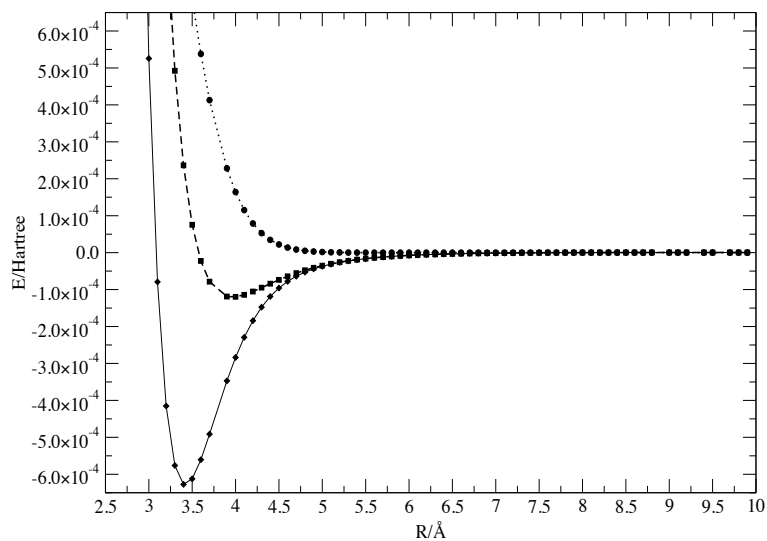


Figure 4.44: Calculated MP2 interaction energy values with the cc-pVDZ basis set for the H-shaped geometry at long range. Solid line represents the calculated *ab initio* potential energy values, the dotted line represents the calculated BSSE, the dashed line the sum.

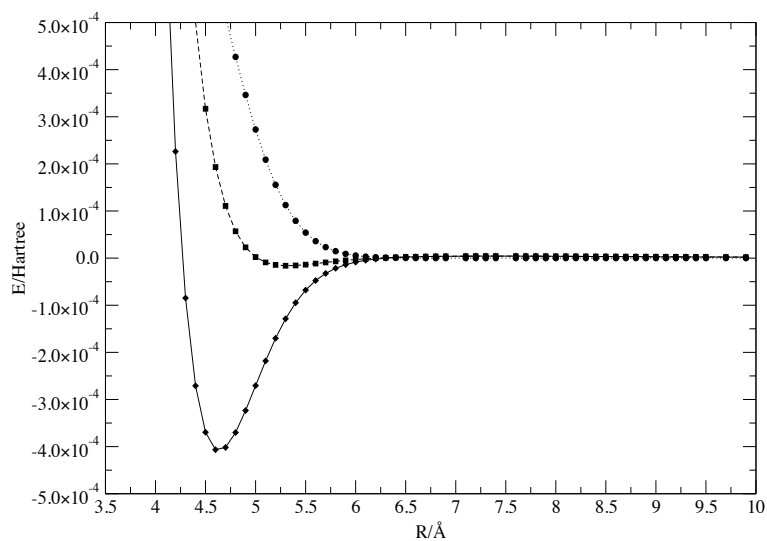


Figure 4.45: Same as Fig. 4.44 for L-shaped geometry.

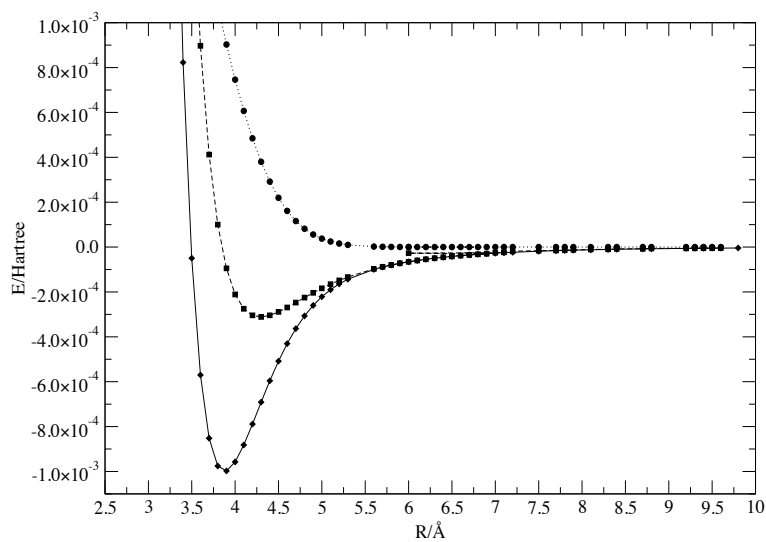


Figure 4.46: Same as Fig. 4.44 for T-shaped geometry.

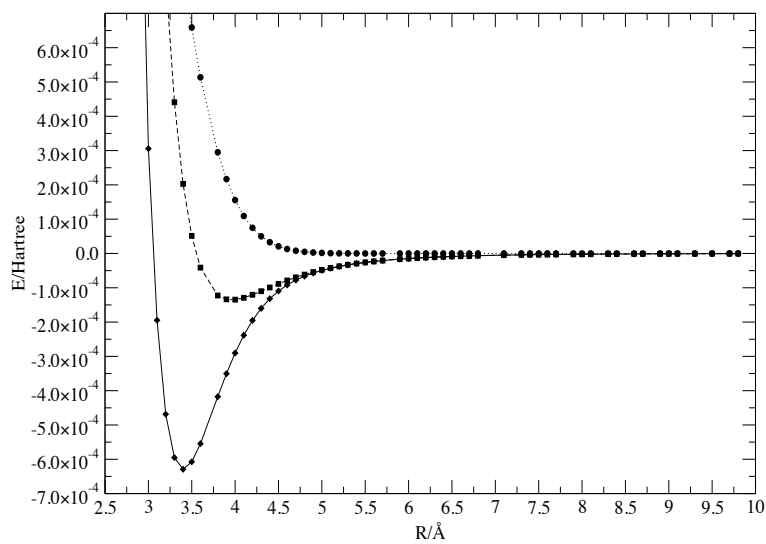


Figure 4.47: Same as Fig. 4.44 for X-shaped geometry.

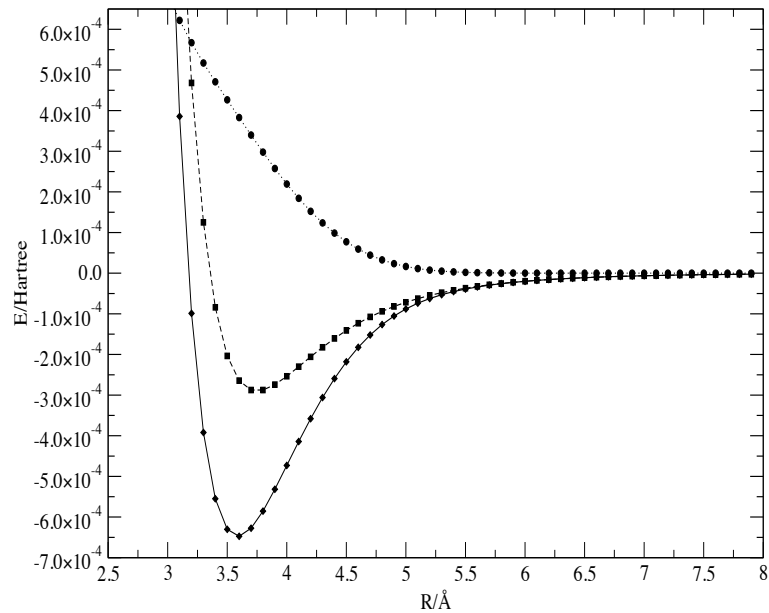


Figure 4.48: Calculated MP2 interaction energy values with the cc-pVTZ basis set for the H-shaped geometry at long range. Solid line represents the calculated *ab initio* potential energy values, the dotted line represents the calculated BSSE, the dashed line the sum.

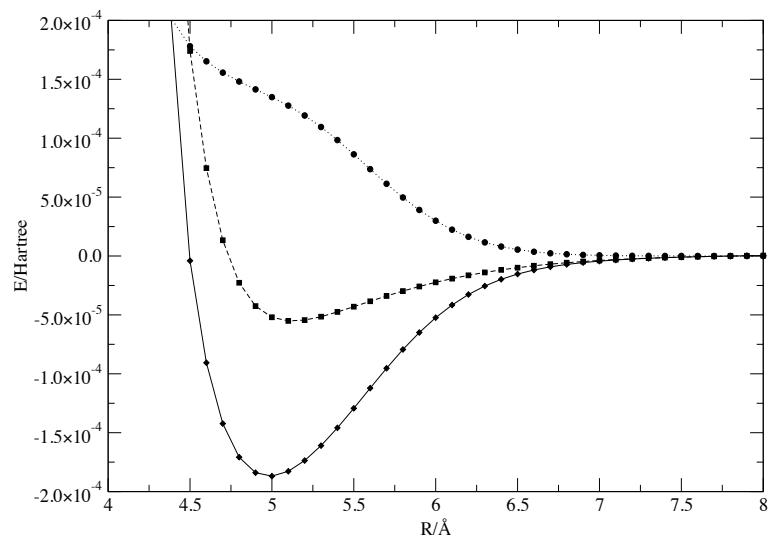


Figure 4.49: Same as Fig. 4.48 for L-shaped geometry.

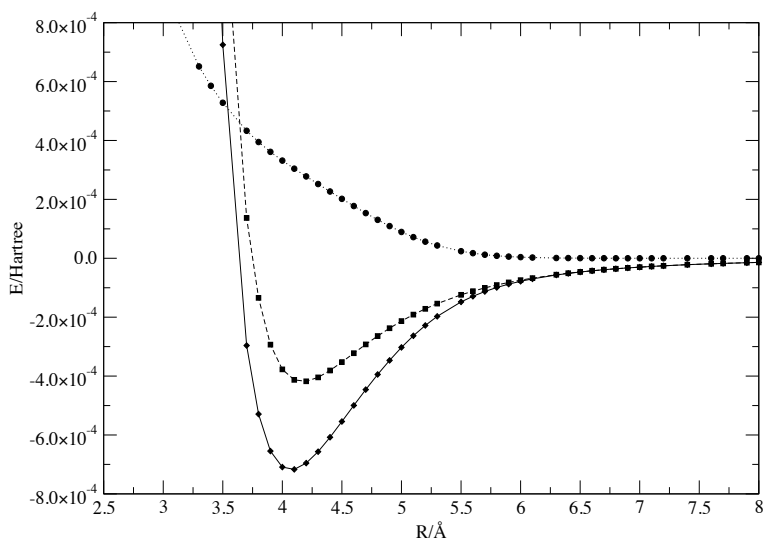


Figure 4.50: Same as Fig. 4.48 for T-shaped geometry.

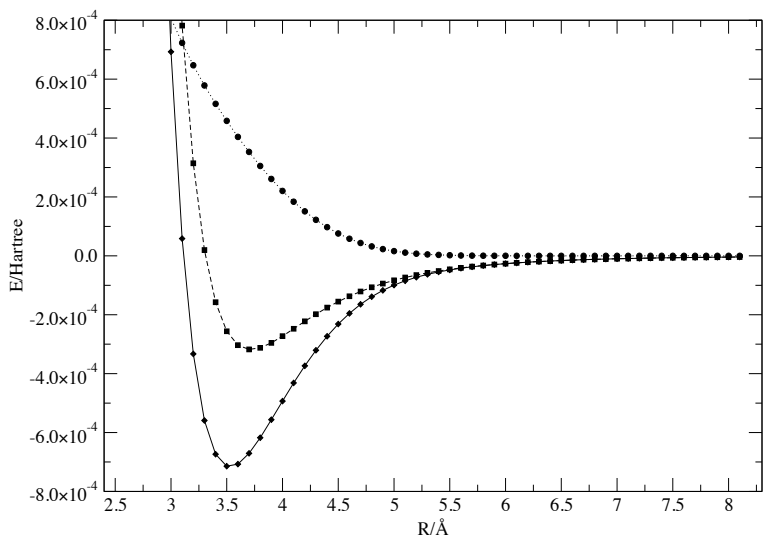


Figure 4.51: Same as Fig. 4.48 for X-shaped geometry.

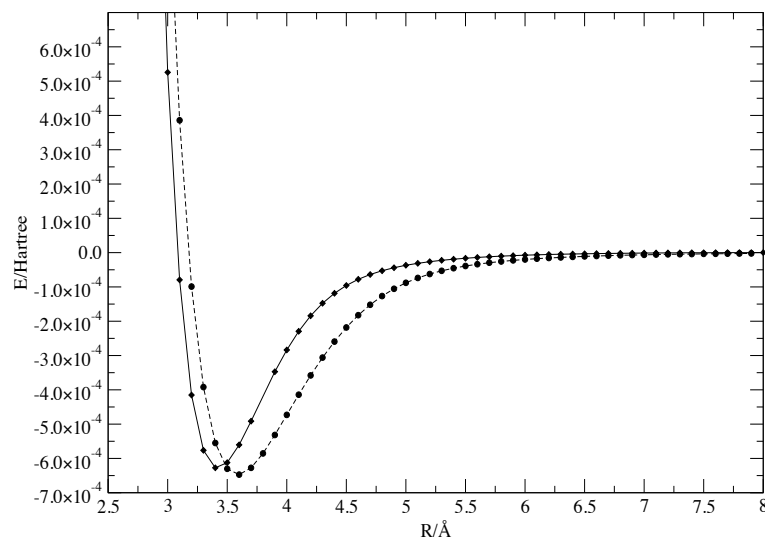


Figure 4.52: Interaction MP2 energy values for the H-shaped geometry at long range calculated using the cc-pVDZ (solid line) and cc-pVTZ (dashed line)

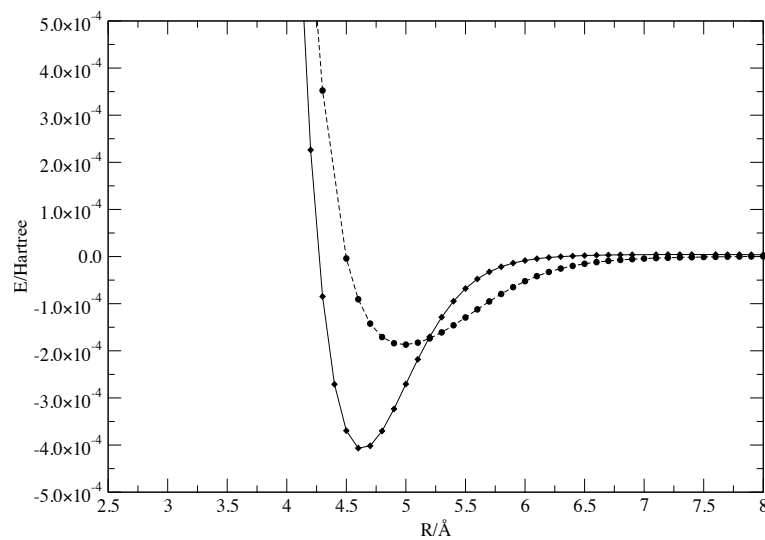


Figure 4.53: Interaction MP2 energy values for the L-shaped geometry at long range calculated using the cc-pVDZ (solid line) and cc-pVTZ (dashed line)

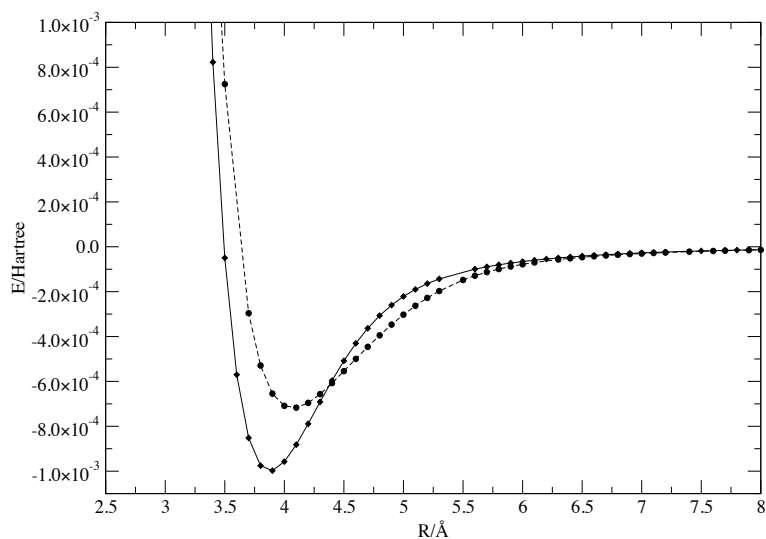


Figure 4.54: Interaction MP2 energy values for the T-shaped geometry at long range calculated using the cc-pVDZ (solid line) and cc-pVTZ (dashed line)

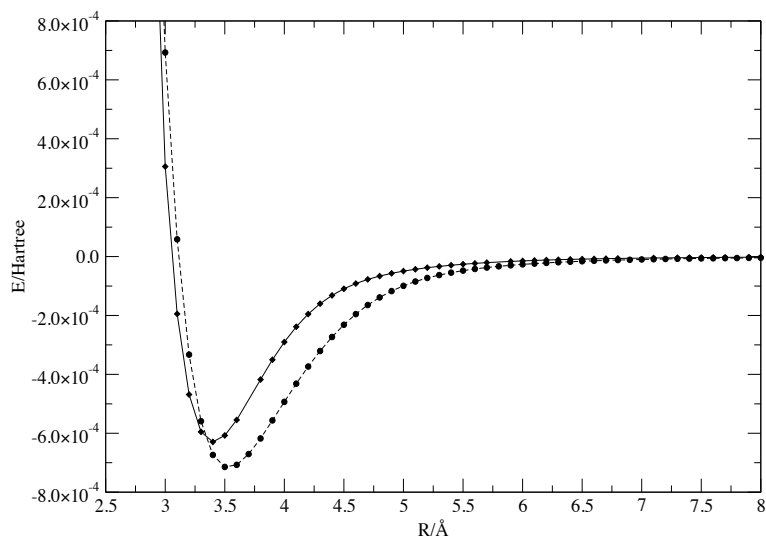


Figure 4.55: Interaction MP2 energy values for the X-shaped geometry at long range calculated using the cc-pVDZ (solid line) and cc-pVTZ (dashed line)

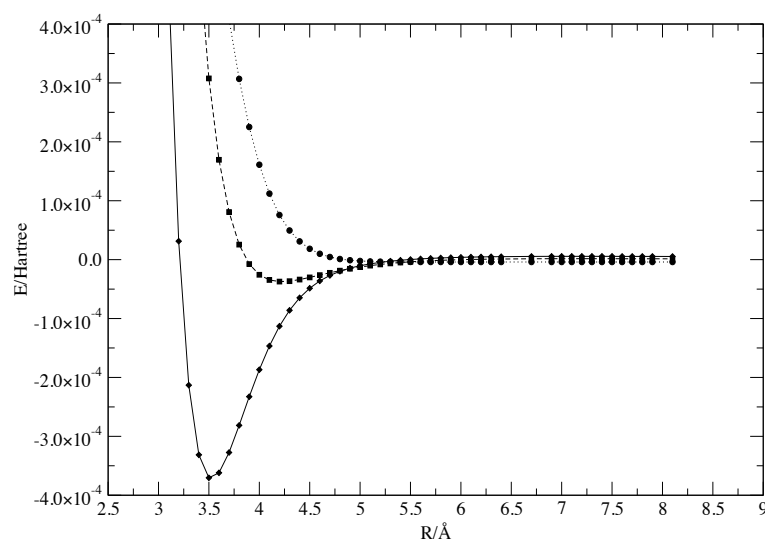


Figure 4.56: Calculated CCSD(T) interaction energy values with the cc-pVDZ basis set for the H-shaped geometry at long range. Solid line represents the calculated *ab initio* potential energy values, the dotted line represents the calculated BSSE, the dashed line the sum.

#### 4.5.2 CCSD(T) *ab initio* results

In order to improve the accuracy of the *ab initio* potential energy values we carried out additional calculations at the CCSD(T) level of theory for the same geometries considered for the MP2 ones. Results obtained using the cc-pVDZ basis set are shown in figures 4.56- 4.59. CCSD(T) results qualitatively reproduce the MP2 values. Also for CCSD(T) calculations, in fact, the T-shaped geometry is the most stable structure and the value of  $R$  at the energy minimum is about  $3.8 \text{ \AA}$ . At the same time, hand, the interaction energy is in general smaller than the MP2 one and the BSSE correction is always greater than the interaction energy value, for all the geometries investigated, making the results of limited validity. In addition, while the BSSE corrections for the MP2/cc-pVDZ results are generally as large as the interaction energy, those calculated for the CCSD(T)/cc-pVDZ ones are larger. Finally, the interaction energy curves corrected for the BSSE (dashed lines in the plots) show the same shift in  $R_{eq}$  as that found for the MP2/cc-pVDZ calculations. Also in this case the effect is attributed to an incorrect evaluation of the BSSE when using the cc-pVDZ basis set. For this reason, we improved the level of the calculations by making use of the cc-pVTZ basis set. Figures 4.60-4.63 show the plots of the potential energy values for the various geometries of  $(\text{N}_2)_2$  as a function of the intermolecular distance  $R$ . In particular, the CCSD(T)/cc-pVTZ calculated interaction energy values (solid line), the related BSSE energy values (dotted line) and the sum

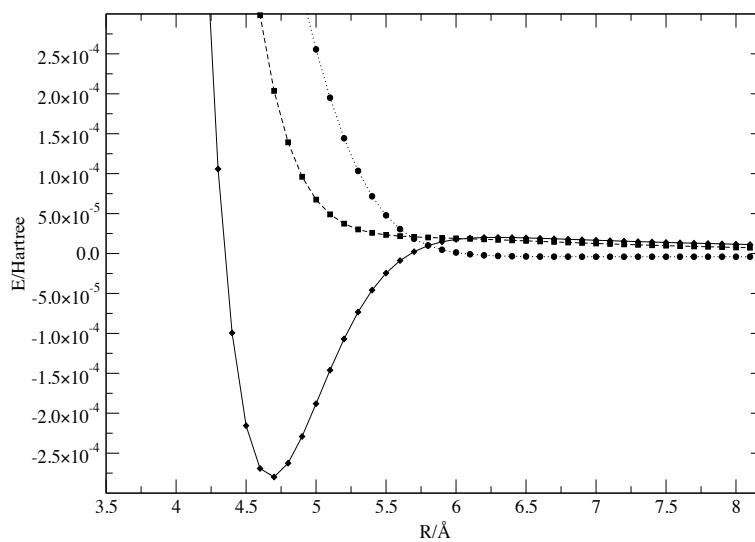


Figure 4.57: Same as Fig 4.56 for L-shaped geometry.

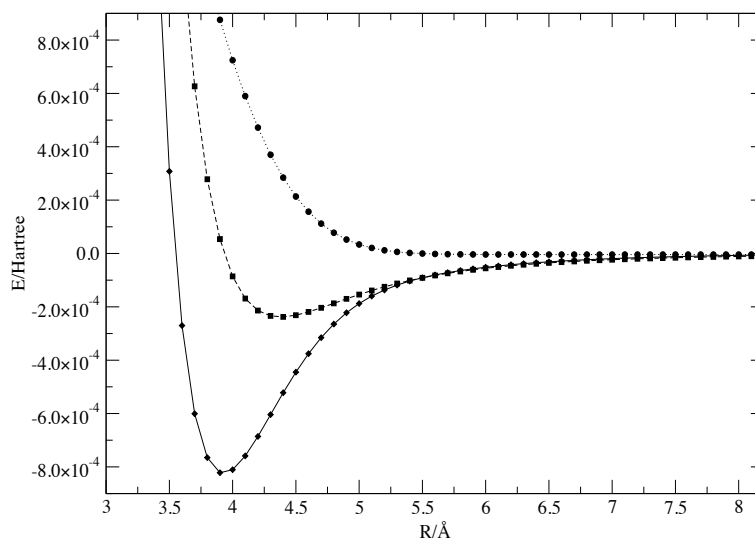


Figure 4.58: Same as Fig 4.56 for T-shaped geometry.

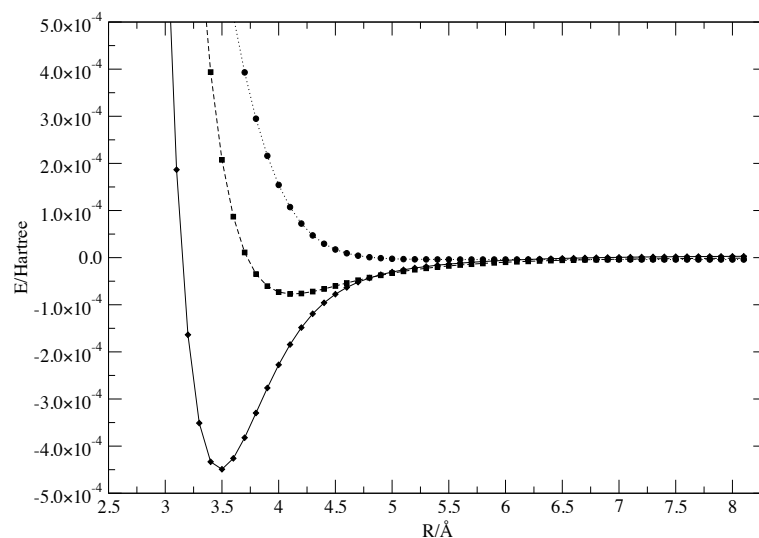


Figure 4.59: Same as Fig 4.56 for X-shaped geometry.

between CCSD(T) and BSSE results are shown. In Table 4.8 the features of the different potential energy curves (as for the MP2 calculations) around the minimum for each geometry are listed.

It can be pointed out that the trend found in improving the basis set for the MP2 calculations is confirmed for the CCSD(T) ones. In fact, we found that for the H and T-shaped geometries the interaction energy value at the minimum decreases when using the cc-pVTZ basis set with respect to the CCSD(T)/cc-pVDZ one, while it increases for the L and X-shaped geometries. Moreover, as for previous MP2 calculations, the application of the BSSE corrections to the interaction energy values with the cc-pVTZ does not lead to a strong variation of the position of the minimum. In this case, although the BSSE correction values are not small there is a significant improvement. In fact, for all geometries the calculated corrections are definitively smaller than the values of the interaction energy. This is not true only for the L-shaped geometry for which the value of the BSSE correction is almost as large as the corresponding interaction energy. Also for this set of calculations, we found that the most stable structures are the T and X-shaped configurations.

### 4.5.3 MP2 versus CCSD(T)

In order to compare the results obtained for MP2 with those obtained with CCSD(T) level of theory, we plotted the interaction potential energy values, calculated with the cc-pVDZ basis set, for both the MP2 and CCSD(T) calculations. In figures 4.64-4.71 the comparison of the calculated interaction with respect to the values obtained using the cc-pVDZ basis set is shown. The similar

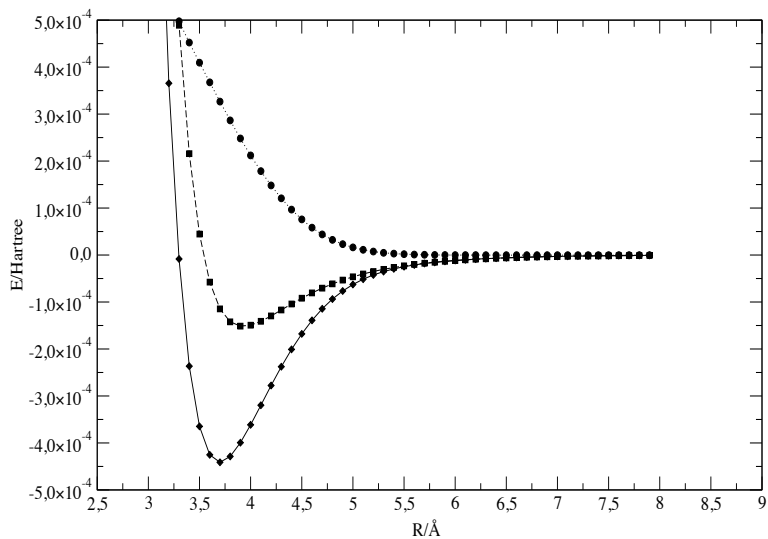


Figure 4.60: Calculated CCSD(T) interaction energy values with the cc-pVTZ basis set for the H-shaped geometry at long range. Solid line represents the calculated *ab initio* potential energy values, the dotted line represents the calculated BSSE, the dashed line the sum.

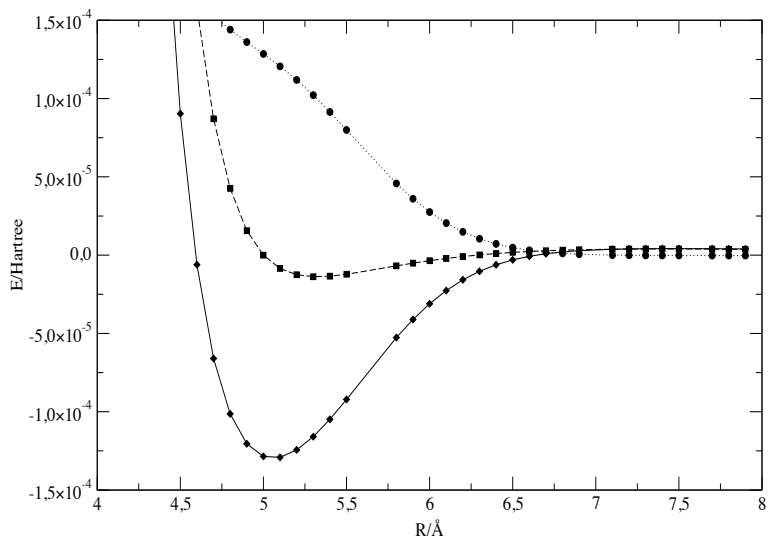


Figure 4.61: Same as Fig. 4.60 for L-shape geometry.

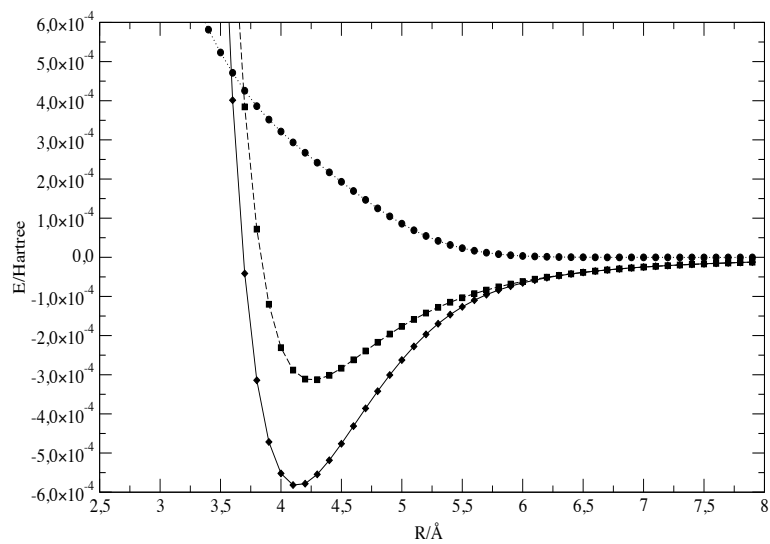


Figure 4.62: Same as Fig. 4.60 for T-shape geometry.

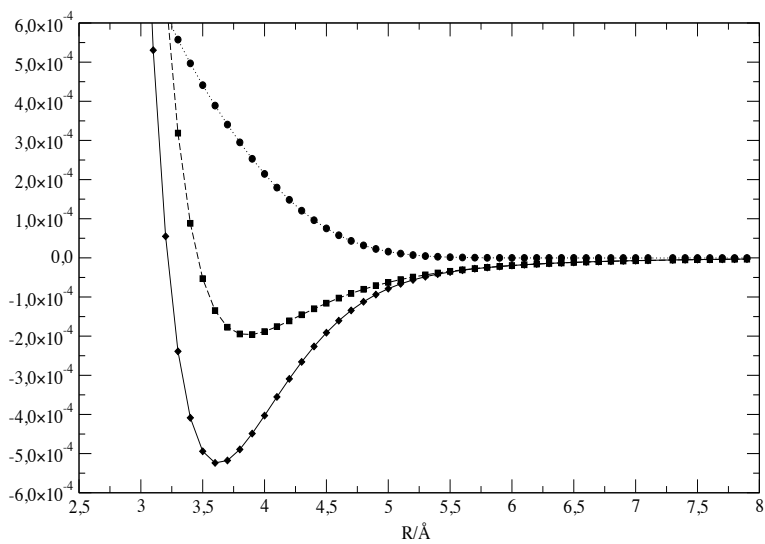


Figure 4.63: Same as Fig. 4.60 for X-shape geometry.

	cc-pVDZ			cc-pVTZ		
	$R_{eq}$	$E_{int}$	BSSE	$R_{eq}$	$E_{int}$	BSSE
	(Å)	( $\mu$ H)	( $\mu$ H)	(Å)	( $\mu$ H)	( $\mu$ H)
<b>H</b>	3.5	-370	678	3.7	-441	326
<b>L</b>	4.7	-280	483	5.1	-129	121
<b>T</b>	3.9	-822	875	4.1	-582	293
<b>X</b>	3.5	-449	657	3.6	-524	389

Table 4.8: Intermolecular equilibrium distance, Interaction energy ( $E_{int}$ ), BSSE correction, calculated at CCSD(T) level with two different basis sets.

curves obtained when using the cc-pVTZ basis set are shown in figures 4.68-4.71. It is important to point out here that the calculated energy values are not corrected for the BSSE.

The comparison between CCSD(T) and MP2 calculations shows, in general, that the CCSD(T) energies are smaller than those of MP2 calculations. This agrees with the fact that the accuracy of the CCSD(T) method is higher level with respect to the MP2 one.

In particular, the effect is stronger with the cc-pVDZ while for the improved cc-pVTZ basis set, the effect is less evident. Thanks to this result, we can conclude that the cc-pVDZ basis set is unsuitable for describing the  $N_2 - N_2$  interaction, and, at least, the cc-pVTZ basis set must be used as a starting point for the use of larger basis sets, such as the cc-pVQZ one. Finally, it is important to point out that, while most of the performed calculations are usually successful, some calculations fail to complete correctly. These errors are, in general, convergence problems encountered in the short-distances calculations. In this region, in fact, the method used to generate the initial guess orbitals, for the SCF iteration, can cause errors. The GAMESS-US code, in fact, for the generation of the initial orbitals carries out an extended Huckel calculation using an Huzinaga MINI basis set and projects them onto the current basis set. In most of the case encountered, this problem gives an error in the reordering of the orbitals that cause the abnormal termination of the job. This can be avoided by using a different method for the generation of the initial orbitals (e.g. diagonalization of the one-electron part of the Hamiltonian, use of the resulting orbital from a previous calculation on a similar system etc.) when, however, are in general less accurate than the Huckel ones. In other cases the difficulties of the method in calculating the initial guess orbitals leads to a linear dependence problem. In this case the GAMESS code has a built-in function, called QMTTOL, which lets the user to set the threshold for the linear dependence. Any function in the Symmetry-Adapted linear

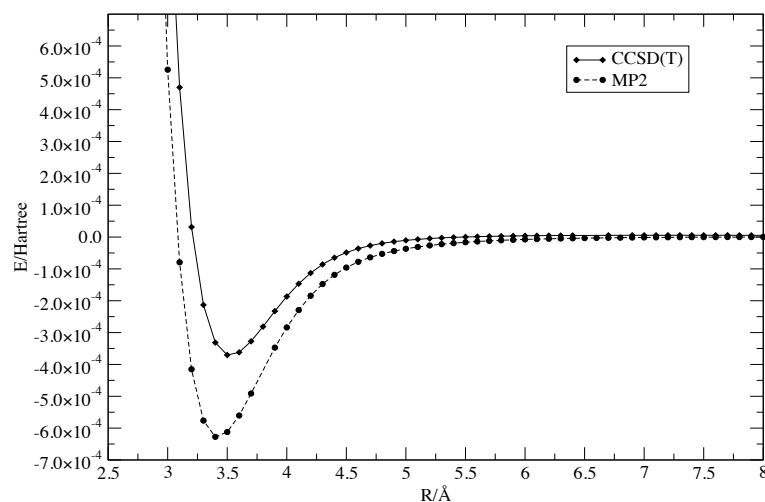


Figure 4.64: Calculated interaction energy values with the cc-pVDZ basis set for the H-shaped geometry at CCSD(T) (solid line) and MP2 (dashed line) levels of theory.

combination variational space whose eigenvalues of the overlap matrix is below this tolerance is considered to be linearly dependent. Such functions are dropped from the variational space (what is dropped, however, is not the individual basis function, but rather some linear combination(s) of the entire basis set that represents the linear dependent part of the function space). In the best cases, this may cause an increase of the final energy of the order of tens of microhartrees (depending on the number of orbitals removed). In the worst cases, however, it can give convergence errors difficult to eliminate.

## 4.6 Building an overall potential energy surface

Since our main focus is on the overall description of the possible processes (including reactive processes), we extended our calculations by performing also some calculations of gradients for automatic geometry optimization and transition states search and we investigated the possibility of extending the the LAGROBO functional to deal with four atom systems.

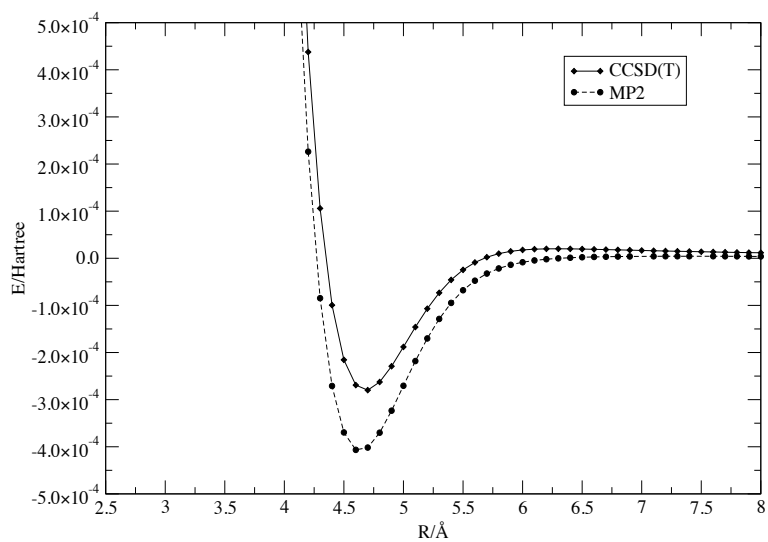


Figure 4.65: Same as Fig. 4.64 for the L-shaped geometry.

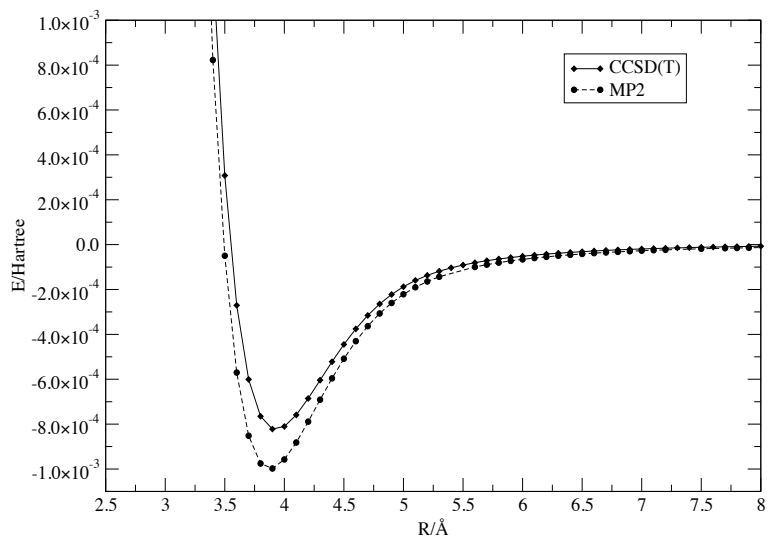


Figure 4.66: Same as Fig. 4.64 for the T-shaped geometry.

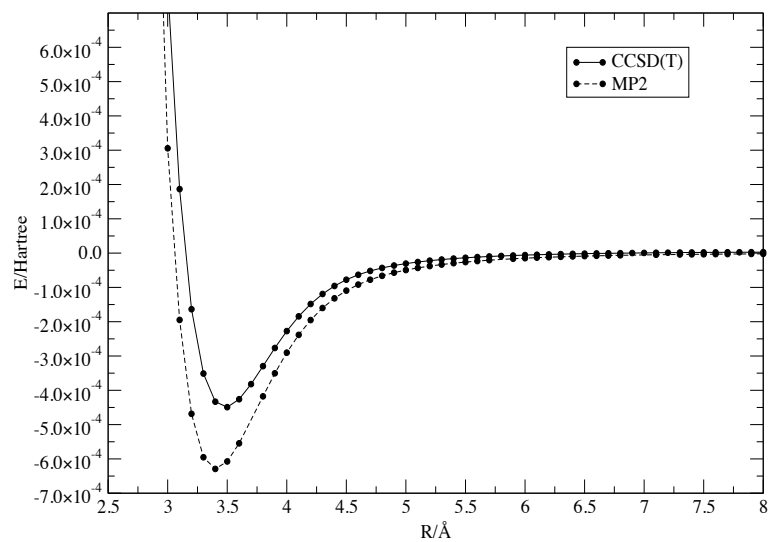


Figure 4.67: Same as Fig. 4.64 for the X-shaped geometry.

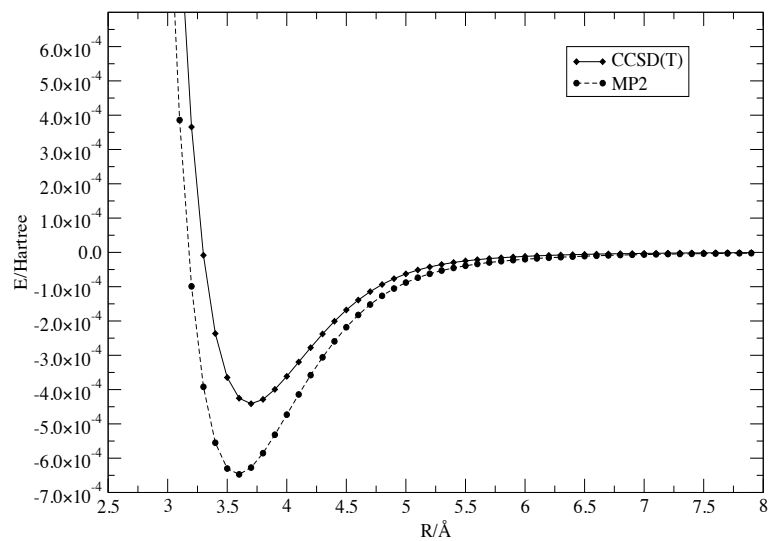


Figure 4.68: Calculated interaction energy values with the cc-pVTZ basis set for the H-shaped geometry at CCSD(T) (solid line) and MP2 (dashed line) levels of theory.

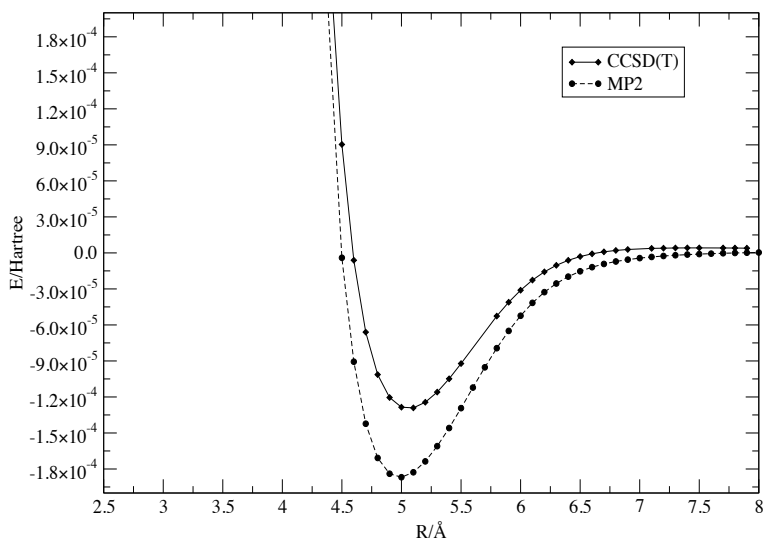


Figure 4.69: Same as Fig. 4.68 for the L-shaped geometry.

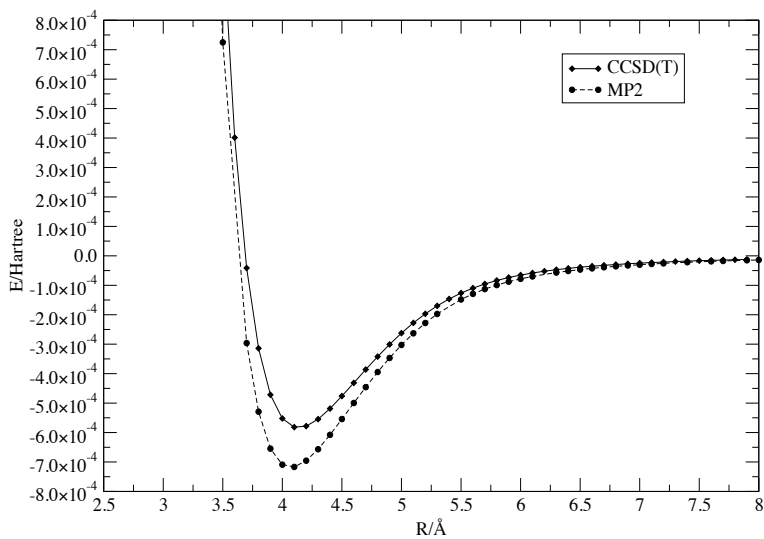


Figure 4.70: Same as Fig. 4.68 for the T-shaped geometry.

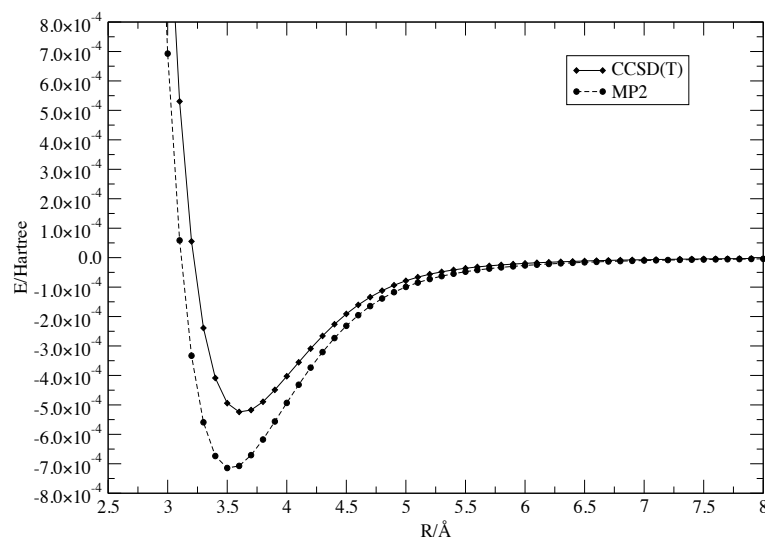


Figure 4.71: Same as Fig. 4.68 for the X-shaped geometry.

#### 4.6.1 Possible reactive processes

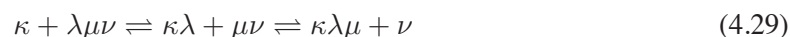
To investigate possible reactive paths for  $\text{N}_2 + \text{N}_2$  we started from two particular H conformations, in which one  $\text{N}_2$  bond is at its equilibrium internuclear distance, while the other one is stretched either of  $0.8 \text{ \AA}$  ( $\text{H}_{0.8}$ ) or  $1.4 \text{ \AA}$  ( $\text{H}_{1.4}$ ). In both configurations  $R=0.5 \text{ \AA}$ .

To optimize the geometries the calculations were performed by varying  $R$  under the effect of the energy gradient. For the first conformation, the  $\text{H}_{0.8}$ , one local minimum in which the two monomers, arranged as a rectangle (see Fig. 4.72), are separated by  $1.3 \text{ \AA}$  was found. In this case the internuclear distance of each molecule is  $1.4760 \text{ \AA}$ . For the  $\text{H}_{1.4}$  configuration the optimization finds a local energy minimum when one molecule at near equilibrium is inserted into the other (see Fig. 4.73) whose bond is stretched to  $2.51 \text{ \AA}$ .

This seems to indicate that an exchange reaction between these two molecules can occur. Moreover, the fact that the minimum energy path shows a barrier followed by a minimum at  $R=0$  indicates the formation of a well at the transition state sandwiched by two barriers (as also found for the  $N + N_2$  system). For this reason, we performed additional calculations, at the same level of theory, in order to search for possible transition states, starting from the results obtained by optimizing the  $H_{0,8}$  and  $H_{1,4}$  configurations (in particular, we used the optimized values of the internuclear distances) and varying  $R$  from 2.0 to 0.0 Å. All these calculations have been carried out at MP2 level of theory using the cc-pVDZ basis set. The calculated energy values are plotted in Fig. 4.74 and Fig. 4.75, respectively. As shown by the figures, the  $H_{1,4}$  values show a minimum at  $R=0$  and confirm the possibility of an insertion (while the  $H_{0,8}$  values show a repulsive barrier).

#### 4.6.2 Four atom systems fitting tools

A possible approach to the fit of potential energy values could be based on the four atom version of the Paniagua procedure. Here we give the details of the LAGROBO one since it has been already used for atom-diatom systems. As previously discussed, the general formulation of the LAGROBO PES is given by a combination of the ROBO functionals  $V_L^{ROBO}$  of all the reaction channels contributing to the reactive process, weighed by the coefficient  $w_L$  related to the closeness of the considered geometry to the collinear one. When considering a four atom system the possible single process arrangements are:



It is important to point out that we have to include, in principle, 12 contributing  $V_L^{ROBO}$  terms, related to the possible 12 processes. In this case the  $V^P$  terms have the form:

$$V_L^{ROBO} = D_L F_L + I_L \quad (4.30)$$

where the product  $D_L F_L$  is the ROBO-like model potential of process  $L$  and  $I_L$  is a corrective term due to the effect of the remaining atom-atom pairs (in the case of four atom systems this is just one term). The ROBO terms ensure the correct reproduction of both the asymptotic properties and the characteristics of the fixed collision angle MEPs derived from the *ab initio* data (possibly modified to incorporate corrective experimental information). They are given the simple quadratic form

$$D_L F_L \equiv D(\alpha, \sigma; \tau, \delta, \gamma) \left[ \frac{\rho^2}{\rho_o^2(\alpha, \sigma; \tau, \delta, \gamma)} - \frac{2\rho}{\rho_o(\alpha, \sigma; \tau, \delta, \gamma)} \right] \quad (4.31)$$

To shape the fixed angle MEPs the parameters of the different  $V^P$  ROBO terms (the location of the reaction channel energy minimum,  $\rho_o(\alpha, \sigma; \tau, \delta, \gamma)$ , and of its depth,  $D(\alpha, \sigma; \tau, \delta, \gamma)$ ) are given as functions of the angles  $\alpha$  and  $\sigma$  parametrically dependent on the other angles  $\tau, \delta$  and  $\gamma$ .

For the generic tetratomic system  $\kappa, \lambda, \mu, \nu$  the  $\alpha$  and  $\sigma$  angles were first defined as

$$\begin{aligned}\alpha &= \arctan\left(\frac{n_{\mu\nu}}{n_{\kappa\lambda}}\right) \\ \sigma &= \arccos\left(\frac{n_{\lambda\mu}}{\rho}\right) \\ \rho &= \sqrt{n_{\kappa\lambda}^2 + n_{\lambda\mu}^2 + n_{\mu\nu}^2}\end{aligned}\quad (4.32)$$

( $n_{\eta\xi}$  is the BO coordinate of the  $\eta\xi$  pair of atoms) while the angles  $\tau, \delta$  and  $\gamma$  are defined as

$$\begin{aligned}\tau &= \sqrt{\phi'^2 + \psi'^2 + \theta'^2} \\ \delta &= \arctan\left(\frac{\psi'}{\theta'}\right) \\ \gamma &= \arccos\left(\frac{\phi'}{\tau}\right)\end{aligned}\quad (4.33)$$

with

$$\phi' = 2\pi - 2\phi\psi' = 2\psi - 2\pi\theta' = 4\theta$$

The physical angles  $\phi, \psi$  and  $\theta$  defining the geometry and the relative orientation of the tetratomic system are shown in Fig. 4.76. The term  $I_L$  concerned with the interaction of the diatom  $\kappa\nu$  with the diatomic pair  $\lambda\mu$  is expressed as

$$I_L \equiv I_L(n_{\kappa\nu}; \bar{n}) = D_{\kappa\nu} S(\bar{n})(n_{\kappa\nu}^2 - 2n_{\kappa\nu}) \quad (4.34)$$

where  $\lambda$  and  $\mu$  with  $\bar{n} = (n_{\kappa\lambda} + n_{\mu\nu})/2$ ,  $D_{\kappa\nu}$  being the dissociation energy of the  $\kappa\nu$  diatom,  $S(\bar{n})$  being a switching function equal to  $1 + \cos[\pi(\bar{n} + p)/2p]$  for  $\bar{n} < p$  and zero elsewhere. This functional representation, however, leads to some discontinuities which made some trajectories not to converge.

Accordingly, the second problem of this phase was the adoption of a new formulation of the angular variables (see Fig. 4.77) to avoid the just mentioned discontinuities.

As can be seen in the figure, in the new formulation of the LAGROBO functional the angular coordinates are redefined as follows:  $\phi$  is still the angle formed by the  $\kappa - \lambda$  and  $\lambda - \mu$  bonds (as in the old formulation),  $\varepsilon$  is the angle formed by the  $\lambda - \mu$  and  $\mu - \nu$  bonds and  $\zeta$  is the dihedral angle formed by the  $\kappa\lambda\mu$  and  $\lambda\mu\nu$  planes. The use of the  $\phi, \varepsilon$  and  $\zeta$  coordinates to describe the relative orientation of atoms involves a new definition of the functions  $D, \rho_0, \sigma$  and  $\alpha$  in these coordinates.

In particular, a full analytic dependence of these functions on the  $\phi$ ,  $\varepsilon$  and  $\zeta$  coordinates has been worked out. Accordingly, one has:

$$\begin{aligned}
 D(\phi, \varepsilon, \zeta) &= d_0 + \left( d_1(\varepsilon - \varepsilon_0)^2 + d_2(\varepsilon - \varepsilon_0)^3 + (d_3 + d_4\varepsilon^2)(\phi - d_5 - d_6\varepsilon^2)^2 \right) \\
 &\quad \times \exp \left[ d_7(\varepsilon - \pi) (\zeta - d_8 \exp(d_9(\varepsilon - \varepsilon_0)^2)) \right] \\
 \rho_o(\phi, \varepsilon, \zeta) &= (r_1 + r_2 \exp [r_3(\varepsilon - \pi)^2]) (\phi - \phi_0)^3 \\
 &\quad \times (1 + r_4(\varepsilon - \pi)(\zeta - \zeta_0)^2 + r_5(\varepsilon - \pi)(\zeta - \zeta_0)^3) \\
 \alpha_o(\phi, \varepsilon, \zeta) &= ((a_1 + a_2(\varepsilon - \varepsilon_0))(\phi - \phi_0) + (a_3 + a_4(\varepsilon - \varepsilon_0))(\phi - \phi_0)^2 \\
 &\quad + (a_5 + a_6(\varepsilon - \varepsilon_0))(\phi - \phi_0)^3) \exp [a_7(\varepsilon - \pi)(\zeta - \zeta_0)^2] \\
 \sigma_o(\phi, \varepsilon, \zeta) &= (s_1 + s_2(\varepsilon - \varepsilon_0) + s_3(\phi - \phi_0)^2) \exp [s_4(\varepsilon - \pi)(\zeta - \zeta_0)^2] \quad (4.35)
 \end{aligned}$$

where the angles  $\phi_0$ ,  $\varepsilon_0$  and  $\zeta_0$  are the values of  $\phi$ ,  $\varepsilon$  and  $\zeta$  at the transition state.

### 4.6.3 An estimate of the thermal rate coefficient

Due to the limited number of potential energy values and their limited accuracy we decided not to carry out a global fitting. We concentrated instead our efforts into the investigation of the suitability of the Q5cost model to carry out a preliminary analysis of the PES using directly the calculated *ab initio* points. Efforts already paid along this direction led us to create single surface (multiple geometries) files to evaluate qualitatively some features of the reactive process.

To this end, the potential energy values calculated for the X-shaped geometry and those obtained for the  $H_{1,4}$  after optimization, at the same level of theory, have been plotted together as a function of  $R$ , as shown in Fig. 4.78. The choice of comparing the  $H_{1,4}$  plot with the one of the X-shaped geometry is motivated by the fact that the latter is barrier less at small and intermediate range, while it increases significantly as  $R$  becomes smaller than 1. This leads to a crossing of the two curves at  $R$  corresponding to 1.2 - 1.4 Å. This seems to confirm the possibility of a reactive path in the  $N_2 + N_2$  PES in which the two monomers, arranged in an X-shaped fashion, interact each other in a perpendicular way until they reach a first energy minimum at  $R \simeq 1.4$  Å and then a second minimum (located at  $R \simeq 1.2$  Å) that leads to a rearrangement in which one molecule is inserted into the other, as depicted in Fig. 4.73. This suggests that a more detailed study of this reaction should be carried out for future optimization calculations at higher level of theory.

This allows us to consider the minimum of the well of the insertion calculation as a saddle to

reaction and to calculate using a crude transition state approach the thermal rate coefficient. The use of the crude transition state approach to evaluate the thermal rate coefficient leads to the use of the equation

$$k = \frac{k_b T}{h} e^{\frac{-\Delta E}{RT}} \quad (4.36)$$

The use of this equation gives an estimate of  $k$  corresponding to  $4.25 \times 10^{-27} \text{ cm}^3 \text{ molecule s}^{-1}$  due to the fact that  $\Delta E = 759.442 \text{ KJ/Mol}$  and  $T = 1000 \text{ K}$ .

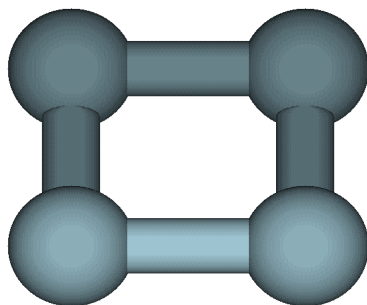


Figure 4.72: Sketch of the nitrogen molecules as obtained from the  $H_{0.8}$  optimization.

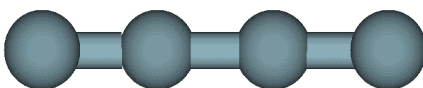


Figure 4.73: Sketch of the nitrogen molecules as obtained from the  $H_{1.4}$  optimization.

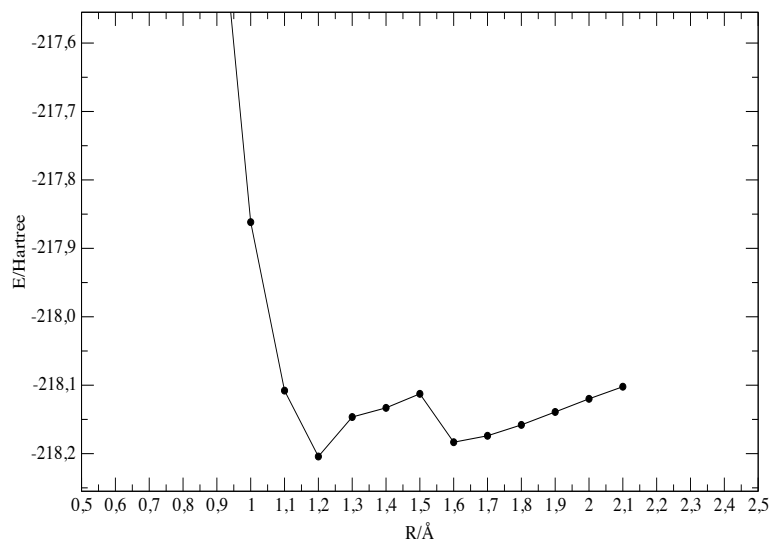


Figure 4.74: Calculated single energy values vs  $R$  for the  $H_{0.8}$  configuration

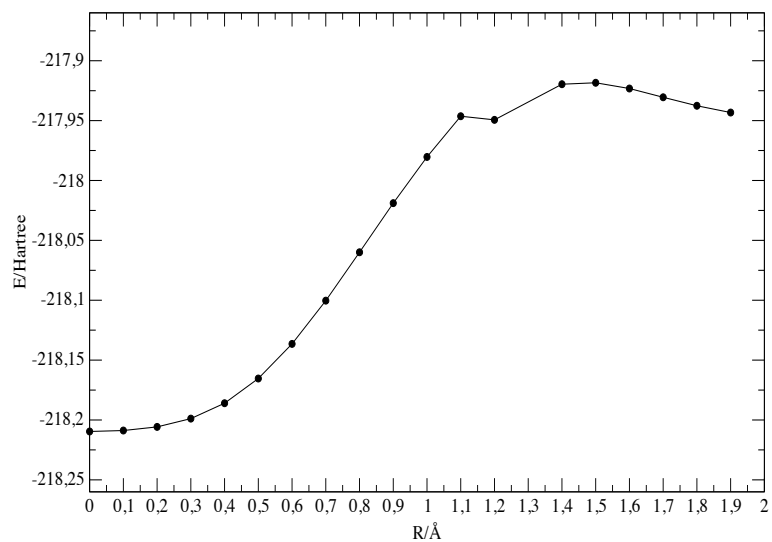


Figure 4.75: Calculated single energy values vs  $R$  for the  $H_{1.4}$  configuration

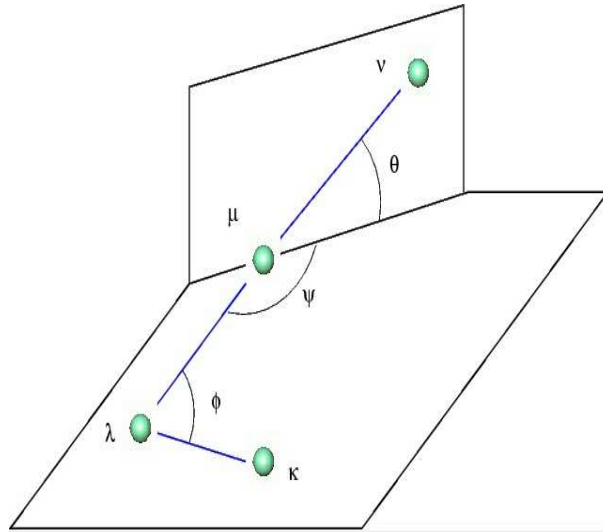


Figure 4.76: Sketch of the angular variable definition

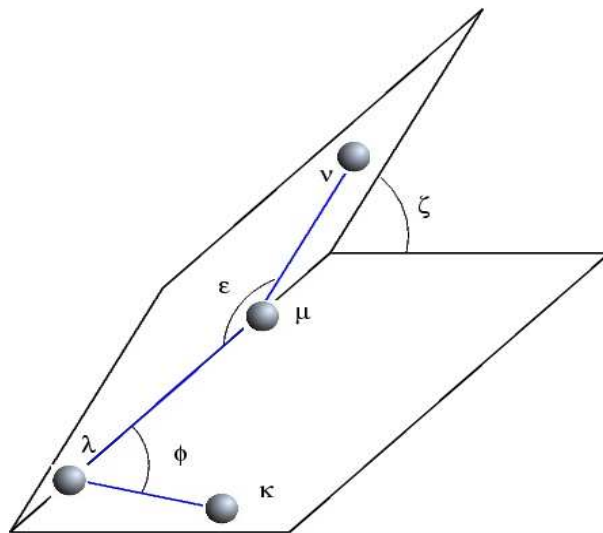


Figure 4.77: Sketch of the new angular variable definition

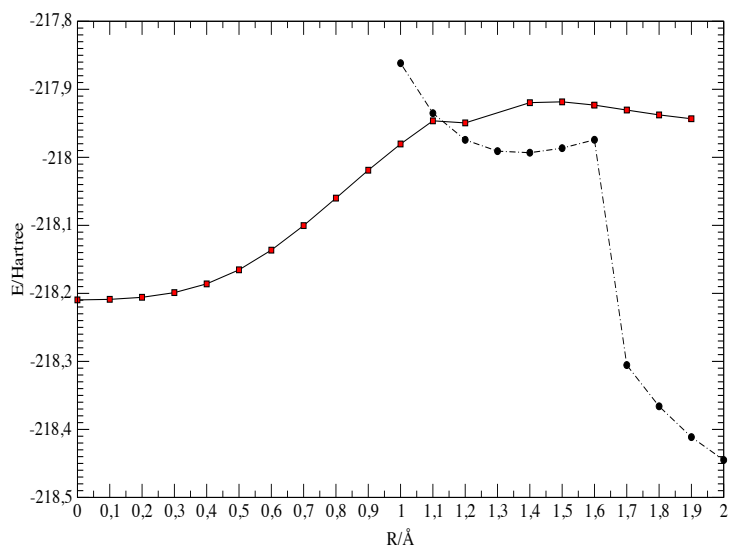


Figure 4.78: Interaction energy values calculated at MP2/cc-pVDZ.

## Chapter 5

### Conclusions

The study carried out in this thesis represents an attempt to design a complete workflow for dealing with quantum reactive scattering calculations of the reactive properties of atom-diatom systems on the grid.

The first and more detailed investigation has been carried out for atom-diatom systems. In the CDK laboratory the related know-how is well consolidated and the software components sufficiently well validated. As a matter of fact, the related workflow can count on the fact that *ab initio* calculations have been performed at high level accuracy (by several groups), that the set of calculated potential energy values is large enough to allow the fitting using different functional forms, that quantum reactive scattering codes are well structured and implemented on the grid and, finally, that the statistical and graphical analysis of the results is properly made. In addition to the appropriate dealing with the physical quantities, the related programs are already suited for the implementation of the Q5cost model and for its possible extension to quantum dynamics.

Less mature is the area of four atom systems. In fact, the work has been confined to the tuning of the job parameters to calculate the *ab initio* potential energy values for sufficiently heavy four atom systems. The search for a proper basis set and for a sufficiently high level method is still ongoing, though both aspects are still progressing having in mind the structuring of quantum chemistry data according to a Q5cost scheme.

However, both the structures found in the electronic structure and the progress made in the grid implementation of the code represent a solid base for future work. As a matter of fact, the work done on the  $N + N_2$  and  $N_2 + N_2$  systems illustrated in the thesis is unprecedented.

## Bibliography

- [1] A. Froman, *J. Chem. Phys.* **36**, 1490 (1962).
- [2] D. Cremer, *Z. He, J. Phys. Chem.*, **100**, 6173 (1996).
- [3] J. Olsen, O. Christiansen, H. Koch, P. Jorgensen, *J. Chem. Phys.*, **105**, 5082 (1996).
- [4] M. L. Leininger, W.D. Allen, H. F. Schaefer, C. D. Sherrill, *J. Chem. Phys.*, **112**, 921, 3 (2000).
- [5] F. Boys, Bernardi, *Mol. Phys.*, **19**, 553 (1970)
- [6] Gaussian 09, Revision **A.1**, M. J. Frisch, G. W. Trucks, H. B. Schlegel, G. E. Scuseria, M. A. Robb, J. R. Cheeseman, G. Scalmani, V. Barone, B. Mennucci, G. A. Petersson, H. Nakatsuji, M. Caricato, X. Li, H. P. Hratchian, A. F. Izmaylov, J. Bloino, G. Zheng, J. L. Sonnenberg, M. Hada, M. Ehara, K. Toyota, R. Fukuda, J. Hasegawa, M. Ishida, T. Nakajima, Y. Honda, O. Kitao, H. Nakai, T. Vreven, J. A. Montgomery, Jr., J. E. Peralta, F. Ogliaro, M. Bearpark, J. J. Heyd, E. Brothers, K. N. Kudin, V. N. Staroverov, R. Kobayashi, J. Normand, K. Raghavachari, A. Rendell, J. C. Burant, S. S. Iyengar, J. Tomasi, M. Cossi, N. Rega, J. M. Millam, M. Klene, J. E. Knox, J. B. Cross, V. Bakken, C. Adamo, J. Jaramillo, R. Gomperts, R. E. Stratmann, O. Yazyev, A. J. Austin, R. Cammi, C. Pomelli, J. W. Ochterski, R. L. Martin, K. Morokuma, V. G. Zakrzewski, G. A. Voth, P. Salvador, J. J. Dannenberg, S. Dapprich, A. D. Daniels, O. Farkas, J. B. Foresman, J. V. Ortiz, J. Cioslowski, and D. J. Fox, Gaussian, Inc., Wallingford CT, 2009.
- [7] DALTON, a molecular electronic structure program, Release 2.0 (2005), see <http://daltonprogram.org/>
- [8] GAMESS-US, General atomic and molecular electronic structure system, M. W. Schmidt, K. K. Baldridge, J. A. Boatz, S. T. Elbert, M. S. Gordon, J. H. Jensen, S. Koseki, N. Matsunaga,

- K. A. Nguyen, S. J. Su, T. L. Windus, M. Dupuis, J. A. Montgomery, *Journal of Computational Chemistry*, **14**, 1347 (1993).
- [9] GAMESS-UK is a package of ab initio programs. See: "http://www.cfs.dl.ac.uk/gamess-uk/index.shtml", M.F. Guest, I. J. Bush, H.J.J. van Dam, P. Sherwood, J.M.H. Thomas, J.H. van Lenthe, R.W.A Havenith, J. Kendrick, "The GAMESS-UK electronic structure package: algorithms, developments and applications", *Molecular Physics*, Vol. 103, No. 6-8, 20 March-20 April 2005, 719-747.
- [10] GAMESS-US documentation: <http://www.msg.ameslab.gov/group/documentation.html>.
- [11] A.M. Arthurs, A. Dalgarno, *Proc. R. Soc. Lond. A* 256, 540 (1960).
- [12] C.F. Curtiss, F.T. Adler, *J. Chem. Phys.* 20, 249 (1952).
- [13] C.F. Curtiss, *J. Chem. Phys.* 21, 2045 (1953).
- [14] G. Gioumousis, C.F. Curtiss, *J. Math. Phys.* 2, 96 (1962).
- [15] C.F. Curtiss, *J. Chem. Phys.* 49, 1952 (1968).
- [16] L.W. Hunter, C.F. Curtiss, *J. Chem. Phys.* 58, 3884 (1973).
- [17] E.A. McCullough Jr, R.E. Wyatt, *J. Chem. Phys.* 51, 1253 (1969).
- [18] E.A. McCullough Jr, R.E. Wyatt, *J. Chem. Phys.* 54, 3578 (1971).
- [19] E.A. McCullough Jr, R.E. Wyatt, *J. Chem. Phys.* 54, 3592 (1971).
- [20] R. Kosloff, *Annu. Rev. Phys. Chem.* 45, 145 (1994).
- [21] N. Balakrishnan, C. Kalyanaraman, N. Sathyamurthy, *Phys. Rep.* 280, 79 (1997).
- [22] J.Z.H. Zhang, *Theory and Application of Quantum Molecular Dynamics*, World Scientific, Singapore, 1999.
- [23] S.C. Althorpe, D.C. Clary, *Ann. Rev. Phys. Chem.* 54, 493 (2003).
- [24] S.K. Gray, G.G. Balint-Kurti, *J. Chem. Phys.* 108, 950 (1998).
- [25] R.S. Judson, D.J. Kouri, D. Neuhauser, M. Baer, *Phys. Rev. A* 42, 351 (1990).
- [26] G.G. Balint-Kurti, R.N. Dixon, C.C. Martson, *Int. Rev. Phys. Chem.* 11, 317 (1992).
- [27] C.C. Marston, G.G. Balint-Kurti, R.N. Dixon, *Theor. Chim. Acta* 79, 313 (1991).

- [28] G.G. Balint-Kurti, F. Götgas, S.P. Mort, A.R. Offer, A. Laganà, O. Gervasi, *J. Chem. Phys.* 99, 9567 (1999).
- [29] A. Aguado, M. Paniagua, M. Lara, O. Roncero, *J. Chem. Phys.* 106, 1013 (1997).
- [30] A. Aguado, M. Paniagua, M. Lara, O. Roncero, *J. Chem. Phys.* 107, 10085 (1997).
- [31] I. Miquel, M. González, R. Sayós, G.G. Balint-Kurti, S.K. Gray, E.M. Goldfield, *J. Chem. Phys.* 118, 3111 (2003).
- [32] P. Gamallo, M. González, R. Sayós, C. Petrongolo, *J. Chem. Phys.* 119, 7156 (2003).
- [33] S.C. Althorpe, *J. Chem. Phys.* 114, 1601 (2001).
- [34] R. Chen, H. Huo, *J. Chem. Phys.* 105, 3569 (1996).
- [35] D. Skouteris, A. Laganà, G. Capecchi, H.J. Werner, *Int. J. Quantum Chem.* 96, 562 (2004).
- [36] D. Skouteris, A. Laganà, G. Capecchi, H.J. Werner, *Int. J. Quantum Chem.* 99, 577 (2004).
- [37] D. Skouteris, L. Pacifici, A. Laganà, *Mol. Phys.* 102, 2237 (2004).
- [38] F. Götgas, G.G. Balint-Kurti, A.R. Offer, *J. Chem. Phys.* 104, 3927 (1996).
- [39] S. Gómez-Carrasco, O. Roncero, *J. Chem. Phys.* 125, 054102 (2006).
- [40] M.D. Feit, J.A. Fleck Jr, A. Steiger, *J. Comp. Phys.* 47, 412 (1982).
- [41] M.D. Feit, J.A. Fleck Jr, *J. Chem. Phys.* 301, 2578 (1984).
- [42] D. Kosloff, R. Kosloff, *J. Comput. Phys.* 52, 35 (1983).
- [43] V. Mohan, N. Sathyamurthy, *Comput. Phys. Rep.* 7, 213 (1988).
- [44] J.V. Lill, G.A. Parker, J.C. Light, *J. Chem. Phys.* 89, 483 (1982).
- [45] J.C. Light, I.P. Hamilton, J.V. Lill, *J. Chem. Phys.* 82, 1400 (1985).
- [46] Z. Bacic, J.C. Light, *J. Chem. Phys.* 85, 4594 (1986).
- [47] F. Le Quéré, C. Leforestier, *J. Chem. Phys.* 94, 1118 (1991).
- [48] F.J. Lin, J.T. Muckerman, *Comp. Phys. Commun.* 63, 538 (1991).
- [49] D.H. Zhang, J.Z.H. Zhang, *J. Chem. Phys.* 101, 1146 (1994).

- [50] G.C. Corey, J.W. Tromp, D. Lemoine, in *Numerical Grid Methods and their Applications to Schrödinger Equation*, C. Cerjan Ed., Kluwer, Dordrecht, 1993; p. 1.
- [51] J.T. Muckerman, R.V. Weaver, T.A.B. Kennedy, T. Uzer, in *Numerical Grid Methods and their Applications to Schrödinger Equation*, C. Cerjan Ed., Kluwer, Dordrecht, 1993; p. 89.
- [52] J.A. Fleck Jr., J.R. Morris, A. Steiger, *Appl. Phys.* 10, 129 (1976).
- [53] C. Lanzcos, *J. Res. Natl. Bur. Stand.* 45, 255 (1950).
- [54] T.J. Park, J.C. Light, *J. Chem. Phys.* 85, 5870 (1986).
- [55] S.K. Gray, *J. Chem. Phys.* 96, 6543 (1992).
- [56] V.A. Mandelshtam, H.S. Taylor, *J. Chem. Phys.* 102, 7390 (1995).
- [57] V.A. Mandelshtam, H.S. Taylor, *J. Chem. Phys.* 103, 2903 (1995).
- [58] A. Vibok, G.G. Balint-Kurti, *J. Chem. Phys.* 96, 7615 (1992).
- [59] A. Vibok, G.G. Balint-Kurti, *J. Chem. Phys.* 96, 8712 (1992).
- [60] G.G. Balint-Kurti, in *Reaction and Molecular Dynamics*, A. Laganà, A. Riganelli Eds., *Lecture Notes in Chemistry*, Vol. 75, Springer-Verlag, Berlin, 2000; p. 74.
- [61] G.G. Balint-Kurti, R.N. Dixon, C.C. Martson, *J. Chem. Soc. Faraday Trans.* 86, 1741 (1990).
- [62] A.J.H.M. Meijer, E. Goldfield, S.K. Gray, G.G. Balint-Kurti, *Chem. Phys. Lett.* 293, 270 (1998).
- [63] R. A. Marcus, *J. Chem. Phys.*, **45**, 4493 (1966)
- [64] V. Aquilanti, S. Cavalli, G. Grossi, *Advances in Molecular Vibrations and Collision Dynamics*, p. 147 (1992)
- [65] F. T. Smith, *J. Chem. Phys.*, **31**, 1352 (1959)
- [66] T. H. Gronwall, *Annals of Mathematics*, **33**, 279 (1932), *Phys. Rev.*, **51**, 655 (1937)
- [67] P. M. Morse, H. Feshbach, *Methods of Theoretical Physics*, McGraw-Hill, New York (1953)
- [68] V. Fock, *Kgl. Norske Videnskab. Forh.*, **41**, 138 (1958)
- [69] J. H. Macek, *J. Phys. B*, **1**, 831 (1968); C. D. Lin, *Phys. Rev. A*, **25**, 1535 (1982)

- [70] L. M. Delves, *Nucl. Phys.*, **9**, 391 (1959), **20**, 275 (1960)
- [71] V. Gallina, P. Nata, G. Viano, *Nuovo Cimento*, **24**, 835 (1962)
- [72] W. Zickendraht, *Ann. Phys.*, **35**, 18 (1965), *Phys. Rev.*, **159**, 1449 (1967)
- [73] F. T. Smith, *J. Math. Phys.*, **3**, 735 (1962); F. T. Smith, *Phys. Rev.*, **120**, 1058 (1960).
- [74] R. T. Pack, G. A. Parker, *J. Chem. Phys.*, **87**, 3888 (1987)
- [75] G.A. Parker, S. Crocchianti, M. Keil, in *Lecture Notes in Chemistry*, **75**, 88 (2000).
- [76] *Theory of Chemical Reaction Dynamics I*, M. Baer Ed. CRC Press Inc., Raton, Indiana
- [77] W. A. Lester, Jr., *Dynamics of Molecular Collisions Part A*, W. H. Miller Ed., p. 6
- [78] D. Skouteris, J.F. Castillo, D.E. Manolopoulos, *Comp. Phys. Comm.*, **133**, 128 (2000).
- [79] G. Herzberg, *Molecular Spectra and Molecular Structure I. Spectra of Diatomic Molecules*, Van Nostrand, New York, 1950.
- [80] M. Baer, D.J. Kouri, in *Theory of Chemical Reaction Dynamics*, D.C. Clary Ed., Reidel, Dordrecht, 1986; p. 167.
- [81] A. Ohasaki, H. Nakamura, *Phys. Rep.* 187, 1 (1990).
- [82] A. Elkowitz, R. Wyatt, *Mol. Phys.* 31, 189 (1976).
- [83] J.M. Bowman, *Adv. Chem. Phys.* 61, 115 (1985).
- [84] R.B. Walker, E.F. Hayes, in *Theory of Chemical Reaction Dynamics*, D.C. Clary Ed., Reidel, Dordrecht, 1986; p. 105.
- [85] J.M. Bowman, *J. Phys. Chem.* 95, 4960 (1991).
- [86] J.M. Bowman, in *Reaction and Molecular Dynamics*, A. Laganà, A. Riganelli Eds., Lecture Notes in Chemistry, Vol. 75, Springer-Verlag, Berlin, 2000; p. 101.
- [87] R.T. Pack, *J. Chem. Phys.* 60, 633 (1974).
- [88] Y. Sun, R.S. Judson, D.J. Kouri, *J. Chem. Phys.* 90, 241 (1989).
- [89] EGEE website: <http://public.eu-egce.org>.
- [90] gLite website: <http://glite.web.cern.ch/glite>

- [91] The Globus Project: <http://www.globus.org>.
- [92] <http://firb.miur.it/> .
- [93] <http://www.grid.it> .
- [94] Metachem: Metalaboratories for complex computational Chemistry Applications, [http://www.cost.esf.org/domains\\_actions/cmst/Actions/Metachem](http://www.cost.esf.org/domains_actions/cmst/Actions/Metachem).
- [95] COMPCHEM website: <http://compchem.unipg.it>.
- [96] A. Laganà, A. Riganeli and O. Gervasi *Lecture Notes in Computer Science*, **3980**, 665-674 (2006).
- [97] W. L. Hase, R. J. Duchovic, X. Hu, A. Komornicki, K. F. Lim, D. -h. Lu, G. H. Peslherbe, K. N. Swamy, S. R. Vande Linde, A. Varandas, H. Wang, and R. J. Wolf VENUS96: A General Chemical Dynamics Computer Program, *Quantum Chemistry Program Exchange*, **16**, 671 (1996)
- [98] Smith, W., Forester, T.R.: DL\_POLY2: a general-purpose parallel molecular dynamics simulation package. *J. Mol. Graph.*, **14**, 136(1996).
- [99] <http://www.univie.ac.at/columbus/>.
- [100] Skouteris, D., Castillo, J.F., Manolopoulos, D.E.: ABC: a quantum reactive scattering program. *Comp. Phys. Comm.*, **133**, 128 (2000).
- [101] H. Meyer, U. Manthe, L. Cederbaum, *Chem. Phys. Lett.*, **165**, 73 (1990).
- [102] U. Manthe, H. D. Meyer, L. S. Cederbaum, *J. Chem. Phys.*, **97**, 3199 (1992) .
- [103] D. M. Ceperley, *Rev. Mod. Phys.*, **67** 279 (1995).
- [104] C. Angeli, G. L. Bendazzoli, S. Borini, R. Cimiraglia, A. Emerson, S. Evangelisti, D. Maynau, A. Monari, E. Rossi, J. Sanchez-Marin, P. G. Szalay, A. Tajti, *IJQC*, **107**, 2082 (2007).
- [105] COST in Chemistry Action D23 <http://costchemistry.epfl.ch/docs/D23/d23.htm>
- [106] E. Rossi, A. Emerson, S. Evangelisti, *Lect. Not. in Comp. Science*, **2658**, 316 (2003).
- [107] Specification of XML can be found at the site (<http://www.w3.org/XML>) ; A.Holmer, XML IE5 Programmer Reference, *Wrox Press*, Chicago, IL, USA, 1999.

- [108] HDF5 a general purpose library and file format for storing scientific data.  
*<http://hd5.ncsa.uiuc.edu/HDF5/>*
- [109] P. Murray-Rust, H. S. Rzepa, M. Wright, *New J. Chem.*, 618(2001).
- [110] P. Casarini, L. Padovani, "The Gnome DOM Engine", accepted paper at the Extreme Markup Laes 2001 Conference, March 2001; see also <http://gdome2.cs.unibo.it/>.
- [111] A. Laganà, E. Garcia, J. Mateos, *Chem. Phys. Lett.*, **176**, 273 (1991)
- [112] A. Aguado, C. Suárez and M. Paniagua, *J. Chem. Phys.*, 101, 4004 (1994).
- [113] L. S. Polak, P. A. Sergeev, D. I. Slovetsky, *High Temp.*, **25**, 13 (1977); Y. B. Golubovskii, V. M. Telezko, *High Temp.*, **22**, 340 (1984)
- [114] A. Laganà, E. Garcia, L. Ciccarelli, *J. Phys. Chem.* 91, 312 (1987).
- [115] A. Laganà, E. Garcia, *J. Chem. Phys.* 98, 502 (1994).
- [116] A. Laganà, G. Ochoa de Aspuru, E. Garcia, *AIAA Journal* 94, 1986 (1994).
- [117] A. Laganà, G. Ochoa de Aspuru, E. Garcia, *Temperature dependence of quasiclassical and quantum rate coefficients for  $N + N_2$* , Centro Stampa, Università di Perugia, Perugia (Italy), 1996.
- [118] I. Armenise, M. Capitelli, E. Garcia, C. Gorse, A. Laganà, S. Longo, *Chem. Phys. Lett.* 200, 597 (1992).
- [119] I. Armenise, M. Capitelli, R. Celiberto, G. Colonna, C. Gorse, A. Laganà, *Chem. Phys. Lett.* 227, 157 (1994).
- [120] F. Esposito, I. Armenise, M. Capitelli, *Chem. Phys.* 331, 1 (2006).
- [121] F. Esposito, M. Capitelli, *Chem. Phys. Lett.* 418, 581 (2006).
- [122] N. Faginas Lago, A. Laganà, R. Gargano, P.R.P. Barreto, *J. Chem. Phys.* 125, 114311 (2006).
- [123] E. Garcia, A. Laganà, *J. Phys. Chem. A* 101, 4734 (1997).
- [124] D. Wang, J. R. Stallcop, W. M. Huo, C. E. Dateo, D. W. Schwenke, H. Partridge, *J. Chem. Phys.*, **118**, 2186 (2003)
- [125] C. Petrongolo, *J. Mol. Struct.* 175, 215 (1988).

- [126] C. Petrongolo, *J. Mol. Struct. (Theochem)* 202, 135 (1989).
- [127] E. Garcia, A. Laganà, *J. Chem. Phys.* 103, 5410 (1995).
- [128] A. Laganà, G. Ochoa de Aspuru, E. Garcia, *J. Phys. Chem.* 99, 17139 (1995).
- [129] A. Laganà, G. Ochoa de Aspuru, E. Garcia, *J. Chem. Phys.* 108, 3886 (1998).
- [130] D. Wang, J.R. Stallcop, W.M. Huo, C.E. Dateo, D.W. Schwenke, H. Partridge, *J. Chem. Phys.* 118, 2186 (2003).
- [131] K. S. Sorbie, J. N. Murrell, *Mol. Phys.*, 29, 1387 (1975).
- [132] A. Laganà and E. García, *Mol. Phys.*, 3, 621 (1985).
- [133] W. H. Press, W. T. Vetterling, S. A. Tenkolsky and B. P. Flannery, *Numerical Recipes in Fortran, the Art of Scientific Computing* (Cambridge, University Press, New York, 1992).
- [134] D.M. Hirst, in *Potential Energy Surfaces, Molecular Structure and Reaction Dynamics*, Taylor & Francis, London, 1985; p. 114.
- [135] K.P. Huber, G. Herzberg, *Molecular Spectra and Molecular Structure IV. Constants of Diatomic Molecules*, Van Nostrand, New York, 1979.
- [136] A. Laganà, *J. Chem. Phys.*, 95, 2216 (1991); A. Laganà, G. Ferraro, E.García, O. Gervasi, A. Ottavi, *Chem. Phys.*, 168, 341 (1992).
- [137] A. Laganà, E.García, *J. Chem. Phys.* 103, 5410 (1995).
- [138] A. Laganà, G. Ochoa de Aspuru and E, Garcia, *J. Phys. Chem.* 99, 17139 (1995).
- [139] A. Laganà, *J. Chem. Phys.* 95, 2216 (1991).
- [140] A. Laganà, G. Ferraro, E. Garcia, O. Gervasi, A. Ottavi, *Chem. Phys.* 168, 341 (1992).
- [141] A. Laganà, *Computers & Chemistry* 4, 137 (1980).
- [142] A. Saracibar, PhD Thesis, September (2007).
- [143] S. Rampino, Tesi di Laurea, Università di Perugia, (2007).
- [144] MOLPRO is a package of ab-initio programs written by H.J. Werner, P.J. Knowles, with contributions from J. Almlof, R.D. Amos, A. Berning, D.L. Cooper, M.J.O. Deegan, A.J. Dobbyn, F. Eckert, S.T. Elbert, C. Hampel, R. Lindh, A.W. Lloyd, W. Meyer, A. Nicklass,

K. Peterson, R. Pitzer, A.J. Stone, P.R. Taylor, M.E. Mura, P. Pulay, M. Schutz, H. Stoll, T. Thorsteinsson.

- [145] D. Wang, W. M. Huo, C. E. Dateo, D. W. Schwenke, J. R. Stallcop, *Chem. Phys. Lett.*, **379**, 132 (2003).
- [146] D. Wang, W. M. Huo, C. E. Dateo, D. W. Schwenke, J. R. Stallcop, *Chem. Phys. Lett.*, **120**, 6041 (2004).
- [147] A. N. Wright e C. A. Winkler, *Active Nitrogen*, Academic Press, New York, (1968).
- [148] G. Giordano, L. Maraffa, Proceeding of the AGARD-CP-514 Symposim in Theoretical and Experimental Methods in Hypersonic Flows, 26-1 (1992)
- [149] *Non-equilibrium Vibrational Kinetics*, M. Capitelli Ed., Springer-Verlag, Berlin, 1986.  
*Non-equilibrium Processes in Partially Ionized Gas*, M. Capitelli Ed., J. N. Bardsley Eds., Plenum, New York, 1990.
- [150] R. M. Berns, A. van der Avoird, *J. Chem. Phys.*, **72**, 6107 (1980).
- [151] A. van der Avoird, P. E. S. Wormer, A. P. J. Jansen, *J. Chem. Phys.*, **84**, 1629 (1986).
- [152] E. L. Heck, A. S. Dickinson, *Mol. Phys.*, **81**, 1325 (1994).
- [153] E. L. Heck, A. S. Dickinson, V. Vesovic, *Mol. Phys.*, **83**, 907 (1994).
- [154] S. W. M. Huo, S. Green, *J. Chem. Phys.*, **104**, 7572 (1996).
- [155] J. R. Stallcop, H. Partridge, *Chem. Phys. Lett.*, **281**, 212 (1997).
- [156] A. Wada, H. Kanamori, S. Iwata, *J. Chem. Phys.*, **109**, 9434 (1998).
- [157] O. Couronne, Y. Ellinger, *Chem. Phys. Lett.*, **306**, 71 (1999).
- [158] K. Leonhard, U. K. Deiters, *Mol. Phys.*, **100**, 2571 (2002).
- [159] M. H. Karimi Jafari, A. Maghari, S. Shahbazian, *Chem. Phys.*, **314**, 249 (2005).
- [160] L. Gomez, B. Bussery-Honvault, T. Cauchy. M. Bartolomei, D. Cappelletti, F. Pirani, *Chem. Phys. Lett.*, **445**, 99 (2007).
- [161] C. Møller, M. S. Plesset, *Phys. Rev.*, **46**, 618 (1934).
- [162] J. C. Raich, N. S. Gillis, *J. Chem. Phys.*, **66**, 846 (1997).

- [163] T. B. MacRury, W. A. Steele, B. J. Berne, *J. Chem. Phys.*, **64**, 1288 (1976).
- [164] P. S. Y. Cheung, J. G. Powles, *Mol. Phys.*, **32**, 1383 (1976).
- [165] P. S. Y. Cheung, J. G. Powles, *Mol. Phys.*, **30**, 921 (1975).
- [166] D. J. Evans, *Mol. Phys.*, **34**, 103 (1998).
- [167] D. Cappelletti, F. Vecchiocattivi, F. Pirani, E. L. Heck, A. S. Dickinson, *Mol. Phys.*, **93**, 485 (1998).
- [168] V. Aquilanti, M. Bartolomei, D. Cappelletti, E. Carmona-Novillo, F. Pirani, *J. Chem. Phys.*, **117**, 615 (2002).
- [169] T. H. Dunning Jr., *J. Chem. Phys.*, **90**, 1007 (1989).
- [170] P. J. Hay, R. T. Pack, R. L. Martin, **81**, 1360 (1984).
- [171] P. Piecuch, S. A. Kucharski, K. Kowalski, M. Musial, *Comp. Phys. Commun.*, **149**, 71 (2002).